A COMPLEMENTARY APPROACH FOR THE IDENTIFICATION OF DARK MATTER

Tesis doctoral presentada por

Miguel Peiró García

para optar al título de Doctor en Ciencias Físicas

Tesis doctoral dirigida por:

David G. Cerdeño

Universidad Autónoma de Madrid & Instituto de Física Teórica
IFT-UAM/CSIC

Universidad Autónoma de Madrid

Departamento de Física Teórica

Instituto de Física Teórica IFT-UAM/CSIC

A COMPLEMENTARY APPROACH FOR THE IDENTIFICATION OF DARK MATTER

Miguel Peiró García

Madrid, Mayo de 2014

Esta tesis esta dedicada a todos
los que me quieren mucho, como la...

Contents

Abstract

Castellano

En esta tesis se aborda el problema de la materia oscura en el Universo desde el punto de vista de la física de partículas elementales. Diferentes observaciones han mostrado que el 85 % del contenido total de materia del Universo se corresponde con un nuevo tipo de materia, que no emite ni absorbe luz, y que por lo tanto se conoce como materia oscura. La detección e identificación de este nuevo componente exótico, constituye una de las cuestiones a resolver más importantes de la física moderna.

Actualmente existen numerosos experimentos que tratan de detectar a estas elusivas partículas. Por un lado, se cree que la materia oscura puede ser cazada usando grandes detectores situados bajo tierra con los cuales la materia oscura chocaría y tras esto, depositaría una cierta cantidad de energía en el detector en cuestión. Este tipo de detección se conoce como detección directa de materia oscura. También se espera que la materia oscura pueda detectarse indirectamente, es decir, tratando de detectar partículas, como por ejemplo fotones, que podrían crearse cuando dos partículas de materia oscura se encuentran y chocan en algún punto de nuestra galaxía. Finalmente, los grandes aceleradores de partículas, como el LHC, también podrían detectar materia oscura que se habría creado en los choques de partículas que allí tienen lugar. Esta situación experimental actual es tremendamente excitante. Algunos de estos experimentos han observado posibles indicios que pudieran atribuirse a materia oscura ligeras (más concretamente a partículas con masas alrededor de 10 GeV). Además, los experimentos están aumentando su sensibilidad y pronto serán capaces de cubrir amplias regiones del espacio de parámetros de modelos de materia oscura. Por lo tanto, parece plausible que la materia oscura se pueda detectar en un futuro próximo . La pregunta es entonces, tras una detección en un hipotético futuro, cómo de bien podemos determinar los parámetros que definen la naturaleza de estas partículas de materia oscura. Como se estudia en esta tesis, utilizar la información de las tres fuentes de detección mencionadas es crucial para identificar

esta partícula abundante, pero evasiva, del Universo.

En esta tesis se hace un análisis exhaustivo del problema de la materia oscura desde un punto de vista teórico. En el capítulo 1, se hace una introducción de cuáles han sido las observaciones más relevantes que demuestran la existencia de la materia oscura en el Universo, y que nos han permitido conocer cuales son las propiedades genéricas de este nuevo tipo de materia. También, se describe con detalle cual es la situación experimental actual, tanto en búsquedas directas como indirectas que podrían estar apuntando a la existencia de materia oscura ligera. Además se hace una breve descripción de cómo el descubrimiento del bosón de Higgs en el LHC nos brinda nueva información acerca de las propiedades de estas partículas. En el capítulo 2, se analizan tres modelos supersimétricos, estudiando bajo que condiciones la materia oscura ligera es viable. Como candidatos a materia oscura en estos modelos se tiene al Neutralino (uno de los candidatos mas estudiados en la bibliografía) y al Sneutrino. Para determinar la viabilidad de estos candidatos se han usado los últimos datos experimentales del LHC, así como de otros aceleradores y experimentos de física de altas energías. En el caso del Sneutrino, siendo un candidato mucho menos estudiado en la literatura, se ha mostrado su flexibilidad como candidato a materia oscura ligera y además se ha estudiado analíticamente su relación con los bosones de Higgs del modelo. Finalmente, en este capítulo, se han mostrado cuales son las predicciones de cada uno de los candidatos en experimentos de detección directa e indirecta, comparando con las búsquedas actuales y comentando la situación futura en cuanto al descubrimiento de estos.

En el capítulo 3, se hace un estudio teórico en profundidad de la detección directa de materia oscura ligera. Tras una introducción al formalismo, se muestra la relación de este tipo de búsquedas con la física de partículas, la astrofísica y la física nuclear. En la primera mitad del capítulo, se muestra como el conocimiento de estas áreas es fundamental cuando se trata de entender una posible señal de materia oscura en un detector (lo que denominamos recontrucción de la señal). Una de las partes más importantes de este capítulo se basa en entender como la física nuclear puede afectar a las recontrucciones (a través de las funciones de estructura de los diferentes núcleos usados en los detectores). Un resultado muy importante de este estudio concluye que estos efectos pueden ser tan importantes como los astrofśicos (muy usados y conocidos en anteriores estudios). Con este propósito se utilizan técnicas de estadística Bayesiana. Además se propone un método consistente y robusto para incluir estos efectos en las reconstrucciones. En la segunda mitad del capítulo 3, se analiza cómo maximizar las posibilidades de conocer la naturaleza de la materia oscura si esta es detectada en este tipo de experimentos. Aquí se demuestra que es vital usar más de un tipo de material en el detector, ya que usando

solo Germanio y Xenon (los más comunes actualmente) no permite hacer una buena recontrucción de la señal. Para ello se proponen materiales basados en Flúor, Aluminio y Tungsteno, que son capaces de aportar información complementaria a aquella dada por Germanio y Xenon, y que por tanto permiten en muchos casos determinar unívocamente la naturaleza de la materia oscura a partir de su detección.

El capítulo 4 esta dedicado a las búsquedas indirectas de materia oscura en el centro de la Vía Láctea usando rayos gamma. Esperamos, que en el centro de nuestra de galaxía haya grandes acumulaciones de materia oscura, especialmente si un proceso conocido como contracción adiabática de la materia oscura es dominante en esta región. Esto hace que allí la probabilidad de que dos partículas de materia oscura se aniquilen dando lugar a fotones sea alta. Usando los últimos datos del satélite *Fermi*-LAT (el instrumento actual más sensible en este tipo de búsquedas) extraemos restricciones sobre la sección eficaz de aniquilación de la materia oscura y comparamos con las restricciones extraídas usando datos de por ejemplo las galaxías enanas esferoidales (compuestas principalmente de materia oscura). Esto requiere cálculos precisos y detallados de todos los procesos físicos en los que la materia oscura participa, como el *Inverse Compton Scattering*, y que dan lugar a fotones provenientes desde el centro de nuestra galaxía. Finalmente, se comparan estos límites con las predicciones de los candidatos analizados en el capítulo 2. Por completitud, se muestra que el Sneutrino ligero podría ser el causante de una señal en fotones que viene del centro galáctico y que ha sido observada por el satélite *Fermi*-LAT.

Por último, hemos dejado para el capítulo 5 las conclusiones generales extraídas en cada uno de los capítulos, haciendo especial énfasis en la importancia del trabajo realizado en esta tesis.

English

This Thesis is devoted to the dark matter problem in the Universe from the point of view of elementary particle physics. Different observations have shown that 85% of the total matter content of the Universe corresponds to a new type of matter that does not emit or absorb light, and is therefore referred to as dark matter. The detection and identification of this exotic component constitutes one of the most important questions in modern physics.

Currently there exist numerous experiments aimed at detecting these elusive particles. On the one hand, dark matter can be hunted using huge detectors placed underground where dark matter would collide and thus it would release some amount of energy in the detector. This sort of detection is named dark matter direct detection. It is also expected that dark matter might be detected indirectly, this is, by trying to detect particles like photons that could be created when two dark matter particles annihilate. Finally, inside large particle accelerators, such as the LHC, dark matter could be detected as well since it is expected to be created in the particle collisions which take place there. This experimental situation is exciting. Some of these experiments might have already seen hints that could be attributed to light dark matter particles (more specifically to particles in the mass range of 10 GeV). Furthermore, the experiments are increasing their sensitivity and will soon be able to cover wide ranges of the parameter space of dark matter models. It thus seems plausible that DM can be detected in the near future. The question is then, upon a hypothetical future detection, how well can we determine the DM parameters. As it is argued in this thesis, using the information from these three sources is crucial to identify this abundant, but elusive component of the Universe.

In this thesis a comprehensive analysis of the dark matter problem is done from a theoretical point of view. In chapter 1, we introduce the most relevant observations that show the existence of the dark matter, and they have also allow us to determine what are its general properties. It is also described in detail the current experimental situation, both about direct and indirect searches, that might be pointing out the existence of light dark matter. Besides, we comment on the new implications that the discovery of the Higgs boson at the LHC has on the properties of dark matter particles. In chapter 2, we will analyze three supersymmetric models studying under what conditions light dark matter particles are viable. As dark matter candidates in these models we have the Neutralino (one of the most studied candidates in the literature) and Sneutrino. To determine the viability of these candidates the most recent experimental constraints from the LHC are used, as well as from other accelerators and in general high energy physics

experiments. For the Sneutrino, being a less studied candidate, we will show the flexibility of the model to provide a light dark matter candidate, and furthermore the connection of Sneutrinos to the Higgs bosons of the model is analyzed by means of analytic expressions. Finally, in this chapter, we will show the direct and indirect detection prospects of each candidate comparing with the current situation and comment on future implications.

In chapter 3, a deep theoretical study of direct detection of light dark matter is done. After an introduction to the formalism, we will show the relation between these kind of searches and particle physics, astrophysics and nuclear physics. In the first half of the chapter, we show how important are the uncertainties in these fields when interpreting a potential dark matter signal in a detector (we denominate this as reconstruction of the signal). One of the key points of the chapter is based on the understanding of the effect that the nuclear uncertainties have in a reconstruction (through the structure functions of different nuclei used as detectors) and how these uncertainties can be as important as the astrophysical ones (very used and understood in previous studies). For this purpose we use Bayesian statistics techniques. Besides, we will propose a consistent and robust method to include nuclear uncertainties in the reconstructions. In the second half of the chapter, we analyze how to maximize the probability to extract the properties of the nature of the dark matter if it is detected in one of these experiments. Here we have demonstrated that it is vital to use more than one kind of detector materials, since by using only Germanium and Xenon (the most common nowadays) it is not possible to fully reconstruct the signal. We propose other materials based on Fluorine, Aluminium and Tungsten that are able to provide complementary information to that of Xenon and Germanium, and thus allowing in many cases to determine univocally the nature of dark matter.

Chapter 4 is dedicated to indirect dark matter searches in the centre of the Milky Way using gamma-rays. As it is known, the centre of our galaxy concentrates big accumulations of dark matter, specially if a process known as adiabatic contraction is dominant in this region. This makes the probability of two dark matter particles annihilating there very high. Using the latest data from the *Fermi*-LAT satellite (the most sensitive instrument for this type of searches) we extract constraints on the annihilation cross section of dark matter particles, comparing them with other constraints extracted for instance using dwarf spheroidal galaxies (composed by dark matter mainly). This requires very precise and detailed calculations of all physical processes in which dark matter is involved, such as the Inverse Compton Scattering that produce photons at the galactic centre. Finally, we compare these limits with the predictions of the candidates presented in chapter 2. For the sake of completeness, we show that the Sneutrino might

be responsible of a photon excess observed by *Fermi*-LAT coming from the inner part of the galaxy.

Finally, we have left for chapter 5 the general conclusions extracted in each of the chapters, making a special emphasis on the importance of the work done in this thesis.

Chapter 1

Introduction and motivation

Physics is a natural science that involves the study of matter. More broadly, it is the general analysis of nature, conducted in order to understand how the Universe behaves. Of course, for this purpose, a key point is to know the content of the Universe. As far as we know, the energy density of the Universe is divided up in the following way: around the 73% corresponds to Dark Energy (DE), the 23% owing to Dark Matter (DM) and finally about the 4% of the energy density comes from the Atoms [1]. Therefore, it seems to be clear that the identification of the dark matter nature, whatever it is, is one of the biggest problems in modern physics.

The history of DM goes back to the beginning of the past century. The first evidence of DM is usually attributed to the Swiss astronomer Fritz Zwicky, who studied the peculiar velocities in the Coma cluster back in the 1930's [2]. But already before him in the 1920's, the British astronomer James Jeans, suggested the presence of about three "dark" stars to each luminous star, by studying the vertical motions of stars near the Galactic plane [3]. However, the scientific community almost ignored these hints until mid 1970's. Was the American astronomer Vera Rubin and collaborators from 70's onwards, who finally supported the existence of a considerably amount of a dark population presents in the galaxies. At that time, the hypotheses that such population was made of stars and gas were not convincing.

On the one hand, in the early 80's, it was already known that the nature of this dark population could not be baryonic, otherwise it would be in conflict not only with Big Bang Nucleosynthesis (BBN) but also with the tiny temperature fluctuations present in the Cosmic Microwave Background (CMB), first discovered in 1964. On the other hand, at that time the Standard Model of particle physics (SM) was a very well established microscopic theory of nature whose culmination took place in the mid 70's with the

discovery of quarks. Although this theory unifies satisfactorily the Strong, Weak and Electromagnetic (EM) interactions in an elegant way (by means of the symmetries), it does not include a succesful non-baryonic DM candidate. At the beginning, theorists tested the possibility that neutrinos (being electrically neutral would not interact with photons) could account for DM, however neutrinos are so light that they failed in reproducing the large scale structures (LSS) we see today. Actually, the problem of the neutrinos as DM candidates is just an example of the lack of validity of any Hot DM (HDM) candidate, they predict galaxies to be younger than what it is seen. This highlighted the need to extend the SM to include a satisfactory DM candidate.

There have been tens of candidates proposed in the literature emerging from theories Beyond the SM (BSM) until now. Among them, there is a class of particles which has specially attracted the attention of the community, Weakly Interacting Massive Particles (WIMP's). These WIMP's, as the name indicates, are particles which only interacts with ordinary matter via Weak interaction, and they were already proposed in the late 70's [4, 5]. Since they are massive as well, they form the Cold Dark Matter (CDM), which already at that time was known to satisfy most of the astronomical constraints [6]. The main advantage of this kind of particles is that they can naturally account for the observed amount of DM in the Universe nowadays. Furthermore these particles are already predicted in some of the best motivated extensions of the SM, like Supersymmetry (SUSY) for instance.

Another important feature of WIMP's is their detectability. In the mid 80's, it was proposed that if the galactic halo was made of particles with weak interactions and masses ranging from one to thousands of GeV, it was feasible to detect them in current (at that time) neutrino detectors, by means of their elastic scattering with target nuclei [7]. This gave rise to a whole set of experiments that today are grouped into what we call direct detection of DM. Another promising way to detect DM is the so called indirect detection. It is based on the search for the cosmic radiation produced by DM annihilations or decay into SM particles, which later produce a flux of cosmic rays and photons. For WIMP's, the flux rates predicted at the Earth are promising, and therefore several experimental collaborations have built telescopes tuned to detect those fluxes. Last but not least important, DM can also be produced directly at the earth. It is expected that if DM is mainly composed by WIMP's, these might be produced at particle accelerators, such the Large Hadron Collider (LHC), and escaping from the detectors after being produced which would leave a missing energy signal.

1.1 Evidences of Dark Matter

Let us now mention in more detail the most convincing and historically relevant evidences that have led us to the belief that the Universe is permeated by a mysterious and dark substance.

The first strong evidence in support of the presence of DM at the scale of cluster of galaxies was given by Fritz Zwicky in 1933 [2]. Much later, Vera Rubin's group measured, what is probably the most used evidence by the community nowdays, the flat rotation curves [8–10]. Modern techniques, such as gravitational lensing or sophisticated X-ray spectroscopy, have just increased the number of supporting evidences. For a review on the astronomical evidences of DM the reader is referred to [3] (Buscar mas referencias).

1.1.1 Cluster of galaxies

Zwicky's method was based on the virial theorem [2]. This theorem relates the total kinetic energy of a system to its virial,

$$\overline{\sum m_i v_i^2} = -\frac{1}{2}\overline{\sum \mathbf{r}_i \cdot \mathbf{F}_i} \ , \tag{1.1}$$

where the index i runs over all the objects composing the system, m_i and v_i are their individual masses and velocities, and finally the vectors $\mathbf{r}_i$ and $\mathbf{F}_i$ denote their positions and total force acting on the object as a result of its interaction with all of the other objects of the system.

He used the Coma cluster, which is composed by around 1000 galaxies, to infer its total mass from the velocities of the objects inside using the equation 1.1. For a gravitationally dominated system, and assuming a uniform distribution of mass over a sphere of radius R (the radius of the cluster), the formula 1.1 can be written in the following way,

$$\overline{\sum m_i v_i^2} = M v_0^2 = -G\frac{M^2}{R} \ , \tag{1.2}$$

with the relative velocity between the cluster and the Earth given by v_0. M is the averaged mass of cluster, so it can be calculated once the velocity of the cluster is known. The galaxy velocities cannot be calculated in general, but the relative (along the line of sight) velocities could be found via Doppler redshift, and Zwicky used this for his calculation. He found that the averaged mass of the cluster was around $10^{10} M_\odot$. However, the average luminosity of the cluster is near 10^7 solar luminosities, and since the stars should have a mass to light ratio (M/L) of order one, the mass inferred is around $10^7 M_\odot$. Zwicky's analysis revealed a discrepancy between the kinematical (based only

the gravitational interaction of the objects) and luminosity measurement (assuming that the cluster is dominated by stars) of three orders of magnitude. These measurements opened the possibility of the existence of some kind of non-luminous (hence dark) matter that provides the greater part of the mass of the cluster.

At that time, tests of Einstein's theory were just starting and the first cosmological measurements were taking place. Probably to imagine some kind of non-luminous matter was quite revolutionary, and taking into account that galaxies were some distant and complex objects, it is not surprising that Zwicky's discover was mostly ignored during few decades until someone else found hints of this new DM.

1.1.2 Galactic rotation curves

Forty years later, Vera Rubin and Kent Ford began a detailed analysis of the kinematical properties of the nearby Andromeda galaxy (M31). Until then, the old technology required several hours or even nights of observation to accumulate enough light to measure the frequency shifts of a given portion of Andromeda. New technology came up in the 70's, allowing V. Rubin to performed a more precise measurement of the Hydrogen cloud's velocity. According to Newtonian dynamics the circular velocity of an object at r is given by:

$$v_c(r) = \sqrt{G\frac{M(r)}{r}} \ , \tag{1.3}$$

where $M(r)$ is the mass enclosed by an sphere of radius r. This velocity is expected to decrease far away from the center, when the enclosed mass starts to be constant. For M31, what they were expecting is that hydrogen cloud's velocity decrease like $1/r^{1/2}$ when the radius is large enough to close all the luminous matter of the galaxy. However the found results showed a different behaviour.

In the left panel of Figure 1.1 the rotation curve as a function of the distance measured by Rubin and Ford for M31 is shown. The data for large radii shows an almost scale independent behavior pointing out the possibility that there could be some non-luminous mass contributing rather significantly to the Andromeda's total mass. Vera's group needed some more time to reveal that Andromedas was not an exception but all spiral galaxies they looked at showed the same behavior [9, 10].

At the mid 80's other groups measured the rotation curves in spiral galaxies as well. In the right panel of Figure 1.1 we can see the rotation curve for the spiral galaxy NGC 3198 measured by Albada et al. in 1984. The results were also the same, at some distance

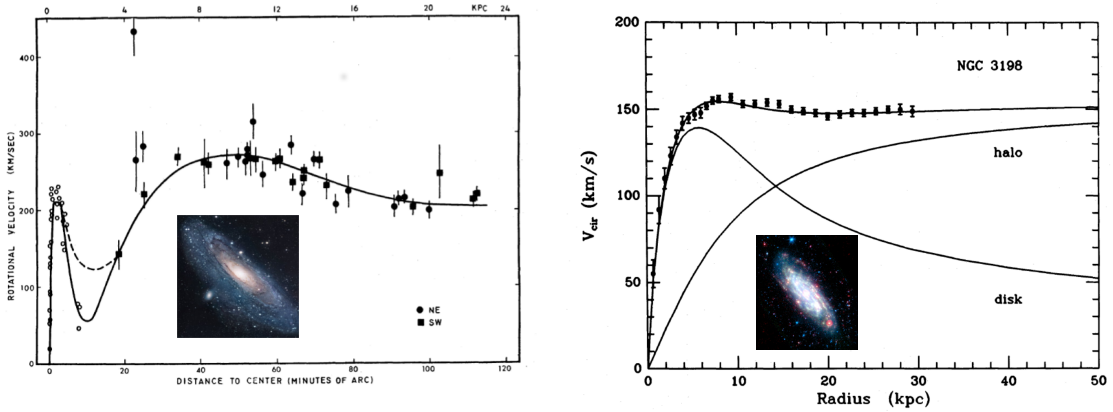

Figure 1.1: Left: Original M31 rotation curve as a function of the distance to the galactic center, measured by Rubin and Ford in [8]. The solid and dashed lines correspond to different analytical fits to the data. Figure taken from [8]. Right: Original NGC 3198 spiral galaxy rotation curve measured by Albada *et al.* Figure taken from [11]. The insets are images of each of the galaxies M31 and NGC 3198.

from the galactic center, the rotational velocities remain constant. It was then clear that spiral galaxies might contain a vast amount of DM.

1.1.3 Dark Matter at cosmological scales

The presence of DM had been confirmed at galactic and extragalactic scales as we have already mentioned. However, still one question did not have an answer: was DM dominating at cosmological scales as well?.

At galaxy clusters scale, the clearest indication for Dark Matter's existence comes from different kind of measurements like gravitational lensing [12, 13], gas temperature through X-ray's emission [14, 15] and the movement of the cluster itself. For instance in Refs. [14, 15] , the masses of the galaxies in the Coma cluster, as well as, the hot gas mass in the same cluster were measured using two different and independent ways. The first method was based on Zwicky's method, and the second one was using the X-ray map ROSAT [16]. Both gave the same total mass. Assuming that this cluster is big enough to be a representative part of the whole universe, they were able to measure a baryon density and, thus, an approximate Dark Matter density.

However, the most precise measurements of the energy and matter budget of Universe come from the CMB. According to the current cosmological paradigm, the Universe was a very hot, dense, and ionized soup. The tight coupling between radiation and matter

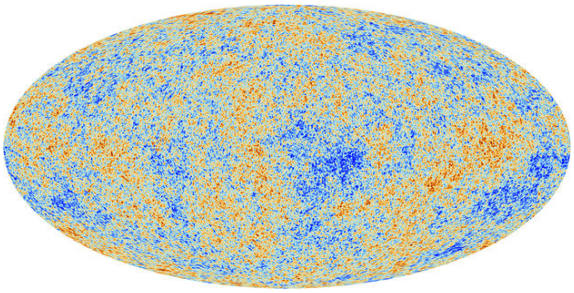

Figure 1.2: The anysotropies of the CMB as observed by PLANCK. Figure taken from [26].

density before decoupling prevented baryons to collapse, and caused a phase oscillation of primordial adiabatic perturbations. At the time of photon's decoupling, these perturbations were imprinted in what today is known as CMB. The CMB is like a temperature picture of the Universe (due to the oldest light that traveled freely from the decoupling moment until now) when it was 380.000 years old. For reviews on CMB physics see for instance [17, 18]. The first measurement of the CMB fluctuations was made by the COBE satellite [17], which already supported the existence of a CDM component of the Universe [19]. The new century brought us the CMB precision era with the Wilkinson Microwave Anisotropy Probe (WMAP) satellite [20]. The tiny fluctuations of the CMB temperature[1] and its power spectrum were measured with an unprecedented sensitivity [21–25], and again supported the existence of large amount of CDM at cosmological scales. Although WMAP reached a very high precision, the PLANCK satellite is the latest and most precise measurement of the CMB ever done. Figure 1.2 shows the temperature map of the CMB as measured by PLANCK satellite.

PLANCK results further confirm the success of the current cosmological model ΛCDM. According to this, the energy of the Universe is dominated by DE (Λ), and the matter content is dominated by CDM whose density is [1],

$$\Omega_{CDM}h^2 = 0.1199 \pm 0.0027 \ , \tag{1.4}$$

in units of h^2, the Hubble constant squared. This is the number density of CDM in the Universe, and it is a very useful and powerful number, since it serves, as we will see later, to constrain DM candidates.

[1] These correspond to density fluctuations and they are the seeds of all structures we see today.

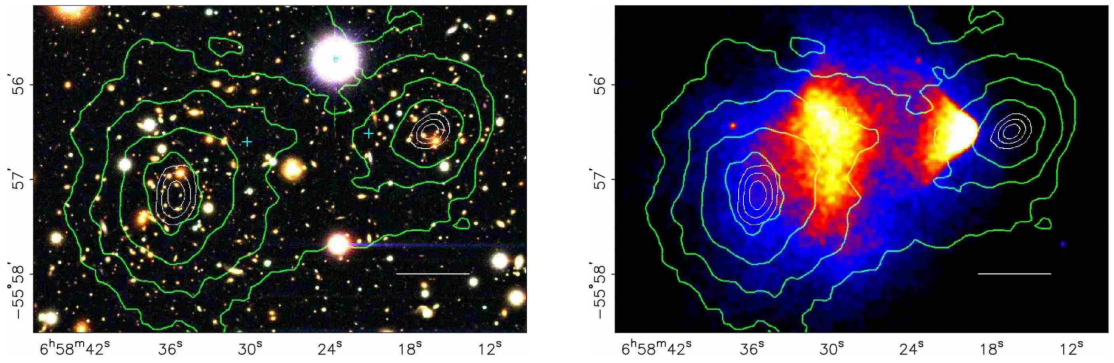

Figure 1.3: The Bullet cluster in different wavelengths with equidensity levels of the gravitational potential of the cluster inferred using weak lensing (green contours). Left: Visible wavelengths. Right: X-ray wavelenghts. Figure taken from [28].

1.1.4 The Bullet cluster

It seems clear that the matter content at scales of the whole Universe, cluster of galaxies and galaxies is dominated by DM. However, the nature of DM is still under debate. There exist different possibilities or alternatives to explain what is DM made of. The most accepted solution is that DM is composed of one (or more) non-baryonic and electrically neutral kind of particles. Nevertheless, it is worth mentioning that since all evidences of DM until now are related somehow to the effect of gravity at large distances, there have been attempts to explain the astronomical observations by modifying the Newton's law of gravity. Among this class of models, probably the best known is the Modified Newton Dynamics (MOND) proposed in the mid 80's [27]. Let's see what the Bullet cluster might point out in this debate.

The Bullet cluster (1E 0657-558) is a group of two colliding cluster of galaxies which receives its name from the small cluster which, as it can be seen in Figure 1.3, is escaping from the big cluster [28–30]. These clusters should have collided some time ago and as a result of that collision, each individual structure was distorted. Part of the baryonic component in form of the stars of the galaxies were almost unaffected by the collision (see the left panel of Figure 1.3). Unlike this, the other baryonic component of the galaxies, in form of a hot gas, interacted slowing down the velocity and reaching very high temperatures and, in consequence, emitting high intensity X-rays (right panel of Figure 1.3). However, weak lensing measurements have revealed that most of the mass of the cluster does not follow the baryonic component but it follows the distribution of galaxies, as it can be seen represented by green isodensity contours in Figure 1.3.

This would be easily explained if DM was composed by collisionless particles which at the moment of the cluster collision just past away from each other. This observation is difficult to reconcile with MOND theories alone, yet it has been argued that the marriage of MOND and HDM in form of neutrinos could explain this issue [31].

1.2 Particle Dark Matter

As we have already seen, there are several strong evidences supporting the existence of DM. Furthermore, the Bullet cluster seems to indicate that DM must be composed of particles, or at least most of it. Since neither baryons nor neutrinos[2] can account for these observations, the SM must be extended in order to explain this problem. In the DM market there exist many particle candidates, motivated either theoretically or phenomenologically, and with quite different prospects for detection. See Ref. [33] and references therein for a description of the most relevant particle candidates.

1.2.1 A casting of the candidates

For particle to be a good DM candidate there are several requirements. In Ref. [34], the authors propose a ten point test that any particle has to pass in order to be considered as a viable DM candidate. This section summarizes the most important conditions, at least from a theoretical point of view.

Relic abundance: As we have seen in Section 1.1.3 the CMB provides an excellent constraint on the DM abundance of the Universe. Any particle aspiring to be a viable DM candidate should match the appropriate relic density. Strictly speaking, this constraint only puts an upper bound since the hypothesis of multi-component DM[3] would be in perfect agreement with the CMB. Besides, this requirement is related to the fact that whatever the candidate is, it must be stable at least at time scales comparable to the age of the Universe, otherwise we would not observe DM nowadays. In particle physics, this can be achieved by imposing a symmetry[4] which makes the candidate stable. Even if it is not stable, its decay lifetime must exceed $\tau \gtrsim (4.354 \pm 0.012) \times 10^{17}$ s [1].

[2] Not only that they belong to HDM but also since their relic density is given by $\Omega_\nu = m_\nu/91.5$ eV, in order to be Dark Matter the neutrino mass (this is the sum of the three neutrino flavor masses) should be $m_\nu = 9.15$ eV, much higher than the cosmological upper bound [32]. This implies that neutrinos are only a fraction of dark matter.

[3] In other words, the abundance of the particle considered would be lower than the CMB prediction.

[4] As we will see later, R-parity in SUSY prevents the lightest particle to decay. K-parity and T-parity play the same role in Universal Extra Dimensions (UED) and Little Higgs models respectively.

Cold: The *Hot*, *Warm* and *Cold* DM terminology was adopted in the 80's [35], and it refers to the free-streaming length of DM particles in the early Universe. It can be naively understood in the following way: after the Universe became matter dominated, the Dark Matter density perturbations started to grow, and baryons and photons got trapped around gravitational potential wells. When the photons decoupled from the primordial plasma, the baryons were still trapped and thus the perturbations grew more and more. This process led to the formation of the LSS we observe today. It all started with the DM density fluctuations and hence must be related with DM microphysics somehow. Now, if DM is composed by hot particles, or in other words, relativistic particles, their free-streaming length would be huge, allowing only big (of the order of the length) structures to form and erasing small structures. In this picture, the small structures would have been generated from the fragmentation of the big ones, which are predicted to be younger than expected as well. These kind of processes have been shown to be in contradiction with current N-body simulations [36].

Unlike HDM, non-relativistic DM particles would form structures with a variety of sizes, since their free-streaming length would be much smaller. These kind of DM is denoted by CDM. N-body simulations have shown a great agreement with observations when CDM was used, however, there are still some open problems that CDM seems to be unable to explain. The *missing satellites problem* [37], and *too big to fail* [38] are an example. The Warm DM (WDM) paradigm was born as one of the most successful alternatives to CDM in solving the problems at small scales being indistinguishable at large scales. The free-streaming length is between hot and cold DM particles. The Lyman-α-forest provides one of most powerful tools to constrain the mass of WDM candidates [39]. Nonetheless, it is worth mentioning that it has been demonstrated that, unless new production mechanisms are invoked, WDM does not work better than CDM at small scales, since its power spectrum falls off too rapidly [40].

Neutral: The most obvious feature of this new matter is that it should be non-luminous, or in other words, it cannot interact with photons[5], which makes it electrically neutral. It should be an SU(3) singlet, colorless, since otherwise the phenomenological consequences might be disruption of the disk in spiral galaxies, dissociation of light elements during BBN, very high γ-ray fluxes and change in the CMB power spectrum [34].

Consistent with BBN: The prediction of abundances of light elements, in agreement with the observations, is one of the most challenging successes of Big Bang cosmology. This prediction is driven by a set of coupled Boltzmann equations relating the densities

[5] Interaction with photons at loop level gives rise very interesting phenomenological consequences.

of protons, neutrons and light elements. These equations are dependent on the expansion rate of the Universe, H, which at the same time is affected by the relativistic degrees of freedom present in the plasma. Therefore, deviations of the SM expectations of degrees of freedom would lead to different predicted abundances of light elements, like ^{4}He, which can be used as a constraint of some candidates [41–43].

Furthermore, these predictions can be notably altered by particles decaying during or after BBN era. For example, those decays producing EM showers can destroy light elements. Also, hadronic decays may change the neutron to proton ratio altering ^{4}He and ^{2}He abundances. This can be used to restrict the mass, density, lifetime and hadronic branching ratios of a decaying particle [44].

Stellar evolution: A good DM candidate must be in agreement with stellar evolution. If DM was very light and weakly interacting, it might be produced inside stars, and once produced, it can escape from the core without further interaction. This would be an energy loss mechanism of the stars and possibly would modify its evolution. In addition, these particles may be detected at the Earth, so current null results place stringent constraints.

As we have seen, there exist several and different requirements for a particle to be a good DM candidate. However, during the last three decades theorists have found many possible particles fullfiling the aforementioned criteria. It is possible to classify all the proposals by their general properties, and in the following we will summarize this classification and show that WIMP DM is most promising realization.

1.2.2 WIMP's and more

First and foremost, the density of any DM candidate must be lower than the predicted CMB density in the ΛCDM cosmological model. In the literature there exists many different DM production mechanisms to account for the correct abundance, however among all of them, the *freeze-out* mechanism is one of the most popular ones [45].

The *freeze-out* mechanism goes as follows: the DM particles are in thermodynamic equilibrium in the early Universe. When the temperature drops below the mass of the DM particles, $T < m_{DM}$, it is only kinematically possible to annihilate DM particles not to create them, and hence the population of DM particles started to be exponentially suppressed. At some temperature[6], the equilibrium is broken since the expansion rate, H, is higher than the interaction rate of DM with the plasma. Then, the number density of DM particles over the entropy density becomes constant, and the DM particles *freeze-*

[6] This temperature is known as decoupling temperature, T_f.

out. We refer the reader to Appendix A for a detailed calculation of the process. In this framework, the relic density of a DM particle is inversely proportional to its annihilation cross section into the particles present in the plasma,

$$\Omega h^2 \propto \frac{1}{\langle \sigma v \rangle}. \tag{1.5}$$

$\langle \sigma v \rangle$ is the thermal average of the annihilation cross section times velocity. It is remarkable that when a cross section of the order of Weak scale interactions is used, the resulting abundance is $\mathcal{O}(10^{-1})$, just like predicted by the CMB. WIMP's are weakly interacting massive particles, or in other words, CDM candidates with the correct density. This outstanding match[7] gives WIMP's a well deserved popularity. One advantage of this mechanism is the independency of the UV part of the theory. Since WIMP's have a relatively large cross section, they remained in thermodynamical equilibrium before decoupling, so in this case this is independent of the early thermal history of the Universe, as well as, new interactions that might appear at high energy scales. The superweakly interacting massive particles (SuperWIMP's) have been also proposed [46]. In this scenario the correct relic density is achievied by late decays of a metastable WIMP into these kind of particles. It would be very difficult to probe experimentally a framework like this, but still it could leave some traces [34, 46].

The assumption that DM is a thermal relic is somehow restrictive. There is a bound on m_{DM} called unitarity bound. Is based on the fact that $\langle \sigma v \rangle \sim m_{DM}^{-2}$ since there is a maximum of the cross section imposed by the partial wave unitarity of the S matrix [47, 48]. Using the relic density derived from the CMB power spectrum, the mass of the thermal relics must be lower than few hundreds of TeV. Nevertheless, there is a class of DM candidates with masses much above few hundreds of TeV, which being not able to be produced thermally have to invoke a non-thermal mechanism, these are called WIMPzillas [49]. There are two necessary conditions for this scenario to work: first, the WIMPzillas have to be stable, and second, they could never attained the thermal equilibrium. The second condition is automatically satisfied if $m_{DM} > T_c$, where T_c is the temperature of creation of the WIMPzillas[8].

There is also a mechanism known as *freeze-in* which could be seen as the opposite to *freeze-out*. This mechanism was proposed a few years ago [50], and the DM candidates grouped under this production mechanism are known as Feebly Interacting Massive Particles (FIMP's) because their interaction with the plasma is so feeble that they never attained thermal equilibrium. This is a UV independent mechanism, however it needs a

[7] Sometimes referred as the WIMP miracle.

[8] To extract this inequality we have used the unitarity bound.

crucial assumption: the earlier history of the universe makes the abundance of FIMP's negligibly small, whether by inflation or some other mechanism [50].

To sum up, we have seen that there are several requirements that a good DM particle candidate has to fullfil, and also that regarding the production mechanisms there is a variety of classes of particle candidates. Among all of them, the natural prediction of the abundance, the UV independence and, as we will see later, the appearence in some of the best motivated theories BSM, make thermal relics represented by WIMP's the most plausible realization of DM in our Universe. In the following, we will introduce in more detail the WIMP paradigm, taking into account the prospects for detection as well as some theoretical considerations.

1.3 The WIMP paradigm

The idea that DM is composed by WIMP's is rather attractive. They fulfill all requirements previously mentioned, and their thermal history is independent of the high temperature physics in the early Universe. The WIMP paradigm is often presented as strong evidence for new Terascale physics connected to ElectroWeak Symmetry Breaking (EWSB). However, this should be taken with a grain of salt, since this statement is valid only "within a few orders of magnitude" level . Therefore, in this section the main advantages and disadvantages of the WIMP paradigm are presented. Some special emphasis will be putted on the current existing possibilities for their detection, and we will also mention some of the theories that incorporate these WIMP's for free, paying special attention to SUSY theories.

1.3.1 Miracle or coincidence?

The key idea of this paradigm is that particles were in thermal equilibrium in the early universe. This means that the production rate of particles from the thermal bath is equivalent to the annihilation rate, Γ. As it is shown in figure 1.4, if we adiabatically lowered the temperature of a static universe below the DM mass (defining $x = m/T$ this is when $x > 1$), then the DM abundance would freeze out to a value that is thermally suppressed by $\exp(-m/T)$. However, we know that the universe is expanding at a rate given by H. Because of this, freeze-out occurs when the expansion rate overtakes the annihilation rate, $H > \Gamma$, which in terms of x is $x_f \approx 20$ (shown as a dotted vertical line).

According to equation A.11, the WIMP density is proportional to the factor $\langle\sigma v\rangle(T_\gamma)^3/M_{pl}$,

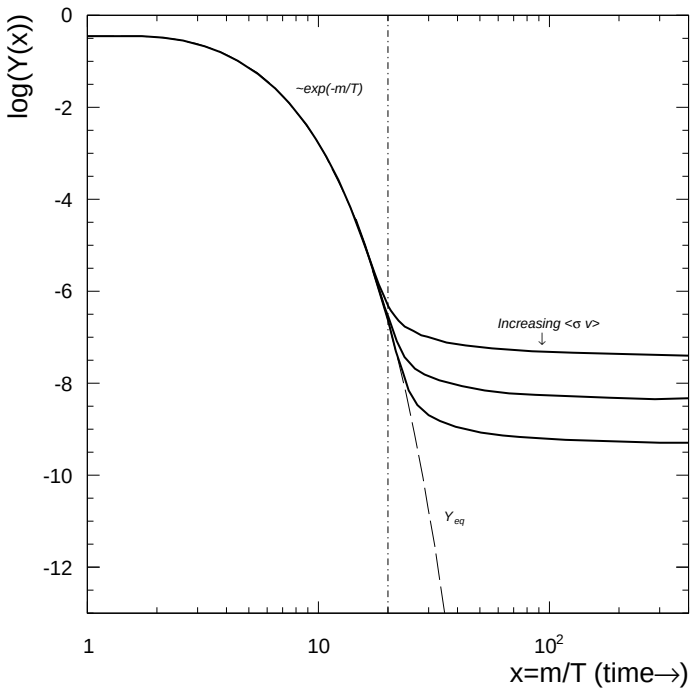

Figure 1.4: Comoving number density of thermal relics as a function of the temperature (time). These curves have been calculated for an s-wave annihilator of mass 1TeV.

where M_{pl} is the Planck mass and T_γ is the CMB radiation temperature. It is remarkable that in this scenarios, the Weak scale, represented by the WIMP cross section, the Planck scale and the CMB scale are combined in such a way that they cancel out to give the correct relic abundance. Is this a miracle or just a coincidence?. Whatever it is, it is an elegant fact that WIMP physics could arrange into the same equation these three scales, which in principle are unconnected, giving a very precise prediction of the DM relic abundance in our Universe.

1.3.2 Good prospects for detection

There are currently three very active fields for DM detection. First, direct detection, which attempts to bring DM from the sky into the lab, where one might hope to directly measure DM scattering events against detector material. These experiments are placed deep underground to shield against cosmic rays, and make use of the latest experimental techniques to achieve ultra low background levels [47, 51–55]. A schematic picture of direct detection can be seen in Figure 1.5, reading the diagram from bottom to top.

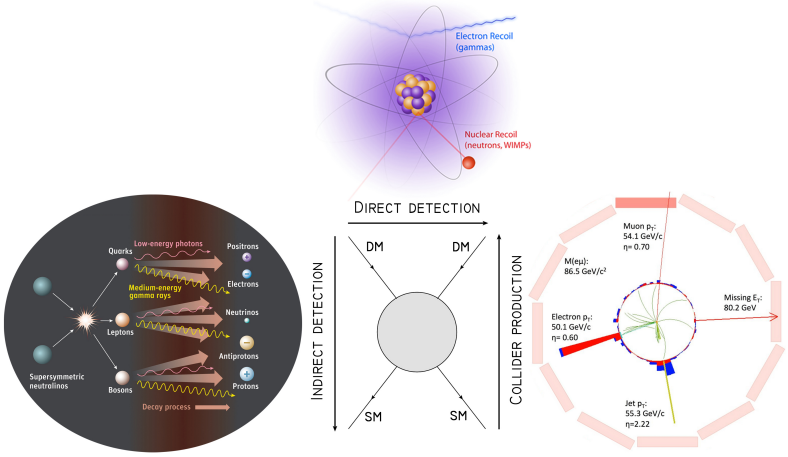

Figure 1.5: Diagrammatic view of the correlation underlaying the three ways for detecting DM. The same processes are involved in the direct, indirect detection and collider production.

WIMP's are expected to be in our Sun's local system, and thus crossing the Earth constantly. The DM flux across the Earth is expected to be quite high, of the order of 9×10^4 particles per second and per centimeter squared[9]. However, WIMP's are weakly interacting, so they rarely will interact with the quarks composing the detector materials. As we will see later, scaling up the detectors or improving the low energy sensitivity, will help to maximize the chances of detection. In any case, since WIMP's are thermal relics, they are expected to interact with quarks with cross sections of the order of few pb, which makes direct detection a very promising tool for their detection.

Secondly, indirect detection, which places the lab into the sky and expects to measure the byproducts created by DM annihilations in our Galaxy [53, 54, 56–59]. It is based on the search for the cosmic radiation produced by DM annihilations or decay into SM particles, which later produce a flux of cosmic rays and photons. In figure 1.5 this is represented by the diagram read from left to right. For WIMP's, the flux rates predicted at the Earth are promising, and therefore several experimental collaborations have built telescopes tuned to detect these fluxes. As in the direct detection case, the relic density constraint impose an annihilation cross section of the order of pb. Since DM particles in the Milky Way halo have very low velocities, around few hundred of Km/s, in this regime thermal relics have a cross section of $\langle \sigma v \rangle \approx 3 \times 10^{-26}$ cm^3/s.

Finally, DM might be also created at the Earth itself, in collisions of SM particles, and then observed after they escape away from the detector [54, 60–62]. Many of the

[9] Assuming a local DM density of 0.4GeV/cm^3, a DM mass of 100 GeV and a central velocity of 220 km/s.

proposed WIMP candidates can be produced copiously at the colliders, either directly or as decay products of the other particles. In figure 1.5 this is represented by the diagram read from right to left. These measurements would then provide information regarding the masses and couplings of both the DM candidate and the other particles with which it interacts and which are important in calculating its density. WIMP's are also expected to interact with the Higgs boson. This newly discovered particle seems to interact with ordinary matter as the SM predicts, leaving a small room to exotic decays such to a DM pair.

At first sight, the WIMP DM scenario offers a rich phenomenology as well as good prospects for detection. Needless to say that the situation will not be so simple when one considers a full theory, namely some of the correlations existing between these three different detection methods might be broken, making the situation less clear. Now that the main general features of WIMP DM have been described, and the observational evidences have been also tested against the WIMP scenarios, in the following section we will introduce the theoretical frameworks. The most popular WIMP candidates will be described with special emphasis on those candidates appearing in SUSY theories.

1.3.3 Who knows these WIMP's? SUSY knows!

The SM is one the great successes of physics. It describes the microscopic world in nature, including three out four of the known fundamental forces, and more importantly describing these interactions by the corresponding gauge symmetries. The SM symmetry group is $SU(3)_c \times SU(2)_L \times U(1)_Y$ describing Strong, Weak, and Electromagnetic interactions respectively. Along the last decades, each of the particles described by this theory have been discovered, culminating with the Higgs boson discovery at the LHC. In spite of the great success, still there are some open questions for which the SM does not provide an answer.

First and foremost, is that the SM does not include a viable DM candidate and therefore must be extended. As we have seen the only non-baryonic possibility in the SM were the neutrinos, however, the relic abundance predicted is too low and the LSS formation too poor, so it would be rule out as the main DM component. As a matter of fact, new symmetries at TeV scale shed light on this puzzle and the simplest possibility of a new symmetry is a discrete Z_2 parity. The hypothetical existence of this symmetry gives rise to many WIMP candidates in different theories as we are going to see.

In the second place, the so-called *hierarchy problem* [63, 64] provides an important motivation for physics BSM. The predicted Higgs mass in the SM receives quadratic

divergent contributions from all the matter fermions (quarks and leptons, f) in the theory,

$$\Delta m_h^2 = \frac{-2y_f^2}{16\pi^2}\Lambda^2, \tag{1.6}$$

where Λ is the cut-off scale. Assuming that the SM is the only theory valid up to the Planck mass, the cut-off scale would be M_{pl}. Since the mass of the Higgs boson is expected to be of the order of the EW scale, as the perturbativity, vacuum stability and triviality bounds suggest, the amount of fine tuning required to cancel out these corrections at all orders would be huge. The minus sign of the equation 1.6 might be hiding a possible answer to this question. This sign is due to the Fermi-Dirac distribution function which governs the fermion statistics, however, for bosons governed by Bose-Einstein statistics this sign is positive. This is precisely the motivation for SUSY. This global symmetry predicts a bosonic degree of freedom (called partner or superpartner) for each fermonic degree of freedom and vice versa. Thus, for each fermion in the SM, there is a SUSY bosonic partner and for each SM gauge boson, there is a fermionic partner. The cancellation of equation 1.6 is now trivial since each SM fermion contribution will cancel out due to the corresponding SUSY bosonic partner contribution. We will describe in more detail the fine points of SUSY in chapter 2.

There are several WIMP candidates appearing in different SUSY constructions. These are the Lightest Supersymmetric Particle (LSP) which ensure their stability by means of a discrete Z_2 parity called R-parity. The most studied and popular candidate is the *neutralino* [47, 65–70]. This particles are the linear superposition of the fermionic partners of the SM bosons, including the Higgs, and thus they are weakly interacting particles. Another example of SUSY WIMP's are the *sneutrinos* [71–76]. These are the scalar superpartners of the SM neutrinos. Depending on model building details, sneutrinos as viable DM candidates can be purely right-handed (RH) or a mixture of left and right components. These are the two candidates we are going to explore in more detail in this thesis, so we will come back to them in the next chapter. Before moving to other theories, let us mention a couple of non-WIMP candidates in SUSY that have also received much attention. Under some conditions, *gravitinos* can be the lightest supersymmetric particle and thus a candidate for DM [77–83]. Finally, the *axinos* are also a viable DM candidate in some SUSY theories.

As far as theory is concerned, extra dimensions theories provides a good alternative scenario to SUSY frameworks to solve the *hierarchy problem*. Interestingly, it offers a good solution to the DM puzzle. Physics in extra dimensions was initiated at the beginning of the twentieth century through the Kaluza-Klein (KK) theory, and was

largely ignored until the appearance in the 70's of the string theory. In this theories, the SM is embedded in a 3+1 dimensional brane living in higher dimensions, as a result, the Planck scale is reduced up to the TeV scale. Every multidimensional field corresponds to a Kaluza-Klein tower of 4-dimensional particles with increasing masses. A KK-parity, as in the SUSY case with R-parity, makes the lightest KK particle stable and therefore a viable candidate. The most studied is the *KK photon*, which corresponds to the first massive excitation of the hypercharge gauge boson [54, 84, 85]. Since these particles are WIMP's, the phenomenology of this scenario is very similar to that of neutralinos [86].

Another remarkable alternative is represented by Little Higgs models. The Higgs in this model is a pseudo Nambu-Goldstone boson associated with spontaneous global symmetry breaking in an extended electroweak sector, which occurs at a scale around the TeV scale. EW precision data requires a T-parity to be conserved and thus making the lightest particle of the model stable. This particle is typically the heavy partner of the hypercharge gauge boson and can play the role of WIMP dark matter [87–89]. Finally, there is yet another theoretically well motivated candidate called *mirror baryons* which are present in Mirror DM models [90].

For the sake of completeness, let us mention some minimal extensions of the SM which account for the DM problem providing a suitable WIMP. These theories, however, should be seen as *effective* descriptions of bigger constructions like SUSY, and motivated by their phenomenological implications. Falling into this class we find: singlet scalar[10], fermionic, and vector DM models with a Higgs portal interaction with SM particles [91–93]. The inert doublet model is also a popular possibility since the 70's [94]. It includes a second scalar $SU(2)$ doublet under the SM gauge group as well as a Z_2 parity under which this doublet is odd. The DM implications of this model have been extensively studied in the literature [54, 95].

To conclude, there are many well motivated theories including not only WIMP DM like SUSY or extra dimensions, but also non-WIMP candidates. Despite of the success of the SM, there are still some questions that cannot be addressed by this simple theory, and hence a motivation for an extension emerges. SUSY provides a solution to either theoretical problems, like the *hierarchy problem*, or more phenomenological issues like the DM puzzle, and therefore it will be used in this thesis as a theoretical framework to study some aspects related with the detection of WIMP DM. To finish with the introductory chapter, let us summarize the current DM experimental picture.

[10] Either real or complex scalar has been proposed.

1.4 The current experimental situation

Since the beginning of this thesis DM searches have experimented an astonishing improvement. The technology that surrounds this hunting has evolved enormously in the past few years, ensuring in many cases, that the sensitivity of the experiments even exceeded the expectations. Perhaps, the direct search of DM is the most representative field in this context since there are several collaborations around the world hardly competing for being the first in claiming the discovery (or putting the best limits). Be that as it may, the physics community is doing great efforts trying to shed light on the DM problem, and what is probably more important, learning how to combine different strategies that would give us the necessary insight to finally solve this mystery.

1.4.1 Direct detection: light WIMP's?

Let me now start by summarizing the situation regarding DM direct detection. As it is commented previously, direct detection experiments are based on the elastic scattering of DM off nuclei inside a suitable detector. If a WIMP hits a nucleus, the latter will recoil releasing certain amount of energy that will be deposited inside the detector. These are designed to detect the energy transferred to the nucleus during the collision, and kinematics dictates that it must be of $\mathcal{O}(10)$ keV[11]. There are three different methods based on the way in which the energy released is deposited in the detector: detecting the heat that is generated by the collective vibration of the lattice (phonons) once the nucleus recoils. By the electric current that occurs if the nucleus is ionized, and by photons emitted by the material when the nucleus moves through it[12]. The expected rate of WIMP interactions tends to be exceeded, in the keV energy range, by ambient radiation from radioisotopes and cosmic rays, and thus sensitive high radiopure detectors and deep underground sites are required for shielding. For this reason, novel techniques make use of two of the mentioned detection processes, which allows a more powerful background rejection and therefore higher sensitivities. Even though it is difficult to disentangle a DM signal from the backgrounds, it exists a distinctive DM signal that would be difficult to mimic by any known background. Since the Earth changes its velocity respect to the Sun during the year, the relative velocity between the WIMP wind and the Earth (lab) also changes. This means that the energy transferred to the nucleus by WIMP's changes along the year, producing what it is known as *annual modulation* of the DM signal [96].

[11] The actual energy however depends on the WIMP mass, nucleus mass, and velocity of the WIMP.
[12] This process is known as scintillation.

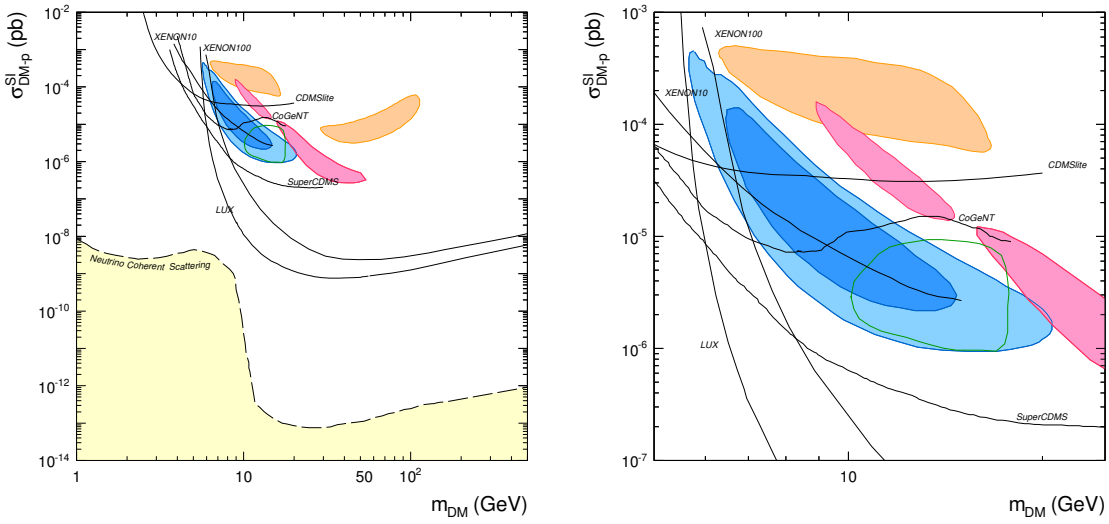

Figure 1.6: Left: The current experimental situation of direct detection experiments represented in the DM cross section and mass plane under the *standard assumptions*. Right: Same as in left but the light WIMP region is zoomed.

In a given detector, the number of events as well as the energy deposited by the recoiling nucleus depends on the WIMP-nucleon cross section and the WIMP mass. It also depends on the velocity of the WIMP and the nucleus form factor. This two quantities are usually approximated at first order as an isotropic Maxwell-Boltzmann (MB) distribution, and the convolution of a spherical Fermi density respectively [97]. These are the so-called *standard assumptions*. Under these hypothesis the different collaborations, using different target materials, are allowed to compare their results using only two unknowns: the WIMP cross section and its mass.

Nowadays, direct DM searches are one of the most controversial and exciting fields. As it is depicted in Figure 1.6, several collaborations may have seen hints of collisions of DM particles in their detectors, but at the same time these hints would be ruled out by other experiments, considering the *standard assumptions*. Recently, the CDMS collaboration has reported three events with a statistical significance of almost 3σ over the expected background in their silicon (Si) targets, which if interpreted in terms of a DM particle, would correspond to a WIMP mass around 8 GeV and a spin-independent WIMP-nucleon cross section of 2×10^{-5} pb [98] (blue contours in fig.1.6). But this is not the only potential excess reported. Since DAMA collaboration and later DAMA/LIBRA, observed an *annual modulation* in the event rate of their NaI target pointing to the light DM mass region [99, 100] (orange contours), some other, such as CoGeNT [101] using

germanium (Ge), and CRESST [102] with a $CaWO_4$ target (magenta contours), have also claimed an excess of events in their data compatible with light DM. CoGeNT seemed to observed an *annual modulation* in the total rate as well [103], which has been very recently reinforced by new data [104]. This results might point out to the necessity of dropping the *standard assumptions*, namely the MB velocity distribution of DM particles in the halo, in order to be reconciled with DAMA results [104]. Moreover, the CoGeNT collaboration itself reanalyzed the data again with a more powerful statistical method, and released new results which would be difficult to reconcile with DAMA [105], but yet compatible with a DM signal produced by a light particle (empty green contour).

In contrast to this situation, other experiments have been able to place important constraints based on null observations, generally excluding the interpretation of these potential signals in terms of standard picture (labelled lines in fig.1.6). The most stringent bounds are from LUX [106], XENON [107–109], CDMS [110, 111], SIMPLE [112], KIMS [113], and a combination of CDMS and EDELWEISS data [114]. It is also worth mentioning that CDMS performed a further analysis looking for a possible modulation in their data since a Ge detector is used like in the CoGeNT experiment. However, no significant modulation was found [115]. Finally, very recently the SuperCDMS collaboration has released a new data set in which they do not find any hint of DM collisions and thus an upper bound is derived, which is specially stringent for low masses [116]. Finally, we have included in the left panel of Fig. 1.6 the irreducible neutrino background (bottom yellow region), where it is expected that direct detection experiments loose their sensitivities to WIMP scatterings [117].

It seems that the reconciliation of null results with the potential signals is not an easy task, specially after LUX bounds came up in 2013. On the one hand, theorists have shown that invoking non-standard couplings of WIMP to protons and neutrons (e.g. isospin violating couplings) it is still possible to reconcile some of the positive results with LUX and XENON bounds [118–122] since even performing halo-independent analysis the situation is not much relaxed [122, 123]. On the other hand, experimentalists are trying to understand and putting in the same context all the DM-like signals and null results. For instance, it is known that specially for light WIMP's, a deeper understanding of the scintillation efficiency of Xe based detectors is needed since the upper bounds are profoundly sensitive to this quantity [121].

All in all, the WIMP light mass region shows anomalies that have to be understood. Furthermore, the detectors are more sensitive to WIMP's lighter than 100 GeV, and hence this region is going to be probed soon. This motivates us to study this region from different perspectives, not only analyzing models but also making specific predictions for

the future of direct detection experiments. It is also worth mentioning that, as we are going to see in a moment, indirect detection experiments might be starting to see the nose of a light WIMP.

1.4.2 Indirect detection: light WIMP's again?

Indirect searches are aimed to hunt DM through the detection of the final products after the collision of two DM particles or its decay. According to the electric charge carried by the byproducts it is possible to classify these searches in: cosmic ray, and gamma ray and neutrino astronomy. The former includes the production of electrons and positrons, protons and antiprotons, deuterium and antideuterium. Gamma ray astronomy includes the direct production of photons as well as photons produced in the hadronization of colored particles or decay of leptons, and also in astrophysical processes such as synchrotron radiation and X-rays. Finally, WIMP's are also expected to produce neutrinos when they get trapped inside stars like our Sun. Generally, all these searches are designed to look for energy ranges or places where the WIMP signal would overcome the background from ordinary astrophysical processes. A good example of this are searches for charged particles. In this case the experiments focus on fluxes of antiparticles (positrons, antiprotons, antideuterons) which are expected to be very low since they are less abundant in the Universe than their corresponding particles. In the case of gamma rays, this is performed by looking at regions of the sky which are believed to be DM dominated since these are expected to maximize the signal over noise ratio (S/N).

Like in the case of direct searches, several such intriguing astrophysical signals have existed for some time on indirect searches. Although in the following we are going to focus on gamma rays, let us say few words in the field of cosmic rays. In 2008, the PAMELA satellite data showed a steep increase of the positron fraction ($e^+/(e^+ + e^-)$) spectrum ranging from 10 to 100 GeV [124]. Interestingly enough, the antiproton to proton flux ratio showed no deviation from the expected background [125]. In 2011, this finding was supported by the Fermi Large Area Telescope (LAT) collaboration and it extended in energy up to 200 GeV [126]. New measurements, with an unprecedented sensitivity, came up in 2013 by the AMS-02 collaboration. According to this, the positron fraction shows an increase up to 350 GeV [127], however it seems to exist a discrepancy with Fermi-LAT measurements. If this increase is interpreted in terms of annihilating DM, it would correspond to a TeV candidate, with tuned couplings to leptons[13], and with a cross

[13]It must be *leptophilic*, or in other words, a particle annihilating almost exclusively into leptons since there is not such feature in the antiproton spectrum.

section much higher than the thermal one [58]. It worth remarking that a self-consistent astrophysical interpretation of the whole data is also possible [128].

The WIMP gamma ray astronomy is nowadays a controversial field too. Since photons are not charged they are expected to travel straightly to the Earth from the emission source. Therefore, usually the targeted regions for WIMP searches are those expected to have higher concentrations of DM, namely: the Galactic Center (GC), wide regions of the Galactic Halo (GH), Dwarf Spheroidal Galaxies (dSph) such as Sagittarius, Segue1 and Draco, LSS in the relative nearby Universe like Virgo and Coma clusters, and the extragalactic isotropic and anysotropic flux of redshifted gamma rays. Regarding the GeV energy range, the current main experiments are the Fermi-LAT satellite and the ground-based Imaging Atmospheric Cherenkov Telescopes (IACT). Apart from this, the morphology of the photon spectra in the GeV energy range makes these experiments more sensitive to WIMP masses below 100 GeV.

The Fermi-LAT is the world leading telescope to detect gamma rays in the GeV energy range (from 30 MeV to 300 GeV approximately). The collaboration have analyzed several targets with no conclusive evidence of a DM signal, allowing to put upper bounds on the annihilation cross section [129–134]. However, Fermi data is public, and thus many other independent groups have analyzed it with different conclusions than the official one. Over a year ago, evidence in support of a sharp feature in the γ-ray spectrum with an energy around $E_\gamma \simeq 130$ GeV was found in the GC data of the Fermi-LAT with a significance of 3.2σ [135–138]. When interpreted in terms of DM annihilations it corresponds to a thermal averaged cross section of $\langle \sigma v \rangle_{\gamma\gamma} \simeq 1.27 \times 10^{-27} \mathrm{cm}^3/\mathrm{s}$ for an Einasto profile, larger than would be expected by a one loop suppressed process. The absence of a gamma-ray continuum accompanying the line, its possible interpretation in terms of DM, monoenergetic pulsars winds [139] and instrumental effects [140–143], has raised important questions about statistics and suspicions about systematics, especially since the same feature is observed in photons from the Earth limb.

This controversial situation has triggered an analysis searching for sharp-like signatures of the *Fermi*-LAT collaboration using the GC region data [133]. In this analysis the energy range considered extends from 5 to 300 GeV using 3.7 years of data, as well as five different optimized (to maximize the signal to noise ratio) regions of interest (ROI's). They found no significant global excess of a spectral line and place constraints on the thermal cross section ranging from $\langle \sigma v \rangle_{\gamma\gamma} \sim 10^{-29} - 10^{-27}$ cm^3/s depending on the WIMP mass and the Milky Way DM profile assumed. In this work the collaboration also showed that the 130 GeV feature cannot be attributed to photons in the Earth limb but that it has some characteristics which disfavours the WIMP interpretation. These

limits begin to explore, specially for light DM masses, the usual regions in which a loop suppressed cross section lies[14] and thus start to constrain some regions of the parameter space of WIMP models.

The GC may be hiding a potential DM signal as well. Since 2010, several groups have claimed the presence of a residual gamma ray spectrum in Fermi data [144–149]. Surprisingly, when interpreted in terms of DM it would correspond to annihilating particle with a mass below 100 GeV[15], and a cross section close to the thermal. The main problem that this kind of analysis have to face is the background treatment. The GC is the great unknown place of our Galaxy, and therefore it is likely that there would exist physical processes that are not well modeled, or even not known yet. For this reason, the background estimation in this region, necessary to claim an excess, can be different or having components that would mimic a DM signal.

1.4.3 The discovery of the Higgs boson at the LHC

The physics community, and more concretely the particle physics community, has lived an historical moment with the Higgs boson discovery at the LHC [150, 151]. Although it is known an incomplete theory, this discovery represents the triumph of the SM and the quantum field theory as the microscopic description of nature. Moreover, the discovered Higgs seems to have properties very similar to those predicted by the SM [152–156] and a mass around 125 GeV. In the following we will refer to this Higgs boson as the SM-like Higgs boson unless otherwise stated.

The SM-like Higgs boson carries weak quantum numbers provided the mass of the $W^{\pm}$ and Z^0 gauge bosons, so a coupling between DM and Higgs would yield to weak scale interactions of DM with matter. For this reason, in most of the models WIMP's and the Higgs boson interact, and hence the later can be seen as a *portal* to the dark Universe. If this happened, once produced the Higgs particle at the LHC it would have a non zero probability to decay into DM particles which subsequently would escape the detectors leaving no trace. This process is known as Higgs invisible decay. This kind of decay is not present in the SM, therefore if discovered, it would be an indication of new physics and namely DM at the LHC. Several groups have analyzed this possibility using LHC data placing an upper limit on the Higgs invisible decays [157–162]. Regarding

[14] Since DM must be electrically neutral, one loop cross sections are $\mathcal{O}(\alpha_{em}^2)$ suppressed and thus expected to be three or more orders of magnitude below the thermal cross section.

[15] The actual mass depends not only on the annihilating final state but also on the statistical details of the analysis.

light WIMP's, their contribution to the invisible Higgs decay increases as the mass of the WIMP decreases. So the lighter is DM the more invisible the Higgs would be. This is translated into stronger constraints on light WIMP's that, as we will see, are difficult to avoid but yet possible. It is also worth mentioning that the Higgs production is not the only way one would expect to create DM at the LHC. It is also possible to create DM as the final state (among several possible different final states) of a long decay chain. However, this is something very dependent on the model considered and hence we will not mention further on this.

More generally, the Higgs boson decays might include, not only invisible particles such as WIMP's, but also new particles predicted by extensions of the SM. For instance, as we will explain in the following chapter, in the case of SUSY the Higgs sector is extended and more complex than in the SM. The SM-like Higgs boson could decay into a lighter Higgs boson or in general to other scalars that would decay inside the detectors. These late decays would produce final states different from those expected in the SM, resulting in a clear indication of physics BSM. These sort of decays are often referred as non-Standard Higgs decays. Using the latest data from the LHC, and in some cases also from former colliders like LEP and Tevatron, it is possible to constrain the contribution of these channels [157, 159, 163, 164].

Summarizing, the discovery of the SM-like Higgs boson at the LHC has opened a new era for particle physics. The connections of this Higgs with DM are evident in many models, and therefore something to be exploited either theoretically or experimentally. Although until now there is not evidence of invisible or non-Standard decays of the Higgs, we expect that sooner or later will appear. It would give us a crucial piece of information about DM interactions, and therefore more precise predictions (expectations) might be made for direct and indirect searches.

1.5 An overview: exciting times are coming

This chapter has served us for several purposes. In the first place, we have seen the motivations that make us think in the presence of a mysterious substance called DM. For a long time, the gravitational evidences supporting its existence has been piling up arriving to be evident that our knowledge of the Universe is still very incomplete. After an astonishing understanding of the CMB radiation, we have been able to predict the density of DM in the Universe, $\Omega_{CDM}h^2 = 0.1199 \pm 0.0027$. Furthermore, the Bullet cluster has taught us that it is rather complicate to explain the DM problem in terms

of modified gravity, and more importantly, it is a strong motivation for particle DM theories.

In the second place, the WIMP paradigm provides a class of candidates which naturally account for the observed DM cosmological abundance. As we have mentioned, this paradigm connects different corners of physics under the relic density prediction, which is an elegant fact at least. Besides, WIMP candidates have good prospects for detection, either directly or indirectly, and being produced at the LHC through Higgs decays. Another strong motivation for WIMP's is that they naturally appear in theories BSM like SUSY or ED.

Finally, a set of this class, light WIMP's, might account for the anomalies seen by direct detection experiments. Real DM signals or not, the light mass region is going to be probed sooner since the experiments are more sensitive to these particles. The same situation is faced in indirect searches. There are interpretations of the Fermi data which suggest the presence of a signal from the GC, and pointed to the light DM mass region. The morphology of the photon spectrum also makes this region the most constrained (or the sooner probed). Although the LHC has not shown such hints, the constraints on the Higgs invisible decays are very restrictive for light WIMP's as well. All this makes light WIMP's worthy of study in this thesis.

To conclude, we are living *the moment of truth for WIMP DM* [54]. In the present moment we are facing a critical situation for WIMP searches since if DM does not show any clear indication of its presence in direct, indirect or the LHC, we will witness the inevitable decline of WIMP's. On the contrary, if WIMP's are discovered by any experiment, the community must be ready to understand the implications and maximize the information extracted from it. For this purpose, it is important to understand how to use data from different experiments although not all have to have discovered WIMP's, to know the predictions of different models, and to accept different explanations of the data since nature does not have to be simple.

Chapter 2

Light supersymmetric dark matter

In this chapter search for low mass WIMP's will be presented, as described in chapter 1, in the context of different SUSY constructions. We will focus our attention in two scenarios which are the most studied in SUSY, the Minimal Supersymmetric Standard Model (MSSM), and the Next-to-MSSM (NMSSM), where we will analyze the DM phenomenology taking into account the latest experimental results.

The SM is a great theory. It has probably more successes than any other known theory, but it leaves also some questions unsolved. Apart from the above mentioned *hierarchy problem* (Section 1.3.3), and the DM problem, there are some other theoretical issues. The strong CP problem is one of them. There is no reason why the strong sector of the SM does not violate the CP-symmetry including a term proportional to $\theta_{QCD} F_{\mu\nu} \tilde{F}^{\mu\nu}$. Measurements of the neutron electric dipole moment suggest that the parameter θ_{QCD} is very small, far away from order one, and therefore a large fine tune is required. Other problem is the neutrino oscillations. The SM predicts that neutrinos are massless particles, however, it was found that neutrinos have a non zero mass, tiny, but not zero. This fact suggests that there might be other mechanisms, different from the Higgs mechanism, that could explain neutrino masses or it might be pointing to the presence of a fourth generation. But from the experimental side we have already found some hints of physics BSM. One of the most studied problems is the muon anomalous magnetic moment, a_μ. Experimentalist have achieved an impressive accurate measurement, while higher order corrections in the SM have been calculated by theorists. Both quantities show a discrepancy of almost 3σ [165],

$$\delta a_\mu = a_\mu^{exp} - a_\mu^{SM} = (249 \pm 86) \times 10^{-11}, \tag{2.1}$$

which serves as a strong motivation for the necessity to extend the SM. These, and other problems, can be solved by SUSY.

Finally let us say a few words about unification. The coupling constants of the Strong, Weak and EM interactions evolve with energy, and their evolution is given by the Renormalization Group Equations (RGE's). These equations strongly depend on the particle content of the theory. In the SM, the evolution of the coupling constants never meets a point where the three of them coincides. On the contrary, in the MSSM, the three of them meet at a scale close to 10^{16} GeV, known as the Grand Unification scale. This implies that these three interactions of nature might belong to the same interaction described by a larger gauge group, which is known as unification of forces.

2.1 Supersymmetry grounds and current status

As already stated in the previous chapter, SUSY is a well motivated theory which extends the SM with a global symmetry (supersymmetry) relating the known fermions and bosons of the SM with the corresponding bosons and fermions superpartners, respectively. Formally, it is an extension of the space-time symmetry reflected in the Poincare group and its naturalness lies, precisely, in this construction based on symmetry. Besides, being a symmetry related to space-transformations, the local symmetry concept introduces gravity in a natural way, the so called Supergravity (SUGRA). If supersymmetry exists in nature, acting on a physical state with any generator of the symmetry gives another physical state. For example, acting on an electron with a momentum operator produces another physical state, namely, an electron translated in space or time. Space-time symmetries leave the quantum numbers of the state invariant, in this example, the initial and final states have the same mass, electric charge, etc. In an exactly supersymmetric world, then, acting on any physical state with the supersymmetry generator, Q_α, produces another physical state. As with the other space-time generators, Q_α does not change the mass, electric charge, and other quantum numbers of the physical state. In contrast to the Poincare generators, however, a supersymmetric transformation changes bosons to fermions and vice versa. The basic prediction of supersymmetry is, then, that for every known particle there is another particle, its superpartner, with a spin differing by 1/2.

Supersymmetric transformations require the presence of additional auxiliary fields (complex scalars) denoted by F. These transformations give consistent results when applied over a generic complex scalar, ϕ, but when applied over a generic fermion, χ, its equations of motion do not hold off-shell. This is because the degrees of freedom of a complex scalar do not match those of a spinor. To avoid this, the presence of F is necessary.

The Wess-Zumino model represents the most general SUSY invariant free Lagrangian,

$$L_{WZ} = \partial_\mu \phi_i^* \partial^\mu \phi + \chi_i^\dagger i\bar{\sigma}^\mu \chi_i + F_i^* F_i + h.c., \tag{2.2}$$

where the index i runs over the internal degrees of freedom. Now, the next step would be to introduce the interaction between the fields, imposing that they are renormalizable. The most general form of these interactions would be,

$$L_{int} = W_i(\phi, \phi^*) F_i - \frac{1}{2} W_{ij}(\phi, \phi^*) \chi_i \chi_j, \tag{2.3}$$

where the sum is implicit over i and j. W_i and W_{ij} are arbitrary functions of the bosonic fields, the latter being symmetric in the indices i and j. When the invariance under SUSY transformations is imposed, these functions are the derivatives of a very important function, the *superpotential*,

$$\mathcal{W} = N_i \phi_i + M_{ij} \phi_i \phi_j + y_{ijk} \phi_i \phi_j \phi_k. \tag{2.4}$$

This function encodes all the interactions of the theory, and thus it will be used to specify the SUSY model under consideration. M_{ij} has dimensions of mass, while y_{ijk} is the Yukawa coupling between a scalars and two fermions. Let us point a couple of remarks about this function. SUSY invariance requires that $\mathcal{W}$ has holomorphic[1] properties, and thus for instance the term $q\bar{u}h^*$ that gives mass to the up-type quarks in the SM is forbidden. To solve this issue, in SUSY at least two Higgs doublets are required, one to give masses to up-type fermions and the other for the down-type ones. Besides, the superpotential is used to eliminate the auxiliary fields F through their equations of motion.

SM particles and superpartners are grouped into the same multiplet which is accordingly called supermultiplet. There are two kind of supermultiplets, the chiral and gauge supermultiplets, which contain SM fermions and their corresponding SUSY scalars, and the gauge bosons with their SUSY fermion partners, respectively. All particles belonging to the same multiplet share the same quantum numbers although they differ in their masses and spins. The fact that the spins are different is a consequence of the commutation relations of the Q_α with the Poincare generators. Nonetheless, since Q_α and the momentum operator, P_μ, commutates another consequence is that the mass of the SUSY partners is the same as for the SM particles. In that case, we would have already discovered many SUSY particles, but unfortunately we have not. This is an indication

[1] The presence of complex conjugate scalars, ϕ^*, is not possible

that SUSY is not an exact symmetry of the Universe but it must be broken by some SUSY breaking mechanism.

Since in this thesis we analyze the phenomenological aspects of SUSY, for the most theoretical aspects of SUSY we refer the reader to the textbooks [166–168] and reviews [169, 170][2]. In the following sections we will try to introduce the minimal particle content of SUSY theories necessary to contextualize the present status of SUSY searches at the LHC.

2.1.1 SUSY breaking

If nature is supersymmetric it must be broken. As we have already argued, no SUSY particles have been found until now, which rules out the possibility that these particles share the same mass as their SM partners, they have to be heavier.

When SUSY is considered as a theory defined at EW scale, an *ad hoc* strategy it is usually adopted for breaking the symmetry. This is done by parametrizing the breaking in terms of effective soft breaking terms which explicitly break the symmetry, all of them contained in the soft[3] part of the Lagrangian, $\mathcal{L}_{soft}$. In other words, the soft SUSY breaking mechanism give masses to all SUSY particles explicitly, and these masses are named soft masses. This is nothing but a parametrization of the lack of knowledge about the high energy dynamics that breaks SUSY, and therefore is not free. When this mechanism is invoked, the number of free parameters of the theory is 109, and would lead SUSY to be an unpredictive theory. This is usually solved by assuming certain hypothesis like forbidding CP-violating terms in the Lagrangian, or that some of the soft masses are equal.

However, there are already some dynamical high energy mechanism to explain SUSY symmetry breaking. The presence of a hidden sector that communicates with the visible sector (i.e. our world) very weakly, is an scenario which is often considered. In this case, SUSY would be defined as a high energy theory motivated by the unification of the coupling constants or string theory, and the RGE's would drive the parameters up to the EW scale. In the literature three usual mechanisms can be found. In the first place, the so called *gravity-mediated* scenario, makes use of gravitational interactions between the hidden and visible sectors leading to soft masses suppressed by M_{pl} [171]. An appealing feature of this scenario is that it provides a WIMP DM candidate. Secondly, *Gauge Mediated Supersymmetry Breaking* (GMSB) invokes gauge interactions at the

[2] Due to the overwhelming bibliography about SUSY we are forced to point just a very few of references.
[3] The *soft* adjective means that they do not introduce quadratic divergences.

loop level between the two sectors [172]. Unlike in *gravity-mediated* constructions, in this scenario the Gravitino would constitute the DM [173] but it does not fall into the WIMP class. Finally, *Anomaly Mediated Supersymmetry Breaking* is a difficult but yet possible realization [174].

In this thesis we will use just two out of the four previously described mechanisms. In the context of the MSSM, we will define the soft parameters at high energy in a gravity mediated scenario, and we will use the RGE's to evolve them up to the EW scale. On the contrary, for the NSSM scenarios considered, we will use a *soft* mechanism providing masses to the SUSY particles directly at EW scale.

2.1.2 SUSY spectrum and R-parity

The minimal SUSY extension is the MSSM. This theory just doubles the SM particle content with the corresponding superpartner. In table 2.1, the SM particles together with their superpartners are shown. As expected from the algebra of SUSY[4], the SM particles and their partners posses a spin differing by 1/2. This table already introduces the notation, denoted by symbol in the table, of the SUSY particles used along this thesis. The naming convention for the SUSY particles is as indicated in Table 2.1: bosonic partners get an additional 's' at the beginning of the name (e.g. Tau - Stau), while the fermionic partners get the suffix 'ino' appended to the name (e.g. Higgs - Higgsino).

To be more precise, in Table 2.1 the three generations are not represented. In this way, as for the third generation shown there, we can find the Down quark and the corresponding Sdown squark. More important, in the SM the left and right chiralities of the fermions transform as doublets and singlets of $SU(2)$, respectively. In SUSY, the left and right components must then belong to different supermultiplets, and have distinct spartners, e.g., $q_L \to \tilde{q}_L$ and $q_R \to \tilde{q}_R$. These two squarks are quite different, but we can use the index L and R to identify them, although the concept of chirality is nonsense for a scalar whose only helicity is 0. In general, $\tilde{f}_L$ and $\tilde{f}_R$ mix, and the physical mass state is a combination of them.

Notice that in general, Gauginos and Higgsinos mix with each other, and the experimentally observable mass states would be combinations of them. These are generically named Neutralinos $\widetilde{\chi}^0_{1,2,3,4}$, which have zero electrical charge, and Charginos $\widetilde{\chi}^{\pm}_{1,2}$, which are electrically charged and mix $\widetilde{W}^{\pm}$ and $\widetilde{H}^{\pm}$.

The construction of the superpotential, $\mathcal{W}$ (see Eq. (2.4)), includes the presence of parameters that are strongly subject to phenomenological constraints. These terms would

[4] Usually called *superalgebra*.

SM Fermion (Sfermion)	Symbol	Spin	R-parity
Quarks (Squarks)	$(q, \widetilde{q})$	(1/2,0)	(+1,−1)
Top (Stop)	$(t, \widetilde{t})$	(1/2,0)	(+1,−1)
Bottom (Sbottom)	$(b, \widetilde{b})$	(1/2,0)	(+1,−1)
Leptons (Sleptons)	$(l, \widetilde{l})$	(1/2,0)	(+1,−1)
Tau (Stau)	$(\tau, \widetilde{\tau})$	(1/2,0)	(+1,−1)
Neutrino (Sneutrino)	$(\nu_l, \widetilde{\nu}_l)$	(1/2,0)	(+1,−1)
SM Gauge boson (Gauginos)	**Symbol**	**Spin**	**R-parity**
Photon (Photino)	$(\gamma, \widetilde{\gamma})$	(1,1/2)	(+1,−1)
Z (Zino)	$(Z, \widetilde{Z})$	(1,1/2)	(+1,−1)
W's (Winos)	$(W, \widetilde{W})$	(1,1/2)	(+1,−1)
B (Bino)	$(B, \widetilde{B})$	(1,1/2)	(+1,−1)
Gluons (Gluinos)	$(g, \widetilde{g})$	(1,1/2)	(+1,−1)
Higgs (Higgsinos)	$(H^{0,\pm}, \widetilde{H}^{0,\pm})$	(0,1/2)	(+1,−1)

Table 2.1: MSSM particle content and its properties.

induce a rapid disintegration of the proton, whereas the proton is very stable, with a lifetime exceeding $\sim 10^{33}$ years. One way to avoid these dangerous terms is by introducing a new symmetry known as R-parity. This parity is given by the following combination of baryon number (B), lepton number (L) and spin (S):

$$R = (-1)^{3(B-L)+2S} . \tag{2.5}$$

This is a multiplicative conserved quantum number in the SM, since all the SM particles have a positive R-parity, $R = +1$. On the contrary, all SUSY particles would posses a negative R charge, $R = -1$, as it can be seen in the last column of Table 2.1. The phenomenological implications of this symmetry are tremendous. First, all the SUSY particles would be produced in pairs. Second, the sparticles would decay into and odd number of sparticles. And finally and very important in the context of this thesis, the lightest supersymmetric particle (LSP) must be stable, providing a potential DM candidate. For this reason, along this chapter, we will only work in models with R-parity conservation, although there are also very interesting models with a rich phenomenology associated to R-parity violation [83, 175–177].

2.1.3 Constraints on SUSY

Most of the current searches for physics BSM are negative, and specifically, no sparticle has ever been detected. This has allowed experimental collaborations to place lower bounds on the sparticles masses. Experiments at LEP and Tevatron collider have made direct SUSY searches using the missing energy signature [178–180]. LEP established lower limits on many electrically charged and without strong interactions sparticles. The lightest chargino mass was constrained to be $m_{\tilde{\chi}_1^\pm} \gtrsim 103$ GeV. Also the sleptons were constrained, specifically, $m_{\tilde{e}} > 100$ GeV, $m_{\tilde{\mu}} > 99$ GeV, $m_{\tilde{\tau}_1} > 80.5$ GeV and $m_{\tilde{\nu}} > 43$ GeV. Tevatron placed the best limits on squarks and gluinos masses some time ago, however, the LHC has improved these searches substantially and therefore we turn our attention to the LHC limits.

For the LHC, the most recent experimental limits on sparticle masses can be found in Refs. [181–184] derived for a simplified SUSY model. This means that a set of assumptions is made for extracting the lower limits. These assumptions are generally R-parity conservation and a massless LSP, but already highlight that these bounds must be treated with care when applied to a specific model. For the first two generation of squarks a lower bound of 1 TeV can be set while being consistent with Refs. [183, 184]. In the same way, the lower limit on lightest stop mass is set to be $m_{\tilde{t}_1} > 650$ GeV, while for the lightest sbottom we impose $m_{\tilde{b}_1} > 700$ GeV [183, 184]. Regarding the gluino mass, the limit is $m_{\tilde{g}} > 1.2$ TeV, which holds when the LSP has non-vanishing mass, and can be independent of squark masses [183]. The situation is far more complicated with EW neutralinos and charginos at the LHC, since the limits are dependent on the specific modes of decay and m_{LSP}, and therefore should be analyzed in a benchmark model determined by a specific choice of the model parameters.

But SUSY can be searched also indirectly. Low energy observables, such as the decay of $b \to s\gamma$, receive important contributions from the sparticles. Thus, there are great experimental efforts nowadays in determining these observables as accurate as possible. First, the recent measurement of the branching ratio of the $B_s \to \mu^+\mu^-$ process by the LHCb [185] and CMS [186] collaboration, collectively yields $1.5 \times 10^{-9} < \text{BR}(B_s \to \mu^+\mu^-) < 4.3 \times 10^{-9}$ at 95% CL [187]. This branching ratio is strongly dependent on the Higgs sector of the SUSY construction, and hence it places an important constraint on SUSY scenarios. Secondly, in SUSY theories there exist two main contributions to flavor changing decay process $b \to s\gamma$: On one hand, charged Higgs-top loop tends to enhance the contribution to this observable respect to the SM prediction in the light charged Higgs regime. On the other hand, we have the chargino-stop loop contribution, which can be

invoked in order to compensate the former contribution. For this to happen, a sufficiently large chargino contribution is needed which requires stops and charginos relatively light. This measurement at 2σ requires the range $2.89 \times 10^{-4} < \mathrm{BR}(b \to s\gamma) < 4.21 \times 10^{-4}$, which takes into account theoretical and experimental uncertainties added in quadrature [188–192].

Finally, direct and indirect searches for DM, as well as its relic abundance, also place severe constraints on the SUSY parameter space. However, since this chapter is devoted to the DM phenomenology of specific candidates in the MSSM and NMSSM models, we will comment on these when analyzing them in the following sections.

2.2 Methodology to search for light SUSY DM

In order to analyze the phenomenology of light SUSY candidates we have performed a series of targeted scans. As we have emphasized previously, light WIMP's are usually very constrained by experimental observations, and thus find them is not an easy task. For this reason we have developed a tool for finding them systematically by means of different public codes properly linked.

First of all, we want to present the code which acts as a control for all the rest and is able to target the search: `MultiNest` [193–195]. This code is a Nested sampling tool, which is a Monte Carlo method whose primary aim is an efficient calculation of the Bayesian evidence. The algorithm also produces posterior samples which can be used to map out the posterior distribution and is used to estimate the profile likelihood. Since we are not interested in a statistical interpretation of the results given in this chapter, we use the mapping of the profile as a targeted search. For this purpose, in our scans we have built a likelihood function, $\mathcal{L}$, whose parameters are the DM relic density and SM-like Higgs mass which are taken as gaussian probability distribution functions around the measured values with 2σ deviations,

$$\log \mathcal{L} = -\sum_i \frac{(x_i - \mu_i)^2}{2\sigma_i^2}. \tag{2.6}$$

Here the index i represents the number of parameters, which in our case is two. x_i is the theoretical prediction for the variable i, and μ_i its measured value. Finally, σ_i is the standard deviation. Note that since our results are not statistically interpreted, the normalization for each of the terms in Eq. (2.6) is arbitrary. Using `MultiNest` allows us to explore the parameter space of the model more efficiently, since relatively few evaluations are needed to converge to regions which maximize the likelihood.

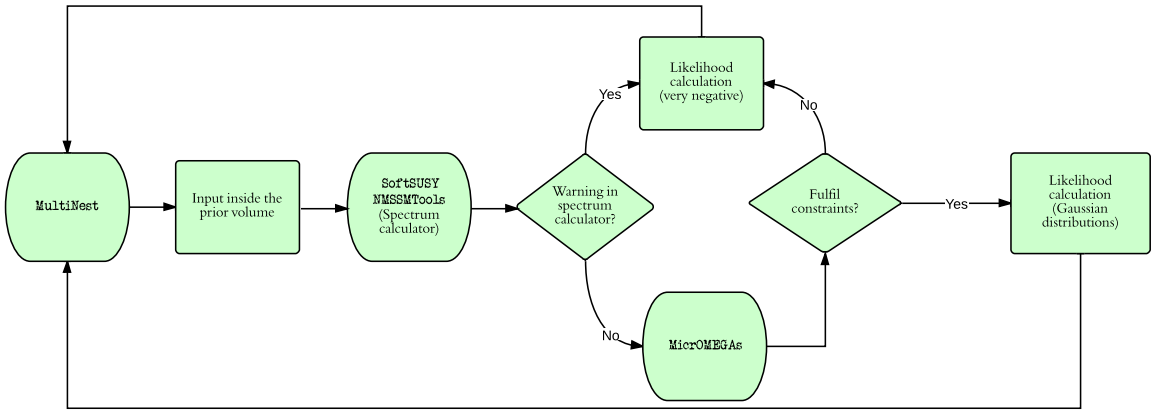

Figure 2.1: Flow chart of the SUSY parameter space scans

The flow chart of the scans is depicted in Figure 2.1. First, `MultiNest` generates a input given by N parameters $(X_0, X_1, ..., X_N)$ or priors, where N is the dimension of the scan. The range of the priors defines the hypervolume $X_1X_2...X_N$ as the region of the parameter space to be analyzed. This inputs are taken by any of these two codes, depending on the model considered, `SoftSUSY` [196] (MSSM) or `NMSSMTools` [197–199] (NMSSM) that calculate the SUSY spectrum for the given point of the parameter space. If there is a *Warning* from the spectrum calculator the point is automatically rejected, and the logarithm of the likelihood of assigned to be very negative which turns in a new point given by `MultiNest`. If no *Warning* is present, the information is passed to `MicrOMEGAs` code which then calculates all the DM and flavor observables [200–203]. This code also contains constraints on masses of the SUSY particles from LEP, and we include also those from the LHC commented above, and again if these are not fulfilled the code assigns a very negative logarithm of the likelihood and starts the process. Finally, if all constraints are fulfilled, the logarithm of the likelihood is calculated according to Eq. (2.6). This information is used by `MultiNest` to mapp out the profile likelihood and converge to the desired region. It is also worth mentioning that we have selected `MultiNest` internal parameters specially to be sensitive to very fine tuned regions, this is, a large number of *live points* and a low tolerance *tol* [204].

Finally, let us mention about the classification of the viable points found. Since we are dealing with three different models, it is better to find a universal classification according to the DM phenomenology. In this sense, the points are divided up into different classes

Annihilation Final State	Color code
$H_0^1 H_0^1$	
$A_0^1 A_0^1$	
$b\bar{b}$	
$c\bar{c}$	
$d\bar{d}$	
W^+W^-	
gg	
$\tau^+\tau^-$	
$\tilde{\chi}_1^0$ Coannihilation	

Table 2.2: Classification of DM annihilation final states according to colors. This code will be used along this chapter.

according to the dominant DM annihilation final state in the early Universe. In table 2.2, we have shown the colors used for this classification for the different annihilation channels. As we will see, this does not mean that all those final states are present in the model analyzed, for instance, in the MSSM is not possible to find a CP-odd Higgs pair ($A_1^0 A_1^0$) final state. Use this will help us to analyze the phenomenology, specially the associated to direct detection searches, but also to connect DM and collider searches.

2.3 The Minimal Supersymmetric Standard Model (MSSM).

The minimal supersymmetric extension of the SM is called MSSM [205, 206]. The particle content of the MSSM is as indicated in Table 2.1. The superpotential (see Eq. (2.4)) is given by,

$$\mathcal{W}_{MSSM} = \mathcal{Y}_u Q U^c H_u + \mathcal{Y}_d Q D^c H_d + \mathcal{Y}_e L E^c H_d + \mu H_u H_d, \tag{2.7}$$

where Q and L are the superfields containing left-handed quarks and leptons respectively, while U^c, D^c and E^c contain the left-handed antiquarks (up and down types) and leptons, which are the charged conjugates of the right-handed quarks and leptons. $\mathcal{Y}$ are 3×3 dimensionless Yukawa matrices in flavor space. Now at this points, it can be seen that there are two Higgs doublets, H_u and H_d, as it was anticipated previously.

Equation (2.7) highlights that the MSSM only introduces one new parameter, μ. The origin of this term is still today a puzzle. The term $\mu H_u H_d$ is allowed by the symmetries, and its presence is necessary to have a suitable vacuum after the EWSB. The μ parameter has dimension one, and it is expected to be of the order of the EW scale. However, as stated earlier the lack of knowledge about how SUSY is broken will introduce many more parameters.

The more general form of the SUSY breaking Lagrangian of the MSSM takes the following form,

$$\begin{aligned} -L_{soft}^{MSSM} &= \frac{1}{2}\left(M_3\tilde{g}\tilde{g} + M_2\widetilde{W}\widetilde{W} + M_1\widetilde{B}\widetilde{B} + c.c.\right) \\ &+\tilde{Q}^\dagger m_{\tilde{Q}_i}^2 \tilde{Q} + \bar{\tilde{U}}^\dagger m_{\tilde{U}_i}^2 \bar{\tilde{U}} + \bar{\tilde{D}}^\dagger m_{\tilde{D}_i}^2 \bar{\tilde{D}} + \bar{\tilde{L}}^\dagger m_{\tilde{L}_i}^2 \bar{\tilde{L}} + \bar{\tilde{E}}^\dagger m_{\tilde{E}_i}^2 \bar{\tilde{E}} \\ &+\left(\bar{\tilde{U}}^\dagger A_{U_i}\tilde{Q}H_u - \bar{\tilde{D}}^\dagger A_{D_i}\tilde{Q}H_d - \bar{\tilde{E}}^\dagger A_{E_i}\tilde{L}H_d + c.c.\right) \\ &+m_{H_u}^2 H_u^* H_u + m_{H_d}^2 H_d^* H_d + (bH_u H_d + c.c.)\,. \end{aligned} \tag{2.8}$$

The M_1, M_2 and M_3 are the gaugino mass matrices. The quantities $m_{\tilde{Q}_i}$ and $m_{\tilde{Q}_i}$ are the left-handed squarks and sleptons mass matrices for the i-th family, and $m_{\tilde{U}_i}$, $m_{\tilde{D}_i}$ and $m_{\tilde{E}_i}$ are the corresponding for the right-handed parts. The A_{U_i}, A_{D_i} and A_{E_i} couplings are called trilinear parameters. In the last line of Eq. (2.8) the soft parameters of the Higgs sector can be seen.

In the following section we will introduce the Higgs and Neutralino sectors of the MSSM for two basics reasons: the Higgs discovery reduces the freedom on the Higgs sector, which can be specially constraining in this case. Also the DM candidate in this scenario is the Neutralino, and since we want to analyze the light DM scenario, the mass matrix of the Neutralino will give us some hints.

2.3.1 The Higgs and Neutralino sectors

Let us start with the Higgs sector. As we already know it is characterized by two Higgs complex doublets,

$$H_u = \begin{pmatrix} H_u^0 \\ H_u^- \end{pmatrix} \qquad H_d = \begin{pmatrix} H_d^+ \\ H_d^0 \end{pmatrix}. \tag{2.9}$$

The EWSB is more complicated than in the SM, and it comes from the effective scalar potential, which after some simplifications reads

$$\begin{aligned} V_{Higgs} = &\left(|\mu|^2 + m_{H_u}^2\right)\left|H_u^0\right|^2 + \left(|\mu|^2 + m_{H_d}^2\right)\left|H_d^0\right|^2 - \left(bH_u^0 H_d^0 + c.c.\right) \\ &+\frac{1}{8}(g_2^2 + g_Y^2)\left(\left|H_u^0\right|^2 - \left|H_d^0\right|^2\right)^2. \end{aligned} \tag{2.10}$$

Now, EWSB can only take place if the b parameter satisfies the following equation:

$$b^2 > \left(|\mu|^2 + m_{H_u}^2\right)\left(|\mu|^2 + m_{H_d}^2\right), \tag{2.11}$$

which in addition can be further restricted by requiring the potential to be bounded from below[5],

$$2b < 2|\mu|^2 + m_{H_u}^2 + m_{H_d}^2. \tag{2.12}$$

After EWSB takes place, the fields H_u^0 and H_d^0 must develop Vacuum Expectation Values (VEVs),

$$\langle H_u^0 \rangle \equiv v_u \qquad \langle H_d^0 \rangle \equiv v_d, \tag{2.13}$$

providing masses to all quarks and leptons. Conventionally, one uses the ratio of these VEV's, which is a very important parameter,

$$\tan\beta \equiv \frac{v_u}{v_d} \quad : \quad 0 < \beta < \frac{\pi}{2}. \tag{2.14}$$

At the minimum of the potential given in Eq. (2.10), $\partial V_{Higgs}/\partial H_u^0 = \partial V_{Higgs}/\partial H_d^0 = 0$, the following boundary condition for the μ parameter holds[6],

$$\begin{aligned} |\mu|^2 &= \frac{m_{H_d}^2 - m_{H_u}^2 \tan^2\beta}{\tan^2\beta - 1} - \frac{1}{2}M_Z^2\,, \\ \sin 2\beta &= \frac{2b}{m_{H_u}^2 + m_{H_d}^2 + 2|\mu|^2}\,. \end{aligned} \tag{2.15}$$

In the beginning of this section the number of degrees of freedom were 8, corresponding to 4 complex scalars. The Higgs mechanism uses 3 degrees of freedom to give longitudinal polarization states, and hence masses, to the $W^\pm$ and Z bosons. So we are left with 5 physical states in the spectrum. These states are: 2 CP-even scalars Higgses, denoted by H_1^0 and H_2^0 (with $m_{H_1^0} < m_{H_2^0}$), 1 CP-odd scalar Higgs, A^0, and 2 charged Higgses $H^\pm$. The minimization conditions of the potential of Eq. (2.10) gives the tree level masses of these scalars:

$$\begin{aligned} m_{H_{1,2}^0}^2 &= \frac{1}{2}\left(m_{A^0}^2 + m_Z^2 \mp \sqrt{\left(m_{A^0}^2 + m_Z^2\right)^2 - 4m_{A^0}^2 m_Z^2 \cos^2 2\beta}\right), \\ m_{A^0}^2 &= \frac{2b}{\sin 2\beta}, \\ m_{H^\pm}^2 &= m_{A^0}^2 + m_W^2. \end{aligned} \tag{2.16}$$

[5] This is a tree level expression.

[6] Notice that this equation is independent of the phase of μ.

The mass of the lightest Higgs in the MSSM is bounded from above at tree level,

$$m_{H_1^0} < m_Z |\cos 2\beta|, \tag{2.17}$$

and therefore the Higgs discovered at the LHC with a mass around 125 GeV is a challenging constraint. To increase the Higgs mass up to values in concordance with the experiments, the radiative corrections must be maximized. In the MSSM, H_1^0 receives important corrections from top-stop loops, which are specially important for heavy stops. The mass of the lightest Higgs boson can be written at one loop approximately as [207, 208]:

$$m_{H_1^0}^2 \simeq M_Z^2 \cos^2 2\beta + \frac{3m_t^4}{16\pi^2 v^2}\left[\log\frac{M_s^2}{m_t^2} + \frac{X_t^2}{m_t^2}\left(1 - \frac{X_t^2}{12M_s^2}\right)\right], \tag{2.18}$$

where $M_s^2 = m_{\tilde{t}_1} m_{\tilde{t}_2}$, $v^2 = v_1^2 + v_2^2$, and $X_t = A_t - \mu \cot\beta$. The corrections are maximized for $|X_t| \simeq \sqrt{6} M_s$, known as maximal mixing scenario, or when the stops are extremely heavy [209, 210].

Now, we move to the Neutralino sector of the MSSM. As explained earlier, Gauginos and Higgsinos mix with each other, and the mass states are thus the combinations, that are generically named Neutralinos $\widetilde{\chi}^0_{1,2,3,4}$, which have zero electrical charge. These are four Majorana states, ordered in mass $m_{\widetilde{\chi}^0_1} < \ldots < m_{\widetilde{\chi}^0_4}$, and the lightest is the LSP in vast regions of the parameter space. By definition, Neutralinos are weakly interacting, and when R-parity is imposed, they represent the most known WIMP.

The Neutralino mass matrix in the basis $(\widetilde{B}, \widetilde{W}^3, \widetilde{H}_d^0, \widetilde{H}_u^0)$ is the following:

$$\mathbf{M}_{\chi^0} = \begin{pmatrix} M_1 & 0 & -M_Z c_\beta s_W & M_Z s_\beta s_W \\ 0 & M_2 & M_Z c_\beta c_W & -M_Z s_\beta c_W \\ -M_Z c_\beta s_W & M_Z c_\beta c_W & 0 & -\mu \\ M_Z s_\beta s_W & -M_Z s_\beta c_W & -\mu & 0 \end{pmatrix}, \tag{2.19}$$

where $(c_\beta, s_\beta) \equiv (\cos\beta, \sin\beta)$ and $(c_W, s_W) \equiv (\cos\theta_W, \sin\theta_W)$ being θ_W the Weinberg angle. The lightest Neutralino mass state would be given by $\tilde{\chi}_1^0 = N_{11}\widetilde{B} + N_{12}\widetilde{W}^3 + N_{13}\widetilde{H}_d^0 + N_{14}\widetilde{H}_u^0$. Therefore, as it can be seen from the mass matrix, in the limit of vanishing M_2 the lightest Neutralino is a Wino, $N_{12}^2 \approx 1$. On the other hand, in the limit of vanishing μ, the composition of the lightest state would be dominated by Higgsino composition, $N_{13}^2 + N_{14}^2 \approx 1$. These two idealized limits are now ruled out by unsuccessful searches at LEP. However, more interesting is the limit of vanishing M_1. In this case the lightest state would be mainly Bino, $N_{11}^2 \approx 1$, and nowadays this scenario is not in conflict with the experimental constraints. In this scenario the problem is the following:

since the Bino interacts very weakly with SM particles, the annihilation cross section is not large enough to account for the observed relic abundance and the Bino's would overclose the Universe. This can be circumvented in some tuned regions of the parameter space, known as *funnel regions*, where the annihilation proceed in a resonant s-channel with the CP-odd Higgs, or by invoking larger mixings with the other components of the LSP. The advantage of the Bino scenario is that since it is very weakly coupled to the SM, the limits on its mass are very much relaxed and it might be lighter than 100 GeV.

2.3.2 Neutralino dark matter

In order for the Neutralinos to be viable dark matter candidates they have to reproduce the correct value for their thermal abundance, $\Omega_{\tilde{\chi}_1^0}h^2$, which is specially hard when they are light. In the low energy description of the MSSM, within the regions where neutralinos are lighter than 100 GeV, there exists three dominant ways in which light neutralinos can annihilate efficiently. The first annihilation mechanism involves the exchange of CP-odd Higgses, the second involves the exchange of a Z boson and, finally, the correct relic density can be also achieved through the exchange of sleptons.

In the region of the parameter space in which neutralinos are lighter than approximately 15 GeV, the first mechanism is the most efficient and the relic density condition is fulfilled when m_{A^0} is around 100-150 GeV and $\tan\beta$ is relatively large [211–213]. According to Eq. (2.16), the pseudoscalar mass and $\tan\beta$ parameter, control the mass of the Higgs sector. Such light pseudoscalar Higgs would pull the Higgs sector and all masses would be around m_{A^0}. This scenario is known as *non-decoupling limit* and it is very restricted. The ATLAS and CMS collaborations have performed searches of both neutral scalars and charged scalars decaying into τ leptons [214, 215]. These unsuccessful searches have placed strong constraints on this scenario, almost ruling out this possibility. As previously mentioned, Neutralinos annihilating into a Z boson holding the resonant condition, $m_{\tilde{\chi}_1^0} \approx M_Z/2$, results in the correct relic abundance as well. This scenario requires a more fine tuning in the Neutralino mass, and thus we are interested.

For the latter mechanism, as depicted in Fig. 2.2, to be efficient, sleptons $\tilde{l}$ are required to be rather light. However, a light CP-odd Higgs boson is not longer necessary and therefore this scenario can escape all constraints [216]. In Ref. [217] this option was investigated concluding that sleptons must lie just above LEP limit in order to achieve the correct relic density. The direct and indirect detection constraints as well as some collider observables have been analyzed, probing that this possibility was still not rejected even for neutralinos as light as 15 GeV [218–220]. Other works pointed out the possibility

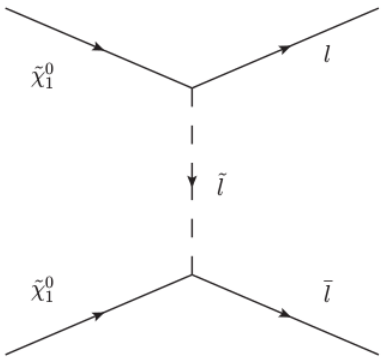

Figure 2.2: Diagram for the Slepton driven annihilation of Neutralinos into leptons in the MSSM.

that Neutralinos might be very light if the Sbottom is also very light, with a mass splitting between them of a few GeV [221].

The Neutralino coupling to Staus involved in the annihilation process of Fig 2.2 is given by [219, 222]:

$$\begin{aligned} g_{\tilde{\chi}_1^0\tilde{\tau}_1\tau_L} &= \sqrt{\frac{2}{v_u^2+v_d^2}}\left(m_Z\cos\theta_\tau(N_{11}s_W+N_{12}c_W)-N_{13}m_\tau\frac{\sin\theta_\tau}{\cos\beta}\right), \\ g_{\tilde{\chi}_1^0\tilde{\tau}_1\tau_R} &= -\sqrt{\frac{2}{v_u^2+v_d^2}}\left(2m_Z\sin\theta_\tau N_{11}s_W-N_{13}m_\tau\frac{\cos\theta_\tau}{\cos\beta}\right). \end{aligned} \tag{2.20}$$

In this equations θ_τ is the Stau mixing angle, which can be expressed as,

$$\cos\theta_\tau = \frac{-m_\tau\left(A_E-\mu\tan\beta\right)}{\left[m_\tau^2\left(A_E-\mu\tan\beta\right)^2+\left(m_{\tilde{L}_3}^2+m_\tau^2-m_{\tilde{\tau}_1}^2-\frac{1}{2}m_Z^2c_{2W}\cos 2\beta\right)\right]^{1/2}}, \tag{2.21}$$

which highlights that the mixing is controlled by $A_E-\mu\tan\beta$. Since the light Neutralinos must be mostly Bino, the lightest mostly right-handed stau exchange will dominate the annihilation cross section. Therefore, this scenario makes fundamental the presence of a mostly right-handed Stau with a mass around 90 GeV, as close as possible to the LEP limit.

Summarizing, in the MSSM with parameters defined at low energy, very light neutralinos are difficult to obtain. Latest experimental results, from the LHC and direct detection experiments, are having a strong impact in this region of the parameter space. As we have mentioned, the only possibility left is a scenario with very light sleptons as close as possible to LEP limits. However, a question that still remains unanswered

is whether or not these effective Supersymmetric models can have a viable origin from a SUGRA theory defined at GUT scale. This is interesting since a conventional way of understanding the origin of the soft supersymetry breaking terms is the breaking of SUGRA at a higher scale. Moreover, since the RGE's are coupled, in these scenarios the freedom for choosing the parameters at EW scale is much lower, and thus the constraints are more restrictive in general. For these reasons, we are going to analyze light neutralinos from a high energy perspective.

The scan

The first crucial ingredient is to allow departures from universality in the gaugino sector which allow Neutralinos in this region of the parameter space to be Bino-like. This is mandatory in order to suppress the coupling to the Z boson and to evade then the experimental constraint on its invisible decay width. Bino-like neutralinos are obtained just by lowering M_1 with respect to M_2 and μ as it can be seen in Eq. (2.19). Actually, M_2 and μ are also parameters involved in the chargino mass matrix and therefore, due to the LEP constraint on chargino mass they are bounded to be M_2,$\mu \gtrsim 100$ GeV. From this condition follows that $m_{\tilde{\chi}_1^0} \simeq M_1$ at the EW scale. For the sake of simplicity, we keep the universal relation between M_2 and M_3. Therefore the gaugino sector is parametrized at GUT scale by:

$$M_1 \ , M_2 \ , M_3 = 3.75 \times M_2 \ . \tag{2.22}$$

Regarding the scalar sector we allow departures in the Higgs soft masses, which can be important for having a CP-even Higgs around 125 GeV without demanding maximal mixing in the stop mass matrix. We use the following soft masses as inputs:

$$m_{H_d} \ , m_{H_u} \ . \tag{2.23}$$

Still in the scalar sector, we allow non-universalities in the slepton soft masses. Since the solution under investigation requires slepton masses close to the LEP limit, and namely, stau masses around 80-90 GeV, this sector is described at high energy by the following inputs:

$$m_{\tilde{L}_3} \ , m_{\tilde{E}_3} \ , m_{\tilde{L}_2} \ , m_{\tilde{E}_2} \ . \tag{2.24}$$

For simplicity we keep the soft masses of the first generation equal to the second one. For the squarks soft masses we have kept all equal, and they are given at GUT scale by:

$$m_{\tilde{Q}} \ . \tag{2.25}$$

Parameter	Range
M_1	1 - 110
M_2	100 - 1000
$\tan\beta$	1.5 - 60
A_U	-7000 - -3000
m_{H_u}	100 - 3000
m_{H_d}	100 - 2000
$m_{\tilde{L}_2}$	1 - 2500
$m_{\tilde{L}_3}$	1 - 1000
$m_{\tilde{R}_2}$	500 - 1500
$m_{\tilde{R}_3}$	1 - 1000
$m_{\tilde{Q}}$	1 - 3000

Table 2.3: Input parameters for the series of scans used in this work. Masses and trilinear parameter are given in GeV. All parameters are defined at GUT scale.

Finally, the three trilinear parameters A_U, A_D and A_E defined at GUT scale, are the family independent, and must play an important role in this study. Specially important might be the top trilinear, A_U, which controls the higgs mass as seen in Eq. (2.18). Also the Stau mixing can play an important role, however, for simplicity we fix it to be zero at GUT scale. Therefore, we choose the following inputs:

$$A_U \ , A_D = 0 \ , A_E = 0 \ . \tag{2.26}$$

A_D plays a role in the mixing of the down sector which is induced by $\mu \tan\beta$ and might modify radiative corrections in the Higgs mass at large $\tan\beta$ [210]. Since the large $\tan\beta$ regime is disfavored by flavor constraints, one would expect that this choice does not have an impact in these scenarios.

Following these criteria we have performed a series of scans in the parameter space where the different input parameters are varied according to Table 2.3. The procedure sketched in Fig. 2.1 has been used, with `SoftSUSY` as the spectrum calculator at EW scale using the RGE's from the GUT scale defined parameters. The constraints on the Higgs sector in this case are implemented through the code `HiggsBounds` [223, 224]. To differentiate between parameters evaluated at GUT and EW scales, we denote the formers with the upper index GUT, like for example M_1^{GUT}. Furthermore, we have definef

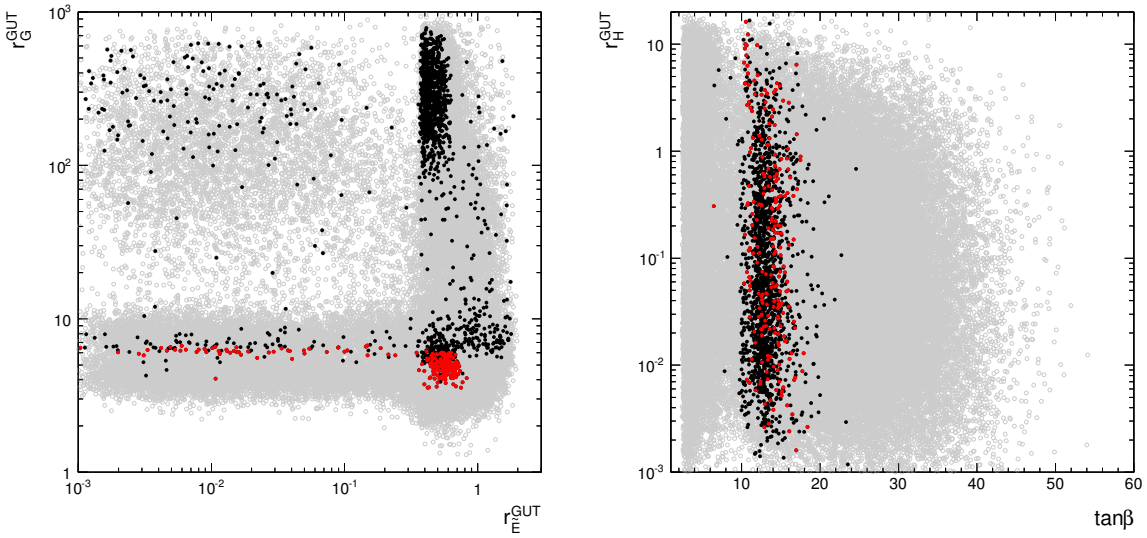

Figure 2.3: Universality patterns in the scalar and gaugino sectors of the MSSM for light Neutralinos.

the ratios,

$$r_G^{GUT} \equiv \frac{M_2^{GUT}}{M_1^{GUT}}, \qquad r_H^{GUT} \equiv \frac{m_{H_d}^{GUT}}{m_{H_u}^{GUT}}, \qquad r_{\tilde{E}}^{GUT} \equiv \frac{m_{\tilde{E}_3}^{GUT}}{m_{\tilde{E}_2}^{GUT}}, \tag{2.27}$$

which control the universality degree patterns in the scalar and gaugino sectors.

In Figure 2.3 the distribution of some of the inputs of the scan are shown. In the left panel r_G^{GUT} versus $r_{\tilde{E}}^{GUT}$ plane is depicted. The gray empty points fulfill all experimental constraints regardless of the Higgs mass, $m_{H_1^0}$, and the Neutralino relic abundance. On top of this, black points encode the correct Higgs mass, $123 < m_{H_1^0} < 128$ GeV, and red full dots besides fulfill the upper bound on the relic density. According to Table 2.2, the red points correspond to a Neutralino annihilation final state of $\tau^+\tau^-$ in the early Universe. As we can see in the plot, the red points encode a precise relation between gaugino masses, $r_G^{GUT} \approx 5$. Since the chargino mass is proportional to M_2, it is restricted by LEP null searches, which pushes r_G^{GUT} to be greater than 2 (the Universal value). Besides, since the light Stau is mostly right-handed (this means $\cos\theta_\tau \approx 1$) and thus it couples strongly to the Bino component of the Neutralino (see Eq. (2.20)), and thus the Bino component of the neutralino benefits of the relic density upper limit pushing r_G^{GUT} beyond 2. On the other hand, the presence of a light right-handed Stau favors $r_{\tilde{E}}^{GUT} < 1$, but surprisingly a pattern emerges as well in this parameter. Most of the red points accumulates around $r_{\tilde{E}}^{GUT} \approx 0.6$, although some points can be found for much

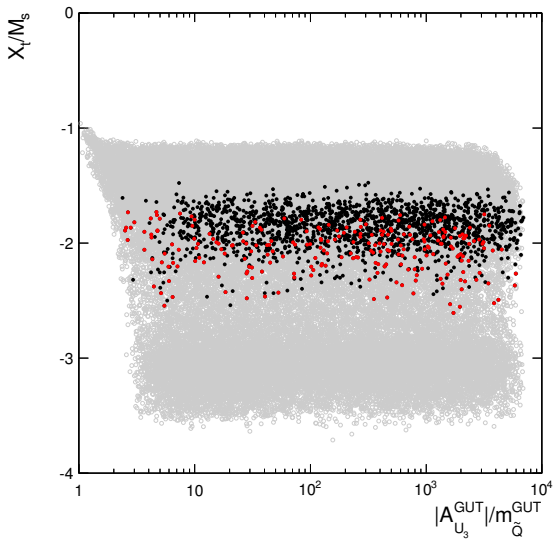

Figure 2.4: Stop mixing as a function of trilinear and soft mass parameters at GUT scale. The color code is the same than in Fig. 2.3.

lower values of $r_{\tilde{E}}^{GUT}$ as well.

In the right panel of Figure 2.3, the r_H^{GUT} is plotted versus $\tan\beta$, with the same color code than in the left panel. In this plane, the effect of the Higgs mass constraint is huge, constraining the $\tan\beta$ values to be around 14, while the relation between the Higgses soft masses is kept unconstrained basically. To understand the effect of $\tan\beta$ in the Higgs mass constraint in Fig. 2.4 we have plotted the Higgs mixing parameters X_t/M_s, defined after Eq. (2.18), versus the Stop trilinear and soft mass, $|A_{U_3}^{GUT}|/m_{\tilde{Q}}^{GUT}$. The Higgs mass constraint is fulfilled when the maximal mixing scenario occurs $|X_t|/M_s \approx \sqrt{6}$ which is dependent on the values of $\tan\beta$. Notice that Stop masses are above 1 TeV approximately, and therefore all remaining colored particles are expected to have multi-TeV masses. Moreover, maximal mixing values are reached for $|A_{U_3}^{GUT}|/m_{\tilde{Q}}^{GUT} > 2$, which is in concordance with the universal case where $A/m > 2$ [225].

Direct detection

Direct detection searches are based on the elastic scattering of DM off nuclei inside a detector. For any WIMP candidate, the WIMP-nucleus elastic cross section depends fundamentally on the WIMP-quark interaction strength. However, since the quantity determining the rate is the WIMP-nucleus cross section, the distribution of quarks in the nucleon and the distribution of nucleons play a crucial role as we will see in the next

chapter. For the moment, in this chapter, the aim is to determine the WIMP-nucleon cross section forgetting about promoting it to the nucleus level. An important simplification in these calculations occurs because the interaction between the DM particle and the nucleus takes place in the extreme *non-relativistic* limit, and hence an effective approach is well motivated.

For the MSSM Neutralinos (and in general for any Majorana fermion) the effective Lagrangian reads

$$L_{eff} = \sum_q \alpha_q \bar{\chi}\chi\bar{q}q + \xi_q \bar{\chi}\gamma_5\gamma_\mu\chi\bar{q}\gamma_5\gamma^\mu q \tag{2.28}$$

where the sum runs over the six quarks, and the coefficients α_q and ξ_q can be found in Refs. [47, 201]. The first term in Eq. (2.28) corresponds to the scalar interactions, those which contribute to the Spin-Independent (SI) interactions, and are generically larger to those coming from the second term, the axial-vector interactions contributing to the Spin-Dependent (SD) interactions. For the SI interactions the Neutralino-nucleon cross section can be written as:

$$\sigma^{SI}_{p,n} = \frac{4\mu^2_{p,n}}{\pi} f^2_{p,n} \tag{2.29}$$

where $\mu_{p,n}$ is the Neutralino-nucleon reduced mass and p, n stand for protons and neutrons respectively. In most cases $f_p \approx f_n$, this scenario is known as *isospin-conservation*. Nonetheless as we will see, scenarios with *isospin-violation* lead to very interesting direct detection phenomenology nowadays. These parameters can be further decomposed,

$$\frac{f_{p,n}}{m_{p,n}} = \sum_q f^{p,n}_q \frac{\alpha_q}{m_q} \tag{2.30}$$

where m_q is the mass of the quark in the sum. The parameter α_q must be calculated from the Higgs and squark exchange diagrams, as shown in Fig. (incluir). The $f^{p,n}_q$ parametrize the quark content of the nucleon. They are determined by the light quark mass ratios, m_u/m_d and m_s/m_d, the sigma term $\sigma_{\pi N}$, and the strange content of the nucleon σ_s. As commented earlier, the DM observables are calculated using `MicrOMEGAs`, for which the following default values are used [201, 203]:

$$\frac{m_u}{m_d} = 0.46, \qquad \frac{m_s}{m_d} = 27.5, \qquad \sigma_{\pi N} = 42.0 \text{ MeV}, \qquad \sigma_s = 34.0 \text{ MeV}. \tag{2.31}$$

It is important to remark at this point that the last two parameters are extracted using lattice QCD calculations, and hence are subject to important uncertainties that affect the cross section calculation.

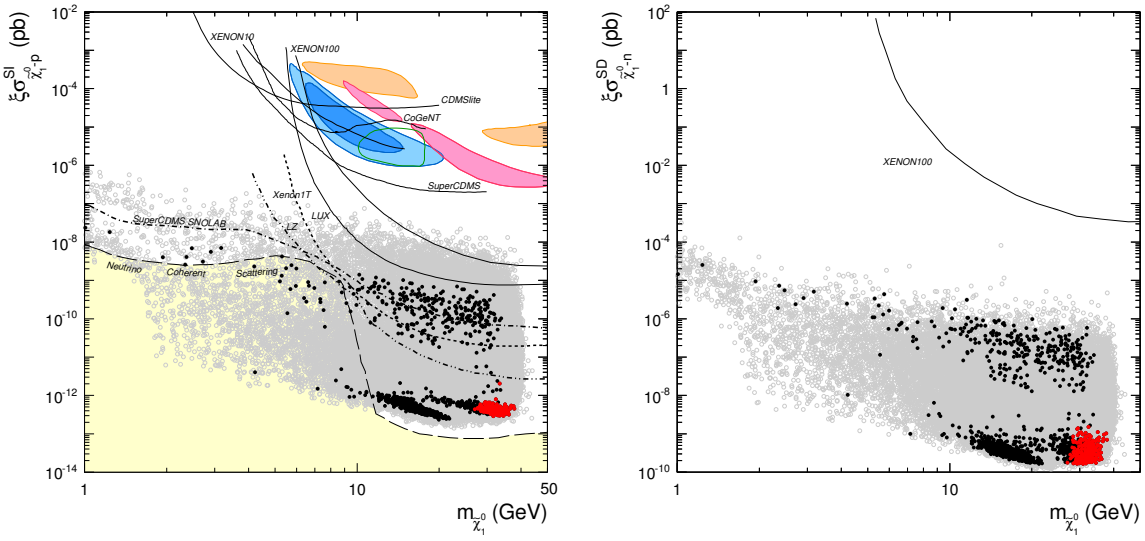

Figure 2.5: Theoretical predictions for $\sigma^{SI}_{\tilde{\chi}^0_1-p}$ and $\sigma^{SD}_{\tilde{\chi}^0_1-n}$ versus the Neutralino mass $m_{\tilde{\chi}^0_1}$. The left panel is the same as Fig. 1.6 but with the Neutralino prospects superimposed following the same color code as Fig. 2.3, and as a reference we have included the future prospects of LZ, XENON1T and SuperCDMS at SNOLAB. Furthermore, the irreducible neutrino background is shown as well as a yellow region in the bottom of the plot [117]. In the right panel the theoretical predictions are compared with current bounds from Xenon100 collaboration [109].

In the left panel of Figure 2.5 the theoretical predictions for the SI cross section of Neutralino off protons, $\sigma^{SI}_{\tilde{\chi}^0_1-p}$, is shown versus its mass. The fractional density, $\xi = \min[1, \Omega_{\tilde{\chi}^0_1}h^2/0.13]$, is included to account for the reduction in the rate in the cases where the Neutralino only contributes to a fraction of the total DM density (assuming that it is present in the DM halo in the same proportion as in the Universe). Notice that this figure is the same as Fig. 1.6 but the Neutralino prospects superimposed using the same color code as in previous figures. The cross sections predicted in these scenarios are remarkably tiny, even out of the reach of future experiments like LZ (dot-dot-dash line), XENON1T (dash line) and SuperCDMS (dot-dash line), although above the irreducible neutrino background [117]. The huge Bino composition of the lightest Neutralino, $N^2_{11} \approx 1$ as a consequence of the fact that $M_1 \ll M_2, \mu$, penalizes the coupling to the scalar Higgs since it is proportional to the Higgsino composition, N_{13} and N_{14}. The remaining contribution comes from the squark s-channel exchange, which is proportional to

$$\sigma^{SI}_{\tilde{\chi}^0_1-p} \propto \frac{|N_{11}|^4}{m^4_{\tilde{q}}}. \tag{2.32}$$

A natural consequence of the LHC bounds is that squarks must be heavy, which reduces

the cross section strongly. The main difference with solutions found in Refs. [217, 219] is the amount of Higgsino *doping*, which increases substantially the cross sections through the Higgs exchange in those cases.

In the right panel of Figure 2.5 the theoretical predictions for the SD cross section of Neutralino off neutrons, $\sigma^{SD}_{\tilde{\chi}^0_1-n}$, is shown versus its mass. As a reference the current bound of Xenon100 collaboration, which is the most stringent for neutron couplings over a wide range of masses, has been included [109]. Although it has been not commented before, the SD cross section is largely governed by Z boson exchange, again because the squarks are constrained to be heavy and hence their contribution is very small. The coupling of the Neutralinos to the Z bosons occurs through the Higgsino mixing, so the cross sections are again pretty suppressed.

This is the first example in which the cross relation between direct detection and relic density shown in Fig. 1.5 is broken. Since the dominant annihilation final state of these Neutralinos is $\tau^+\tau^-$ (remind the red color of the points as indicated in Table 2.2), and this diagram (see Fig. 2.2) does not contribute to the direct detection cross sections, they are uncorrelated. Actually, this might be seen as the reason why WIMP's can predict very low cross section and might not be detected ever in underground laboratories. However, since this is not the only search method for WIMP's, let us move to analyze the indirect detections prospects of these scenarios.

Indirect detection

To calculate the thermally averaged cross section usually one uses an approximation in terms of the expansion in powers of $x \equiv T/m$, $\langle \sigma v \rangle \simeq a + 6bx$. This is a good approximation for non-relativistic particles at the freeze-out temperature as long as there is not s-channel resonances and thresholds for new final states, as in this case. For the diagram shown in Fig. 2.2 in the limit of $\cos\theta_\tau \to 0$, the a and b parameters reads [219]

$$\begin{aligned} a &= \frac{m^2_{\tilde{\chi}^0_1}}{8\pi}\left[\frac{g_{\tilde{\chi}^0_1\tilde{\tau}_1\tau_R} g_{\tilde{\chi}^0_1\tilde{\tau}_1\tau_L}}{(m^2_{\tilde{\tau}^0_1} + m^2_{\tilde{\chi}^0_1})}\right]^2 \\ b &\approx \frac{m^2_{\tilde{\chi}^0_1}}{48\pi}\left[\frac{(g^4_{\tilde{\chi}^0_1\tilde{\tau}_1\tau_R} + g^4_{\tilde{\chi}^0_1\tilde{\tau}_1\tau_L})(m^4_{\tilde{\tau}^0_1} + m^4_{\tilde{\chi}^0_1})}{(m^2_{\tilde{\tau}^0_1} + m^2_{\tilde{\chi}^0_1})^4}\right]. \end{aligned} \tag{2.33}$$

On the one hand, in this limit a parameter, know as the s-wave contribution, is proportional only to the Higgsino mixing N_{13}, and thus in our case is going to be negligible. On the other hand, the b parameter, know as the p-wave contribution, is going to dominate the cross section. However, this cross section is temperature suppressed respect to the

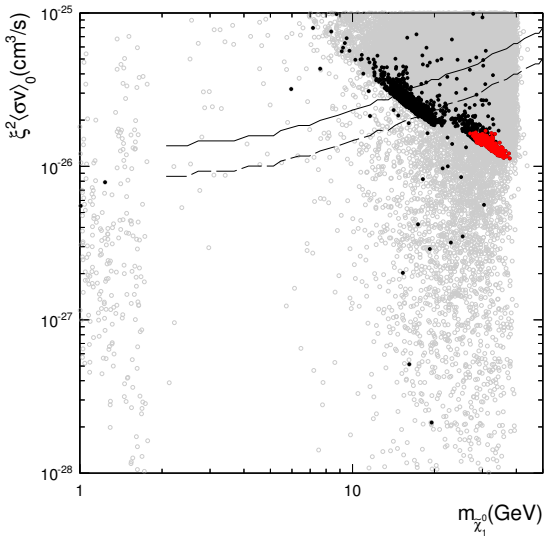

Figure 2.6: Thermally averaged Neutralino annihilation cross section in the galactic halo, $\xi^2\langle\sigma v\rangle_0$, as a function of its mass. The solid and dashed lines correspond to the upper bounds on $\langle\sigma v\rangle$ derived from an analysis of dSph galaxies for pure $\tau^-\tau^+$ for 4 and 10 years of exposure, respectively. The forecast for ten years of exposure has been obtained following Ref. [148]. The colour code is as in Fig. 2.3.

one in the Early Universe, and thus smaller gamma ray fluxes are expected (respect to the canonical cross section).

In Fig. 2.6 the theoretical predictions for the thermally averaged cross section of Neutralinos in the Galactic Halo, $\xi^2\langle\sigma v\rangle_0$, is shown. We have also included the current limits from the observation of 4 [132] and 10 years of dSph galaxies, black and dashed lines respectively. It can be seen that this scenarios are difficult to test but that higher exposures might reach enough sensitive to detect these neutralinos. The cross sections, as expected, are suppressed respect to the canonical (early Universe) value $\langle\sigma v\rangle_0 \sim 3\times10^{-26}$ cm^{2}s^{-1} making its detection challenging.

2.4 The Next-to-MSSM (NMSSM)

Surely, the main motivation of the NMSSM is that it solves the μ-problem of the MSSM. Recalling Eq. (2.15), for the μ parameter to be at the EW scale in the MSSM, the Z boson mass requires some degree of fine tuning between the Higgs soft mass parameters. In the NMSSM, an additional scalar gauge singlet, S, is introduced which generates the μ-term dynamically, that is, an effective μ-term arises spontaneously and the adjustment

by hand disappears [226, 227]. The NMSSM superpotential reads,

$$\mathcal{W}_{NMSSM} = \mathcal{W}_{MSSM} + \lambda S H_u H_d + \frac{1}{3}\kappa S^3, \tag{2.34}$$

where $\mathcal{W}_{MSSM}$ is the MSSM superpotential defined in Eq. (2.7) with $\mu = 0$. Some comments about this superpotential are in order. In the first place, notice that the μ parameter is generated effectively once the singlet S acquires a VEV, so $\mu_{eff} = \lambda v_s$, with $v_s = \langle S \rangle$. In the second place, a cubic term in S proportional to a new parameter κ has been also introduced without motivation *a priori*. A close inspection to this superpotential in the case of $\kappa = 0$ reveals the presence of a global Peccei-Quinn (PQ) symmetry, $U(1)_{PQ}$. Such symmetry gives rise to an axion, not present in the MSSM since that symmetry is explicitly broken by the μ-term. Experimental null searches for that axion constrain the λ parameter to be $10^{-10} < |\lambda| < 10^{-7}$ [227], which pushes v_s to very high values for μ to have an EW order. Again, large fine tuning is required. To avoid this, the $\frac{1}{3}\kappa S^3$ term is imposed in the superpotential which breaks explicitly the PQ-symmetry[7]. Finally, note that two new mass states will appear in the Higgs sector, one CP-even and one CP-odd, and one fermionic state called *singlino*, $\tilde{S}$, will add one more mass state to the Neutralino mixing matrix. These will give rise to a very diverse phenomenology.

Regarding the soft breaking terms, in the NMSSM we have two new terms, one for the mass of the scalar and the trilinear terms from the new dimensionless parameters λ and κ,

$$-L_{soft}^{NMSSM} = -L_{soft}^{MSSM} + m_S^2|S|^2 + \left(\lambda A_\lambda S H_u H d + \frac{1}{3}\kappa A_\kappa S^3 + c.c.\right) \tag{2.35}$$

In this Lagrangian, L_{soft}^{MSSM} is given in Eq. (2.8) with $b = 0$ and the new trilinears are A_λ and A_κ. Note, that the limit in the MSSM with $b = 0$ means that all terms related to μ are zero, as expected, since in the NMSSM they are generated spontaneously as commented before.

2.4.1 The Higgs and Neutralino sectors

As in the case of the MSSM, let us start by reviewing the Higgs sector. The scalar fields in the Higgs sector are augmented respect to the the MSSM case since a new singlet

[7] Notice that still a discrete $\mathbb{Z}_3$ symmetry remains. This symmetry is broken once v_s is generated and hence would lead to the appearance of *topological defects* [227].

scalar S has been introduced,

$$H_u = \begin{pmatrix} H_u^0 \\ H_u^- \end{pmatrix} \qquad H_d = \begin{pmatrix} H_d^+ \\ H_d^0 \end{pmatrix} \qquad S. \tag{2.36}$$

A simple counting of the degrees of freedom reveals the presence of two new mass eigenstates respect to the MSSM, one CP-even and one CP-odd. Without loss of generality the Higgs masses of the CP-even sector are ordered as, $m_{H_1^0} \leq m_{H_2^0} \leq m_{H_3^0}$, and the same for the CP-odd sector, $m_{A_1^0} \leq m_{A_2^0}$.

The Higgs physics in the NMSSM is quite different to the MSSM case due to the presence of the singlet scalar which in general mixes with the doublet part. Firstly, the tree level upper bound on the lightest Higgs mass in the MSSM (see Eq. (2.17)) is lifted,

$$m_{H_1^0}^2 < m_Z^2 |\cos^2 2\beta| + \lambda^2 v^2 \sin^2 2\beta. \tag{2.37}$$

The second term of this equation is the NMSSM contribution and is maximized for high λ and low $\tan\beta$. This contribution is welcomed from the point of view of the discovery of a relatively heavy SM-like Higgs boson at the LHC. It has been argued that the NMSSM alleviates the fine tuning problem of the MSSM, this is, this contribution naturally raises the mass of the Higgs, and hence it is not necessary to implement a *maximal mixing* scenario [228–233].

After radiative electroweak symmetry-breaking the Higgs fields get non-vanishing vacuum expectation values (VEVs). The physical CP-even and CP-odd Higgs eigenstates can be expressed as a linear superposition of the H_d, H_u and S fields. For the CP-even Higgs we will use the following decomposition,

$$H_i^0 = S_{H_i^0}^1 H_d + S_{H_i^0}^2 H_u + S_{H_i^0}^3 S\,. \tag{2.38}$$

Another important difference with the MSSM is the possibility of having an extra scalar Higgs and a pseudoscalar Higgs very light without violating current collider constraints, provided that they are mostly singlet-like. Therefore, if these states are below the Neutralino LSP annihilation threshold, they might modify the DM phenomenology since the cross correlation between the relic abundance and the detection cross sections would be broken. Also, they can play an important role in the relic density constraint for annihilations driven by a s-channel exchange of some of these scalars. If the Neutralino is very light, a light scalar with a mass suitably chosen around $m_{H_1^0, A_1^0} \approx 2m_{\tilde{\chi}_1^0}$ relaxes the relic density constraint thanks to the resonant annihilation.

Regarding the Neutralino sector, a new mass eigenstate is present, the *singlino* $\widetilde{S}$. The mass matrix increases thus in one more dimension. In the basis $(\widetilde{B}, \widetilde{W}^3, \widetilde{H}_d^0, \widetilde{H}_u^0, \widetilde{S})$ is

the following:

$$\mathbf{M}_{\chi^0} = \begin{pmatrix} M_1 & 0 & -M_Z c_\beta s_W & M_Z s_\beta s_W & 0 \\ 0 & M_2 & M_Z c_\beta c_W & -M_Z s_\beta c_W & 0 \\ -M_Z c_\beta s_W & M_Z c_\beta c_W & 0 & -\mu_{eff} & -\frac{\lambda}{\sqrt{2}} v_u \\ M_Z s_\beta s_W & -M_Z s_\beta c_W & -\mu_{eff} & 0 & -\frac{\lambda}{\sqrt{2}} v_d \\ 0 & 0 & -\frac{\lambda}{\sqrt{2}} v_u & -\frac{\lambda}{\sqrt{2}} v_d & \frac{2\kappa \mu_{eff}}{\lambda} \end{pmatrix}. \tag{2.39}$$

In the limit $\lambda \to 0$, the $\widetilde{S}$ is an almost pure state whose mass is given by the last diagonal entry, and interestingly is proportional to κ parameter, as in the case of the lightest pseudoscalar.

For a very light Neutralino to be allowed by the experimental constraints we have pointed out that it must be slightly coupled to SM particles, what in the MSSM was realized by means of high Bino component. However, in the NMSSM, another possibility has opened up. The lightest Neutralino can be *singlino* as well evading the constraints. The *singlino* can annihilate efficiently through the exchange of light singlet Higgses as well as into light Higgs singlets [199, 216, 234].

2.4.2 Neutralino dark matter

Several analysis have addressed light Neutralino DM in the NMSSM [216, 217, 235–241]. Most of them were done in the pre-LHC era, when the constraints on the Higgs sector were much less stringent. This is important because as pointed out in these publications, due to the weak couplings of the singlet-like scalars with the Neutralinos and SM particles, it must be accompanied of a light scalar, either H_1^0 or A_1^0, to annihilate efficiently in the early Universe. Such light scalars will contribute to the branching fractions of the SM-like Higgs and therefore, will increase the *non-Standard* decay modes.

For the relic density calculation, the coupling of Neutralinos to the Z boson can be important [199]. This coupling, as in the MSSM case, is proportional to the Higgsino components of the Neutralino, N_{13} and N_{14}. As already mentioned, the coupling of Neutralinos to scalar and pseudoscalar Higgses play a relevant role. In the limit of a pure singlet-like Higgs, these couplings can be written as [199]:

$$g_{\tilde{\chi}_1^0 \tilde{\chi}_1^0 H_1^0} \approx \sqrt{2} \left(\lambda N_{13} N_{14} - \kappa N_{15}, ^2 \right) \tag{2.40}$$

$$i g_{\tilde{\chi}_1^0 \tilde{\chi}_1^0 A_1^0} \approx -\sqrt{2} \left(\lambda N_{13} N_{14} - \kappa N_{15} .^2 \right) \tag{2.41}$$

So an important parameter for a Singlino-like Neutralino to couple to the scalars is κ. However, as we can see from Eq. (2.39), the mass of the Singlino is proportional to κ,

and therefore light Singlinos are accompanied by small couplings to the scalars[8]. When the scalars contain a non-negligible doublet component, Neutralinos can couple through a Bino-Higgsino mixing as well, just as in the MSSM case.

the scan

Let us remind the reader that, in contrast to the MSSM, in this case all the parameters are defined at EW scale, and the SUSY breaking is realized explicitly by the inclusion of the soft terms at this scale. Like in the MSSM, we are going to allow departures from universality in the gaugino soft masses, since they enter in the Neutralino mass matrix,

$$M_1 \ , M_2 \ , M_3 = 1500 \ , \tag{2.42}$$

where are all in GeV units. However, in this case for simplicity, we have fixed the gluino soft mass M_3 above the current LHC bounds. The remaining parameters are the six free parameters which determine the Higgs sector in the NMSSM,

$$\lambda \ , \kappa \ , A_\lambda \ , A_\kappa \ , \mu_{eff} \ , \tan\beta \ . \tag{2.43}$$

Fixed values are used for the trilinear parameters, $A_U = 3700$ GeV, $A_D = 2000$ GeV, and $A_E = -1000$ GeV, as well as for the soft scalar masses of sleptons and squarks, $m_{\tilde{L}_i} = m_{\tilde{E}_i} = 300$ GeV and $m_{\tilde{Q}_i} = m_{\tilde{U}_i} = m_{\tilde{D}_i} = 1500$ GeV, respectively, where the index i runs over the three families. The conservative choice of the squark masses is motivated by the LHC null searches. Also note that despite of the high trilinear term A_U, since the soft mass of the squarks is at TeV scale the instability against charge- and/or color-breaking minima is avoided [242].

As in the previous case, we have performed a series of scans in the parameter space where the different input parameters are varied according to Table 2.4. We have followed the procedure sketched in Fig. 2.1, with two different scanned regions following the distribution found in Ref. [217]. The spectrum calculator in this case is `NMSSMTools`, using the full 2-loop radiative corrections on the Higgs mass. On the contrary, now the constraints on the Higgs sector are implemented by hand using the latest CMS results on the signal strengths [152]. We have also imposed the presence of a Higgs boson, either H_1^0 or H_2^0 , in the mass range between 123 and 128 GeV. For this reason, we have not included a term dependent on the Higgs mass on the likelihood defined in Eq. (2.6).

[8] Remind that the μ parameter is restricted by the Chargino mass and thus can not be arbitrarily decreased to have light Singlinos. Also the parameter λ is upper bounded by perturbativity.

Parameter	Range
M_1	1 - 200, 1 - 40
M_2	200 - 1000
$\tan\beta$	4 - 20
λ	0.1 - 0.6
κ	0 - 0.1
A_λ	500 - 1100, 3000 - 5000
A_κ	-50 - 50, -30 - 0
μ_{eff}	110 - 250,160 - 250

Table 2.4: Input parameters for the series of scans used in this work in the NMSSM. Masses and trilinear parameter are given in GeV. All parameters are defined at EW scale. Notice that the scan has been divided into two separate regions.

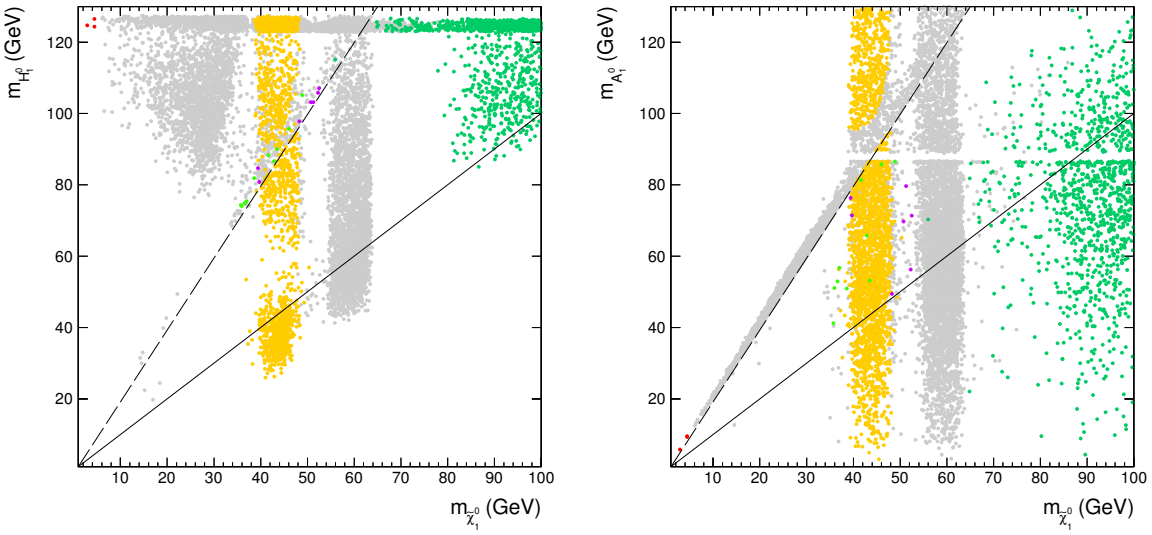

Figure 2.7: Mass of the lightest scalar (left) and pseudoscalar Higgses (right) as a function of the Neutralino mass in the NMSSM. The solid black line is $m_{H_1^0} = m_{\tilde{\chi}_1^0}$ in the left panel and $m_{A_1^0} = m_{\tilde{\chi}_1^0}$ denoting when the corresponding channel is kinematically open. The dashed lines denote the resonances with each Higgs, $m_{H_1^0} = 2m_{\tilde{\chi}_1^0}$ and $m_{A_1^0} = 2m_{\tilde{\chi}_1^0}$. The color code is explained in Table 2.2.

In Figure 2.7 the mass of the lightest Neutralino versus the mass of the scalar (left panel) and pseudoscalar (right panel) Higgs is shown for the scan. As a reference, we have included in each case the line entailing resonance (dashed line), $m_{H_1^0} = 2m_{\tilde{\chi}_1^0}$ and $m_{A_1^0} = 2m_{\tilde{\chi}_1^0}$, and the line which correspond to the kinematical opening of the annihilation channel into H_1^0 and A_1^0 (solid line), $m_{H_1^0} = m_{\tilde{\chi}_1^0}$ and $m_{A_1^0} = m_{\tilde{\chi}_1^0}$. All the points in these cases fulfill all the experimental constraints enumerated previously regardless of direct and indirect detection upper bounds. According to Table 2.2, we can find that most of the points correspond to a $b\bar{b}$ final state (gray points). This is easy to understand, in those cases in which the annihilation is mediated by either H_1^0 or A_1^0, the Yukawa couplings of these Higgses drive the strength of the coupling with the SM fermions. In this case, unless the $b\bar{b}$ channel is kinetically inaccessible, for Neutralino masses below $m_{\tilde{\chi}_1^0} \lesssim m_b$ in which case a $\tau^+\tau^-$ is dominant (red points), the $b\bar{b}$ final state is dominant[9]. As it can be seen, dominant annihilations into $d\bar{d}$ pairs are also present (orange points). This is an interesting feature. It happens when the main annihilation comes from a Z boson exchange, since the gauge couplings to quarks are basically the same unlike the Yukawa couplings of the Higgs bosons. For this possibility to be experimentally allowed, the Neutralino mass must be $m_{\tilde{\chi}_1^0} \gtrsim m_Z/2$, and thus the decay of the Z into a neutralino pair is not accessible and it does not contribute to the invisible Z boson width. Annihilations into W^+W^- gauge bosons are possible as well. In this case, the mass of the Neutralino must be higher than 60 GeV roughly, but notice that this mass is remarkably smaller than $m_{W^\pm}$. Since we are classifying using the annihilations in the early Universe, in the W^+W^- case, the thermal energy available in the plasma play an important role since it allows Neutralinos to annihilate into them although the mass of the Neutralinos is less than the mass of the gauge bosons. Finally, we have found some points in which the annihilation into $c\bar{c}$ (light green) or gg (violet) is dominant. These are very interesting points from a phenomenological point of view. The Higgs boson H_1^0 has three components, as we have seen, singlet and up or down doublet components. In general, although for a light Higgs the singlet component must be larger, the down-type component of the doublet is higher than the up-type, and that is why the annihilation into b-quark (down-type) pairs is the most repeated case. However, sometimes it occurs that the up-type component dominates, and hence the coupling to down-type quarks is suppressed. In this case, the Yukawa c-quark is the greatest, and the annihilation into $c\bar{c}$ is dominant. But, since the coupling of the Higgs with gluons is at one loop dominated

[9] We remind the reader that dominant means the biggest cross section in the early Universe but not that it is a pure final state. Actually, in general, all the points are combinations of different final states.

by the $t\bar{t}$, which is up-type as well, depending on its mass, this channel can be dominant over $c\bar{c}$.

In effect, in Figure 2.7 it is clear that very light Neutralinos ($m_{\tilde{\chi}_1^0} \lesssim 40$ GeV) are allowed only if they are accompanied by a light Higgs boson, preferentially a pseudoscalar Higgs boson. The presence of a light particle ($\lesssim$63 GeV) might alter significantly the branching ratios of the SM-like Higgs. In the NMSSM, the coupling of H_1^0 and A_1^0 to the SM-like Higgs (H_2^0 in this case) differs in a relative sign for our choice of λ and κ parameters [243]. This means that a very light H_1^0 couples stronger, and thus is more constrained by the LHC measurements. This is the reason why for Neutralinos very light, we can find more solutions entailing a light pseudoscalar than a light scalar Higgs boson.

Another important advantage of having light Higgs bosons is that even though the final states $H_1^0 H_1^0$ and $A_1^0 A_1^0$ are not dominant, their contribution to the annihilation of Neutralinos is valuable. For points around the resonance with H_2^0 $\approx$125 GeV, it can be seen in Figure 2.7 that the opening of the H_1^0 channel when $m_{H_1^0} \lesssim m_{\tilde{\chi}_1^0}$ (below the solid line in the left panel) is quite important to achieve the correct relic abundance. Besides, this Figure also shows that this argument can be extended to points around the resonance with the Z boson.

direct detection

Since the direct detection cross sections are *non-relativistic* observables, whose effective Lagrangian is given in Eq. (2.28)[10], the resonance effect is not present. This can explain the behavior of almost all the solutions found here. Unlike the MSSM, the relic density is driven, for light Neutralinos, by a s-channel exchange of a Higgs boson. Since the final states contain quarks, the cross relation commented before is present, and we would expect high cross sections to be present. However, the experimental constraints restrict the Higgs boson to be resonant with the Neutralino. The cross sections in the early Universe and in direct detection for a H_1^0 exchange are proportional to:

$$\langle \sigma v \rangle \sim \frac{1}{\left(s - m_{H_1^0}^2\right)^2} \qquad \text{and} \qquad \sigma^{SI}_{\tilde{\chi}_1^0 - p} \sim \frac{1}{m_{H_1^0}^4}, \tag{2.44}$$

From these expressions we can see that the annihilation cross section (first expression) explotes when $\sqrt{s} = 2m_{\tilde{\chi}_1^0} \approx m_{H_1^0}$ while the SI cross section is insensitive to this fact. So when a resonant annihilation is present, we must expect very small direct detection cross sections. Also note that this effect is reproduced by the SD cross section, for instance when it is mediated by a Z boson.

[10] For a Majorana fermion.

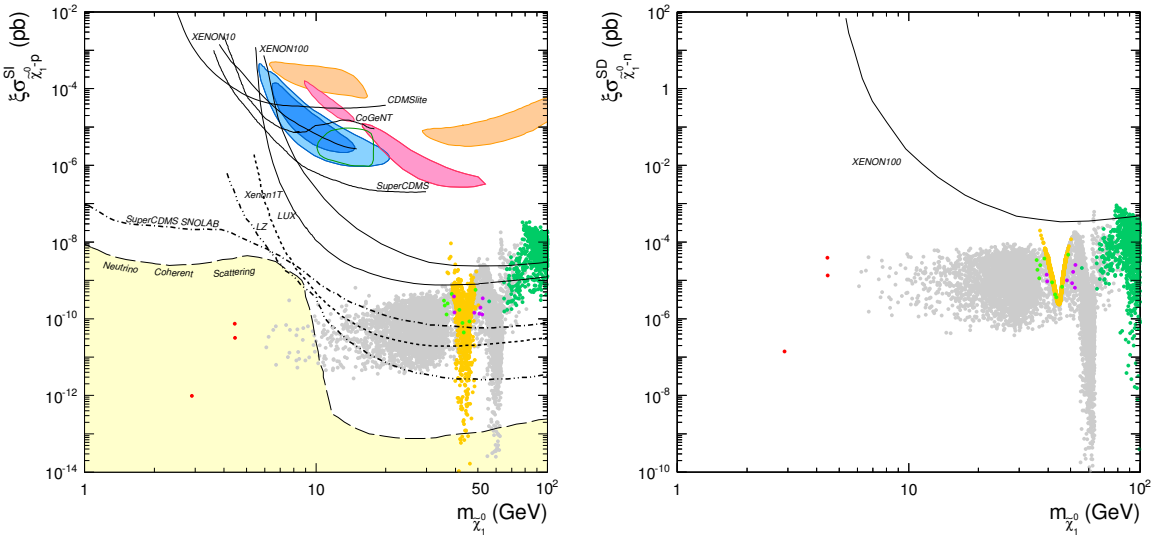

Figure 2.8: Direct detection cross sections SI (left) and SD (right) as a function of the Neutralino mass in the NMSSM. All points fulfill all the experimental constraints regardless, as it can be seen, of direct and indirect DM searches. The color code is explained in Table 2.2.

As for the MSSM case, we have plotted the SI and SD cross sections, left and right panels respectively, of Neutralinos versus their mass, as it can be seen in Figure 2.8. Nedless to say that we are using the quark content derived from Eq. (2.31). As we already know, almost all solutions encode a resonant annihilation in the early Universe which indicates a small elastic scattering cross section off protons and neutrons. This is remarkably visible when the resonance with the Z boson at $m_{\tilde{\chi}^0_1} \approx m_Z/2$ happens. Nonetheless, these points are very interesting. The Z boson exchange with a pair of quarks final state contributes to the SD cross section, while the SI contribution is zero. Therefore, these Neutralinos (yellow points) have high SD cross sections, while the SI contribution comes from the exchange of a scalar Higgs boson, which is subdominant. As we can see in the right panel of Figure 2.8, the SD cross section grows rapidly for the yellow points as we move away from the resonance.

In general, as it can be seen in Figure 2.8, the solutions found here might be detected by future experiments like LZ (dot-dot-dashed), XENON1T (dashed) and SuperCDMS (dot-dashed). Even some of them, for Neutralino masses above 40 GeV, are already excluded by LUX (solid). Less optimistic is that for very low masses (below 10 GeV), all points fall into the region of irreducible neutrino coherent scattering background, and hence they can not be discovered using direct detection experiments. The Neutralino SI

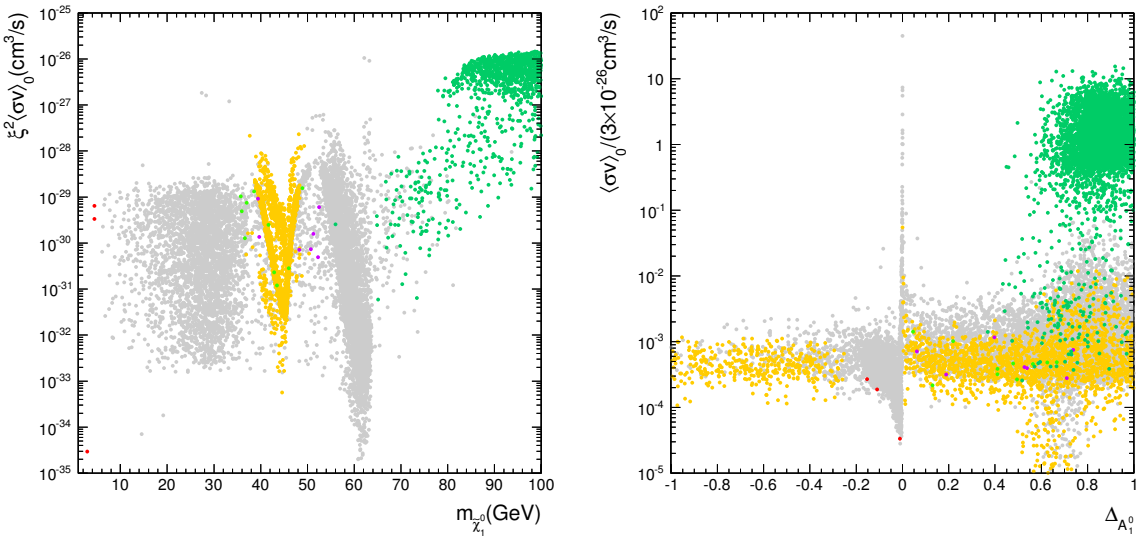

Figure 2.9: Left: thermally averaged cross sections of Neutralinos in the DM haloes weighted by their density squared (ξ^2) as a function of the Neutralino mass in the NMSSM. The color code is as in Table 2.2. Right: thermally averaged cross section of Neutralinos in the DM haloes in units of the canonical value 3×10^{-26} cm^3/s, versus the Δ parameter through Eq. 2.45.

cross section grows for lower masses of the H_1^0, since it goes as $1/m_{H_1^0}^4$ (see Eq. (2.44)), but this scenario as we already commented is very constrained by the SM-like Higgs properties, and besides is resonant. However, in Ref. [241] the authors pointed out the possibility of a very light H_1^0 inducing very high SI cross sections in light of the CDMS-Si results [98] while not being in conflict with Higgs data. This scenario is fine tuned, since accidental cancellations are necessary, and that is the reason why we do not find it in our scan.

indirect detection

Finally, let us analyze the prospects of detection of light Neutralinos in the NMSSM via indirect searches. Resonant annihilations in the early Universe have also an impact on the predicted cross section of DM particles in DM haloes. If no resonance is present, we have argued before that the predicted cross section must be of the order of the canonical value, 3×10^{-26} cm^3/s. However this picture can radically change when considering the case of a resonance. If the DM mass is close to half of the mass of the mediator then a Breit-Wigner enhancement could occur [244] since the cross section is very sensitive to the thermal kinetic energy of DM. The Neutralino cross section is proportional to

[217, 239, 245],

$$\sigma(v)v \sim \frac{1}{16m^4_{\tilde{\chi}^0_1}} \frac{1}{(v^2/4 + \Delta_X)^2 + \Gamma^2_X(1-\Delta_X)/4m^2_{\tilde{\chi}^0_1}} \tag{2.45}$$

where $\Delta_X = 1 - m_X/4m^2_{\tilde{\chi}^0_1}$ and Γ_X is the mediator X width. The module of this parameter, Δ_X, controls the amount of enhancement, or boost, of the cross section at low temperatures (velocities) respect to the one in the early Universe, while its sign controls if the boost is higher or lower than one.

In Figure 2.9 (right panel) we can see the cross section in units of the canonical value versus $\Delta_{A^0_1}$. Obviously, the only points sensitive to $\Delta_{A^0_1}$ are, by definition, those in which the annihilation proceeds through an A^0_1 resonance. At first sight it is clear that the sign of $\Delta_{A^0_1}$ controls if there is an enhancement or a diminishment of the cross section respect to the canonical value. The module of $\Delta_{A^0_1}$ controls the boost, being maximal at $\Delta_{A^0_1}$ equals to 0 in both directions, so when a resonance is present. Note that we plot the actual cross section, it is not weighted with the predicted density through the ξ^2 parameter.

Figure 2.9 (left panel) shows the weighted thermally averaged cross section of Neutralinos, $\xi^2\langle\sigma v\rangle_0$, versus its mass. Since the resonance is affecting most of the points, the cross sections are really tiny, of the order of 10^{-29} cm^3/s and lower. It means that these solutions are far away from the sensitivities of the current experiments, and thus, it would be almost impossible to detect them using indirect detection techniques. However, some of the points have a positive, but really small, $\Delta_{A^0_1}$ and thus the cross section is much higher. As an example of this, we find $b\bar{b}$ final states with cross sections around 2×10^{-27} cm^3/s. This cross section is notably smaller than the actual cross section represented in the right panel, and it is because is penalized by the factor ξ^2, so the predicted density is very small respect to the measured value for those points. The case of the dark green points, W^+W^-, are the only examples in these plots in which the cross section is around the canonical value, as predicted, since no resonance is affecting the annihilation process.

2.5 The NMSSM with right-handed Neutrinos

We have seen that some problem, namely the μ-problem, motivated us to consider an extension of the MSSM, the NMSSM. It was solved by extending the particle content of the theory with a new gauge singlet scalar which spontaneously generates a μ term via its VEV. Now, another problem, in this case of the NMSSM, motivates us to consider

another new extension: the NMSSM with right-handed Neutrinos (NMSSM-RH). It is known that Neutrinos in the SM are massless, while experiments suggest that they have a tiny mass. This is a drawback of the NMSSM, where the Neutrinos are massless. To solve this issue, we consider a further extension of the NMSSM by introducing a new gauge singlet right-handed Neutrino superfield N. This field will generate non vanishing Neutrino Majorana masses with a canonical see-saw mechanism, which is spontaneously triggered by the VEV of the singlet S. The superpotential of the model reads,

$$\mathcal{W} = \mathcal{W}_{NMSSM} + \lambda_N SNN + y_N L H_u N \tag{2.46}$$

where flavour indices are omitted. $\mathcal{W}_{NMSSM}$ is the NMSSM superpotential given in Eq. (2.34), λ_N is a new dimensionless coupling and y_N is the neutrino Yukawa coupling. As in the NMSSM, a global Z_3 symmetry is imposed so that there are no supersymmetric mass terms in the superpotential. Also, as in the previous cases we consider that R-parity is conserved so the LSP is stable, and besides the terms NNN and SSN are forbidden. Clearly, from this superpotencial can be realized the new particle content of this model respect to the NMSSM, one right-handed Neutrino field, N, and one right-handed Sneutrino, $\widetilde{N}$.

The Lagrangian, with the corresponding soft SUSY-breaking terms, reads

$$-L_{soft}^{NMSSM-RH} = -L_{soft}^{NMSSM} + {m_{\tilde{N}}}^2 |\tilde{N}|^2 + \left(\lambda_N A_{\lambda_N} S\tilde{N}^2 + y_N A_{y_N} \tilde{L} H_2 \tilde{N} + \text{H.c.}\right), \tag{2.47}$$

where L_{soft}^{NMSSM} is the NMSSM Lagrangian written in Eq. (2.35), to which we add a soft mass term for the RH Sneutrino, $m_{\tilde{N}}$, and two new trilinear soft terms A_{λ_N} and A_{y_N}.

It can be already guessed that λ_N is a crucial parameter in this construction. Through the term proportional to λ_N in the superpotential given in Eq. (2.46), the right-handed part of the Sneutrinos couple to the singlet component of the Higgs, S. Therefore, the mixing with the doublet component of this Higgs provides a weakly coupling of Sneutrinos to the SM particles. But not only this, the same term will give mass to the right-handed neutrinos once the singlet S acquires a VEV. This mass reads,

$$M_N = 2\lambda_N v_s = \frac{2\lambda_N \mu_{eff}}{\lambda}, \tag{2.48}$$

where μ_{eff} and λ are the usual NMSSM parameters introduced in the previous section. The presence of μ_{eff} in this expression ensures that the right-handed neutrinos will have a mass of the order of the EW scale. Then, in order to reproduce the small masses of the left-handed neutrinos, which are given as

$$m_{\nu_L} = \frac{y_N^2 v_u^2}{M_N}, \tag{2.49}$$

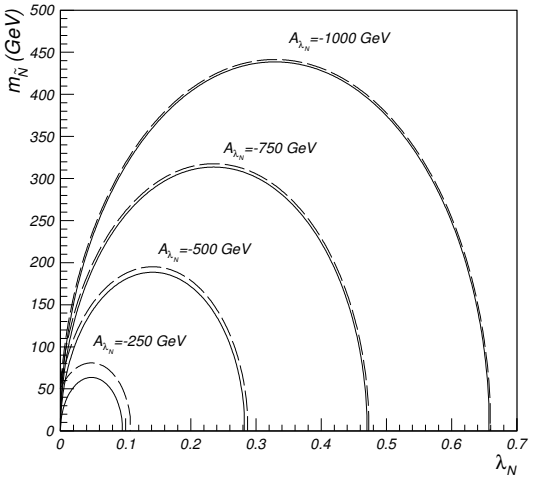

Figure 2.10: Trajectories in the $(m_{\tilde{N}}, \lambda_N)$ plane with fixed RH sneutrino mass, given various values of A_{λ_N}. For each choice of A_{λ_N} the dashed line represents the trajectory along which $m_{\tilde{N}_1} = 50$ GeV and the solid one corresponds to $m_{\tilde{N}_1} = 0$. We have used $\tan\beta = 5$, $\lambda = 0.3$, $\kappa = 0.2$, and $\mu = 200$ GeV.

the low scale seesaw mechanism implies small Yukawa couplings of $\mathcal{O}(10^{-6})$ or less.

The Neutralino and Higgs sectors of this model are exactly the same as in the NMSSM, so the reader is referred to Section 2.4.1 to see the pertinent expressions. Regarding the sneutrino sector, the mass matrix is left to Appendix B. From Eq. B.6 using the expressions given in Eq. (B.5), the lighter (real part) RH sneutrino mass, $m_{\tilde{N}_1}$, can be expressed in terms of the rest of the parameters as follows [246]:

$$m^2_{\tilde{N}_1} = m^2_{\tilde{N}} + |2\lambda_N v_s|^2 + |y_N v_u|^2 \pm 2\lambda_N \left(A_{\lambda_N} v_s + (\kappa v_s^2 - \lambda v_d v_u)^\dagger\right), \tag{2.50}$$

where the sign in front of $2\lambda_N$ is chosen opposite to the sign of $2\lambda_N \left(A_{\lambda_N} v_s + (\kappa v_s^2 - \lambda v_d v_u)^\dagger\right)$. It was shown in Refs.[76, 247] that the RH sneutrino can be a viable candidate for WIMP DM, reproducing the correct relic abundance for a wide range of masses, including the possibility that the RH sneutrino is very light [246]. The flexibility of this construction stems from the fact that the new free parameters $(\lambda_N, m_{\tilde{N}}, A_{\lambda_N})$ can be chosen to fix the sneutrino mass and coupling to the singlet Higgs boson without affecting the rest of the NMSSM spectrum. Without loss of generality we can choose the physical mass of the RH sneutrino, $m_{\tilde{N}_1}$, as a free parameter (and fix the soft mass accordingly). This is the approach that we have taken in this work, and therefore our sneutrino parameter space is defined by $(\lambda_N, m_{\tilde{N}_1}, A_{\lambda_N})$ plus the actual parameters of the NMSSM.

To illustrate the remarkable flexibility of this model, in Fig. 2.10 we show the trajectories for a fixed sneutrino mass in the $(m_{\tilde{N}}, \lambda_N)$ plane for various choices of the trilinear parameter. We observe that very small RH sneutrino masses can be obtained for any choice of the soft mass parameter (for example, increasing $|A_{\lambda_N}|$ larger values of λ_N are possible). This is potentially interesting, since it suggests that no large non-universalities in the soft parameters are needed in order to have a very light RH sneutrino, contrary to what happens with very light Neutralinos in the MSSM, where the Bino mass parameter has to be significantly reduced (see Section 2.3.2).

2.5.1 Sneutrino dark matter

In the context of DM phenomenology, the Sneutrino has been extensively studied in the literature. Let us mention that as we have seen the MSSM contains a LH Sneutrino. This Sneutrino, however, is experimentally problematic since its coupling with the Z boson lead to very high direct detection cross section as well as to a rapid annihilation in the early Universe [71]. The Neutrino oscillations brought RH Neutrinos into the game, and so RH Sneutrinos. For a RH Sneutrino to be a viable candidate several proposals have been done, from non-thermal production mechanisms in the case of a sterile Sneutrino [248], mixed candidates [75, 249–253], to gauge group extensions [254].

As we have seen, in our case, we consider a pure RH Sneutrino state. The Weak scale interactions with the SM particles are effectively given by the mixing existent between the singlet and doublet components in the Higgs mass eigenstates. Therefore, the Higgs sector of the model crucially affects the annihilation rate of the Sneutrinos in the early Universe. The RH Sneutrino couplings to Higgses and Neutralinos originate from the SNN term in the superpotential and Lagrangian. The strength of the interaction is therefore dependent on the value of λ_N and A_{λ_N}. The RH sneutrino annihilation channels include at tree level the following possibilities

(i) $W^+ W^-$, $Z\,Z$, and $f\bar{f}$ via s-channel Higgs exchange;

(ii) $H_i^0\, H_j^0$, via s-channel Higgs exchange, t- and u-channel sneutrino exchange, and a scalar quartic coupling;

(iii) $A_a^0\, A_b^0$, and $H_i^+\, H_j^-$, via s-channel Higgs exchange, and a scalar quartic coupling;

(iv) $Z\, A_a^0$ and $W^\pm\, H^\mp$ via s-channel Higgs exchange;

(v) NN, via s-channel Higgs exchange and via t- and u-channel neutralinos exchange.

The processes suppressed by the neutrino Yukawa (such as s-channel sneutrino annihilation mediated by the Z boson) have not been included, since they are negligible.

Other annihilation products at one-loop include gluons and photons,

(vi) gg, via s-channel Higgs exchange with a quark loop (mainly top, bottom and charm) and squarks;

(vii) $\gamma\gamma$, $Z\gamma$, via a loop of $H^\pm$ and s-channel Higgs exchange with a loop of quarks, $W^\pm$, $H^\pm$, charginos or sfermions.

This model is a perfect example in which the correlation between different processes, like the annihilation in the early Universe and direct detection, takes place. To exemplify this let us show analytically some examples in which this correlation is not broken. To do this we have to remind that this correlation occurs when the final state in the early Universe is fermionic, namely a pair of quarks, then the diagram is the same than in direct detection. Then let us focus on the $f\bar{f}$ case.

This case is very simple to analyse. As we have commented above, there is only one Feynman diagram that contributes to the interactions of Sneutrinos with SM particles, namely the exchange of a CP-even Higgs, H_i^0 along the s-channel depicted in Fig. 2.11 (the s-channel annihilation mediated by the Z boson vanishes for a pure RH sneutrino). For light sneutrinos the main annihilation product is a $b\bar{b}$ pair. Annihilation into $c\bar{c}$ can also be significant, as we discuss later, depending on the composition of the lightest Higgs.

As we have introduced previously in the context of Neutralino DM, under these circumstances it is easy to derive an analytical approximate expression for the thermally averaged annihilation cross section by means of a partial wave expansion $\langle\sigma v\rangle \approx a + bx$, where $x = T/m$ is proportional to the WIMP velocity-square. This approximation holds when one is far enough from resonances and thresholds for new final states[11].

For this specific diagram the integral of the matrix element describing each annihilation process, $\tilde{N}_1\tilde{N}_1 \to X_1X_2$, which we define in terms of the scattering angle in the CM frame, θ_{CM}, as

$$\widetilde{w}_{X_1X_2}(s) \equiv \frac{1}{2}\int_{-1}^{+1} d\cos\theta_{CM}\,|\mathcal{A}(\tilde{N}_1\tilde{N}_1 \to X_1X_2)|^2, \tag{2.51}$$

[11] Although for very light sneutrinos resonances can generally be avoided (as they would require very light CP-even Higgses), the threshold for annihilation into $b\bar{b}$ happens around 4 GeV and therefore we should expect deviations from this approximation for sneutrinos lighter than 6 GeV.

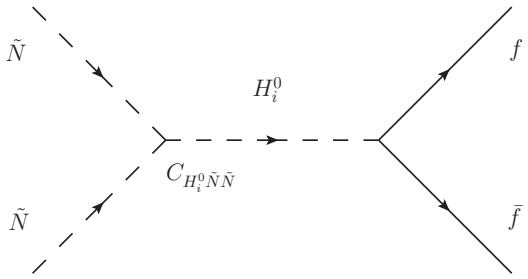

Figure 2.11: Diagram contributing to the annihilation of RH Sneutrinos into $f\bar{f}$.

can be written as

$$\tilde{w}_{b\bar{b}} = \left(\frac{g\, m_b}{2M_W \cos\beta}\right)^2 \sum_{i,j=1}^{3} \frac{C_{H_i^0\tilde{\nu}\tilde{\nu}} C_{H_j^0\tilde{\nu}\tilde{\nu}} S^1_{H_i^0} S^1_{H_j^0}}{\Delta_{ij}} \left(2s - 8m_b^2\right), \tag{2.52}$$

$$\tilde{w}_{c\bar{c}} = \left(\frac{g\, m_c}{2M_W \sin\beta}\right)^2 \sum_{i,j=1}^{3} \frac{C_{H_i^0\tilde{\nu}\tilde{\nu}} C_{H_j^0\tilde{\nu}\tilde{\nu}} S^2_{H_i^0} S^2_{H_j^0}}{\Delta_{ij}} \left(2s - 8m_c^2\right), \tag{2.53}$$

where $C_{H_i^0\tilde{\nu}\tilde{\nu}}$ is the RH sneutrino coupling to the Higgs H_i^0, and Δ_{ij} is the square denominator of the Higgs propagator, both defined in Appendix A of Ref. [247]. Let us remark that the convention used to express the composition of the CP-even Higgs mass eigenstates is the same as in the NMSSM case, $H_i^0 = S^1_{H_i^0} H_d + S^2_{H_i^0} H_u + S^3_{H_i^0} S$.

In terms of the quantities $\tilde{w}_{X_1X_2}$ the annihilation cross section can be calculated numerically as detailed in Appendix B of Ref. [247]. Moreover, the coefficients of the partial wave expansion of the thermally averaged annihilation cross section can also be calculated analytically [255]. Following the prescription of Ref. [256], the expressions for the velocity-independent contribution to the annihilation cross section into a pair of $b\bar{b}$ or $c\bar{c}$ then read

$$\begin{aligned} a_{b\bar{b}} &= \frac{3}{4\pi}\left(\frac{g\, m_b}{2M_W \cos\beta}\right)^2 \frac{(m^2_{\tilde{N}_1} - m_b^2)^{3/2}}{m^3_{\tilde{N}_1}} \mathcal{D}^2, \\ a_{c\bar{c}} &= \frac{3}{4\pi}\left(\frac{g\, m_c}{2M_W \sin\beta}\right)^2 \frac{(m^2_{\tilde{N}_1} - m_c^2)^{3/2}}{m^3_{\tilde{N}_1}} \mathcal{U}^2, \end{aligned} \tag{2.54}$$

where we have defined

$$\mathcal{D} \equiv \sum_{i=1}^{3} \frac{C_{H_i^0\tilde{\nu}\tilde{\nu}} S^1_{H_i^0}}{4m^2_{\tilde{N}_1} - m^2_{H_i^0}} \quad ; \quad \mathcal{U} \equiv \sum_{i=1}^{3} \frac{C_{H_i^0\tilde{\nu}\tilde{\nu}} S^2_{H_i^0}}{4m^2_{\tilde{N}_1} - m^2_{H_i^0}}. \tag{2.55}$$

In most cases the lightest Higgs contribution will dominate in the expressions above

(especially if its mass is small), so that we can define

$$\mathcal{D} \approx \mathcal{D}_1 \equiv \frac{C_{H_1^0 \tilde{\nu}\tilde{\nu}} S^1_{H_1^0}}{4m^2_{\tilde{N}_1} - m^2_{H_1^0}} \quad ; \quad \mathcal{U} \approx \mathcal{U}_1 \equiv \frac{C_{H_1^0 \tilde{\nu}\tilde{\nu}} S^2_{H_1^0}}{4m^2_{\tilde{N}_1} - m^2_{H_1^0}} \,. \tag{2.56}$$

The contribution from the b parameter in the $\langle \sigma v \rangle$ expansion is suppressed (since $x_f \approx 1/20$) and will be neglected in the following discussion.

Notice that

$$a_{c\bar{c}} = \left(\frac{m_{\tilde{N}_1}{}^2 - m_c^2}{m_{\tilde{N}_1}{}^2 - m_b^2} \right)^{3/2} \frac{m_c^2}{m_b^2 \tan^2\beta} \frac{\mathcal{U}^2}{\mathcal{D}^2} \, a_{b\bar{b}} \approx \frac{0.18}{\tan\beta^2} \frac{\mathcal{U}^2}{\mathcal{D}^2} \, a_{b\bar{b}} \tag{2.57}$$

for RH sneutrinos with a mass $m_{\tilde{N}_1} \approx 7 - 9$ GeV. Thus, annihilation into $c\bar{c}$ can only be dominant for small values of $\tan\beta$ and depending on the properties of the Higgs sector. Since it is the lightest Higgs the one that contributes the most to both $\mathcal{D}$ and $\mathcal{U}$, the above condition could happen if its H_u component is much larger than its H_d component. Although this is not a very common situation in our scans, we will keep this possibility open and explicitly consider both cases, where annihilation into either $b\bar{b}$ or $c\bar{c}$ dominates[12].

From Eq. (A.13) the Sneutrino relic density can be approximated as

$$\Omega h^2 \approx \frac{1}{x_f \sqrt{g^*(x_f)}} \frac{1.07 \times 10^9 \, \text{GeV}^{-1}}{M_P \, (a + \frac{b}{2} \, x_f)} \,, \tag{2.58}$$

where $M_P = 1.22 \times 10^{19}$ GeV is the Planck mass and $g^*(x_f)$ is the number of relativistic degrees of freedom at the decoupling temperature. However, very light dark matter with mass smaller or of order 10 GeV would have decoupled when the temperature of the Universe was around 400 MeV, precisely when quarks confined into hadrons. This hadronization implies that the number of relativistic degrees of freedom drops dramatically around the decoupling temperature of very light WIMPs, producing an enhancement of their relic abundance [257]. Furthermore, this enhancement is sensitive to the phase transition model that is considered (in particular, it depends on the deconfinement temperature, T_c). In our analysis we have taken $T_c = 400$ MeV. The reader is referred to Appendix A for a detailed calculation of the relic abundance of light WIMPs.

[12] It should be noted that the contribution from annihilation into $\tau^+\tau^-$ can be larger than that corresponding to $c\bar{c}$. However, it has the same dependence on the lightest Higgs composition than the contribution from b quarks (i.e., $a_{\tau^+\tau^-}$ is proportional to $\mathcal{D}^2$) and because of the different Yukawa couplings $a_{\tau\bar{\tau}} \ll a_{b\bar{b}}$ is always satisfied when $m_{\tilde{N}_1} > m_b$. Thus, we only have two possible regimes, where either $b\bar{b}$ or $c\bar{c}$ is the leading contribution.

For a quick analytical estimate let us momentarily assume that the QCD transition is close to first order and that the relativistic number of degrees of freedom suddenly varies from $\sqrt{g^*} \approx 9$ to 3.7, considering also the uncertainty in T_c. Notice that this implies essentially an increase of a factor 2.5 in the approximate evaluation of $\Omega_{\tilde{N}}h^2$ of Eq. (2.58). In order to reproduce the WMAP result, this results in a condition on the annihilation cross section that can be written as

$$\langle \sigma v \rangle \approx a_{b\bar{b}} \approx 0.77 - 1.9\,\text{pb} \qquad \text{if} \qquad \mathcal{D} \gg \frac{0.4}{\tan\beta}\mathcal{U}\,, \tag{2.59}$$

$$\langle \sigma v \rangle \approx a_{c\bar{c}} \approx 0.77 - 1.9\,\text{pb} \qquad \text{if} \qquad \mathcal{D} \ll \frac{0.4}{\tan\beta}\mathcal{U}\,, \tag{2.60}$$

where the lower (upper) value applies to a RH sneutrino which is heavier (lighter) than $m_{\tilde{N}_1} \sim 8$ GeV and therefore decouples above (below) T_c. These values are generic for a dark matter particle in which s-wave annihilation dominates [60].

So far we have used an analytical approach with several approximations so that the correlation between the sneutrino annihilation cross section and its scattering cross section off nuclei (which we calculate in the next section) is manifest. However, we stress that in our results we use the full calculation of $\Omega_{\tilde{N}}h^2$ following the same numerical method described before. Also, the QCD transition is taken into account.

The quantities $a_{b\bar{b}}$ and $a_{c\bar{c}}$ are very sensitive to the structure of the Higgs sector and the new couplings $C_{H_i^0\tilde{\nu}\tilde{\nu}}$, and our model provides much flexibility in this sense. For example, both $a_{b\bar{b}}$ and $a_{c\bar{c}}$ increase as the mass of the lightest Higgs (which is the leading term) decreases, but they also depend on the composition of this lightest Higgs. We already know, however, that in the NMSSM it is possible to have a very light Higgs without violating the current experimental limits as long as its singlet composition is large enough. Therefore, as we comment later, LUX constraints on the WIMP-nucleon cross section will impose constraints on the amount of annihilation into quarks.

Thus one possible scenario in which a large annihilation cross section can be achieved involves a light singlet-like Higgs. The H_u or H_d components, though small, would determine whether predominant annihilation occurs via $b\bar{b}$ or $c\bar{c}$, according to the expressions above. This kind of scenarios is interesting since the Higgs structure is completely different to that of the MSSM for very light neutralinos in which we have seen that the *non-decoupling* limit is necessary. On the other hand, a light singlet-like Higgs is also one of the possible solutions for the very light neutralinos in the NMSSM providing a welcomed resonant annihilation.

Finally, at this point it is possible to highlight the connection between the invisible Higgs branching fraction and the relic density. A common feature of most dark matter

models featuring light WIMPs is the occurrence of a new invisible channel for the Higgs decay, namely the production of a dark matter pair. This also occurs in this scenario, since the CP-even Higgs boson is the connection of the light RH Sneutrinos with SM particles.

For any of the CP-even Higgses, the decay width of the process $H_i^0 \to \tilde{N}_1\tilde{N}_1$ can be expressed as

$$\begin{aligned}\Gamma(H_i^0 \to \tilde{N}_1\tilde{N}_1) &= \frac{1}{8\pi m_{H_i}^2}\sqrt{\frac{m_{H_i}^2}{4} - m_{\tilde{N}_1}^2}|\mathcal{M}|^2\frac{1}{2} \\ &= \frac{1}{32\pi m_{H_i^0}^2}|C_{H_i^0\tilde{\nu}\tilde{\nu}}|^2\sqrt{m_{H_i^0}^2 - 4m_{\tilde{N}_1}^2} \\ &\approx \frac{1}{32\pi m_{H_i^0}}|C_{H_i^0\tilde{\nu}\tilde{\nu}}|^2 \quad \text{for} \quad m_{H_i^0} \gg 2m_{\tilde{N}_1}\ . \end{aligned} \tag{2.61}$$

As in other models for very light WIMPs, this decay mode can dominate for the lightest Higgs. This can be the case of a generic light singlet DM candidate [91**? ?**]. In order to estimate the invisible Higgs branching ratio we have to compare its decay width into RH sneutrinos with the decay width into fermions, which normally account for the main visible decay channels[13]. The ratio between the lightest Higgs decay widths into RH Sneutrinos and $b\bar{b}$ can be expressed as

$$R_{\tilde{N}\tilde{N}/b\bar{b}} \approx \frac{|C_{H_1^0\tilde{\nu}\tilde{\nu}}|^2}{6m_{H_1^0}^2\,|S_{H_1^0}^1|^2}\left(\frac{2M_W\sin\beta}{g\,m_b}\right)^2\ , \tag{2.62}$$

and we can define a similar quantity to compare with decays into $c\bar{c}$,

$$R_{\tilde{N}\tilde{N}/c\bar{c}} \approx \frac{|C_{H_1^0\tilde{\nu}\tilde{\nu}}|^2}{6m_{H_1^0}^2\,|S_{H_1^0}^2|^2}\left(\frac{2M_W\cos\beta}{g\,m_c}\right)^2\ , \tag{2.63}$$

where we have used the approximation that $m_{H_1^0}^2 \gg 4m_{\tilde{N}_1}^2$. Previously we have introduced two possible regimes in which the correct relic density could be obtained for a Sneutrino annihilating into $f\bar{f}$. Depending on the lightest Higgs composition, the quantities $\mathcal{D}$ or $\mathcal{U}$, defined in Eq.(2.55), provide the leading term for the annihilation into $b\bar{b}$ or $c\bar{c}$, respectively.

The scan

We have carried out a scan in the parameter space of this model in order to look for solutions with light RH sneutrino DM. The parameters of the model that determine the

[13] Actually, if the decay into a pair of very light pseudoscalars, $H_1^0 \to A_1^0A_1^0$, is open, its contribution can also be sizable. In general any other particle with a mass below 62-63 GeV approximately must be included.

Parameter	Range
$\tan\beta$	$4-10,\ 10-20$
λ	$0.1-0.6$
κ	$0.01-0.1$
A_λ	$500-1100$
A_κ	$-50-50$
μ_{eff}	$110-250$
λ_N	0.070.4
A_{λ_N}	$-1100--500$
$m_{\tilde{N}_1}$	$1-50$

Table 2.5: Ranges of variation of the input parameters used in the scan. Masses and trilinear terms are given in GeV units. All the parameters are defined at the EW scale.

phenomenology of the RH sneutrino are varied in the ranges detailed in Table 2.5. Out of convenience we have split the scan in two regions in $\tan\beta$, namely $[4, 10]$ and $[10, 20]$. The rest of the input parameters (which have less impact on the RH sneutrino properties) are fixed. In particular, gaugino soft masses are taken to be $M_1 = 350$ GeV, $M_2 = 700$ GeV and $M_3 = 2100$ GeV, thus satisfying the Grand Unification relation. Slepton and squark soft masses are equal for the three families, $m_{\widetilde{L}_i} = m_{\widetilde{E}_i} = 300$ GeV, and $m_{\widetilde{Q}_i} = m_{\widetilde{U}_i} = m_{\widetilde{D}_i} = 1500$ GeV. Trilinear soft terms are chosen to be, $A_U = 3700$ GeV, $A_D = 2000$ GeV, $A_E = -1000$ GeV. All these parameters are defined at the EW scale. Following the procedure shown in Figure 2.1, the RH sneutrino relic abundance with `micrOMEGAs`. To compute the NMSSM mass spectrum, the masses of Higgs bosons including full two-loop contributions and the relevant low-energy phenomenology observables, we use `NMSSMTools`.

Regarding the Higgs sector, we have imposed the presence of a SM-like Higgs, in the mass range $123-128$ GeV. In our scan the SM-like Higgs corresponds to the second mass eigenstate, H_2^0, as a lighter singlet-like state H_1^0 is needed to couple to RH sneutrinos without violating experimental bounds, namely those on the SM-Like Higgs invisible branching fraction.

The experimental constraints are, in general, easy to overcome in this model. First, the Higgs sector in the NMSSM is richer and offers the possibility of having a light singlet-like Higgs which can contribute significantly to the DM couplings with SM particles while simultaneously presenting a 126 GeV Higgs boson with SM couplings [233]. This

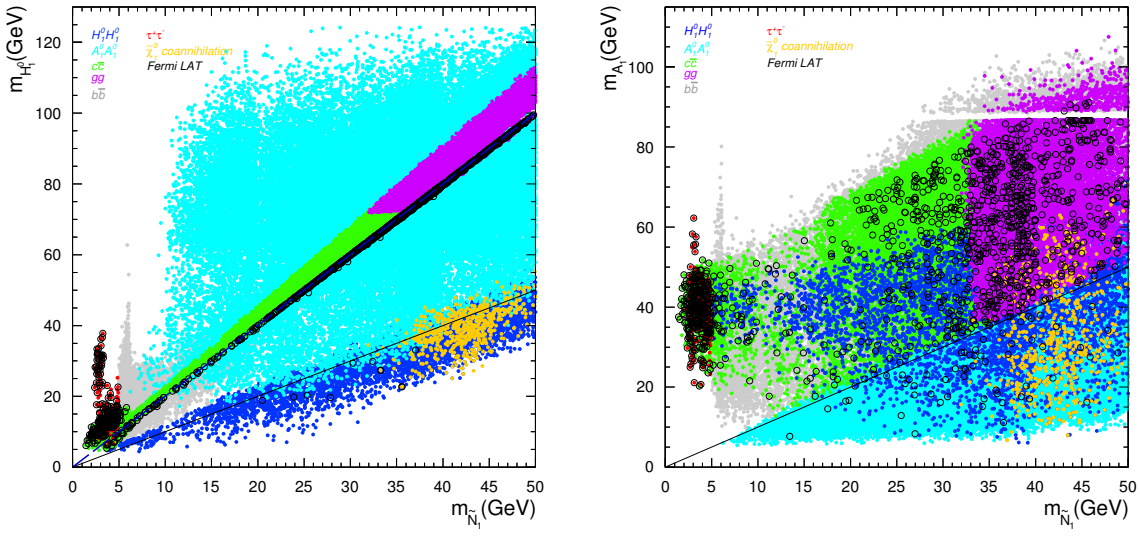

Figure 2.12: Left: Lightest Higgs mass as a function of the RH sneutrino mass. All the points fulfil the experimental constraints and also incorporates the constraints from LUX, CDMSlite, and SuperCDMS, and Fermi LAT bound from dSph on the RH sneutrino annihilation cross section. The different colours indicate the dominant annihilation channel as indicated in Table 2.2. The solid line corresponds to $m_{\tilde{N}_1} = m_{H_1^0}$ and the dashed line to $m_{\tilde{N}_1} = m_{H_1^0}/2$. Right: Same but for the Lightest pseudoscalar mass versus the RH Sneutrino mass.

is something we already knew from the previous section. Also, since light scalar and pseudoscalar Higgs bosons are viable, this opens up new channels as well as the possibility of having a resonance effect when $2m_{\tilde{N}_1} \approx m_{H_1^0}$. Finally, the RH sneutrino mass can be selected through the new inputs of the model (it can be considered a free parameter) without affecting the rest of the NMSSM spectrum.

When the relic density constraint is applied to the scan in the parameter space of the model a clear structure of the Higgs sector emerges, where the lightest Higgs boson has a mass $m_{H_1^0} \lesssim 120$ GeV and is singlet-like, whereas the SM Higgs corresponds to the second-lightest state and reproduces the experimental value for its mass, $m_{H_2^0} \approx 126$ GeV. On top of this, a light pseudoscalar Higgs is often found with $m_{A_1^0} \lesssim 90$ GeV. In the left panel of Fig. 2.12 we have represented the mass of the lightest Higgs as a function of the RH sneutrino mass for all the points that pass all the experimental constraints, incorporating in this case the bounds on direct and indirect DM searches. Similarly, the right panel of Fig. 2.12 displays the mass of the lightest pseudoscalar Higgs as a function of the RH sneutrino mass.

The colours in these plots indicate the various possible annihilation final states and

point towards a rich phenomenology. We have identified the following possibilities,

- $b\bar{b}$ (grey): It is driven by a s-channel Higgs exchange and it is the most common annihilation final state for very light sneutrinos since the b quark Yukawa coupling dominates over the other couplings.

- $\tau^+\tau^-$ (red): This channel is generally dominant when the $b\bar{b}$ final state is closed, i.e. when $m_{\tilde{N}_1} < m_b$.

- $c\bar{c}$ (green): This final state dominates in those regions of the parameter space in which the lightest Higgs is predominantly singlet-like and its composition fulfils $|S^2_{H^0_1}/S^1_{H^0_1}| \gtrsim 5 \tan\beta$.

- gg (pink): This channel is subject to the same conditions as the previous one, but additionally it requires $m_{H^0_1} \gtrsim 80$ GeV, otherwise since it is driven by a top quark loop it is suppressed respect to $c\bar{c}$. Both $c\bar{c}$ and gg channels are mostly produced in resonant annihilations, with $m_{H^0_1} \simeq 2m_{\tilde{N}_1}$ (dashed line in Fig. 2.12).

- $H^0_1 H^0_1$ (blue): In the NMSSM a very light CP-even Higgs is viable as long as it is singlet-like. When this channel is kinematically open, it usually dominates. This fact is well illustrated in Fig. 2.12 where the $H^0_1 H^0_1$ final states are grouped below the solid line that corresponds to $m_{\tilde{N}_1} = m_{H^0_1}$.

- $A^0_1 A^0_1$ (cyan): A very light CP-odd Higgs is also viable in the NMSSM, provided that its singlet component is large as well. When this channel is kinematically allowed, it easily dominates unless the channel $H^0_1 H^0_1$ is open.

- Coannihilation with the lightest neutralino (orange): This is possible when $m_{\tilde{N}_1} \approx m_{\tilde{\chi}^0_1}$. As we have seen, the lightest neutralino can also be very light in the NMSSM if it is mostly bino or singlino. However, since it also contributes to the invisible decay of the SM Higgs, its couplings are constrained. In our scan, co-annihilation effects are important for a small population of points with $m_{\tilde{N}_1} \gtrsim 30$ GeV for which the light neutralino is singlino-like.

Due to the cross correlation several times mentioned along this thesis, in the case of $b\bar{b}$ most of the points with $m_{\tilde{N}_1} \gtrsim 7$ GeV are excluded by direct detection bounds, and the only ones remaining correspond to those which satisfy the resonance condition with the lightest Higgs (for masses below 7 GeV direct detection bounds are less severe). Other channels are less affected by these bounds. This is the case of points in which the main

annihilation channel is $A_1^0 A_1^0$ and those with resonant annihilation ($c\bar{c}$ and gg). As we will argue later, the resulting RH sneutrino scattering cross section for these points is small, below current direct detection bounds.

Finally, black circles on these plots denote the points for which the RH sneutrino annihilation cross section exceeds the upper constraints obtained from Fermi LAT observations of the gamma ray flux of dwarf spheroidal galaxies. This bound excludes points with resonant annihilation and many of the points (but not all) with low mass WIMPs. We will study the effect of this constraint in more detail in a section devoted to indirect searches, as in the cases of the MSSM and NMSSM.

direct detection

Let us finally address the prospects for the direct detection of very light RH sneutrino dark matter. As in the previous cases, the interaction between RH sneutrinos and quarks can be described in terms of an effective Lagrangian, valid in the non-relativistic regime where collision takes place. For a scalar particle the SD cross section is identically zero since it does not have spin to interact with nuclei spins, and thus we are left with only SI interactions. In this case, there is only one Feynman diagram contributing at tree-level to this process, namely, the t-channel exchange of neutral Higgses, leading to a scalar coupling,

$$\mathcal{L}_{eff} \supset \alpha_{q_i} \tilde{N}_1 \tilde{N}_1 \bar{q}_i q_i \ , \tag{2.64}$$

with

$$\alpha_{q_i} \equiv \sum_{j=1}^{3} \frac{C_{H_i^0 \tilde{N}_1 \tilde{N}_1} Y_{q_i}}{m^2_{H_j^0}} \ , \tag{2.65}$$

where $C_{H_i^0 \tilde{N}_1 \tilde{N}_1}$ is the sneutrino-sneutrino-Higgs coupling [247], Y_{q_i} is the corresponding quark Yukawa coupling, and i labels up-type quarks ($i = 1$) and down-type quarks ($i = 2$). The resulting SI part of the sneutrino-nucleon elastic scattering cross section reads

$$\sigma^{SI}_{\tilde{N}-p} = \frac{f_p^2 m_p^2}{4\pi (m_{\tilde{N}_1} + m_p)^2} \ , \tag{2.66}$$

where m_p is the proton mass,

$$\frac{f_p}{m_p} = \sum_{q_i=u,d,s} f^p_{Tq_i} \frac{\alpha_{q_i}}{m_{q_i}} + \frac{2}{27} f^p_{TG} \sum_{q_i=c,b,t} \frac{\alpha_{q_i}}{m_{q_i}} \ , \tag{2.67}$$

and the hadronic matrix elements $f^p_{Tq_i}$ and f^p_{TGP} are extracted using the same values as Eq. (2.31). Expression (2.66) corrects a missing factor in Refs. [76, 246, 247].

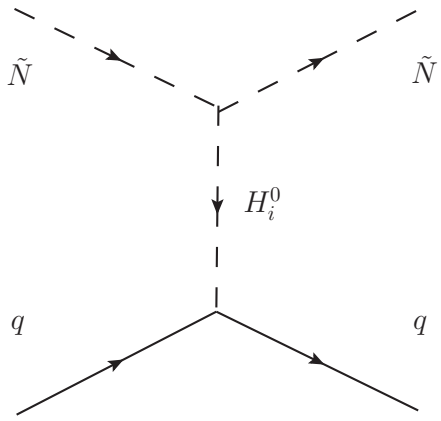

Figure 2.13: Diagram contributing to the spin-independent elastic scattering of RH sneutrino off quarks.

Using the explicit expressions of the quark Yukawa couplings, this quantity can be expressed as

$$\frac{f_p}{m_p} = \frac{g}{2M_W \cos\beta} \sum_{j=1}^{3} \frac{C_{H_j^0 \tilde{\nu}\tilde{\nu}}}{m^2_{H_j^o}} \left(S^1_{H_j^0} \left(f_{Td} + f_{Ts} + \frac{2 f_{TGP}}{27} \right) + \frac{S^2_{H_j^0}}{\tan\beta} \left(f_{Tu} + \frac{4 f_{TGP}}{27} \right) \right) , \tag{2.68}$$

where the term proportional to $S^1_{H_j^0}$ corresponds to the interaction with the down-type quarks (the dominant contribution is due to the quark s) and the term proportional to $S^2_{H_j^0}$ corresponds to up-type quarks.

If the Higgs spectrum features a lightest Higgs with SM-like properties, i.e., with a mass of order 125 GeV, then the approximation $4m^2_{\tilde{N}_1} \ll m^2_{H_1^0}$ holds for very light sneutrinos and the above equation can be approximated as

$$\frac{f_p}{m_p} \approx \frac{0.31\, g}{2M_W \cos\beta} \left(\mathcal{D} + \frac{0.42}{\tan\beta} \mathcal{U} \right) . \tag{2.69}$$

If, on the other hand, the lightest Higgs is lighter than the SM-like one (and necessarily featuring a larger singlet composition), the contribution from this lightest Higgs generally dominates and expression (2.68) can be approximated as

$$\frac{f_p}{m_p} \approx \frac{0.31\, g}{2M_W \cos\beta} \left(\mathcal{D}_1 + \frac{0.42}{\tan\beta} \mathcal{U}_1 \right) \left(\frac{4m^2_{\tilde{N}_1} - m^2_{H_1^0}}{m^2_{H_1^0}} \right) . \tag{2.70}$$

where we have used the quantities $\mathcal{D}_1$ and $\mathcal{U}_1$ defined in Eq.(2.56). Notice that the approximation $4m^2_{\tilde{N}_1} \ll m^2_{H_1^0}$ is not necessarily good now, since the Higgs can be very light, and this leads to the inclusion of the last factor.

For moderate and large values of $\tan\beta$ the contribution from the s quark is the leading one to the spin-independent cross section. However, the second term can become sizable and even dominate for small $\tan\beta$ and if the lightest Higgs is mostly H_u^0. Both in the case of the relic density, as well as in the scattering cross section, the condition that determines when the coupling from down-type quarks dominates over the coupling from up-type quarks is approximately the same, $\mathcal{D}_1 \gg (0.4/\tan\beta)\mathcal{U}_1$ (see equations (2.59) and (2.60)). It should be emphasized that this rarely happens, but we include this possibility here for completeness.

The resulting spin-independent contribution to the RH sneutrino elastic scattering cross section off nuclei is then approximated as

$$\sigma^{\rm SI}_{\tilde{N}p} \approx \frac{1}{4\pi}\frac{m_p^4}{(m_p+m_{\tilde{N}_1})^2}\left(\frac{0.31\,g}{2M_W\cos\beta}\right)^2\left(\mathcal{D}+\frac{0.42}{\tan\beta}\mathcal{U}\right)^2 . \tag{2.71}$$

In those cases where the lightest Higgs is lighter than the SM one, a better approximation (that incorporates the effect of the resonance) is

$$\sigma^{\rm SI}_{\tilde{N}p} \approx \frac{1}{4\pi}\frac{m_p^4}{(m_p+m_{\tilde{N}_1})^2}\left(\frac{0.31\,g}{2M_W\cos\beta}\right)^2\left(\mathcal{D}_1+\frac{0.42}{\tan\beta}\mathcal{U}_1\right)^2\left(\frac{4m^2_{\tilde{N}_1}-m^2_{H_1^0}}{m^2_{H_1^0}}\right)^2 . \tag{2.72}$$

We will use these expressions to extract some analytical predictions for the detectability of sneutrinos. Once more, in our numerical calculations the full expression for $\sigma^{\rm SI}_{\tilde{N}p}$ has been included, without using any numerical approximations.

The theoretical predictions for $\xi\sigma^{SI}_{\tilde{N}-p}$ as a function of the RH sneutrino mass are shown in Fig. 2.14. We also show the most recent experimental upper constraints (solid lines) on the SI scattering cross section, as well as the regions compatible with the various hints for low-mass WIMPs. For reference, the predicted sensitivities of future experiments are also displayed. Finally, the dashed line represents the approximate band where neutrino coherent scattering with nuclei will begin to limit the sensitivity of direct detection experiments [117].

The predicted $\sigma^{SI}_{\tilde{N}-p}$ spans many orders of magnitude for the whole range of light masses. Notice that it is possible to obtain points within the areas compatible with the hints for low mass WIMPs, and in particular within the CDMS II or CoGeNT regions[14].

On the right-hand side of Fig. 2.14, we impose at face value the upper bounds on $\sigma^{SI}_{\tilde{N}-p}$ from direct detection experiments[15] (LUX [106], CDMSlite [98], and SuperCDMS [116])

[14] Of course, since the RH sneutrino is a standard WIMP, this does not solve the question of why they would have not been observed by XENON or LUX.

[15] Strictly speaking, these bounds correspond to the standard halo model with a local dark matter

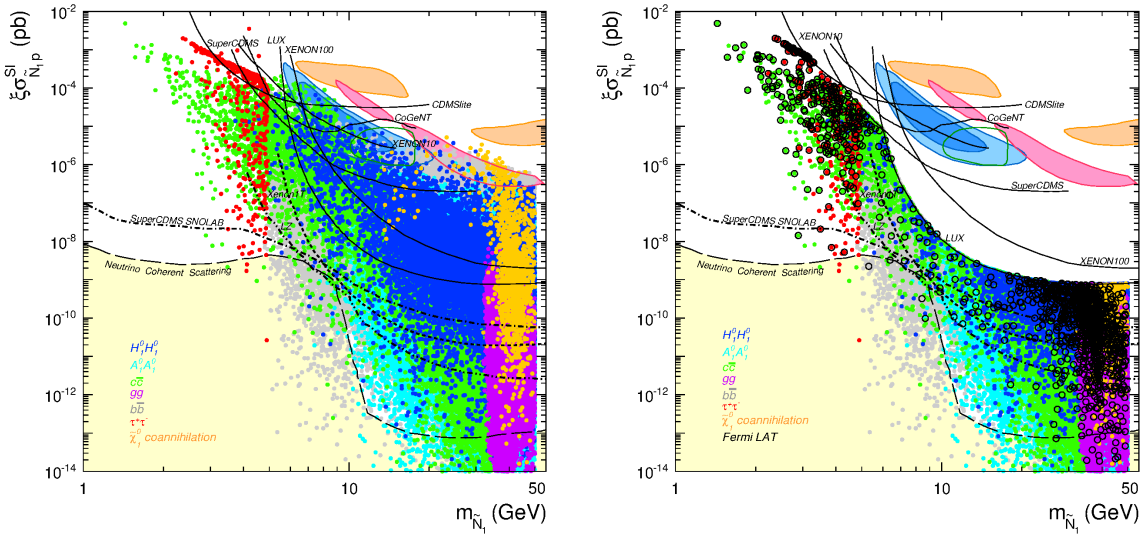

Figure 2.14: Theoretical predictions for $\sigma^{SI}_{\tilde{N}-p}$ as a function of the RH sneutrino mass. Solid lines represent the current experimental upper bounds from direct detection experiments, whereas dotted lines are the projected sensitivities of next-generation detectors. The dashed line correspond to an approximate band where neutrino coherent scattering with nuclei will begin to limit the sensitivity of WIMPs direct detection experiments. Closed contours correspond represent the areas compatible with the observed excesses in DAMA/LIBRA (orange), CRESST (red), CDMS II (blue), and CoGeNT (green). The plot on the right-hand side incorporates the upper constraints from LUX, CDMSlite and SuperCDMS on $\sigma^{SI}_{\tilde{N}-p}$. Black circles correspond to points for which the annihilation cross section exceeds Fermi LAT bounds on dSph galaxies.

As we can observe, there are plenty of points in the parameter space that survive for the whole mass range. Remarkably, the predictions spread over the whole area of the parameter space that will be covered with direct detection experiments in the future. These theoretical predictions motivate futures direct searches with low threshold experiments, such as the ones planned with the proposed future phases of SuperCDMS or LZ.

As shown in Ref. [246], there is in general a correlation between the WIMP annihilation cross section in fermion-antifermion channels and the WIMP scattering cross section off quarks that results from the crossing symmetry of the diagrams involved (and that is generic to any light DM candidate). This effect explains the points with large values for $\sigma^{SI}_{\tilde{N}-p}$ in the $b\bar{b}$ and $c\bar{c}$ channels. However, the correlation is broken if resonant effects

density of $\rho = 0.3$ GeV cm^{-3}, a escape velocity of $v_{esc} = 544$ km s^{-1} , and a central velocity $v_0 = 230$ km s^{-1}. It is well known that deviations from this model can lead to significant shifts in the excluded regions.

are present in the annihilation cross section, since the scattering cross section does not present such resonances (and consequently can be much smaller). As already observed in Fig. 2.12, the points that survive the direct detection constraints for the $b\bar{b}$ and $c\bar{c}$ channels are precisely those in which resonant annihilation takes place (when $m_{\tilde{N}_1} \approx m_{H_1^0}/2$) and for this reason the predicted $\sigma^{SI}_{\tilde{N}-p}$ can decrease by several orders of magnitude. This also explains the smallness of $\sigma^{SI}_{\tilde{N}-p}$ for the points in which annihilation in gg dominates.

Similarly when annihilation into $H_1^0 H_1^0$ or $A_1^0 A_1^0$ channels dominates, the above mentioned correlation does not hold and $\sigma^{SI}_{\tilde{N}-p}$ can be very small as confirmed by in Fig. 2.14. The points with larger values for $\sigma^{SI}_{\tilde{N}-p}$ correspond to those in which the up component of the lightest (scalar or pseudoscalar) Higgs is large and the coupling to the u quark increases.

Finally, black circles on the right-hand side of Fig. 2.14 denote points for which the RH sneutrino annihilation cross section exceeds the Fermi LAT bounds on dSph galaxies. We observe how although this constraint is not very severe, it excludes some points which are not yet probed by direct detection. Its effect is more stringent for light WIMPs and many (but not all) of the solutions with $m_{\tilde{N}_1} \lesssim 5$ GeV can be excluded this way. From the comparison of Fig 2.14 and Fig 2.16 we can observe that that indirect detection can probe points which would be very difficult (or impossible) to test with direct detection, and vice versa. This perfectly illustrates the need for complementary techniques in order to explore the whole DM parameter space.

For clearness, and as a comprehensive summary of our results, we represent in Fig. 2.15 the theoretical predictions for $\sigma^{SI}_{\tilde{N}-p}$ after all the constraints have been applied. The RH sneutrino in the NMSSM is therefore a very flexible candidate for light WIMP dark matter, that could account for future signals in this interesting mass region.

indirect detection

The analysis of the gamma ray spectrum from the Galactic Centre and from dwarf spheroidal galaxies by the Fermi LAT collaboration has shown no clear signal that can be attributed to dark matter[16]. However, these analyses have been used to extract upper constraints on the DM pair annihilation cross section in pure channels that can be interpreted as a lower bound on thermal DM candidates [132, 259] (i.e., those for which the annihilation cross section in the Early Universe is $\langle \sigma v \rangle \sim 3 \times 10^{-26}$ cm^{3}s^{-1}). These constraints are channel dependent, for example, data from dSph galaxies implies $m_{DM} \gtrsim$ 11.3 GeV for the $b\bar{b}$ channel [260]. In the case of the GC, the extracted bounds are

[16] As mentioned in the Introduction, possible hints at low energy exist [129, 144–146, 149, 258].

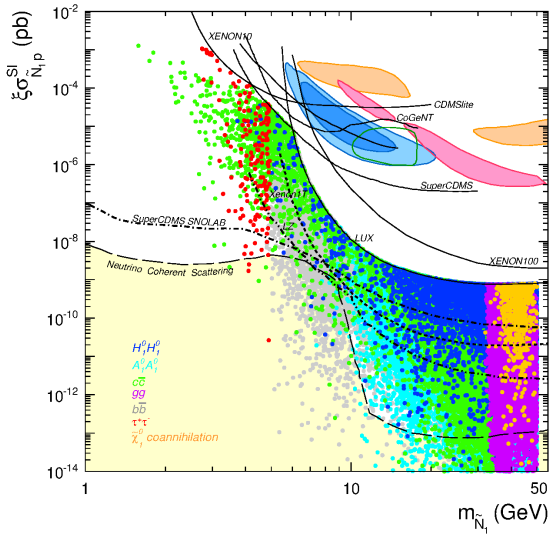

Figure 2.15: Theoretical predictions for $\sigma^{SI}_{\tilde{N}-p}$ as a function of the RH sneutrino mass. All the experimental constraints are included, together with the bounds from direct detection experiments and Fermi LAT data on dSph. The colour code is as in Fig. 2.12.

comparable if the emission from known point sources and from the Galactic disk is subtracted [146, 261]. Nevertheless, without assuming a background model, the bounds are significantly less stringent unless compressed DM profiles are considered [134]. Finally, bounds have also been derived from an analysis of the Andromeda galaxy [262]. and studies of the diffuse gamma ray emission in our Galaxy [130, 263–266]. We will consider only the abovementioned bounds from dSphs data, since these are currently the strongest ones obtained by the Fermi LAT collaboration.

It should be emphasized that when uncertainties associated with the dark matter density profiles of dSph galaxies are included in the analysis of Ref. [132], the resulting constraints on $\langle\sigma v\rangle_0$ can vary up to an order of magnitude [259]. For this reason, even though in our analysis we apply this bound at face value, we have preferred to indicate explicitly the disfavoured points instead of removing them from our plots.

On the other hand, antimatter searches in cosmic rays are also suitable to constrain DM annihilation in the galactic halo. Measurements of the antiproton flux performed by the PAMELA satellite [267, 268] agree very well with the expected astrophysical background. Consequently, these observations can be used to set bounds on the annihilation cross section of light dark matter in hadronic channels. The resulting limits are comparable to those from Fermi LAT on dSphs, although $b\bar{b}$ and $c\bar{c}$ final states are especially constrained below 40 GeV for the most probable set of parameters [269]. Even if these

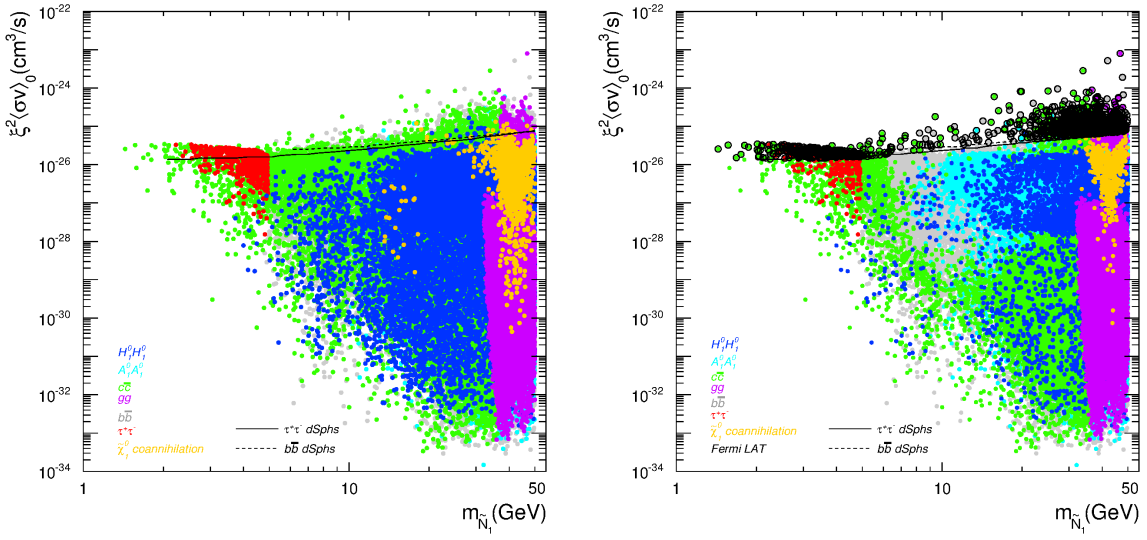

Figure 2.16: Thermally averaged RH sneutrino annihilation cross section in the galactic halo as a function of the RH sneutrino mass. The solid and dashed lines correspond to the upper bounds on $\langle\sigma v\rangle_0$ derived from an analysis of dSph galaxies for pure $\tau^-\tau^+$ and $b\bar{b}$ channels, respectively. The plot on the right-hand side incorporates the constraints from direct detection experiments. The colour code is as in Fig. 2.12.

results are more stringent, they are extremely sensitive to the model that describes the propagation of antiprotons in the Galaxy. In fact, if we take into account the uncertainty in the parameters describing these models, the bounds can be modified up to about an order of magnitude so that the $b\bar{b}$ and $c\bar{c}$ channels might move from a non-constrained region to one with stringent bounds.

Lastly, searches for spectral features in the AMS positron fraction data[127] have been used to derive upper limits on $\langle\sigma v\rangle_0$ for leptonic channels [270]. Since the bound on the $\tau^+\tau^-$ channel is placed above ~ 20 GeV, these findings do not exclude any point in our data set.

In Fig. 2.16, we show the thermally averaged RH sneutrino annihilation cross section in the galactic halo, $\xi^2\langle\sigma v\rangle_0$ as a function of the RH sneutrino mass. The entire set of points fulfil all the experimental constraints and reproduce the right relic abundance. The plot on the right-hand side also incorporates the constraints from direct detection experiments.

As in the previous figures, black circles indicate the points for which the RH sneutrino annihilation cross section exceeds the Fermi LAT constraint. It should be noted that upper bounds on $\langle\sigma v\rangle_0$ are derived for pure channels. Although in our analysis we do

not obtain pure annihilation channels (but a mixture of various), we have implemented the corresponding constraint when the contribution of a specific channel was dominant over the others. For the $H_1^0 H_1^0$, $A_1^0 A_1^0$, and gg channels we consider the same bound as for $b\bar{b}$. On the other hand, for a 10 GeV DM particle, the primary gamma ray spectra for the $\tau^+\tau^-$ and $c\bar{c}$ final states above 1 GeV are very similar [57] and the inverse Compton contribution is negligible for dark mater masses below 500 GeV in the energy range observed by the Fermi satellite [134]. Thus, at first order we will apply the bounds for $\tau^+\tau^-$ to the $c\bar{c}$ final states.

As it is illustrated in Fig. 2.16, Fermi LAT constraints affect a small region of the allowed parameter space, but its effect is particularly severe for light masses. In particular, many of the examples with $\tau^+\tau^-$ and $c\bar{c}$ final states become disfavoured for this reason. In some cases the predicted flux is several orders of magnitude below the current experimental sensitivity. These points correspond to those in which RH sneutrino annihilation proceeds through a resonant s-channel Higgs-mediated diagram $m_{\tilde{N}_1} \simeq m_{H_1^0}/2$ or in which co-annihilation effects help reducing the relic density. According to Eq. 2.45 with $X = H_1^0$, the points which exceed the observed fluxes of Fermi are those with $\Delta_{H_1^0} \gtrsim 0$, as it can be seen perfectly clear in the left panel Fig. 2.12 represented by black points just below the dashed line. In these cases the correlation between the annihilation cross section in the Early Universe and in the DM halo is lost and the latter can be significantly smaller.

2.6 Conclusions on the Neutralino and Sneutrino dark matter scenarios.

We closed the introductory chapter, and opened this one, by noting that SUSY theories do include well motivated WIMP DM candidates. The foregoing discussion has attempted to show to the reader that, in spite of the various experimental constraints existing nowadays, light WIMP DM is still one of the most interesting possibilities found in SUSY theories. The candidates we took into account, Neutralinos and Sneutrinos, serve as a window to the very rich phenomenology related to light DM particles, specially to that of the Higgs sector of each model.

As It has been submitted, the contribution of this chapter rests on three different SUSY models: the MSSM, NMSSM and NMSSM-RH. We started the analysis with the minimal SUSY extension of the SM, the MSSM, where the Neutralino is the LSP in vast regions of the parameter space, and consequently a good WIMP DM candidate. Following

previous studies in the literature, due to the strong constraints on the Higgs sector, the only possibility for light Neutralinos to be viable DM candidates is the presence of light Staus close to the LEP limits. Based on these works, we have presented a novel search of these light Neutralinos in different SUGRA scenarios for the MSSM. By means of a nested sampling algorithm in combination with different public tools, we found out the structure of a given set of soft parameters defined at GUT scale which leads to light Neutralinos at EW scale fulfilling all the experimental constraints. Specially interesting it has been to find that a very well defined structure in the soft Gaugino masses was present. It is also worth mentioning that large non-universalities were not necessary between the three families of RH slepton soft masses. Furthermore, we have also identified the maximal mixing scenario in the stop sector, to raise the Higgs mass around experimentally allowed values, when the stop trilinear is bigger than twice the soft squark masses (taken as universal along this work).

Continuing with the MSSM and more importantly, we have analyzed the Neutralino DM phenomenology, namely direct and indirect detection prospects. The relic density constraint imposes the presence of a very light RH stau, which couples strongly to the Bino component of the lightest Neutralino, and ensures a high annihilation rate in the early Universe through a t-channel exchange. The mass of the Neutralino in these scenario was bounded from below to be $m_{\tilde{\chi}_1^0} \gtrsim 30$ GeV. Regarding direct detection, since the cross relation between direct and relic density processes was broken in this case, we expected low SI and SD cross sections. In effect, the solutions found have a SI cross section of $\mathcal{O}(10^{-12})$ pb, which is really challenging for the next generation of detectors such LZ, XENON1T and SuperCDMS at SNOLAB. However, since these cross sections are above the irreducible Neutrino coherent scattering background, one might expect that these neutralinos would show up eventually in some of the mentioned detectors. Regarding indirect detection prospects, we have shown that, since the Stau sector is almost decoupled in this scenario ($\cos\theta_\tau \approx 0$), the Neutralino thermal cross section into $\tau^+\tau^-$ pairs in DM haloes has an s-wave contribution suppressed. Again, these solutions would be challenging from the point of view of detecting the γ-rays from the annihilations of these Neutralinos in DM haloes, like the MW halo.

The μ-problem motivated us to consider the NMSSM, and in this construction, light Neutralino DM. The Neutralinos in this model incorporate a new mass eigenstate, the *singlino*, which receives its name because it is a singlet under the SM gauge group. As a matter of fact, this guarantees light Neutralinos to be experimentally allowed more easily than in the MSSM. Besides, the Higgs sector is extended with its bosonic counterpart, which enrich the phenomenology of the model, and namely that related to light

Neutralino DM. Using the same sampling technique, we showed that Neutralinos in the NMSSM can be as light as a few GeV without being in conflict with the experimental constraints. Unlike the MSSM Neutralinos found here, these NMSSM Neutralinos have better prospects to be detected either directly or indirectly. The strong relation showed between the Higgs sector, H_1^0 and A_1^0, with Neutralinos determined not only the detection rates but also a high enough annihilation rates in the early Universe to predict an acceptable relic abundance. The latter makes mandatory for the Neutralinos found lighter than $m_Z/2$ to fulfill $2m_{\tilde{\chi}_1^0} \approx m_{H_1^0, A_1^0}$. As we have seen, this has a strong impact on direct detection prospects, both for SI and SD cross sections. Although small cross sections are prospected, the next generation of experiments are expected to have a sensitivity to detect them if they are not lighter than 10 GeV, point in which they cross into the irreducible neutrino background region. The effect of the resonance with a light scalar or pseudoscalar Higgs, however, spans the predictions for $\xi^2\langle\sigma v\rangle_0$ several orders of magnitude, but in general below 5×10^{-27} cm^3/s. For Neutralino masses in the range $m_Z/2 \lesssim m_{\tilde{\chi}_1^0} \lesssim m_Z$, the solutions are dominated either by points resonant with the Z boson, or with the SM-like Higgs, or finally with a lightest scalar (pseudoscalar) Higgs. In this region, again the resonances determine the direct detection phenomenology. Something remarkable was that points resonant with a Z boson could be discovered by its SD interaction with nuclei, while the SI interaction would be tiny and might not show up in detectors that are not SD sensitive, like those which are Argon based. Finally, for $m_{\tilde{\chi}_1^0} \gtrsim m_Z$, the solutions found are in general excluded by direct detection bounds. On balance, the light Neutralino DM in the NMSSM offers a rich phenomenology but that it would be dominated by resonances, and therefore its experimental detection prospects are very different.

Last but not least, the tiny neutrino masses served as a motivation for a further extension of the NMSSM, the NMSSM-RH, where a RH Neutrino was included. Its bosonic partner, the Sneutrino $\widetilde{N}$, is found to be the LSP in great regions of the parameter space of the model, and its couplings with the Higgses provided its WIMPy nature. The notable flexibility of this construction stems from the fact that the new parameters of the model, $(\lambda_N, m_{\tilde{N}_1}, A_{\lambda_N})$, are independent of the rest of the NMSSM spectrum. We have shown that A_{λ_N} and λ_N can be easily chosen in such a way the Sneutrino physical mass lies in the low mass region, without altering other NMSSM low energy observables. The variety of solutions found allowed by experimental constraints is, respect to the two previous cases, remarkable. For very light masses, the Sneutrinos can annihilate efficiently without a resonant condition which showed more clearly the cross relation several times mentioned along these lines. Heavier masses were also found to be viable

showing a clear structure of the Higgs sector. In all cases, the predicted rates in both direct and indirect detection experiments, are very varied.

In summary, and to conclude this chapter, let us say a few words as a comparison between the three scenarios considered here. If a DM signal shows up in some experiment pointing to a DM mass lighter than 20 GeV, the MSSM scenario considered here would be very difficult to reconcile with such signal. Contrary to this, in the two NMSSM constructions analyzed, a very light WIMP DM candidate might be accommodated. More interestingly, such light DM particle would be accompanied by a very light Higgs particle, CP-even or CP-odd, which would be challenging for LHC searches as well. For heavier masses, the MSSM scenario might be discovered via indirect searches, but the NMSSM scenarios could be confronted to this. Then, it would be depend on direct detection experiments, where at some point, the scenarios could be distinguished. Also the LHC might shed light on this, since the MSSM scenario would predict light Stau(s), while the NMSSM scenarios predict light Higgs as mentioned. Therefore, it seems that in the future most of the solutions shown here could be tested, direct or indirectly, and consequently one can expect exciting times for light DM.

Chapter 3

Dark matter direct detection. Complementarity and uncertainties.

So far in this thesis it has been shown that SUSY provides different WIMP DM candidates with rich phenomenologies regarding direct DM searches. The null searches from LUX [106] and SuperCDMS [111, 116] collaborations have placed very strong constraints on DM lighter than 100 GeV. However, we have shown that light Neutralinos in the MSSM and NMSSM are able to evade such constraints, and that Sneutrinos in the NMSSM as well. Now, for these theoretical candidates another question must be faced: is it possible to detect them in the future?. And even more important: if we detect them, what strategy must be followed in order to maximize the information extracted from such detection?.

Of course, these questions have been widely addressed in the literature for specific models and in a model independent way, and there is a general consensus that different detection methods[1] are needed in order to learn as much as possible about the particle DM nature [271–277]. Nonetheless, it has been shown that even only the combination of different targets materials in direct detection experiments might lead to a very good reconstruction of the DM particle properties [278–281]. Along this chapter we will follow this strategy. Using different target materials in direct detection experiments we will try to determine the generic properties of an hypothetical WIMP particle, namely its mass, m_χ, the SI contribution to the WIMP-nucleon cross section, σ^{SI}, and the SD component, σ^{SD}.

If DM is detected, the use of different targets is crucial, as it can serve to unambiguously determine some of the WIMP properties, thus helping to discriminate among the

[1] Generically, direct and indirect detection, collider production and astrophysical probes.

various WIMP candidates. This idea was applied to the case of the COUPP experiment in Ref. [278], emphasizing the relevant role of targets which are sensitive to SD WIMP-nucleus interactions and showing how detection in two complementary targets (in that case C_4F_{10} and C_3FI) could allow a better measurement of the WIMP couplings. The idea of target complementarity has later been applied to the determination of the WIMP mass and cross section from different DM experiments [279, 281] and the relevance of targets sensitive to the SD cross section has been analytically studied in Ref. [280].

In the near future more sensitive experiments are going to continue probing the DM parameter space. This will allow us to clarify the current situation regarding light WIMPs (see Section 1.4.1 for a discussion) and also explore DM candidates with smaller interaction cross sections. In particular, some of the existing experiments are involved in the upgrading of their detectors, moving towards several hundreds kilograms of target material or even reaching the 1 ton scale. This is the case of the XENON1T and LUX collaborations, with a xenon target, SuperCDMS, using germanium, COUPP, with a C_3FI target, and ArDM, using liquid argon [282]. On a similar timescale, the EURECA [283] consortium has plans for a 1 ton scale experiment, able to operate different types of cryogenic detectors consisting of Ge bolometers measuring heat and ionization, and $CaWO_4$ scintillating bolometers measuring heat and light, although other scintillating targets could also be accommodated. The CRESST and ROSEBUD [284] collaborations have worked on R&D and tested other potential scintillating targets, focusing especially on targets that contain nuclei with enhanced sensitivity to SD interactions and low mass WIMPs. According to the characterization and performances of the different scintillating bolometers and their complementarity with Ge and Xe for the determination of the DM properties, some of these materials could be incorporated as additional targets for EURECA, probably in the second phase. The most promising scintillating bolometers in this context are: currently those used by CRESST ($CaWO_4$), and those characterised by the ROSEBUD collaboration (Al_2O_3 and LiF), which contain nuclei which are sensitive to the WIMP SD coupling and are also optimal for searches for low mass WIMPs. Also, bolometers made of CaF_2 and NaI are important, the first one has already been used as scintillating bolometer [285], whereas the construction of a bolometer based on NaI (which is a hygroscopic and fragile material) is an ongoing R&D project of the Zaragoza group [286].

The aim of this chapter is the following: we carry out a systematic study of the performance of various targets used in direct DM searches trying to determine as better as possible the WIMP generic parameters. For this task, some benchmark points (BM) in the (m_χ, σ^{SI}, σ^{SD}) volume are selected, which are already well motivated by the results

of Chapter 2. In order to carry a robust, consistent and realistic analysis, the first thing we will have to do is to identify those sources of uncertainties which can affect to the reconstruction of a hypothetical DM signal. In this context, the importance of the nuclear uncertainties will be stressed, and a comparison with those astrophysical will be done. Then, we will show that 1 ton experiments based on germanium and xenon targets might be unable to determine some of the WIMP parameters (in particular failing to measure the SD component of the cross section). It will be also shown that although C_3FI is a good alternative, the complementary capability of COUPP is limited by its detection technique since it does not provide information about the recoil spectrum. Then, our attention will be turned to other possible experiments and study how their use in combination with germanium and xenon can serve to unambiguously determine m_χ, σ^{SI}, and σ^{SD} in certain scenarios, a situation that we define as *complementarity*. We will concentrate on the scintillating bolometers currently used by CRESST ($CaWO_4$) and on those characterised by the ROSEBUD collaboration (Al_2O_3, LiF, NaI and CaF_2), which contain nuclei which are sensitive to the WIMP SD coupling and are also optimal for searches for low mass WIMPs. It will be demonstrated how for a certain range in the phenomenological parameter space, some of them can provide a good complementary measurement which allows the degeneracy to be disentangled in the SI and SD contributions to the total cross section. This is generally the case when the detection rate in germanium and xenon is dominated by the SI component. On the other hand, $CaWO_4$ and NaI are more convenient targets when the rate in germanium or xenon is mostly SD (since tungsten is heavier and more sensitive to the SI component) and can be used to provide a good measurement of σ^{SI}. Finally, we will close the chapter showing how important is a precise measurement of the quenching factor for complementary purposes selecting a NaI target as a case of study.

Before start let us remark that these analysis were done in the *pre*-LUX era, and thus some of the BM selected are currently ruled out. However the conclusions about the strategies presented remain valid. For keeping the validity one only has to consider a lower cross section (below LUX upper bounds) and increase the exposure accordingly. Since, as we will see, the exposure of the experiment is a multiplicative constant, like the cross section of DM off nucleons, both can be inversely varied without any effect in the expected signal.

3.1 Basics on direct detection: its three pieces.

Let us start by summarising the basic expressions that describe the WIMP rate in a direct DM detection experiment [97] (for a recent review see Ref. [52]). As it has been mentioned earlier, direct detection experiments are based on the detection of the energy deposited when an elastic scattering of a WIMP off a nucleus in the detector takes place. WIMP's around the Earth are expected to be gravitationally bounded to the MW halo, with a velocity $v < v_{esc}$, where v_{esc} is the escape velocity at the Earth position respect to the Milky Way center. In the center of mass frame, the scattering angle, $\cos\theta$, would be uniformly distributed from -1 to 1. Thus in the lab frame, a WIMP which carries an energy $E = m_\chi v^2/2$ would produce a recoil energy

$$E_R = rE\frac{1-\cos\theta}{2}, \tag{3.1}$$

where the dimensionless parameter r is given by

$$r = \frac{4m_\chi m_N}{(m_\chi + m_N)^2}. \tag{3.2}$$

Note that $r \leq 1$, being one only for the specific case $m_N = m_\chi$. Therefore, the recoil energy will be distributed between $0 - rm_\chi v^2/2$. The variation of the rate with the recoil energy can be easily written in terms of the variation of the rate weighted by $1/rE$ using Eq. (3.1).

At this point, the expected recoil energies in direct detection experiments can be calculated. To do this, note that the WIMP velocity at the Earth position is of the order of hundreds of Km/s, which can be concluded from the total gravitational potential of the MW at Sun's position[2]. However, the velocity of the DM particles follow a distribution whose most probable velocity is around $v_0 \approx 220$ Km/s. Using this velocity, the most probable recoil energy would be

$$E_R = rE = \frac{1}{2}m_\chi v_0^2 \approx 15\text{keV}, \tag{3.3}$$

where we have used $m_N = m_\chi = 50$ GeV to maximize the energy. From this estimation it can be already seen how big is the challenge faced by direct detection experiments. The detection of such low energy events highlights the need of these experiments to implement very low energy thresholds.

[2] As it will be explained later, this must be done by modeling the ordinary and dark matter density profiles and applying the Eddington formalism.

To calculate the number of events expected from WIMP collisions is useful to start by writing the number of WIMP's inside a volume moving with certain velocity v as,

$$dN = \frac{\rho_0}{m_\chi} f(\vec{v} + \vec{v_E}) \sigma_{WN} v dt, \tag{3.4}$$

where in dt each WIMP in a this volume would interact with a nucleus inside the detector as $dV = \sigma_{WN} v dt$. In this equation, σ_{WN} is the WIMP-nucleus cross section. $f(v)$ is the WIMP speed distribution normalized to unity and ρ_0 is the local WIMP density. We have made use of a decomposition of the WIMP velocity respect to the center of the Galaxy as the velocity of the WIMP respect to the Earth (lab) v plus the Earth velocity respect to the Galaxy v_E. After some manipulations, the differential event rate for the elastic scattering of a WIMP with mass m_χ off a nucleus with mass m_N and a detector mass M_{det} is given by

$$\frac{dR}{dE_R} = \frac{M_{det}\,\rho_0}{m_N\,m_\chi} \int_{v_{min}}^{v_{esc}} v f(v)\, \frac{d\sigma_{WN}}{dE_R}(v, E_R)\, dv\,, \tag{3.5}$$

The integration over the WIMP velocity is performed from the minimum WIMP speed needed to induce a recoil of energy E_R extracted from Eq. (3.1), $v_{min} = \sqrt{(m_N E_R)/(2\mu_N^2)}$ where μ_N is the WIMP-nucleus reduced mass, to a escape velocity v_{esc} also in the detector reference frame, above which WIMPs are not gravitationally bounded to the Milky Way.

It must be noticed that Eq. (3.5) would be only valid if the detector would be made of a single isotope nucleus target material. In general, a target material is composed by several isotopes, like in germanium where there are $A = 70, 72, 73, ...$ isotopes, each contributing to the whole mass of the detector according to its natural abundance. To take it into account, the previous formula must be extended by a sum over all isotopes, each term multiplied by the percentage given by the natural abundance. This also holds for composite materials like NaI, in which case the whole detector mass must be weighted properly. This is specially important for SD interactions, since if this is not included, the SD contribution to the signal would be overestimated. As an example if we take ^{73}Ge to be 100%, we would be overestimating the signal in 92% approximately. In what follows thus we will consider all natural abundances of the isotopes used.

The WIMP-nucleus differential cross section $d\sigma_{WN}/dE_R$ is computed from the Lagrangian that describes the interaction of a given WIMP with ordinary matter and encodes the particle physics input. The total event rate is then calculated by integrating the differential event rate over all the possible recoil energies,

$$R = \int_{E_T}^{E_{max}} dE_R \frac{M_{det}\,\rho_0}{m_N\,m_\chi} \int_{v_{min}}^{v_{esc}} v f(v)\, \frac{d\sigma_{WN}}{dE_R}(v, E_R)\, dv\,. \tag{3.6}$$

The window for WIMP searches is selected from a threshold energy, E_T, to a maximal recoil energy, E_{max}, and depends on the specific experiment. The total number of DM recoils is $N = Rt$, where t is the live time of the experiment. In the following, we will also refer to the exposure, defined as $\epsilon = M_{det}t$.

In general, the WIMP-nucleon scattering cross section can be separated into a SI and a SD contribution. The total WIMP-nucleus cross section is calculated by adding these coherently, using nuclear wave functions. The differential cross section thus reads

$$\frac{d\sigma_{WN}}{dE_R} = \frac{m_N}{2\mu_N^2 v^2}\left(\sigma_0^{SI,N} F_{SI}^2(E_R) + \sigma_0^{SD,N} F_{SD}^2(E_R)\right), \tag{3.7}$$

where $\sigma_0^{SI,N}$ and $\sigma_0^{SD,N}$ are the SI and SD components of the WIMP-nucleus cross sections at zero momentum transfer, and the form factors $F_{SI,SD}^2(E_R)$ account for the coherence loss which leads to a suppression of the event rate for heavy nuclei. See Ref. [51] for a complete description of these prescriptions.

The three pieces, which give the section's name, are easily recognized from the Eq. (3.5) and Eq. (3.7). First, there is a dependency on the particle physics model coming from the quantities $\sigma_0^{SI,N}$ and $\sigma_0^{SD,N}$, and in a moment, it will be seen their relation to expressions given in the previous chapter for the Neutralino and Sneutrino. Then, we have a dependence on astrophysics encoded by the velocity distribution $f(v)$, and by the DM local density, ρ_0. Finally, there is a dependency on the nuclear structure of the detector itself parametrized by the form factors $F_{SI,SD}^2(E_R)$. Formally, there is still one more dependence on the experimental setup, this is, on the threshold energy E_T, energy resolution of the detector, etc.

3.1.1 Particle physics

Let us start by showing the connections of the rate in Eq. (3.5) with particle physics. Using the Fermi's Golden Rule in the Born approximation we can factorize all the energy (momentum) dependence of the scattering between the WIMP and a nucleus inside a form factor $F^2(q)$ as shown in Eq. (3.7). Then the zero momentum transfer can be written as [47, 51]

$$\begin{aligned}
\sigma_0^{SI,N} &= \frac{\mu_N^2}{\mu_p^2}\left[Z + (A-Z)\frac{f_n}{f_p}\right]^2 \sigma_p^{SI}, \\
\sigma_0^{SD,N} &= \frac{\mu_N^2}{\mu_p^2}\left[S_p + S_n\frac{a_n}{a_p}\right]^2 \left(\frac{4}{3}\frac{J+1}{J}\right)\sigma_p^{SD},
\end{aligned} \tag{3.8}$$

where μ_p is the proton-WIMP reduced mass; S_p and S_n are the expectation values of the total proton and neutron spin operators; f_p, f_n and a_p, a_n are the effective WIMP

couplings to protons and neutrons in the SI and SD case, respectively; and J is the total nuclear spin.[3] Other parameters define the target material, Z its atomic number and A the mass number. In this expression we have defined the WIMP-nucleon cross sections $(\sigma_p^{SI},\sigma_p^{SD})$ as,

$$\begin{aligned} \sigma_p^{SI} &= \frac{4}{\pi}\mu_p^2 f_p^2 \\ \sigma_p^{SD} &= \frac{24G_F^2}{\pi}\mu_p^2 a_p^2\,, \end{aligned} \tag{3.9}$$

by using $S_p = 1/2$, $S_n = 0$, $J = 1/2$, $A = Z = 1$ and the spin of the WIMP equal to the spin of the proton J [287]. G_F is the Fermi coupling constant. Now, one might clearly see the connection with particle physics, for instance, in the case of the Sneutrino, the quantity f_p was already defined in the previous chapter in Eq. (2.67) in the context of an effective Lagrangian [4].

To conclude, let us remark that in the following we will assume the specific case $f_n/f_p = 1$ and $a_n/a_p = -1$ so that only one parameter $\sigma_p^{SD} = \sigma_n^{SD} \equiv \sigma^{SD}$ will be needed to describe SD interactions[5] and the same holds for the SI interactions $\sigma_p^{SI} = \sigma_n^{SI} \equiv \sigma^{SI}$.

3.1.2 Astrophysics

As we have seen, the differential rate Eq. (3.5) depends on some astrophysical parameters, such as the velocity distribution $f(v)$ and the local DM density ρ_0. In this thesis, some basics expressions will be given in the following just for the sake of completeness, and also for the reader to guess how direct detection experiments are affected by the whole MW mass distribution model. However, it is worth mentioning that in general a Maxwell-Boltzmann distribution known as the Standard Halo Model (SHM) is used, as we have commented earlier in Chapter 1. This is done just for simplicity and to compare different experimental results under the same approximations, but a proper and consistent analysis would require a more careful description of the phase-space distribution function.

Studies coming from N-body simulations have led to several expressions for the DM distribution in our galaxy, $\rho_{DM}(r)$, and in clusters of galaxies as well. Probably the most

[3] Notice that for simplicity we have not included here a possible vector coupling (corresponding to non-Majorana DM particles), which would lead to an extra contribution in the expression for $\sigma_0^{SI,\,N}$.

[4] Notice a factor $(1/4)^2$ different between Eqs. (2.67) and (3.9). This is due to a different convention regarding the effective Lagrangian, which at the end is absorbed in a redefinition of f_p.

[5] The analysis can be extended to consider a larger parameter space, which would require further study. This simplification is motivated by the fact that particle models for DM matter generally predict $|\sigma^{SD,\,n}| \approx |\sigma^{SD,\,p}|$.

popular one is the Navarro-Frenk-White (NFW) density profile [288], but the Einasto [289] and Burkert [290] models are also used as we will see in the next chapter. Once the DM density profile is specified, the corresponding phase-space distribution can be extracted in a *self-consistent* way with the help of the Eddington formula:

$$f(\epsilon) = \frac{1}{\sqrt{8}\pi^2}\left[\int_0^\epsilon d\Psi \frac{d^2\rho_{DM}}{d\Psi^2}\frac{1}{\sqrt{\epsilon-\Psi}} + \frac{1}{\sqrt{\epsilon}}\left(\frac{d\rho_{DM}}{d\Psi}\right)\Big|_{\Psi=0}\right] . \tag{3.10}$$

Here it is assumed that this distribution depends only on the relative energy $\epsilon \equiv \Psi - v^2/2$ of the system, being v the relative velocity and $\Psi = \Psi(r)$ the gravitational potential generated by the DM halo and the baryonic matter through $\rho_{\text{Total}} = \rho_{DM} + \rho_{\text{baryons}}$, and defined in such a way as to obey $\Psi(r \to \infty) = 0$. More specifically, it is obtained by solving the Poisson equation, whose solution, for a spherically symmetric profile, can be expressed as:

$$\Psi(r) = -4\pi G\left[\frac{1}{r}\int_0^r \rho_{\text{Tot}}(r')\, r'^2 dr' + \int_r^\infty \rho_{\text{Tot}}(r')\, r' dr'\right] . \tag{3.11}$$

For a given position r, Eq. (3.10) gives a velocity-distribution function with a cutoff at $v_{\text{esc}} \equiv \sqrt{2\Psi(r)}$, where v_{esc} is the escape velocity, such that $f(\epsilon) = 0$ for $v > v_{\text{esc}}$.

Therefore, we see that once the matter content of the Galaxy is specified, the velocity distribution is known at each point of the Galaxy. Very recent estimations making use of different observational data, have extracted the DM velocity distribution at the Earth for different DM profiles [291] that can be used in direct detection studies.

3.1.3 Nuclear physics

The momentum transfer of the scattering is parametrized by the form factors $F^2_{SI,\,SD}(E_R)$ in Eq. (3.8). The calculation of these functions differs in each case. In the SI interaction case, the calculation is easy using the nuclear density, whereas in the SD case the calculation requires a more difficult modeling of the interactions between nucleons inside the nucleus.

In the SI case, using the Born approximation the scattering matrix element reads,

$$\mathcal{M}(\vec{q}) = fA\int d^3x \rho(\vec{x}) e^{i\vec{q}\vec{x}}, \tag{3.12}$$

where the momentum transfer is identified with:

$$F(\vec{q}) = \int d^3x \rho(\vec{x}) e^{i\vec{q}\vec{x}}. \tag{3.13}$$

This is the Fourier transform of the nuclear matter density $\rho(\vec{x})$ with scattering in the centered positions. The nuclear matter density follows somehow the charge density which is well described by a Fermi distribution. An analytical formula was proposed by Helm,

$$F(q) = \frac{3j_1(qr_n)}{qr_n} e^{\frac{-(qs)^2}{2}}, \tag{3.14}$$

where s is the surface thickness in fm, $q(\text{MeV}) = \sqrt{2 \times 0.932(\text{GeV}) A E_R(\text{keV})}$ and $r_n = \sqrt{c^2 - 5s^2 + 7/3\pi^2 a^2}$ fm. Note that $j_1(x)$ is a Bessel function of first kind. In Ref. [51] the authors propose the parameters $s = 0.9$ fm, $a = 0.52$ fm and $c = 1.23A^{1/3} - 0.6$ fm which reproduce very accurately the numerical results obtained by the integration of the Fermi distribution.

From Eq. (3.14) must be noticed that $F^2_{SI}(E_R)$ would have zeros periodically, corresponding to the zeros of the Bessel function. This will yield to a coherence loss of the SI interactions. Once the momentum transferred is different from zero, quickly the form factor would decrease. This happens when the Broglie wavelength $\lambda < r_n$ and the WIMP starts to see the internal structure of the nucleus, and hence ceases the interaction with the nucleus as a whole. Due to the dependence of the momentum transferred on the mass of the nucleus, and thus on A, it can be shown that the coherence is lost approximately,

$$E_R > \frac{2 \times 10^4}{A^{5/3}} \text{keV} \approx 100 \text{keV}. \tag{3.15}$$

This dependence on A is specially unfortunate for heavy nuclei, making that for isotopes roughly heavier than $A = 73$, the increase in the total rate would be far from the typical A^2 dependence.

The situation regarding the SD interactions is much more complex. First we note that in Eq. (3.8) appears two quantities related to the spin of the target nucleus, S_p and S_n. These are the the total spin of protons (neutrons) averaged over all nucleons of the nucleus (A,Z). The expectation values of the spin and angular operators are evaluated, as a rule, in their z-projection by assuming the state with the maximal value of the angular momentum projection $M_J = J$ [292],

$$S_{p(n)} = \langle N|\mathbf{S}_{p(n)}|N\rangle = \langle J, M_J = J|S^z_{p(n)}|J, M_J = J\rangle. \tag{3.16}$$

These quantities are often related to the matrix element of the nuclear magnetic moment, which also contains the matrix elements of the total proton and neutron spin operators, and thus can be used as benchmark to evaluate the accuracy of the $S_{p(n)}$ calculation [292]. For a list of calculations for different target materials we refer the reader to Ref. [292], and more recently calculations using newer techniques can be found in Ref. [293].

As a matter of fact, the factor containing the expectation values $S_{p(n)}$ of Eq. (3.8) has been written to normalize the form factor accordingly $F_{SD}(0) = 1$. However, the SD interaction part of the Eq. (3.7) is derived in terms of the SD Structure Functions (SDSF),

$$S(q) = a_0^2 S_{00}(q) + a_0 a_1 S_{01}(q) + a_1^2 S_{11}(q), \tag{3.17}$$

which are related with the form factor as $F_{SD}^2(q) = S(q)/S(0)$. The coefficients correspond to the isoscalar and isovector couplings which are defined as $a_0 = a_p + a_n$ and $a_1 = a_p - a_n$. Note, that in the literature it is also common to use the proton/neutron decomposition $S_{p(n)}(q)$. In this notation the proton only part is given by $a_0 = a_1 = 1$ and the neutron only part by $a_0 = -a_1 = 1$. However, this notation is somehow misleading since the WIMP does not couple only to protons or neutrons but effectively couples to both [293]. The values of the SDSF at zero momentum transfer can be connected with the expectation values of the spin as follows [294]:

$$\begin{aligned} S_{00}(0) &= C(J)(S_p + S_n)^2, \quad S_{11}(0) = C(J)(S_p - S_n)^2, \\ S_{01}(0) &= 2C(J)(S_p^2 - S_n^2) \quad \text{with} \quad C(J) = \frac{2J+1}{4\pi}\frac{J+1}{J}. \end{aligned} \tag{3.18}$$

It is also usual to find in the literature the SDSF written in terms of a dimensionless variable $u = (qb)^2/2$ related to the momentum transfer q, which also will be used in this thesis. In this expression the parameter b is often referred as the oscillation size parameter, with $b \approx A^{1/6}$ fm. However, this parameter is specific for each calculation and thus it must be properly chosen. As we have said above, we have restricted ourselves to the $a_n/a_p = -1$ case, and hence $S_{11}(u)$ will define our SDSF.

Let us finally remark that the $S_{ij}(q)$ functions exhibit a strong dependence of the spatial distribution of the spin in the nucleus and its magnitude. Therefore, the calculation requires a careful model of the interactions between nucleons and is subject to important theoretical uncertainties as we will see. A complete list of different calculations of the finite momentum transfer SDSF's can be found in Refs. [293, 294].

The SDSFs $S_{00}(q)$ and $S_{11}(q)$ can be calculated using a shell-model (ShM) description of the atomic nucleus, where the nuclear spin properties are obtained by the wave functions of a few valence nucleons, those which do not cancel out the spin of the nucleus in pairs. In particular, $S_{00}(q)$ and $S_{11}(q)$ are related to the transverse electric and longitudinal projections of the axial current. To calculate these quantities in the ShM, the nucleons are placed in energy levels according to the exclusion principle, assuming a particular interaction between nucleons (typically a harmonic oscillator potential) and including as many excited states as possible, making this kind of calculation very

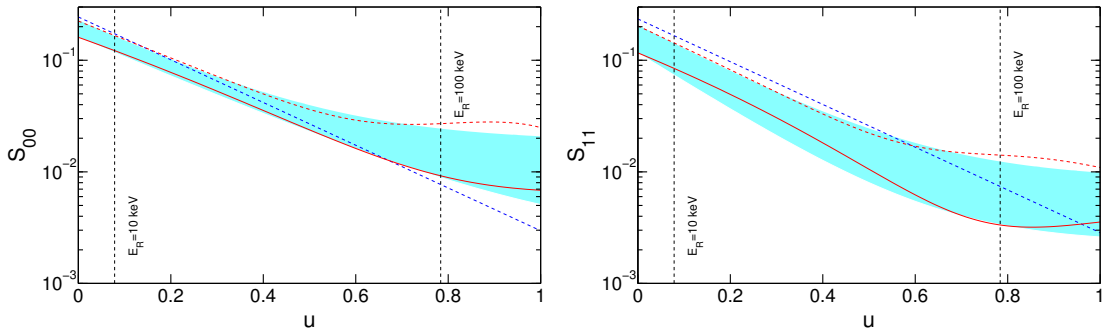

Figure 3.1: Spin-dependent structure functions as a function of u, in the case of $a_p/a_n = 1$ (left panel) or $a_p/a_n = -1$ (right panel). The solid (dashed) red lines correspond to the D-model [295] (R-model [296]) and the dotted blue line indicates the gaussian approximation of Eq. (3.19). The blue region covers the area spanned by the family of curves in Eq. (3.26). The vertical black dashed lines indicate the WIMP search window used in the analysis.

difficult.

ShM calculations are generally more reliable for heavy nuclei than for light ones. The same holds for nuclei close to magic numbers, elements featuring closed shells being more easily modeled. An example is ^{19}F, that has 9 protons and 10 neutrons, thus only one proton above a magic number. On the other hand, the nucleus of ^{73}Ge is much more difficult to model since it has 32 protons and 41 neutrons, the nearest closed shell being the one with 28 nucleons. In this case, deviations of the real nucleus from the ShM should be expected, as well as differences in the results when different ShMs are used. Let us then consider the case of germanium for which the only natural isotope that contributes to the SD cross-section is ^{73}Ge. In this case various ShM calculations are available in the literature. We consider two different, commonly used parametrizations, from Ressel et al. [295] and Dimitrov et al. [296], to which we refer as R- and D-models, respectively. They differ in the methodology and in the choice of the nuclear interaction potential, but both reproduce the value of the magnetic momentum of ^{73}Ge.

The SDSFs for the R-and D-models are plotted as a function of u in Fig. (3.1) by means of red dashed and solid red lines, respectively. The left (right) panel refers to the case $a_p/a_n = 1$ ($a_p/a_n = -1$). The vertical, black dashed lines indicate the values of u that correspond to the WIMP search window that we use in our analysis, from a threshold energy of 10 keV, to an energy of 100 keV (as currently done in CDMS-II)[6]. The dotted

[6] The effect of lowering the threshold, considering SuperCDMS for instance, it is expected to not

blue lines indicate a gaussian approximation (see Eq. (3.19) below). Finally, the blue areas represent the regions spanned by a family of curves, obtained by a parametrization which interpolates between the R- and D-models that will be introduced later.

The two SDSFs differ in the zero momentum value (the R-model being larger for the whole energy range of interest for direct detection), and also in the shape at large energies. They both start as decreasing power-laws at low-energy flattening out as u increases. However the transition happens sooner for the R-model (around $u = 0.5$) than for the D-model. The slope for the D-model is also slightly steeper than for the R-model, especially in $S_{11}(q)$. As we will see these differences play an important role when determining the DM parameters.

There are finally some nuclei for which ShM computations of their form factors are not available. In these cases an approximation was introduced in Ref. [201] that works well in the low momentum transfer regime, but fails towards larger values of q,

$$S_{ij}(q) = S(0)\, e^{-\frac{q^2 R^2}{4}}\,, \tag{3.19}$$

where R, is an effective radius, measured in fm, which can be written as,

$$R = 0.92\, A^{1/3} + 2.68 - 0.78\sqrt{(A^{1/3} - 3.8)^2 + 0.2}\,. \tag{3.20}$$

3.2 Reconstruction of WIMP parameters

Before presenting the results, let us summarize what is the strategy followed to reconstruct consistently the DM parameters.

3.2.1 The Bayesian approach

For a given experimental setup (we use the label a to denote the target) we define an energy window for WIMP searches, from a threshold, E_T^a to a maximum energy E_{max}^a. We divide that energy range into energy bins $\{E_i^a, E_i^a + \Delta E^a\}$ with a width ΔE^a. We then compute, for a choice of DM parameters, the expected number of events $\{\lambda_i^a\}$ in each energy bin, by integrating Eq. (3.5) in the corresponding interval for a given live time and adding a certain level of background events B_i^a. Depending on the analysis we define two different setups labelled as ES_1 and ES_2. The specific energy windows, bin size and background assumed can be found in Appendix 3 for the experimental set-ups ($\mathrm{ES}_{1,2}$) considered.

produce any change since the uncertainty is similar at 10keV than a 3 keV.

We consider the quantities $\{\lambda_i^a\}$ as the experimental information from which we attempt to reconstruct the DM parameters. Our analysis is based on the Bayes theorem, which determines the posterior probability distribution function (pdf) $p(\mathbf{\Theta}|\mathbf{D})$ of a set of parameters $\mathbf{\Theta}$ (for which a prior probability is assumed $p(\mathbf{\Theta})$) from a set of experimental data $\mathbf{D}$, encoded in the likelihood function $p(\mathbf{D}|\mathbf{\Theta})$ (or $\mathcal{L}(\mathbf{\Theta})$),

$$p(\mathbf{\Theta}|\mathbf{D}) = \frac{p(\mathbf{D}|\mathbf{\Theta})p(\mathbf{\Theta})}{p(\mathbf{D})}\,. \tag{3.21}$$

The evidence $p(\mathbf{D})$ in the denominator of Eq. (3.21) is a function of only the experimental data. For our purposes it works as a normalization factor and can therefore be ignored. The pdf in Eq. (3.21), in principle, depends on the priors $p(\mathbf{\Theta})$ and different choices of priors can affect the shape of the final pdf. However, should this happen, it would mean that the experimental data are not constraining enough, not being able to dominate the final probability distribution. Residual prior dependence can be seen, e.g., in Refs. [204, 297, 298]. The scans over the parameter space that allow us to retrieve the pdf are performed with `MultiNest` [193, 194] interfaced with our own code for the computation of the number of recoil events and the likelihood. Scans are performed with 20000 live points and a tolerance of 0.0001 to reach a good sampling of the profile likelihood (see below) as found in Ref. [204].

In our case the experimental data consists of the predicted sets of binned WIMP induced nuclear recoils for each target, $\mathbf{D} = (\{\lambda_i^a\})$. The parameter space is $\mathbf{\Theta} = (m_\chi, \sigma^{SI}, \sigma^{SD})$ and our scans span the following range: $m_\chi = 1 - 10^5$ GeV, $\sigma^{SI} = 10^{-12} - 10^{-6}$ pb, and $\sigma^{SD} = 10^{-8} - 1$ pb. Logarithmic flat priors are assumed for the three variables.

The likelihood $\mathcal{L}(\mathbf{\Theta})$ is computed for each point in the scan, computing the number of recoil events N_i^a in the i-th bin for the experiment a, and comparing it with the prediction of the benchmark model in the same bin, λ_i^a for the same target, assuming that data from each experiment follow independent Poissonian distributions,

$$\mathcal{L}(\Theta) = \prod_a \mathcal{L}^a(\Theta) = \prod_a \prod_i \frac{N_i^a(\mathbf{\Theta})^{\lambda_i^a} e^{-N_i^a(\mathbf{\Theta})}}{\lambda_i^a!}\,. \tag{3.22}$$

Notice that this is equivalent to the product of the likelihoods for each experiment $\mathcal{L}^a$. The number of recoil events N_i^a in the i-th bin for each experiment is obtained by integrating Eq. (3.5) between E_i^a and $E_i^a + \Delta E^a$, for a given live time and including a certain number of background events $b^a/\Delta E^a$. b^a indicates the number of background events in the whole energy for target a, so that, assuming no energy dependence, $b^a/\Delta E^a$ is the predicted number of background events in each energy bin. We scan over b^a,

included in the scan as a nuisance parameter. We assume the number of background events b^a follows a Poissonian distribution function with a mean value that coincides with the nominal background level expected for the different experiments (see Appendix 3).

In the next sections, the results of our scans will be plotted by means of two-dimensional plots. When the probability for a subset of the original $\mathbf{\Theta}$ is considered, one can account for the presence of the hidden parameters in two different ways:

- by marginalizing over them, obtaining the pdf for the j-th parameter integrating over all the others

$$p(\Theta_j|\mathbf{D}) = \int p(\mathbf{\Theta}|\mathbf{D})\, d\Theta_1 ... \, d\Theta_{j-1}\, d\Theta_{j+1}\, d\Theta_n; \tag{3.23}$$

- by maximizing over them, obtaining the so-called profile likelihood (PL)

$$\mathcal{L}(\Theta_j) = \max_{\Theta_1,...,\Theta_{j-1},\Theta_{j+1},\Theta_n} \mathcal{L}(\mathbf{\Theta}). \tag{3.24}$$

The PL is usually more sensitive to small fine-tuned regions with large likelihood, while the integration implemented for the pdf allows to account for volume effects. Thus, a parameter space characterized by a complicated likelihood function $\mathcal{L}(\mathbf{\Theta})$ may result in different pdf and PL for the same parameters. In our work, to avoid the inclusion of too many figures, we will only represent the results for the PL. In the following sections, we demand closed contours in the PL 68% and 99% confidence regions (i.e. a good reconstruction of the DM parameters) as a requirement for complementarity. In general, when closed contours are obtained in the distribution of the PL for the DM parameters we have also observed closed contours in the pdf.

3.2.2 On the spin-dependent inclusion importance

Usually, the analysis of the experimental collaborations are done by using the *standard assumptions* and assuming that the SD interactions are zero, i.e. considering a scalar WIMP. One of the main points of the work presented in this chapter is precisely to learn how if these assumptions are dropped the reconstruction of an hypothetical DM signal is affected.

The first thing one might consider is: if we reconstruct a signal taking into account only SI interactions but the WIMP producing that signal is a spin 1/2 particle, how does it affect to the reconstruction?. For this first exercise, we first particularize our analysis

	m_χ [GeV]	σ^{SI} [pb]	σ^{SD} [pb]	λ	λ^{SI}	λ^{SD}
BM1	100	10^{-9}	10^{-5}	37.2	36.4	0.8
BM2	50	10^{-9}	10^{-5}	42.1	41.2	0.9
BM3	100	10^{-9}	10^{-3}	79.6	36.4	43.2

Table 3.1: Phenomenological parameters defining the three benchmark models. We include the predicted total number of recoil events, λ, as well as the number of events λ^{SI} (λ^{SD}) due to SI (SD) interactions, for the experimental setup described in the text.

for the case of a germanium detector with a total exposure of $\epsilon = 300$ kg yr. This could, e.g., correspond to the 1 Ton phase of SuperCDMS, operating for a whole year with an efficiency of 30%. We define the experimental setup according to ES_1, see Appendix 3 for more details. As it is indicated there, we also include a background with a rate of 4×10^{-8} days^{-1} kg^{-1} keV^{-1}, which is of the order of the background expected for the SuperCDMS experiment in SNOLAB [299]. For the considered exposure this means a total of 0.02 background events in each of the energy bins considered (i.e., we are almost dealing with a background free experiment). We assume that this background is flat (energy independent).

To generate the data, we use three different benchmark points to define the DM nature. In table 3.1 we show the cross sections and masses used together with the expected number of SI only and SD only events. The resulting two-dimensional profile likelihood for these quantities[7] are given in Fig. 3.2. An obvious thing to observe is that the reconstruction of these two parameters is good for benchmarks BM1 and BM2, since in these cases the SI contribution is the dominant term in the detection rate. This is obviously not the case in BM3, where SD interactions play a more important role. For this benchmark point, ignoring the SD contribution term leads to an overestimation of the SI independent cross-section of approximately a factor two (in order to account for the total detected rate).

Another feature that can be observed, and is consistent with the existing literature, is that the goodness of the reconstruction is very dependent on the mass of the DM candidate [300, 301] (see also Refs. [281, 302, 303]). In particular, we can see how in benchmark BM1 the 99% confidence level contours are open for heavy WIMPs, whereas this is not the case for BM2 and BM3. In principle, increasing the DM mass makes

[7] Note that, since we are scanning over only two parameters, there is no need of marginalization or maximization.

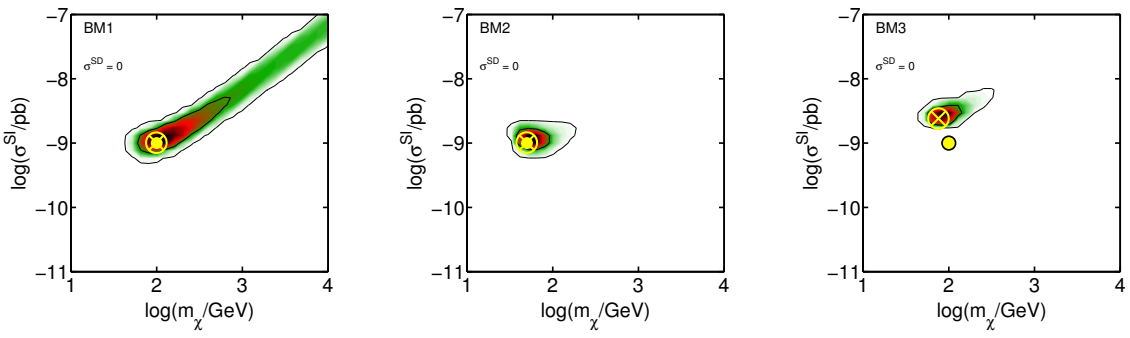

Figure 3.2: Two-dimensional profile likelihood in the plane (m_χ, σ^{SI}) for benchmarks BM1, BM2 and BM3, from left to right, assuming in the reconstruction that $\sigma^{SD} = 0$. The inner and outer contours are 68% and 99% confidence level regions, respectively. The yellow dot indicates the benchmark values in each case, and the encircled yellow cross marks the positions of the best-fit point.

the recoil energy spectrum flatter, as a consequence of the dependence of v_{min} which enters through the reduced mass. Thus one expects to produce a worse fit to the recoil spectrum as we scan more massive DM candidates. In benchmarks BM2 and BM3 this is the reason why heavy masses are disfavoured, however in BM1 the number of events in each energy bin is too low to pick up this tendency and very massive DM candidates can still produce a good fit to the data. The presence of a flat background also enhances this effect. On the other hand, the contours do not extend to low WIMP masses because particles with masses below $m_\chi \sim 30-40$ GeV produce a much steeper spectrum. Notice finally that the assumption $\sigma^{SD} = 0$ leads to a lower limit for the SI cross-section that allows us to reconstruct the value of σ^{SI} up to approximately a factor 5 (for a fixed value of DM mass).

An unbiased reconstruction of DM parameters, however, has to include the possibility that $\sigma^{SD} \neq 0$. In fact, when we allow for a non-negligible SD contribution to the WIMP scattering cross-section, we find that a new degeneracy in the parameter space arises: the same detected rate can be explained by a DM with either pure SD or pure SI interactions or, in general, a given combination of both as we see from Eq. (3.7). This implies that the closed contours in Fig. 3.2 can extend towards arbitrarily small values of σ^{SI}.

3.3 Uncertainties

From the previous chapter, we have pointed out that there exist several uncertainties related to direct detection of DM experiments. At that point, we emphasized the uncertainty related to the content of the nucleon (see discussion around Eq. (2.31)), which must be calculated from lattice QCD techniques. This uncertainty, however, has no impact on the methodology used now, since what we consider as benchmark points are definitions at the level of WIMP-proton cross section, and hence is not included.

Other uncertainties can affect the reconstruction of the DM parameters. Namely, the astrophysical uncertainties, which have been shown to induce an important effect on the reconstruction, must be included. Furthermore, we have shown that the uncertainties related to the SDSF calculations might be also important. These affect the reconstruction of the SD cross section and mass of the DM particle, and therefore, they have to be properly included. The aim of this section is to introduce to the reader the nuclear uncertainties and its effect on the reconstruction. We are going to show that these uncertainties might be as important as the astrophysical ones, which are widely studied in the literature. Furthermore, we will give a formula which can be used to systematically include these uncertainties when reconstructing a DM signal.

3.3.1 The Milky Way velocity distribution function

As it has been already introduced before in this thesis, the rate of DM particles colliding with a target at the Earth depends on the velocity distribution of DM particles surrounding it. It was also introduced, how these distribution depends on the MW matter (dark and baryonic) profile densities. Now, let us comment how all this can affect to the information extracted from direct detection experiments. For much more complete discussions on the topic we refer to Refs. [304–309].

It is worth mentioning that there are "astrophysical independent" techniques to compare different data sets from different experiments [310, 311]. These methods are impressive for assessing the compatibility of data from different experiments, however, they need to assume an specific WIMP mass. Another way to treat the velocity distribution in a more general way, without assumptions on it, is to determine the WIMP mass from the moments of the energy spectra for two experiments [279]. However this method leads to a systematic underestimate of the WIMP mass if it is comparable to or larger than the mass of the target nuclei [308]. It has been argued as well that the WIMP mass can be fully reconstructed by parametrizing the logarithm of the distribution using a polyno-

mial functional and thus not imposing any distribution *a priori* [312]. Very recently, it has been pointed out a method that yields the velocity distribution which best describes a set of direct detection data as a finite sum of streams with optimized speeds and densities, however, it needs a high number of detected events to improve the statistics and it implies to deal with a high number of free parameters [313]. All in all, we think that the most general way to analyze direct detection data seems to be including properly the uncertainties on the velocity distribution function.

As we have pointed out, usually collaborations used the so-called *standard assumptions*, among which a SHM is considered. This model is an isotropic, isothermal sphere with density profile $\rho(r) \propto r^{-2}$. In this case the solution of the collisionless Boltzmann equation is the so-called Maxwellian velocity distribution. This velocity distribution formally extends to infinity, since the profile do so. Nonetheless, the MW is finite, and no WIMP particles are expected to be gravitationally bounded with velocities above the escape velocity. An *ad hoc* strategy is to cutoff the distribution above v_{esc}, either sharply or smoothly.

Dark matter only simulations, however, show that in MW-like halos the velocity distributions deviate systematically from a multivariate Gaussian, and thus from a Maxwellian functional form. Several phenomenological fits have been proposed in the literature to account for non-standard velocity distributions. In this thesis, we have used the following *ansatz* for the velocity distribution [314]:

$$F(v) = N_k^{-1} v^2 \left[e^{-v^2/k v_0^2} - e^{-v_{esc}^2/k v_0^2} \right]^k \Theta(v_{esc} - v), \tag{3.25}$$

where $N_k = v_0^3 e^{-y_e^2} \int_0^{y_e} dy\ y^2 (e^{-(y^2-y_e^2)/k} - 1)^k$ and $y_e = v_{esc}/v_0$ and v_0 is the central velocity. This distribution fits the high speed tail of the smooth component of the speed distributions found in simulations. The k parameter is the power-law index of the distribution and it describes the behavior for the highest velocities, near the escape velocity of the distribution. This parameter can also be related to the profile DM density via Eq. (3.10), and for some values related to the NFW profile at large radii. In the limit of vanishing k the standard halo model is recovered, namely for $k \approx 0$ with a sharp cutoff, and for $k = 1$ with a smooth one.

Using this equation allows us to incorporate the astrophysical uncertainties as nuisance parameters in our scans. The three parameters that define the velocity distribution function vary in the ranges $v_{esc} \in [478, 610]$ km s^{-1}, $v_0 \in [170, 290]$ km s^{-1}, and $k \in [0.5, 3.5]$. The local DM density is also subject to observational uncertainties. Its value can be estimated from a set of experimental constraints that fix the local gravitational

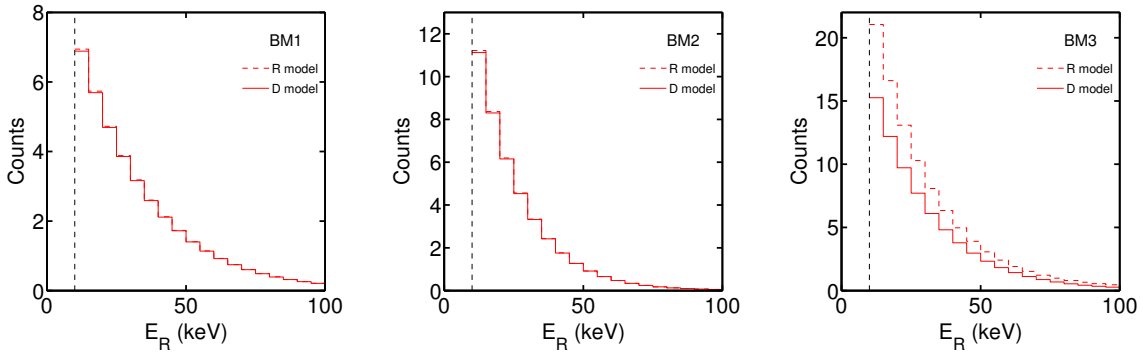

Figure 3.3: Predicted DM spectra for benchmarks BM1, BM2 and BM3 (from left to right) for the experimental setup described in the text. The solid and dashed red lines correspond to the predictions using the R- and D-model for the SDSF, respectively. The vertical dashed line indicates the energy threshold E_T.

potential of the Milky Way, with typical values ranging from 0.2 to 0.6 GeV cm^{-3} [315–318].

3.3.2 The spin-dependent structure functions

Regarding nuclear uncertainties, we have to separate into SI and SD form factors. On the one hand, the SI form factor is well determined from the charge density inside the nucleus, and thus it is expected to be well described by Eq. (3.14). Note that there might exist physical phenomena that are not accounted by this description, like quantum corrections of the density and spatial deformations. However, in the former case, the expected momentum transfer must be too high for the WIMP to access to the very inner region of the nucleus, and then it can be safely neglected in direct detection processes. The latter case has been argued to be relatively small [319]. On the other hand, the effect of variations in the SD form factors has not been previously addressed and constitutes the objective of this section.

As we have seen before, there exits an intrinsic difference between different calculations of the SDSF. Choosing germanium as a case study as in the previous case, we consider the two calculations, R- and D-models, for the SDSF of ^{73}Ge (the isotope that contributes to the SD cross-section) that were introduced earlier, performing the Bayesian inference for both SDSFs. Strictly speaking, we have to select one SDSF from which the simulated data for a given benchmark is generated and, then, one SDSF for the computation of

the likelihood in Eq. (3.22) at the moment of the scan. The two choices are independent, leaving us with four possibilities of combining the two SDSFs. In particular, we can either use the same (R- or D-) model for the generation of the simulated experimental data and for the parameter reconstruction or we can generate the data with one model and perform the reconstruction with the other one. This last possibility gives an idea on how sizable the mis-reconstruction of DM parameters can be if we use an incorrect model for the SDSF, this is, one different to the real one.

Now, let us address how this differences can affect the reconstruction of the DM parameters. For this purpose, we consider the the same phenomenological benchmark points, given in Table 3.1. Let us remind the reader the experimental setup chosen for the Germanium case studied: total exposure of $\epsilon = 300$ kg yr, the energy window for WIMP searches in the range $E_T = 10$ keV and $E_{max} = 100$ keV, and an energy independent background with a rate of 4×10^{-8} days^{-1} kg^{-1} keV^{-1} corresponding to the experimental setup ES$_1$. The simulated energy spectra for the three benchmark points can be seen in Fig. 3.3, where the solid red line corresponds to the results when the D-model is used and the dashed red line is obtained for the R-model. This will help the reader to understand the whole picture. Practically no difference is observed for benchmarks BM1 and BM2. This happens because for these two benchmark points the main contribution to the total detection rate is due to SI interactions. On the contrary, in BM3 the SD contribution is important and we observe how the predicted rate is significantly higher for the R-model than for the D-model. This is a consequence of the higher value of S_{11} for the R-model in the whole energy range (see Fig. 3.1).

The results for the first benchmark, BM1, are displayed in Fig. 3.4 (profile likelihood) and Fig. 3.5 (pdf). The four rows correspond to the possible combinations of SDSFs and we indicate which model is used in the generation of data and in the calculation of the likelihood in the scan. Comparing the distribution of the profile likelihood with that of the pdf, we can observe the effect of maximization versus marginalization. There are regions of the parameter space that are contained in the 99% confidence level contour of the profile likelihood which are however left out of the credible interval contours of the pdf. This happens because the good agreement with the data is produced only in a small volume of the three-dimensional parameter space and the integration in the third dimension decreases the corresponding value for the pdf [8].

[8] The contours in the two-dimensional plots for the profile likelihood look smoother than for the pdf. This occurs, in particular, when integrating over regions with an almost flat likelihood, where it is difficult to obtain uniform sampling. The resulting pdf can present unphysical structures. The fact that the background is included as a free parameter in the scan introduces additional fluctuations.

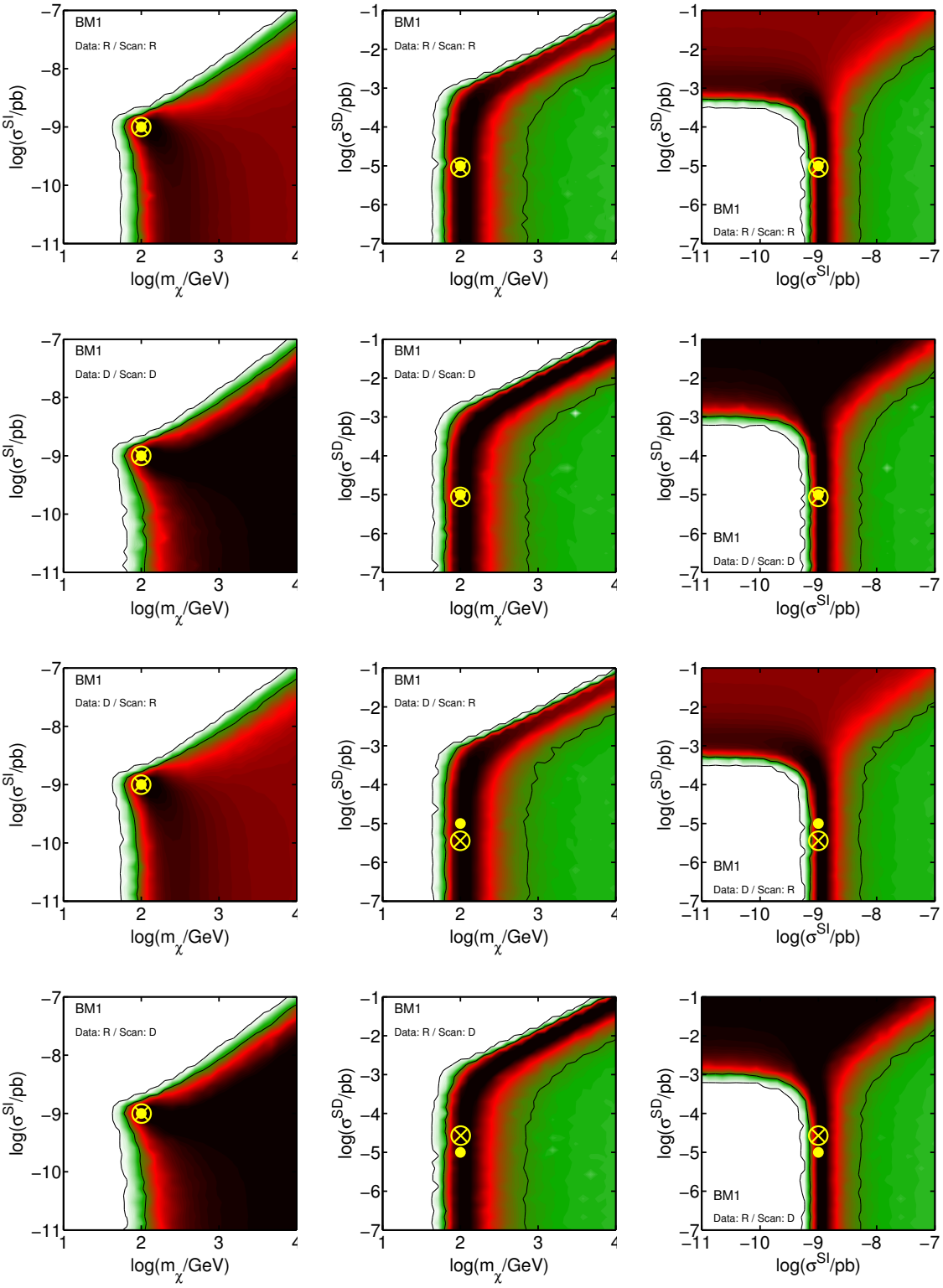

Figure 3.4: Two-dimensional profile likelihood for the reconstructed parameter space (m_χ, σ^{SI}, σ^{SD}) in BM1. In the first and second rows the model used for the SDSF in the simulated experimental data and in the scan for parameter reconstruction is the same. In the third and fourth rows the reverse is done (see the captions of the different panels). Inner and outer contours are 68% and 99% confidence levels, respectively. The yellow dot indicates the benchmark value, while the yellow encircled cross denotes the best-fit values.

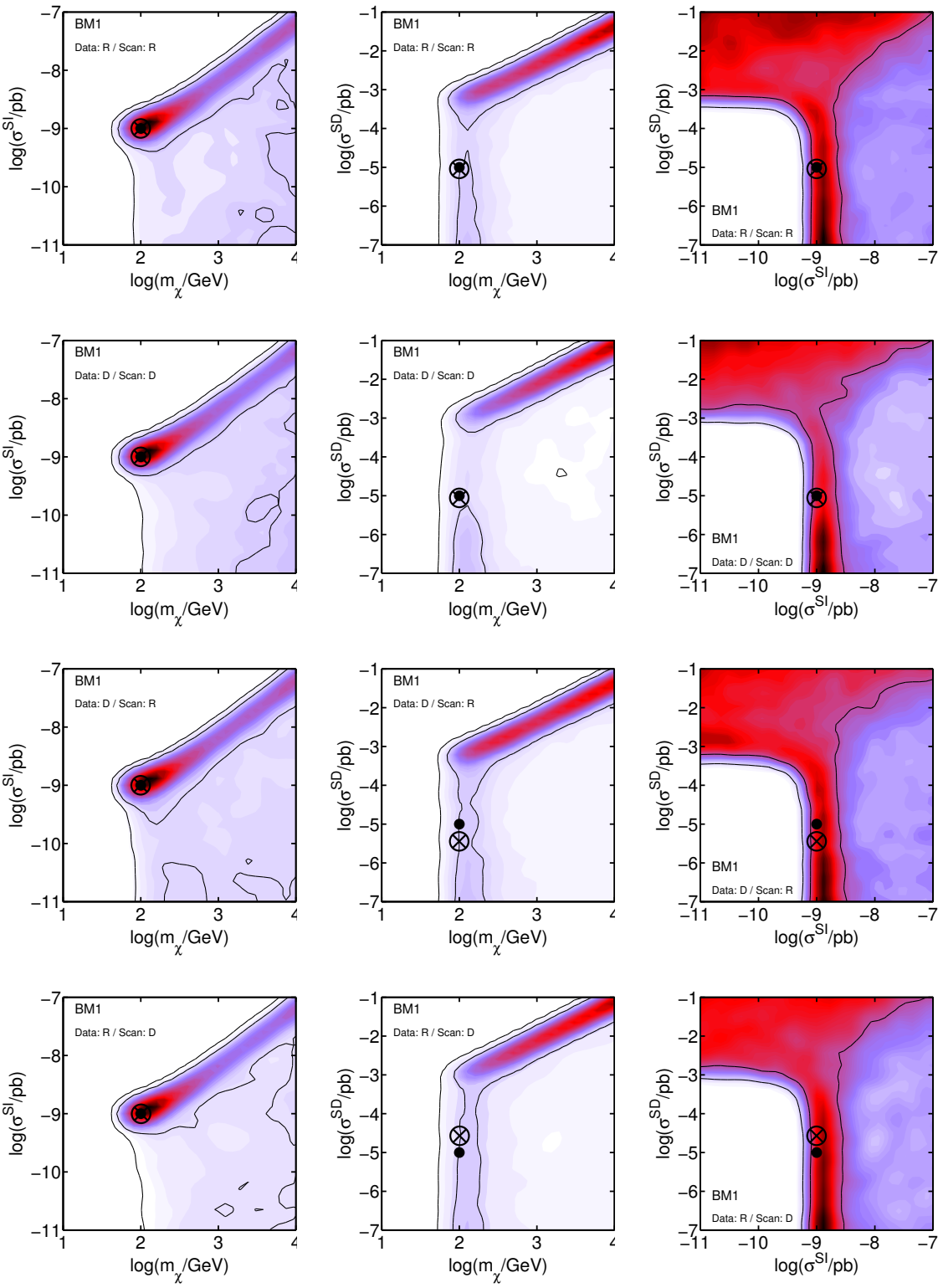

Figure 3.5: The same as in Fig. 3.4 but for the marginalized pdf.

The plots in the first column of Figs. 3.4 and 3.5 represent the reconstruction of the WIMP mass and SI cross-section, and they can therefore be compared with the leftmost plot of Fig. 3.2. We observe that σ^{SI} can now be arbitrarily small as long as the σ^{SD} is large enough to reproduce the observed DM rate and that the assumption $\sigma^{SD} = 0$ leads to over constrained contours. The SD form factor (that results for both R-and D-models of the SDSF) is steeper than the SI form factor. Thus, in principle using the information from the energy spectrum it would not be possible to properly fit BM1 data with only SD interactions (large values of the WIMP mass provide in this case a better fit, since they would correspond to a flatter energy spectrum). However, the number of recoils events in the high energy bins is too small to be sensitive to those differences.

Similarly, there is no lower bound for the SD cross-section. This is evidenced in the second column of both Figs. 3.4 and 3.5, where σ^{SD} is plotted as a function of the WIMP mass. As commented above, when trying to fit the energy spectrum of a point dominated by SI interactions (such as BM1) in terms of axial interactions, we get better results for large WIMP masses, due to the SDSF being steeper. The trend is evident in the pdf plots where larger values of masses are associated to a brighter pdf than lower masses, but the small number of events prevents this tendency to have any significant effect on the shape of the contours.

Finally, the degeneracy in the reconstruction of the SI and SD contributions for a given set of experimental data is clearly evidenced in the third column of Figs. 3.4 and 3.5, where σ^{SD} is plotted versus σ^{SI} and the resulting compatible regions show an "inverse L" pattern. The lower left corner of the plot is empty since both the SD and SI cross-section are too small to produce the simulated number of nuclear recoils, however, as stressed in the previous paragraphs, both σ^{SI} and σ^{SD} can be sizable if the WIMP mass is also large. These plots also show that for this particular benchmark point SD interactions provide the dominant contribution to the WIMP rate for $\sigma^{SD} \gtrsim 10^{-3}$ pb.

The interpretation of the results for the different rows allows us to determine to what extent the uncertainties in the SDSF affect the reconstruction of DM parameters. We stress again that for BM1 the differential event rate is dominated by SI interactions, thus we do not observe significant differences when changing the SDSF in the computation of the simulated recoils (see the left panel in Fig. 3.3). As a consequence, the plots on the first line are indistinguishable from those in the third line in Figs. 3.4 and 3.5. The same happens between the second and fourth lines. On the other hand, small differences arise when different SDSF are used in the computation of the likelihood. As already pointed out, the R- and D-models differ in the zero-momentum value, as well as in the slope. Indeed, we find that when the R-model is used in the scan to reconstruct the DM

parameters (rows one and three) the resulting σ^{SD} can be smaller than when the D-model is used (rows two and four). This happens because the SDSF of the R-model is always larger than in the D-model, so the correct number of recoils is reproduced with a slightly smaller σ^{SD}. Notice in particular how, although the best-fit value for σ^{SD} is correctly reconstructed when the same SDSF is used for generating and reconstructing the points (first two rows), there is a mismatch when different models are used. For example, if data are generated with the R-model and scanned using the D-model (third row), the best-fit value for σ^{SD} is lower (by about a factor two) than the actual one. Of course, the contrary occurs when data are generated with the D-model and scanned with the R-model (fourth row). This behaviour can be observed for the three benchmark points. Regarding the reconstructed WIMP mass, the distribution is similar when either the R- or D-model is used, although the latter slightly favours heavier WIMPs to compensate for the steeper slope.

Let us now consider the second benchmark, BM2. We proceed as in the previous case and show in Figs. 3.6 and 3.7 the corresponding reconstruction of the phenomenological parameters in terms of the profile likelihood and pdf, respectively. The difference between profile likelihood and pdf (due to the volume effect) is now more striking, especially regarding the SD component and WIMP mass. As we see in Fig. 3.6 the regions with a best likelihood lie around the correct mass but span many orders of magnitude in σ^{SD}. These regions, however, have a small volume and are disfavoured when the pdf is plotted. We should emphasize at this point that the information from both sources has a different statistical meaning and therefore this is no evidence of inconsistency.

As in the previous scenario, the detection rate in this benchmark point is due almost entirely to SI interactions, and there are no differences between the simulated data with either the R- or D- model for the SDSF (see the middle plot in Fig. 3.3). However, the number of events is now significantly larger and this allows a better determination of the slope of the recoil spectrum. This has two effects: first, the WIMP mass can be more accurately predicted (points with a heavy WIMP being now more disfavoured than in the previous example), and second leads to larger differences in the reconstruction of σ^{SD} when different models for the SDSF are used. Notice, for example, how heavy WIMPs are a viable possibility only if the contribution from the SD cross-section is sufficiently large (otherwise the shape of the spectrum is not flat enough). In spite of this, the degeneracy between σ^{SI} and σ^{SD} persists. The main difference in the reconstruction using the R- or D-model is again the value of the lowest σ^{SD} compatible with the data (when σ^{SI} is negligible), which is smaller for the R-model. Also the contours corresponding to the 68% confidence level extend towards larger WIMP masses in the case of the reconstruction

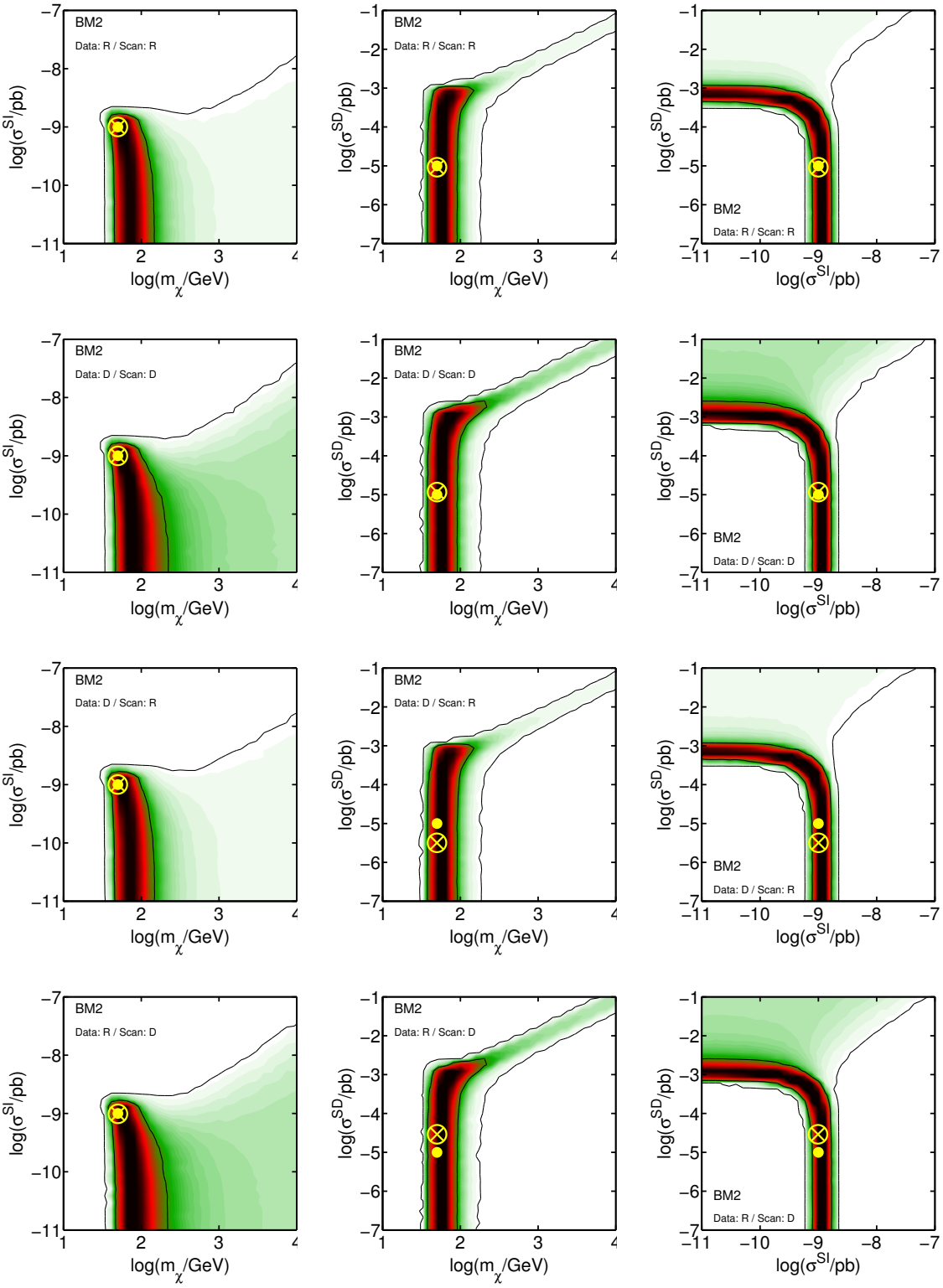

Figure 3.6: The same as in Fig. 3.4 but for benchmark BM2.

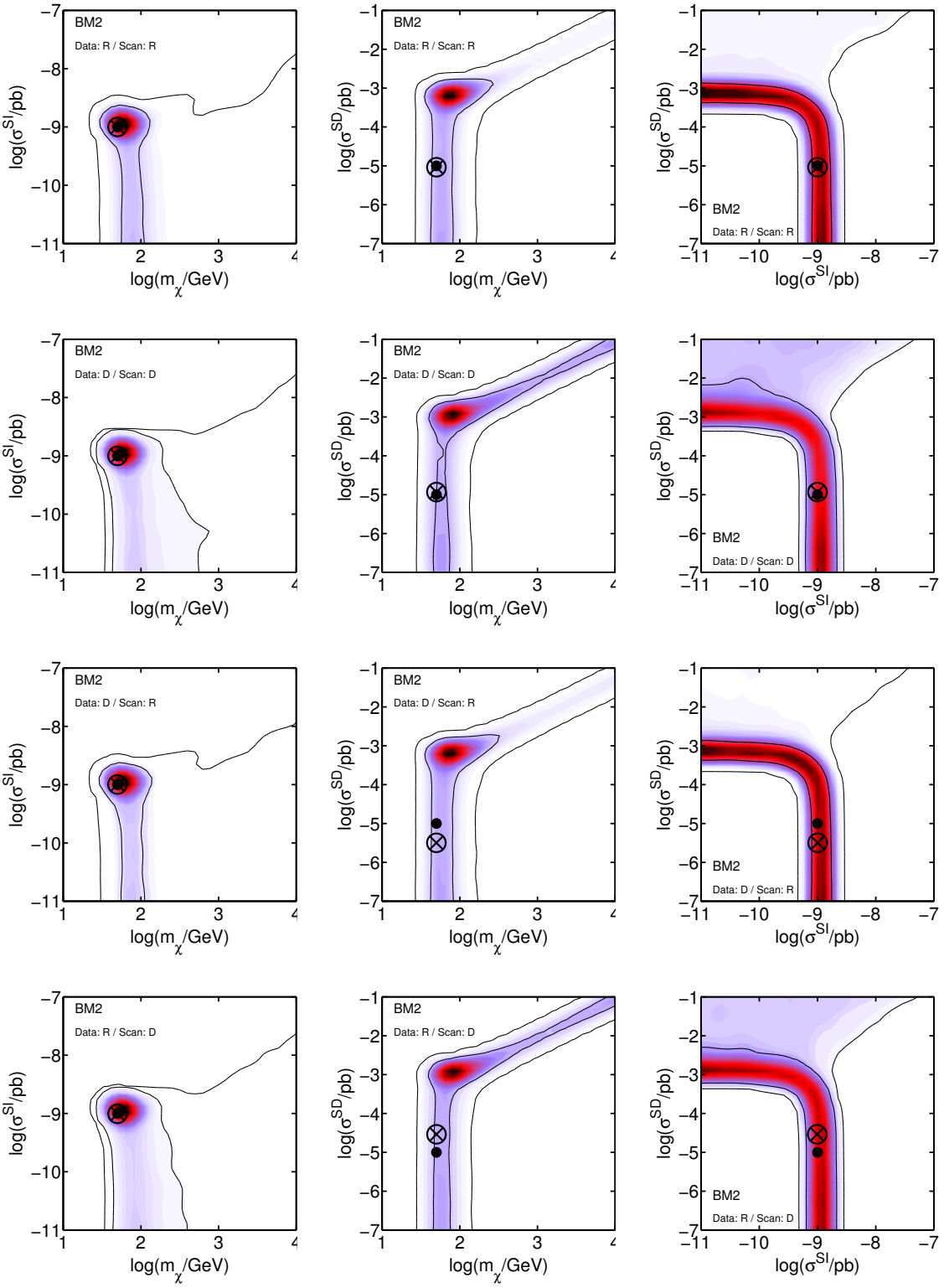

Figure 3.7: The same as in Fig. 3.5 but for the benchmark BM2.

using the D-model, in order to compensate for its greater steepness.

Let us finally address the third choice of benchmark point, BM3. Contrary to the previous two cases, the SD cross-section is a significant contribution to the total event rate, as we can see in Table 3.1 (although not entirely dominant). Therefore we expect that variations in the SDSF play a more important role in the reconstruction of the DM parameters. The results are displayed in Figs. 3.8 (profile likelihood) and 3.9 (pdf).

Ignoring the contribution from the SD term is not a good approximation in this scenario. Notice that the reconstruction of σ^{SI} in the limit when $\sigma^{SD} = 0$ is larger (by approximately a factor 2) than the nominal value of the BM3 point. This can be appreciated on the lower parts of the plots in the third column of both Figs. 3.8 and 3.9 (and is consistent with the results of Fig. 3.2). Moreover, the reconstructed value of σ^{SD} also varies, depending on whether the scan is performed with the R- or D-model of the SDSF, once more due to the different prediction in the zero-momentum value. As we already noted in the previous benchmark point, an effect in the reconstruction of the WIMP mass can also be appreciated between these two possibilities. The reconstruction performed with D-model favours heavier masses (in fact the 68% confidence level contours of the pdf are open for heavy WIMPs) than those obtained for R-model, since the D-model for the SDSF is steeper and this can be compensated with a larger value of the WIMP mass, which flattens the spectrum.

Parametrization of uncertainties in the spin-dependent structure functions

In the previous section we have shown that the choice of model for the SDSF has an important effect in the reconstruction of DM parameters. So far our conclusions are based on the comparison of the results obtained using two different computations for the SDSF of ^{73}Ge. In order to consider these effects in a more systematic way, in this section we attempt to include uncertainties in the SDSFs as part of the scan.

To do this, a description of the structure functions has to be found in terms of a relatively small number of parameters. We propose the use of the following family of functions, which reproduces non-trivial features in the shape of SDSFs,

$$S_{ij}(u) = N\left((1-\beta)e^{-\alpha u} + \beta\right) . \tag{3.26}$$

The parameter N acts as an overall normalization that allows us to fit the value at zero-momentum, β controls the height of a possible tail at large momentum and α provides the slope of the decreasing part in the the low-momentum regime[9].

[9]We have explicitly checked that although a five-parameters fit is able to reproduce better some

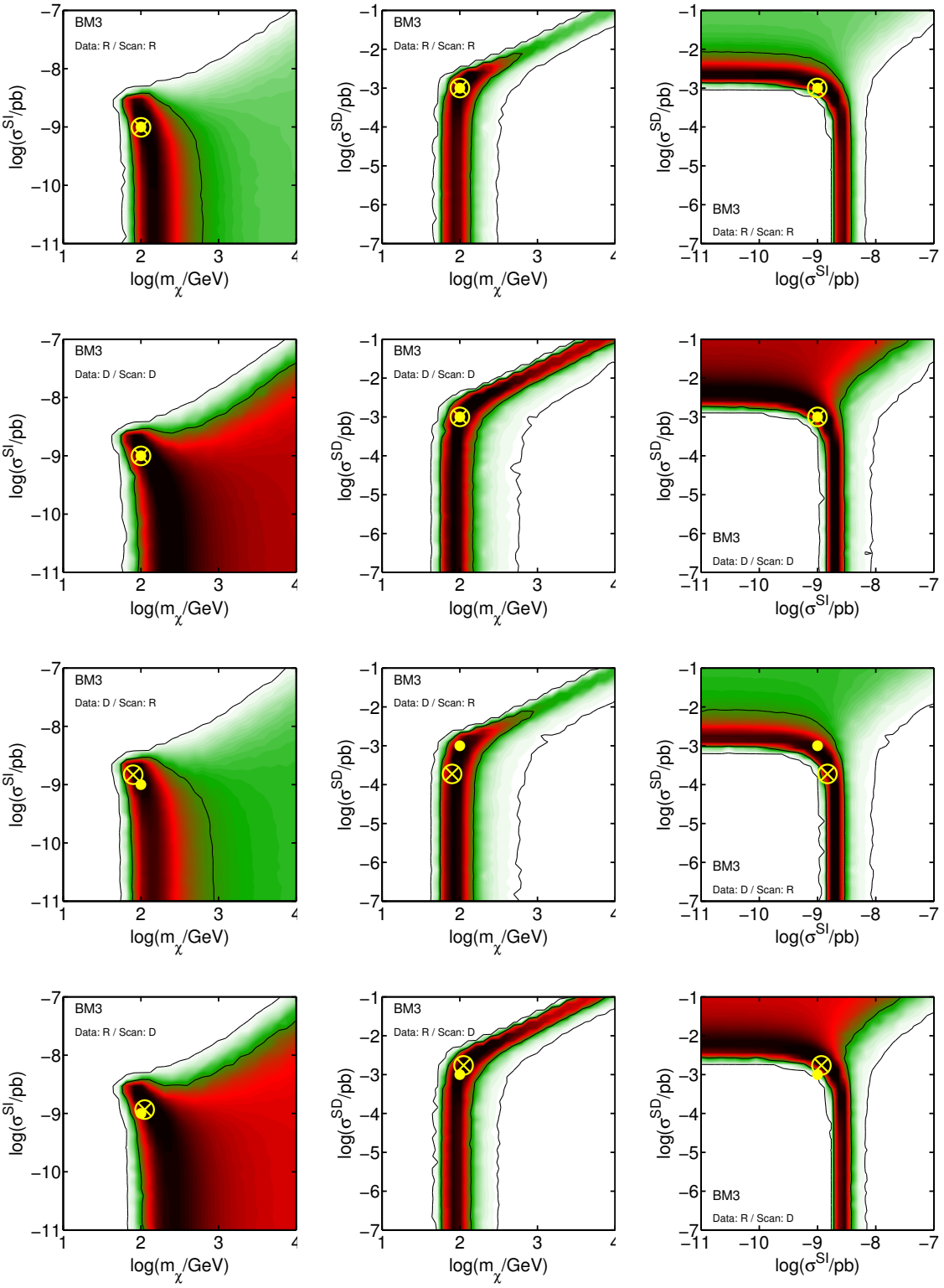

Figure 3.8: The same as in Fig. 3.4 but for benchmark BM3.

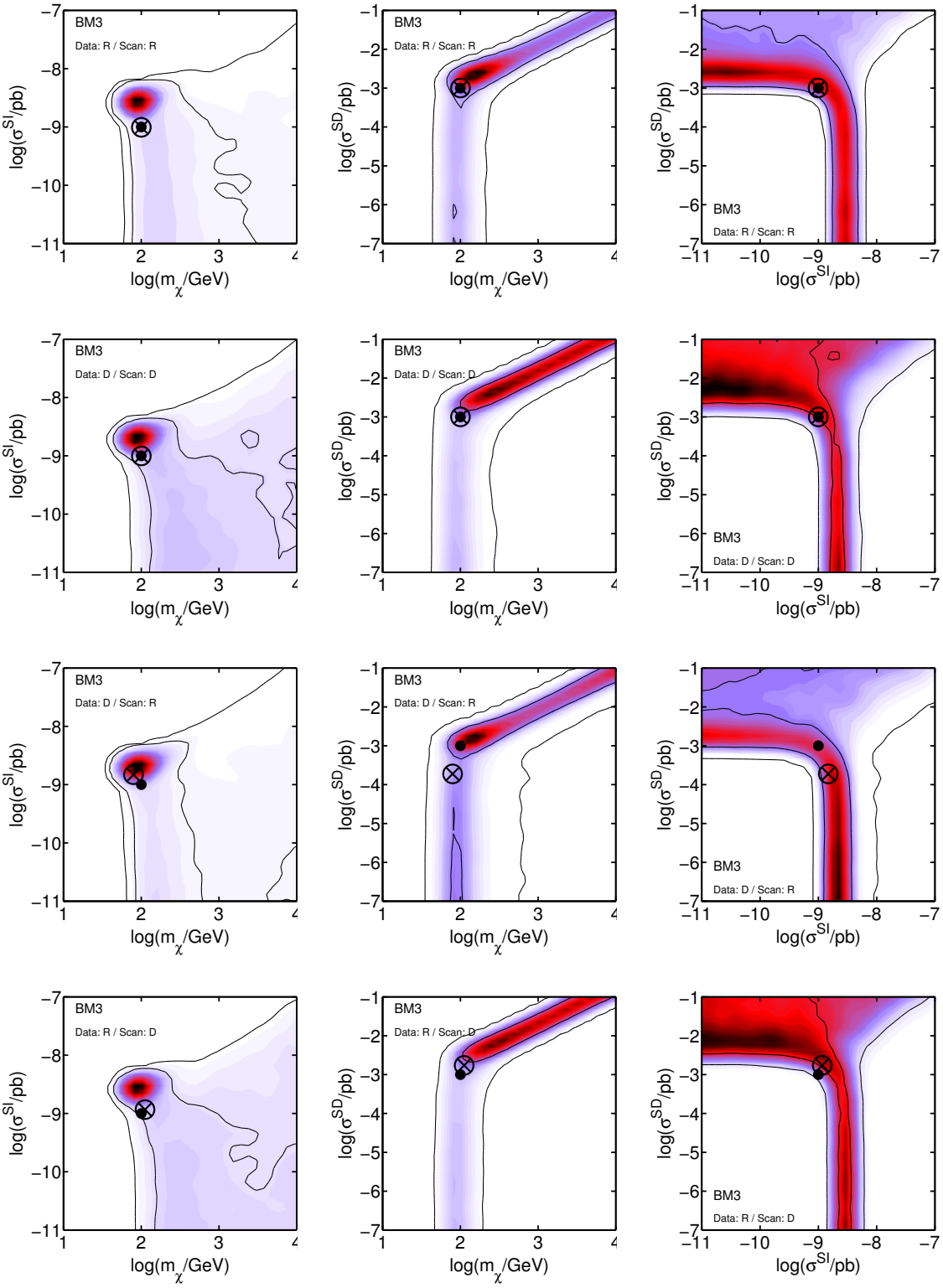

Figure 3.9: The same as in Fig. 3.5 but for the benchmark BM3.

Germanium detectors

In order to account for uncertainties in the SDSFs we have determined the maximum and minimum values of the three parameters N, α and β in Eq. (3.26) which define an area that contains the calculations of the R- and D-models. The range considered for $S_{11}(q)$ is the following: $N = [0.12, 0.21]$, $\beta = [0.020, 0.042]$, and $\alpha = [5.0, 6.0]$. For illustrative purposes we display in Fig. 3.1 the area (in blue) spanned by the family of curves that can be obtained by varying the above parameters in the given ranges. As we see, the R- and D-models correspond approximately to the extremes of the above intervals.

We repeat the scan for each benchmark extending the parameter space including N, α and β. The number of events $\{\lambda_i\}$ of the simulated experimental data are obtained assuming a SDSF with ($N = 0.16$, $\beta = 0.031$, $\alpha = 5.5$) which is located in the center of the above-mentioned ranges. Fig. 3.10 shows the resulting reconstructed contours in the profile likelihood of the DM properties in the three benchmark models. For comparison, we also indicate by means of blue lines the contours of the reconstructed DM parameters when nuclear uncertainties are not included and where the values of N, α, and β are fixed to their central values.

We observe that in the case of BM1 the differences with respect to the case with no uncertainties are very small. One can only observe a slight widening in the determination of σ^{SD} when uncertainties in the SDSF are included, but otherwise the reconstructed regions in the parameter space show very little differences. This occurs because in BM1 the DM candidate interacts mainly through SI interactions and it is thus fairly independent of the details of the SD term. Something similar occurs in the case of BM2, although the widening of the reconstruction of σ^{SD} is more evident now. Also the 68% confidence level curves corresponding to the WIMP mass extend to slightly larger values (notice that the logarithmic scale makes this effect more difficult to observe). Finally, it is in benchmark BM3 that the largest effects are found, since the SD contribution is larger. Once more, a widening in the determination of σ^{SD} is observed, which is now more evident in the 68% confidence level lines. Also the inclusion of uncertainties in the SDSF enlarge the contours for large WIMP masses.

Xenon detectors

For the sake of completeness, we have repeated the same procedure for Xenon detectors. Liquid Xenon based detectors are one of most common target materials used by direct

features of the SDSF in certain nuclei (e.g., ^{129}Xe and ^{131}Xe), this has a negligible impact in the reconstruction of DM parameters.

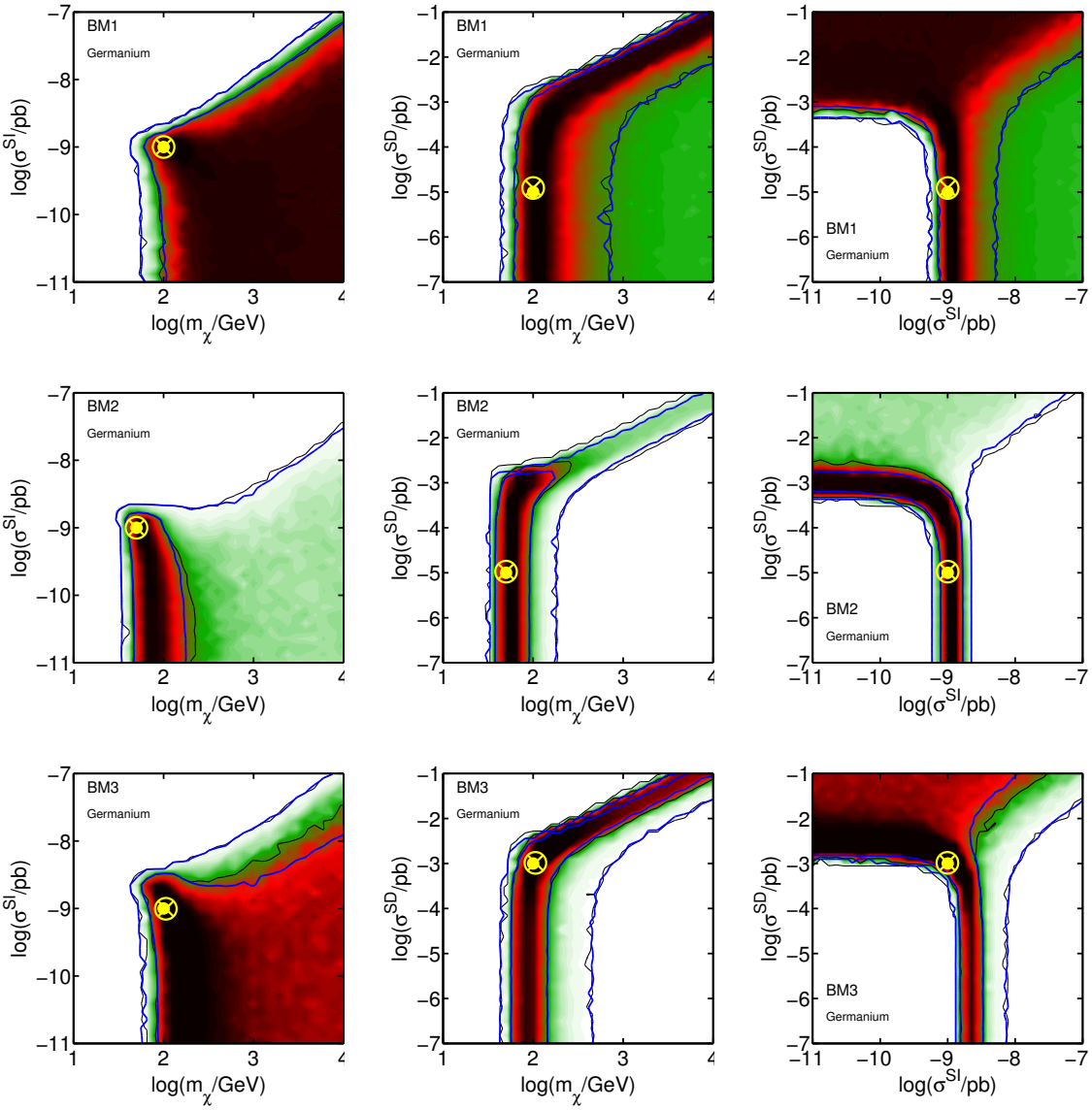

Figure 3.10: Two-dimensional profile likelihood for the reconstructed parameter space (m_χ, σ^{SI}, σ^{SD}) in benchmark models BM1, BM2, and BM3 (from top to bottom), including nuclear uncertainties in the SDSF through the three-parameter model introduced in Eq. (3.26). The inner and outer black contours are 68% and 99% confidence levels, respectively. The solid blue line corresponds to the case without uncertainties. The yellow dot indicates the benchmark value of the parameters, while the yellow encircled cross the position of the best-fit values.

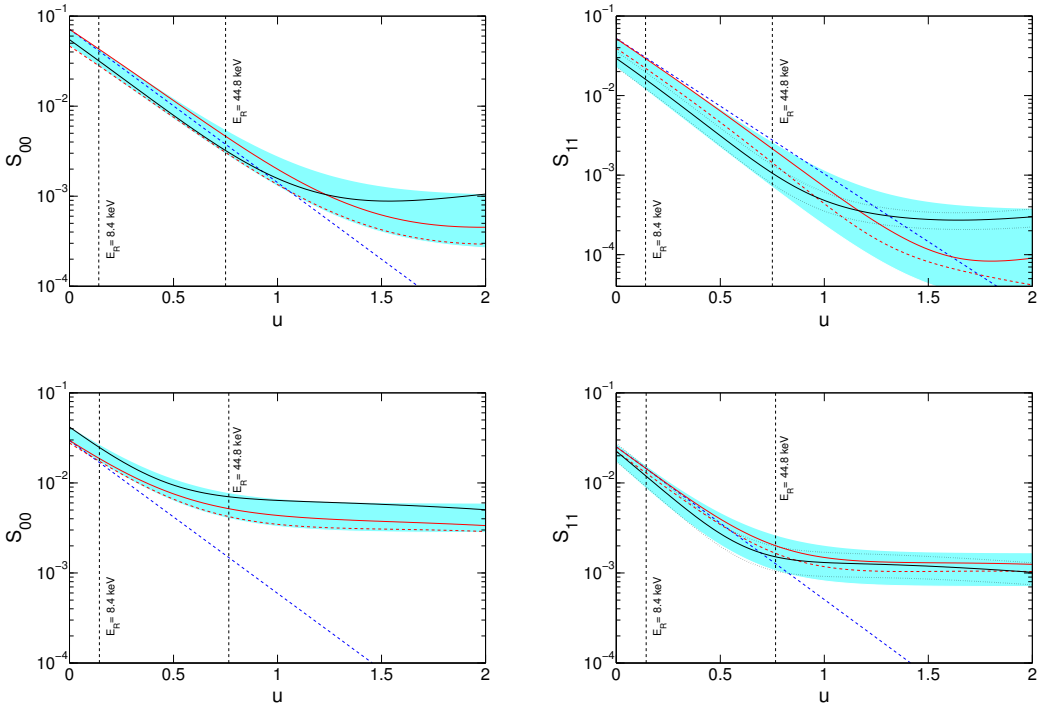

Figure 3.11: The same as in Fig. 3.1 but for the case of ^{129}Xe (top row) and ^{131}Xe (bottom row). The solid (dashed) red lines correspond to the ShM calculation using the Bonn A (Nijmegen II) potential [320]. The solid black line corresponds to the determination of Ref. [321] and the dotted black lines are the errors associated to it (the errors for S_{00} are negligible and are not shown). The dotted blue line indicates the gaussian approximation of Eq. (3.19). The blue region covers the area spanned by the family of curves in Eq. (3.26) with the parameters defined in the text. The vertical black dashed lines indicate the WIMP search window used in the analysis.

DM detection experiments. For instance, LUX and XENON collaborations use them, and have being able to place the most stringent constraints up to date (see Section 1.4.1 for more details). Natural Xenon contains two isotopes ^{129}Xe (with a 26.4% isotopic abundance) and ^{131}Xe (21.29%) which are sensitive to the SD component of the WIMP interaction (in particular to the SD cross-section of the WIMP with neutrons). As in the case of Germanium, we consider various parametrizations of the SD form factor for these nuclei from Ref. [320], in which the nuclear shell model was applied to two different potentials describing the nucleon-nucleon interaction, the Bonn A [322] and Nijmegen II [323] potentials. We also include a recent result from Ref. [321] in which the so called gcn5082 interaction [324] is used. Then we repeat the analysis of the previous

section modeling the uncertainties in the xenon SDSF by means of the parametrizations in Eq. (3.26), changing the values of the (N, α, β) parameters to define the area that contains the above-mentioned models for the SDSFs. In particular, for the S_{11} component in ^{129}Xe we consider $N = [0.029, 0.052]$, $\alpha = [4.2, 4.7]$, and $\beta = [1.0 \times 10^{-3}, 7 \times 10^{-3}]$. Similarly, in ^{131}Xe the ranges for S_{11} are $N = [0.017, 0.027]$, $\alpha = [4.3, 5.0]$, and $\beta = [4.2 \times 10^{-2}, 6.1 \times 10^{-2}]$. The various models for the SDSFs are represented in Fig. 3.11, together with the envelopes for S_{00} and S_{11} in both isotopes. We consider the same exposure as in the previous case ($\epsilon = 300$ kg yr) but the energy range of the WIMP detection window is now taken to be $E_R = [8.4, 44.8]$ keV, mimicking that of the XENON100 experiment.

Uncertainties in the SDSF for xenon have the same qualitative effect as in germanium. Namely, the predictions for the WIMP mass and the SD component of its scattering cross-section are affected. The resulting contours for the profile likelihood benchmarks BM1, BM2 and BM3 are displayed in Figs. 3.12. We can observe that the effect is similar in magnitude to the case of germanium (despite being a heavier nucleus than germanium, the isotopic abundance of the elements sensitive to the SD coupling is larger in xenon). Once more, deviations are larger for BM2 and BM3 than in BM1.

The inclusion of uncertainties on SDSF through the parametrization in Eq. (3.26) is a procedure that can be applied to other nuclei. In the case of germanium and xenon, the existence of different SDSF computations allowed us to define the ranges in which the three parameters of Eq. (3.26) are varied.

3.3.3 Comparison between nuclear and astrophysical uncertainties

To put our results in context, we need to compare the effects of nuclear uncertainties in the SDSF that we just discussed with those originating from astrophysical uncertainties in the parameters of the DM halo.

In Figs. 3.13 and 3.14 we represent the one-dimensional profile likelihood for the DM parameters (m_χ, σ^{SI}, σ^{SD}) for benchmarks BM1, BM2 and BM3 in the cases of a germanium and xenon detector, respectively. We display the reconstruction when no uncertainties are considered (blue line), when only nuclear uncertainties in the SDSF are included (solid black line) and when only astrophysical uncertainties are included (dashed black line). As noted before, the effect of nuclear uncertainties in the SDSF is more evident for BM3 than in BM1 and BM2 in both germanium and xenon, since in the latter the SD component is more important. The prediction for the WIMP mass is extended towards larger masses, and as we see for BM3 the effect cannot generally be neglected. Similarly,

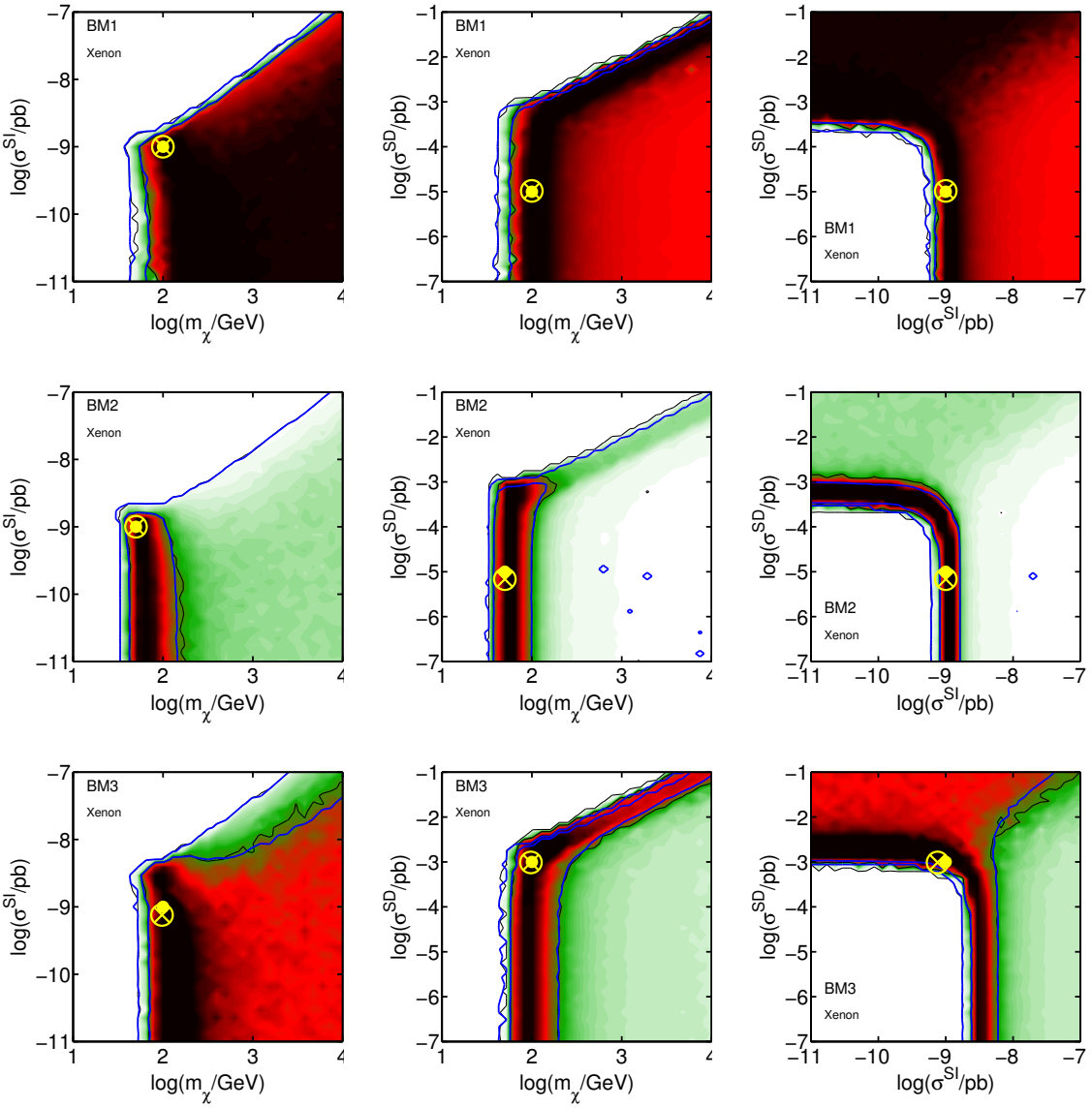

Figure 3.12: The same as in Fig. 3.10 but for the case of a xenon detector.

the predicted σ^{SD} can vary significantly. In BM3 the reconstruction extends towards larger values (in BM2 and BM1 the effect is smaller). On the other hand, astrophysical uncertainties affect both the reconstruction of the three DM parameters, m_χ, σ^{SI} and σ^{SD} and are equally relevant, irrespectively of whether the main contribution comes from the SD or SI component. We can see how nuclear uncertainties generally have a smaller effect than astrophysical ones, but they can be comparable in some benchmark scenarios, especially regarding the mass reconstruction. This is the case, e.g., of BM3 in a xenon detector.

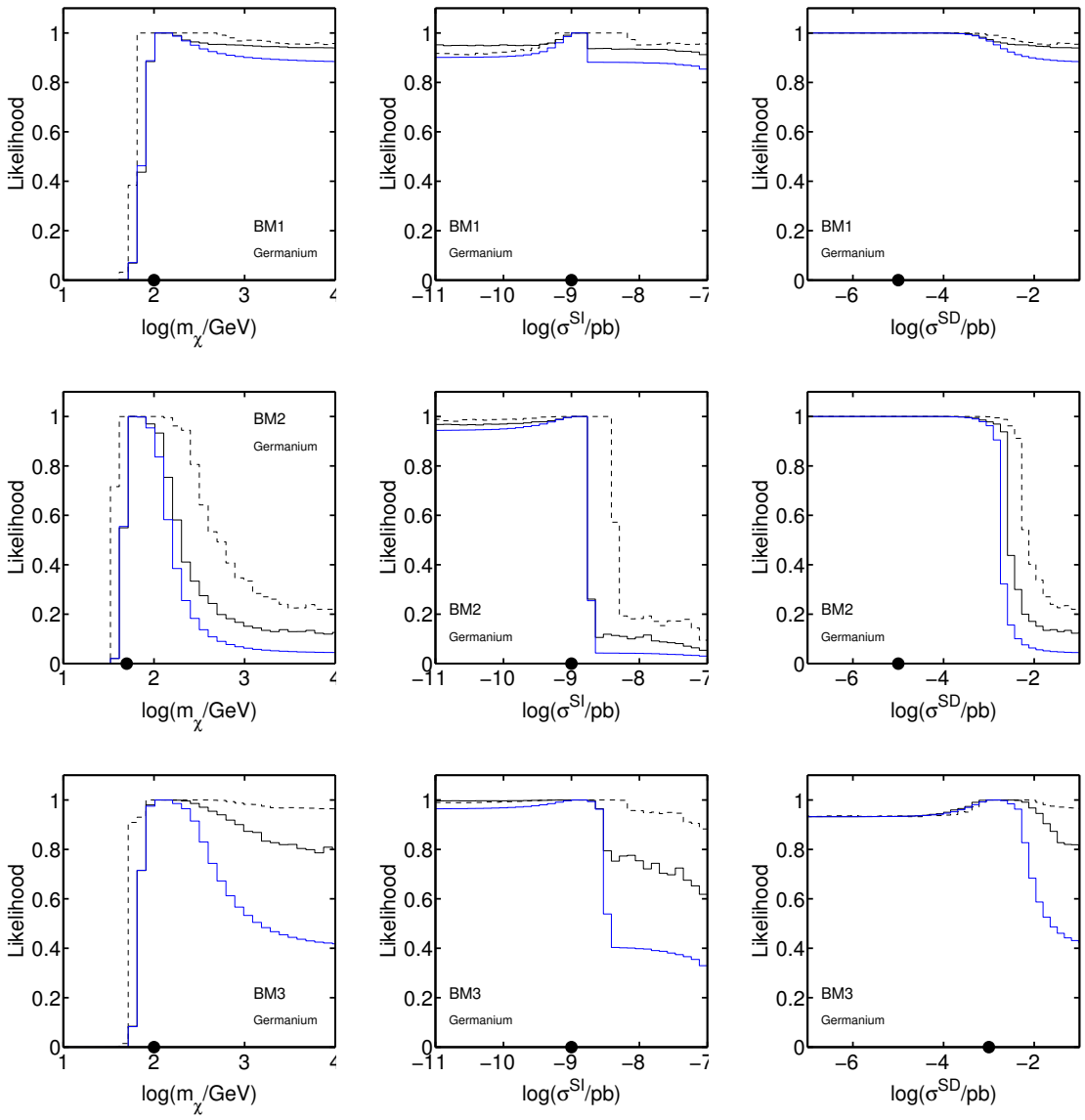

Figure 3.13: One-dimensional profile likelihood for m_χ, σ^{SI}, and σ^{SD} in BM1, BM2, and BM3 from top to bottom, respectively in the case of a germanium detector. The solid blue line corresponds to the case without uncertainties, the black solid line represents the results when nuclear uncertainties in the SDSF are included, and the dashed black line denotes the case when astrophysical uncertainties are included. The black dot represents the benchmark value of the parameters.

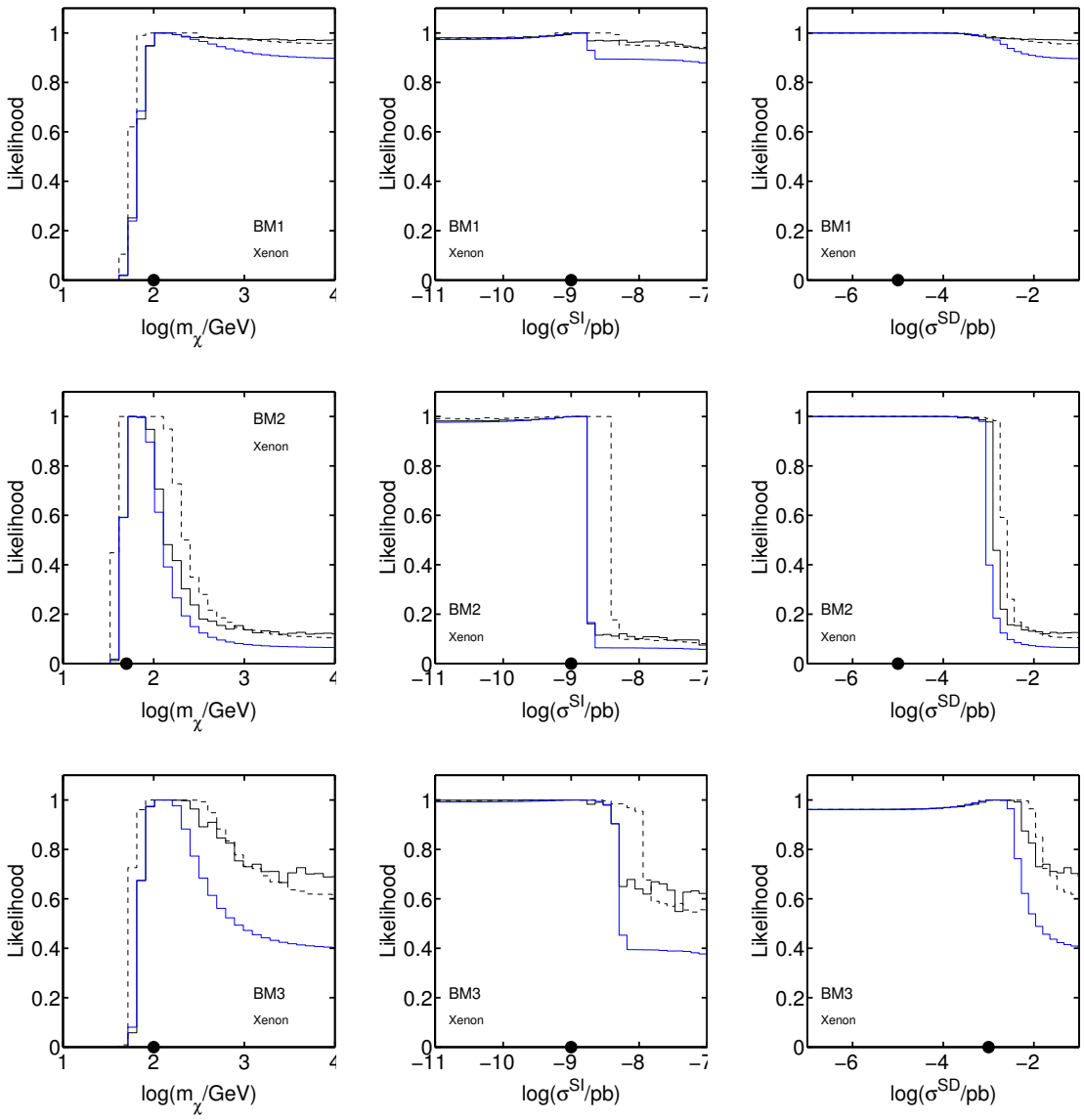

Figure 3.14: The same as in Fig. 3.13 but for the case of a xenon detector.

3.4 Complementarity of different targets

The detection of WIMP DM in more than one target could provide more information about the nature of these particles [278–281]. First, the consistency of the energy spectra measured by experiments using different target nuclei would confirm that the events were due to WIMP scattering (rather than, for instance, neutron background) [51]. Furthermore, part of the astrophysical uncertainty can potentially be removed, and in fact the comparison of the differential rates could be used to determine the moments of the

halo WIMP velocity distribution [312]. This is one of the motivations for the multitarget project EURECA.

The use of targets which are sensitive to both the SI and SD components of the WIMP-nucleus cross section might allow us to determine the WIMP couplings to matter in an unambiguous way, potentially discriminating between different DM models. In Ref. [278] this idea was put to the test by studying two of the possible targets of the COUPP experiment (C_3FI and C_4F_{10}). These two materials are sensitive to different combinations of SI and SD WIMP-nucleon couplings and it was shown that this information could be used, in the case of a hypothetical detection, to discriminate the LSP in the MSSM from the lightest Kaluza-Klein particle (LKP) in the universal extra dimension scenario. This is a direction that we explore in more detail in this work. In particular, *we investigate how well we can reconstruct the DM properties assuming an observation in more than one direct detection experiment and define complementarity as the capability of a combination of targets to determine these properties with a certain precision.*

Let us start by assuming a future detection of WIMP DM in a single direct detection experiment. As explained in the former subsection, the phenomenological parameters defining the WIMP DM particle can be extracted from the study of the total number of events and the differential recoil rate. However, one can easily understand that this procedure does not lead to an unique solution and the parameter space is indeed affected by degeneracies, since in general the experimental information is not enough to constrain the three unknown quantities.

To illustrate this more clearly, we note that the total number of WIMP recoil events can be expressed as

$$N = \mathcal{C}_{SI}\ \sigma^{SI} + \mathcal{C}_{SD}\ \left(2S_p\sqrt{\sigma^{SD,p}} + 2S_n\sqrt{\sigma^{SD,n}}\right)^2 , \tag{3.27}$$

where the coefficients $\mathcal{C}_{SI/SD}$ contain the integration in velocities and energies (and a dependence on the WIMP mass) for a given exposure,

$$\mathcal{C}_{SI} \equiv \int dE_R \int \left(\frac{\epsilon\,\rho_0 f(v)}{2\mu_n^2 m_\chi v}\right) A^2\, F_{SI}^2\, dv\,, \tag{3.28}$$

$$\mathcal{C}_{SD} \equiv \int dE_R \int \left(\frac{\epsilon\,\rho_0 f(v)}{2\mu_n^2 m_\chi v}\right) \left(\frac{J+1}{3J}\right) F_{SD}^2\, dv\,. \tag{3.29}$$

Notice that all the dependence on the astrophysical halo parameters and most of the dependence on experimental setup, such as target material, energy threshold, energy resolution, are contained in them (there is also a dependence on the target material in S_p and S_n). As previously stated, we particularise our analysis to the specific case

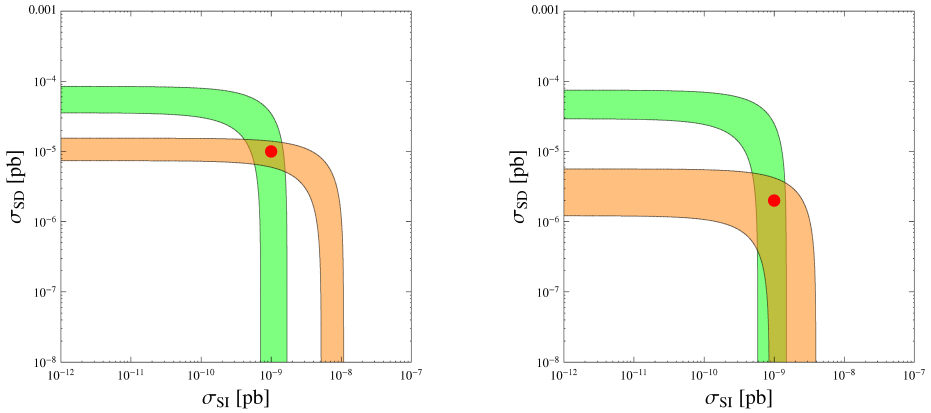

Figure 3.15: Schematic view of the reconstruction of σ^{SI} and σ^{SD} from the observed number of WIMP recoil events in two different DM experiments (orange and green shaded areas, respectively). Even assuming a precise measurement of the WIMP mass, a single experiment cannot unambiguously determine the SD and SI cross sections. The detection on a second experiment, however, provides extra information that may allow to further constrain these two parameters. On the left hand-side we display an example in which experiments are complementary, i.e. they intersect leaving only a closed region compatible with both data sets. On the right hand-side we illustrate the case in which the two experiments are not totally complementary, since the region where they overlap is not bounded from below. The nominal WIMP parameters for each case are shown with a dot.

$\sigma^{SD,p} = \sigma^{SD,n}$ and therefore Eq. (3.27) contains three unknown quantities: the SI and SD components of the WIMP scattering cross section and its mass. Even if we assume that the WIMP mass can be determined independently with a reasonable accuracy, we are still left with two parameters to reconstruct. Thus, given only one experimental result, the same number of events can be accounted for by different combinations of SI and SD couplings. This is illustrated in Fig. 3.15, where each of the color shaded areas corresponds schematically to the region in the $(\sigma^{SI}, \sigma^{SD})$ plane that is compatible with the detection of a certain number of recoils in one particular detector. The detection of a WIMP in a second experiment with a different target can provide complementary information with which this degeneracy can be partially resolved, since changing target implies that also the $\mathcal{C}_{SI/SD}$ coefficients in Eq. (3.27) are different.

Fig. 3.15 depicts two possible situations. On the left hand-side we consider an example in which two targets are complementary and allow a good reconstruction of both the SD and SI couplings. This is the case, for example, if one target is mostly sensitive to SI interactions and the other one to SD ones. It can be seen that the region compat-

ible with both experiments is closed, a situation that we call complementary. On the right hand-side we show another case in which complementarity is not present since the overlapping region is unbounded from below. This is generically the case when the two targets are mostly sensitive to the SI coupling, and therefore, is a very common situation. In particular, as we will argue in Section 3.4.1, this could happen when combining signals from germanium and xenon detectors. Notice that this example suggests that in such a case the SI coupling can be relatively well reconstructed but only an upper bound can be derived for the SD one.

The extension of the overlapping region is a result of the various uncertainties. First of all, there is an obvious statistical component: if the detected number of events is small, it is subject to large statistical fluctuations and therefore the reconstruction of parameters is poor. Thus, the larger the exposure of the experiment (or alternatively, the larger the scattering cross section), the narrower the reconstructed band is. On top of this, astrophysical and nuclear uncertainties further contribute to worsening the reconstruction. This is clearly a limiting factor that needs a careful implementation in order to describe a realistic experimental situation. Finally, in the examples above we have assumed that the mass of the WIMP is known, but in the following the WIMP mass is part of the parameter space we scan over and it will be determined along with the rest of the parameters.

3.4.1 The big three

Two technologies which have been very successfully applied to direct DM searches are semiconductor cryogenic detectors (e.g., the germanium detectors of CDMS and EDELWEISS) and noble liquid detectors (a xenon target in the case of XENON10, XENON100 and LUX). Both techniques show great potential and there are plans to extend target masses up to several hundred kilograms or even one ton within the next years (e.g., SuperCDMS, EURECA, XENON1T and LZ). It is therefore conceivable that a future WIMP observation could take place in any of these targets. Let us therefore start by contemplating that possibility and assessing how well the DM properties can be reconstructed in germanium and xenon targets for different WIMP scenarios. For concreteness we consider experimental setup ES_1 (see Appendix 3).

We consider the set of WIMP benchmark points from Table 3.2, which take into account various mass choices and include cases in which either the SI or the SD contribution dominates the detection rate. Notice, that two out of the four benchmarks are the same than in the previous section, namely M-SI corresponds to BM1 and L-SI to BM2. Again,

Benchmark Point	m_χ (GeV)	σ^{SI} (pb)	σ^{SD} (pb)	N_{Ge}	N_{Xe}	$N_{\mathrm{C_3FI}}$
M-SI	100	10^{-9}	10^{-5}	37 (37)	54 (52)	42 (32)
L-SI	50	10^{-9}	10^{-5}	40 (40)	64 (62)	49 (35)
L-SD	50	4×10^{-10}	6×10^{-4}	44 (16)	93 (14)	560 (16)
VL-SI	15	10^{-8}	10^{-5}	29 (29)	28 (28)	15 (9)

Table 3.2: Set of benchmark points used in this thesis. We consider three regimes for the WIMP mass, very light (VL), light (L) and medium (M). The label SI or SD in each benchmark indicates which component of the scattering cross section dominates the detection rate in germanium and xenon targets. For reference we also include the expected number of WIMP recoil events in Ge, Xe and C_3FI for an exposure $\epsilon = 300$ kg yr, where the number in parenthesis corresponds to the contribution from only SI interactions.

we simulate the expected differential spectrum by considering a 1 ton experiment with a 30% live time operating for a year, i.e. a total exposure of $\epsilon = 300$ kg yr. The expected DM signal is computed as described in the previous section, and implemented in the scan as experimental information, in the attempt to reconstruct the DM phenomenological parameters.

Figure 3.16 shows the PL of the three phenomenological parameters m_χ, σ^{SI}, and σ^{SD} projected onto the three two-dimensional planes (σ^{SI}, m_χ), (σ^{SD}, m_χ), and (σ^{SD}, σ^{SI}), for a DM particle corresponding to benchmark M-SI. The first row shows the determination of parameters after a detection in a germanium detector alone. The yellow dot indicates the nominal value of the benchmark point and the circled cross the best-fit point. Consistently with the previous discussion, we observe a large degeneracy in the three parameters, with a significant uncertainty in both components of the cross section and the mass. As already pointed out in the previous section (see also [299]), the reconstructed values of the SD or SI cross section show no upper bound for large values of the WIMP mass. Consequently, the 68% confidence level contours are not closed, but extend beyond the limits of the plots. Moreover, the scan does not manage to reconstruct the correct value of the σ^{SD}.

The second row in Fig. 3.16 corresponds to the combination of data from germanium and xenon detectors. An improvement is visible since large regions of the parameter space are associated with a smaller value of the PL and the best-fit point is now closer to the nominal value. However, both the shape and the area of the outer contours remain very similar to the case with only germanium.

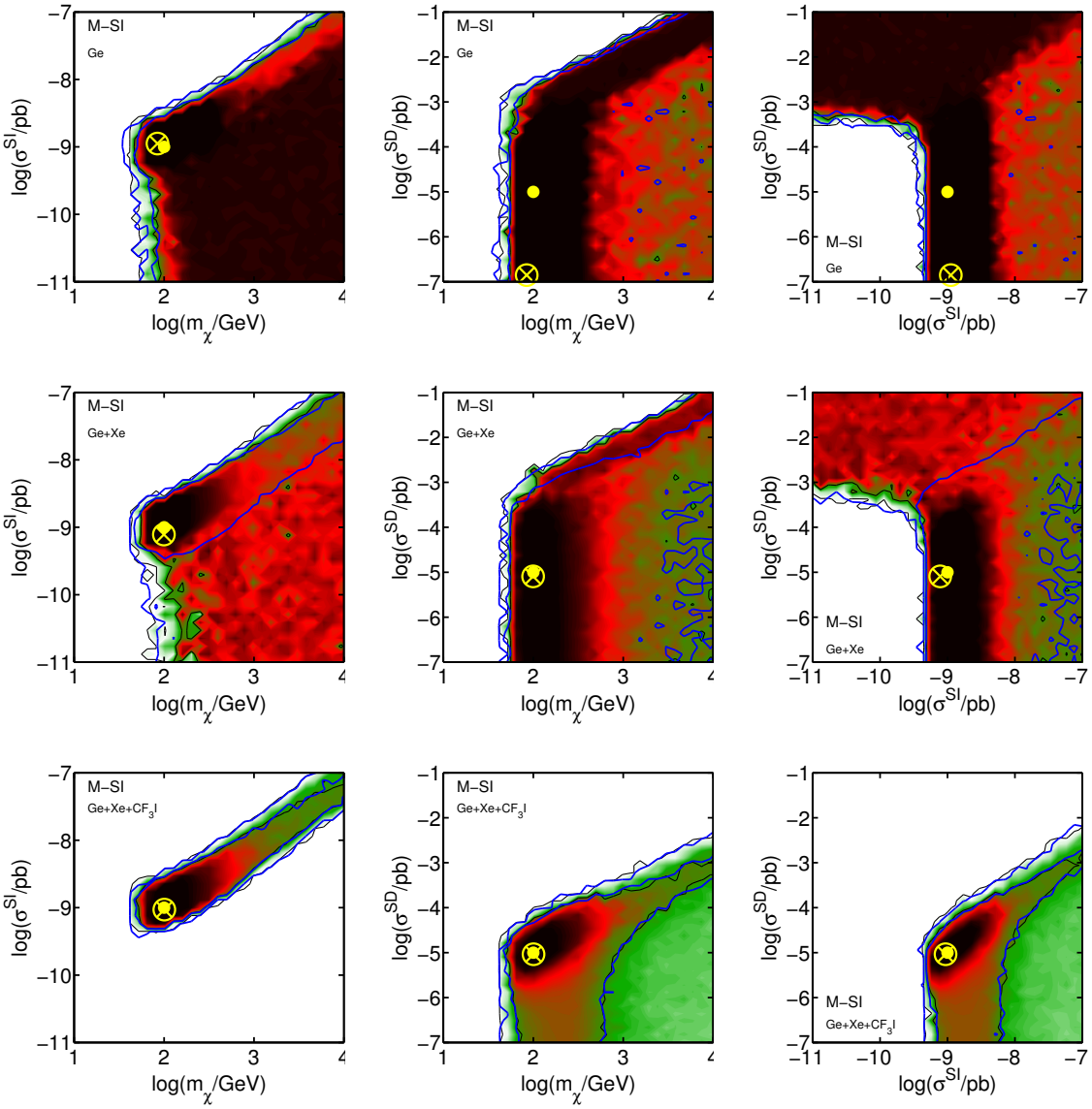

Figure 3.16: Profile likelihood for the DM parameters in the (σ^{SI}, m_χ), (σ^{SD}, m_χ), and (σ^{SD}, σ^{SI}) planes for the benchmark point M-SI. The plots in the first row are obtained assuming a detection only in a Ge experiment, the second row shows the combination between Ge and Xe targets, and the third row corresponds to Ge+Xe+C_3FI. From the inside out, contours are 68% and 99% confidence intervals. The yellow dot represents the nominal values for the benchmark point and the yellow circled cross the best-fit point. The coloured regions bounded by black contours correspond to the case where nuclear uncertainties are included, whereas the blue empty contours are the results of a scan with fixed nuclear parameters.

Finally, the third row of Fig. 3.16 considers the combination with data from a hypothetical 1 ton version of COUPP. Since the target material, C_3FI, incorporates fluorine (which has a large nuclear spin) it has a larger sensitivity to the SD component. Thus, the allowed region is drastically reduced. In particular, the solutions with large SD cross section are not compatible anymore with the data, a more stringent upper limit on σ^{SD} is produced (at least for the 99% confidence region), which translates into a lower limit on σ^{SI}. Note that the experimental setup in COUPP does not allow the recoil energy to be measured and therefore does not provide more information on the WIMP mass.

Blue contours in Fig. 3.16 indicate the 68% and 99% confidence regions for the PL of scans performed without including the nuclear uncertainties associated with the SD structure factors and fixing their parameters to the central value of the range considered in our scans. We observe that the effect of these uncertainties can greatly affect the reconstruction of parameters, significantly enlarging the areas compatible with the observation in two experiments (see the second row of Fig. 3.16).

These results depend on the benchmark point, but the general conclusion on how different experiments combine remains valid. When the number of events increases, either because the scattering cross section is larger or because the WIMP mass is closer to the optimal sensitivity for these targets, the determination of the DM parameters is better. For example, Fig. 3.17 represents the hypothetical detection of a WIMP with properties determined by case L-SI in Table 3.2, in which $m_\chi = 50$ GeV. Since the number of recoils is higher, the 68% and 99% contours in the PL are smaller. In particular, using only data from Ge and Xe detectors there is a good reconstruction of the WIMP mass, as well as a significant improvement in the determination of σ^{SI}. Notice that even then, the SD cross section is not properly determined, as only an upper bound is obtained. As before, after the inclusion of C_3FI data, the SD cross section is better reconstructed (i.e. lower and upper limits are obtained) at the 68% confidence level, with the upper limit being valid also at the 99% confidence level. A good reconstruction of σ^{SD} has also the consequence of providing a lower bound for σ^{SI} and reducing the uncertainty on m_χ. Both quantities are now determined with an uncertainty of approximately one order of magnitude, an extremely interesting scenario made possible by the nice interplay between the three experiments.

The importance of nuclear uncertainties is evidenced when we consider the combination of the signal in Ge and Xe. For a fixed SD form factor it is not possible to provide a good fit to both signals with a SD-dominated energy spectrum. This produces an upper limit on σ^{SD}. On the other hand, when also the signal in CF_3I is included, selecting only points with a SI-dominated rate, the details of the SD form factor become irrelevant

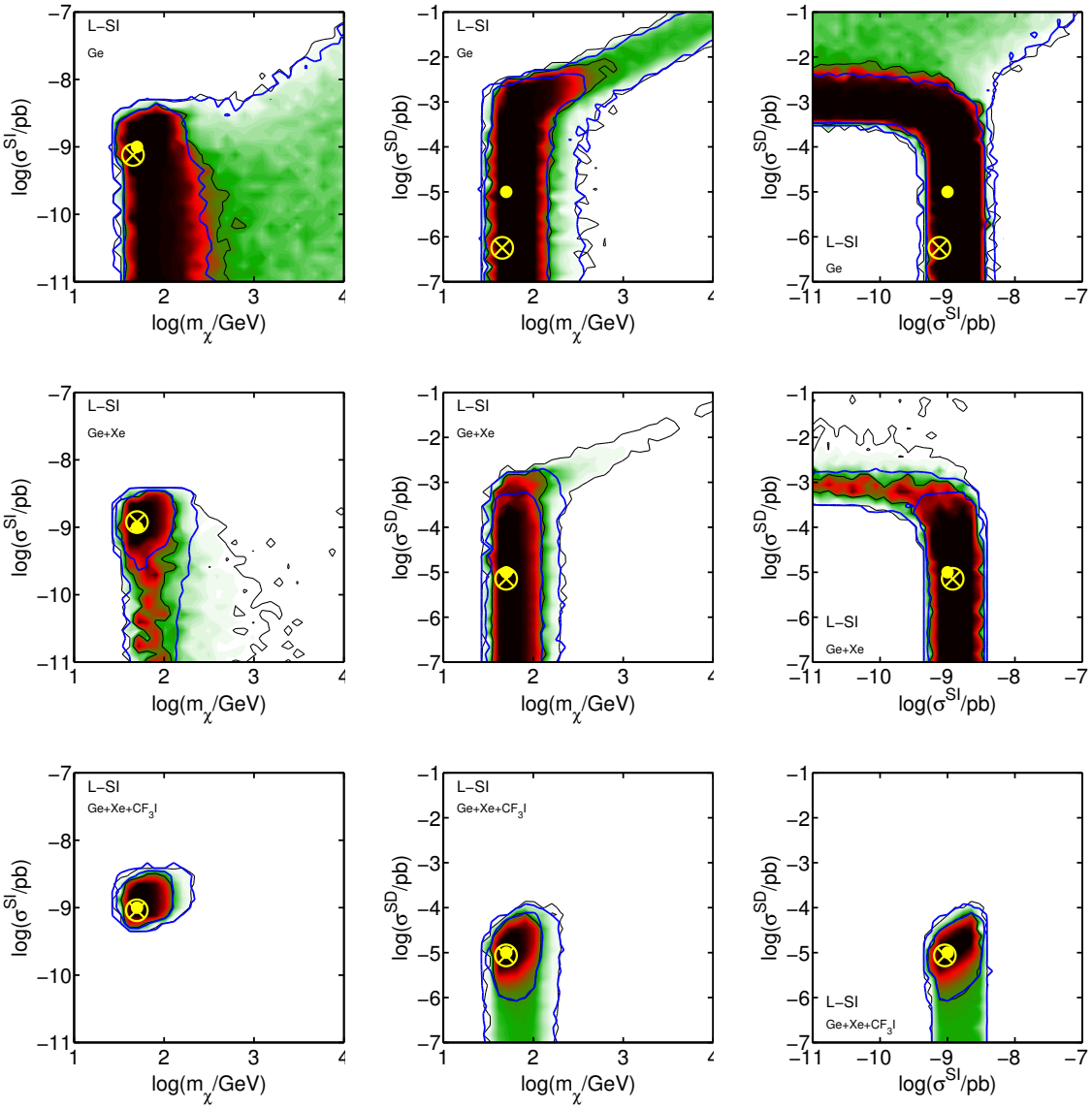

Figure 3.17: The same as in Fig. 3.16, but for the benchmark point L-SI.

again and we see no difference between the blue and the black contours.

The last example considered is given in Fig. 3.18, corresponding to the case L-SD, in which the SD contribution to the number of DM events dominates. As in the previous cases, the combination of data from Ge and Xe is not enough to determine the SI and SD contributions (only a combination of both). Including CF_3I data has the effect of excluding small values of σ^{SD} (contrary to what happened for M-SI and L-SI). Moreover, small SI cross sections also produce a slightly worse fit to the data now. Thus comple-

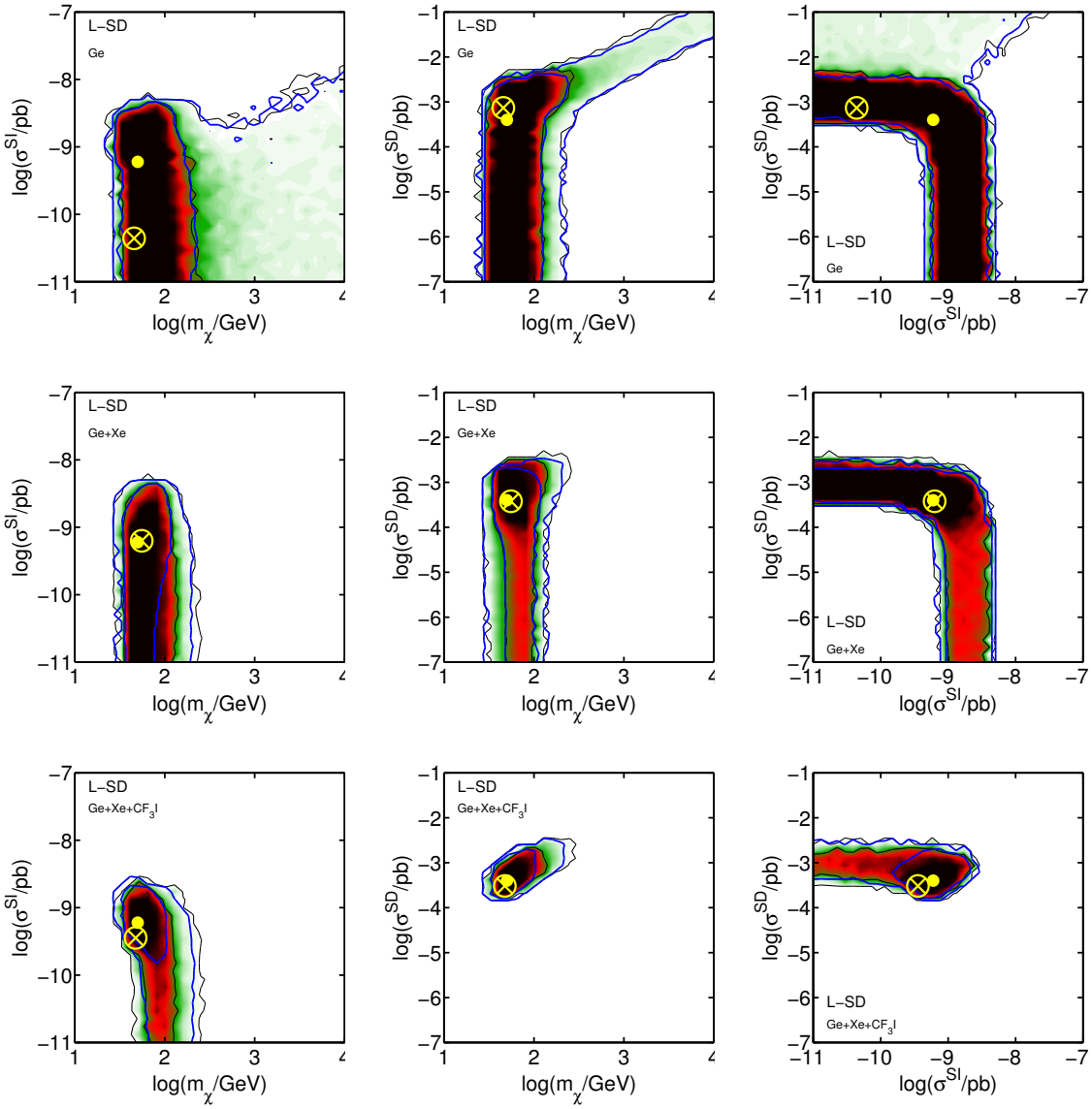

Figure 3.18: The same as in Fig. 3.16, but for the benchmark point L-SD.

mentarity could be obtained for the 68% confidence region but only if we do not include nuclear uncertainties.

To sum up, although 1 ton experiments based on germanium or xenon have an excellent discovery potential for WIMP DM, they are mostly sensitive to the SI part of the WIMP-nucleus interaction. As a consequence, the combination of data from both detectors would generally not allow the determination of the DM parameters in an unambiguous way. If we look for complementary information, the obvious alternative is a target that

is sensitive to the SD component. CF_3I is certainly a good choice in this respect, since it incorporates fluorine ^{19}F, which has an unpaired proton and a large nuclear nuclear spin J. However, COUPP would not provide information about the recoil spectrum, which limits its complementarity capability. Even considering a 1 ton phase the degeneracies in the reconstruction of DM parameters would not be completely removed.

3.4.2 Complementarity of bolometric targets

A much more appealing situation could come from an experiment which is sensitive to the SD WIMP-nucleon interaction and in which the energy spectrum can be accurately determined, as well. This can be the case of certain scintillating bolometric targets that have been developed and studied by the ROSEBUD and CRESST collaborations and are planned or could be used by the EURECA project. We will consider the following targets:

- $CaWO_4$: This is a material which has been tested and used as a WIMP target by ROSEBUD and it is the current target in CRESST [102]. The sensitivity to SD interactions comes from tungsten, for which the isotope ^{183}W (with a natural isotopic abundance of 14.3%) has an unpaired neutron. However, tungsten is a very heavy material and therefore it is mostly sensitive to the SI component of the WIMP interactions. For this reason, we should expect compatibility with experiments based on Ge or Xe to be limited. Notice that our analysis does not include the possibility (shown by CRESST) of disentangling O, Ca and W nuclear recoils.

- Al_2O_3: Sapphire is a very promising DM target because it is sensitive to low mass WIMPs (Al and O are both light nuclei). It is also sensitive to SD interactions (^{27}Al has 100% isotopic abundance and $J = 5/2$) and recent tests indicate very high light yields [325, 326] and a particle discrimination threshold below 10 keV seems to be possible [325].

- LiF: This target is also sensitive to low mass and SD interactions (Li and F are light nuclei, ^{19}F has 100% isotopic abundance and $J = 1/2$, ^{7}Li has 92.5% isotopic abundance and $J = 3/2$). However, up to now, low particle discrimination thresholds have not been obtained and more R&D is needed on this target to be used for DM searches.

In this section we determine the conditions under which the different scintillating bolometric targets can provide good complementary information when combined with

Benchmark Point	m_χ (GeV)	σ^{SI} (pb)	σ^{SD} (pb)	N_{CaWO_4}	$N_{Al_2O_3}$	N_{LiF}
M-SI	100	10^{-9}	10^{-5}	27 (27)	14 (4)	25 (2)
L-SI	50	10^{-9}	10^{-5}	30 (30)	17 (5)	35 (2)
L-SD	50	6×10^{-10}	4×10^{-4}	20 (18)	505 (3)	1295 (1)
VL-SI	15	10^{-8}	10^{-5}	8 (8)	23 (18)	29 (11)

Table 3.3: Total recoil events for the set of benchmark points expected on each of the bolometric targets considered in this work for an exposure $\epsilon = 300$ kg yr.

germanium and xenon detectors. As in the previous section, for each benchmark and for each detector target, we simulate the number of recoils predicted in the different energy bins. This constitutes our set of observables. Then, we perform a scan on the three-dimensional parameter space (m_χ, σ^{SI}, σ^{SD}) and apply the Bayesian inference method to determine the reconstruction of these quantities. Astrophysical and nuclear uncertainties are included as described above.

We start by considering the same exposure for all the experiments, $\epsilon = 300$ kg yr, and study the same benchmark scenarios as in the previous section. In Table 3.3 we indicate the number of recoil events for each of the bolometric targets. Initially we assume zero background for the three targets and postpone the discussion about the influence of the background level to the end of this section. In Figs. 3.19, 3.20, 3.21 and 3.22 we represent the PL for reconstructed DM parameters in benchmark points M-SI, L-SI, L-SD, and VL-SI, respectively. The black contours correspond to the combination of Ge and Xe data with a bolometric target: $CaWO_4$ for the upper row, Al_2O_3 in the middle and LiF for the lower row. For comparison, the blue contours illustrate the results when only germanium and xenon detectors are used.

We observe how in general Al_2O_3 and LiF provide good complementarity with germanium and xenon in points for which the detection rate in the latter is dominated by SI contributions. This is the case of benchmark points M-SI and L-SI. The area in the parameter space that is compatible with the simultaneous observation of a WIMP in the three experiments becomes much narrower than the case with only Ge and Xe. Although the WIMP mass cannot be completely reconstructed in some of these cases (e.g., in M-SI), a lower constraint is generally obtained for σ^{SD} (which would suffice, e.g., to discriminate the observation from the case $\sigma^{SD} = 0$ of scalar DM). In the examples for which the number of DM events is larger, such as in L-SI, the extra information on the recoil spectrum results in a better determination of the WIMP mass and consequently

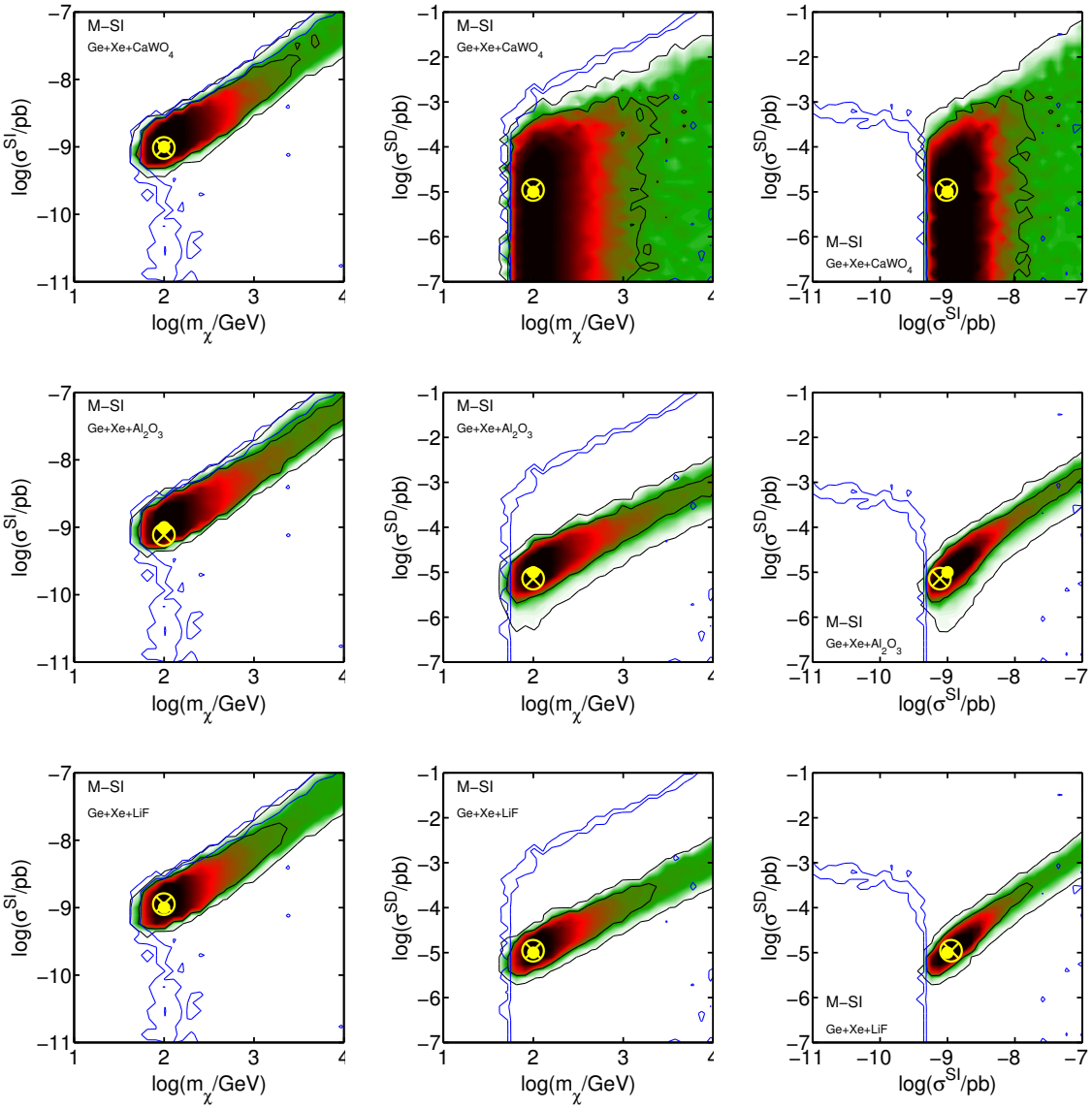

Figure 3.19: Profile likelihood for the DM parameters in the (σ^{SI}, m_χ), (σ^{SD}, m_χ), and (σ^{SD}, σ^{SI}) planes for the benchmark point M-SI after the combination of data from a Ge detector, a Xe detector, and a bolometric target ($CaWO_4$, Al_2O_3 and LiF from top to bottom, respectively). The exposure is $\epsilon = 300$ kg yr for all the experiments. From the inside out, contours enclose 68% and 99% of confidence interval. The yellow dot represents the nominal point and the yellow cross the posterior mean. The blue lines correspond to the case when only Ge and Xe are used.

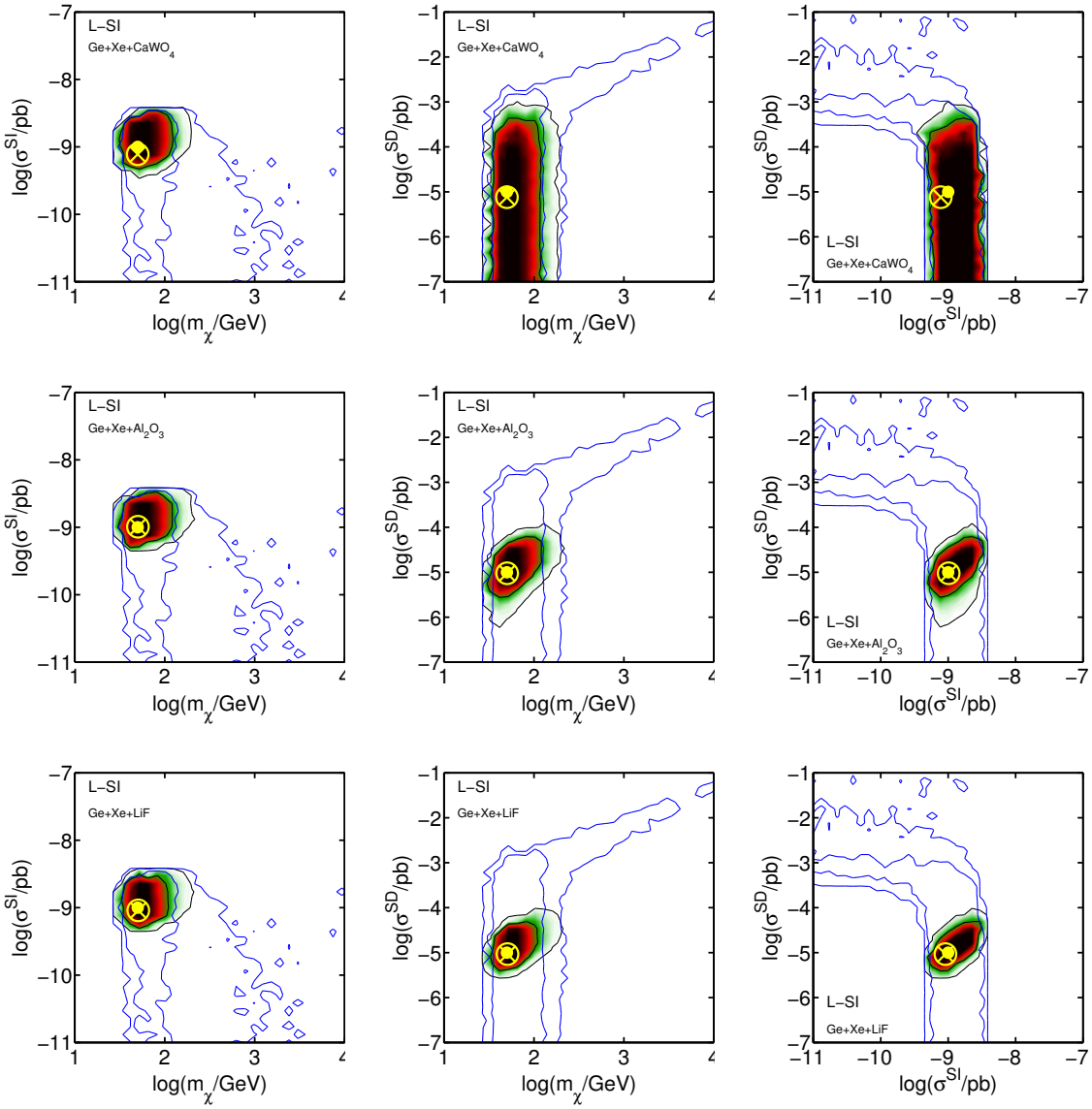

Figure 3.20: The same as in Fig. 3.19 but for the case of L-SI.

leads to closed contours in the three quantities. This is the situation that we describe as complementary. Although in these cases data from $CaWO_4$ does not allow a complete complementarity, an upper bound can be obtained in the value of σ^{SD} which, in turn, leads to a lower bound on σ^{SI} and a good determination of the latter (see, e.g., the case of L-SI in the top row of Fig. 3.20).

On the contrary, $CaWO_4$ performs better for benchmark points where SD contributions dominate the rate for germanium and xenon. Since tungsten is a heavier nucleus

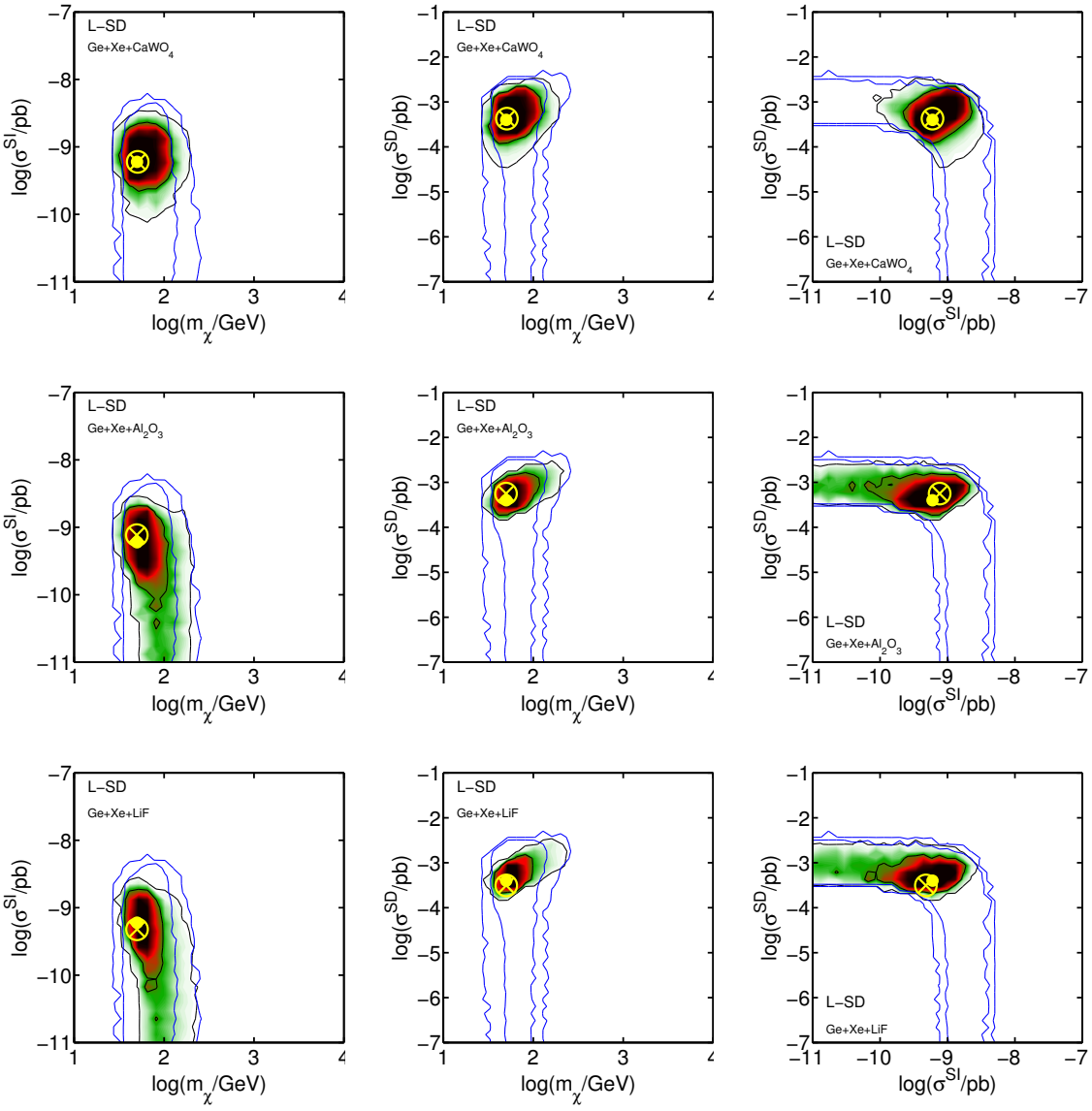

Figure 3.21: The same as in Fig. 3.19 but for the case of L-SD.

than both germanium and xenon, it is more sensitive to σ^{SI}. This is, e.g., what happens in L-SD, where the reconstructed contours are closed and the reduction in the best fit areas is very significant. In this kind of points, Al_2O_3 and LiF do not perform that well since they are mostly sensitive to the SD component. In any case, they can be used to obtain a lower bound on σ^{SD} which clearly rules out the possibility $\sigma^{SD} = 0$.

It should also be noticed that in the case of the benchmark point M-SI represented in Fig. 3.19 the reconstruction of the DM mass has no upper bound. This is a generic

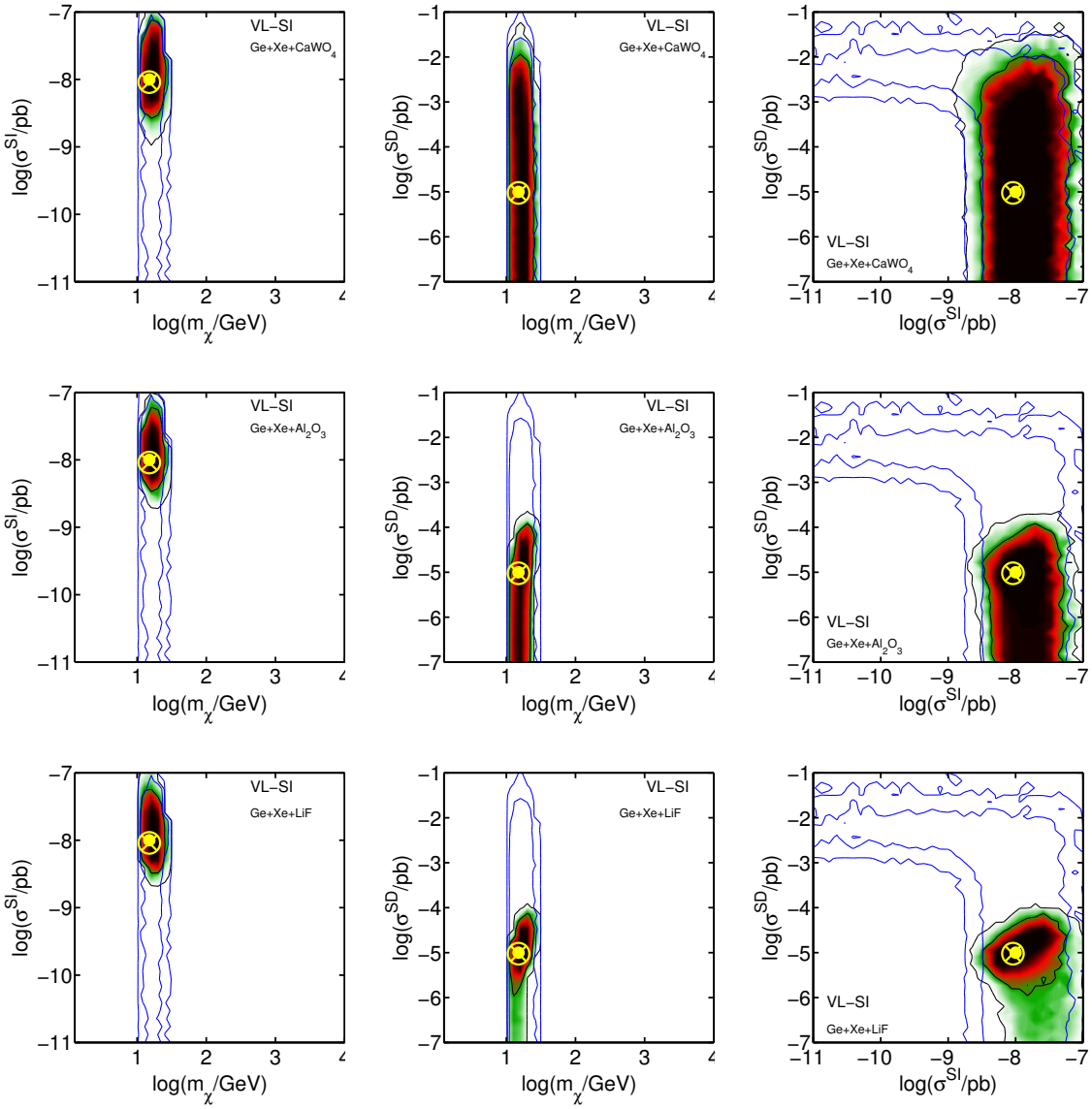

Figure 3.22: The same as in Fig. 3.19 but for the case of VL-SI.

feature for heavy DM particles, due to the fact that the spectrum becomes flatter and the fit to the mass is more inaccurate. The combination with bolometric targets does not improve this situation significantly. For this reason, we expect a worse reconstruction for DM particles heavier than in M-SI.

Very light WIMPs, on the other hand, constitute an interesting possibility that can also be explored with the aid of bolometric targets. In particular, as we said above, both Al_2O_3 and LiF can be sensitive to low-mass DM particles. In Fig. 3.22 we show the case

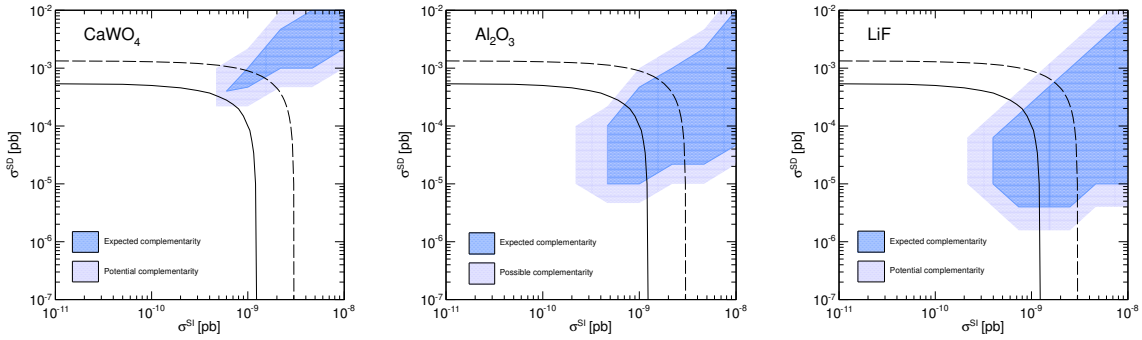

Figure 3.23: The dark blue region represents the area of the (σ^{SI}, σ^{SD}) plane for which complementarity is obtained for $CaWO_4$, Al_2O_3 and LiF in the case of a WIMP mass of $m_\chi = 50$ GeV. The light blue region is a measure of the uncertainty of our grid scan (see text). The black line corresponds to the upper constraint obtained from XENON100 data (using the BonnA result for the SD structure function [322]). Points above the dashed line predict more than 4.9 events in XENON100 and are therefore excluded by the recent experimental result [108] following a Feldmans-Cousin method [327]. For reference, points along the solid lines predict 2 events in XENON100.

of a WIMP with $m_\chi = 15$ GeV and scattering cross section as in VL-SI. Data from germanium and xenon are enough to determine the WIMP mass rather accurately, but a large uncertainty remains in both σ^{SI} and σ^{SD} as can be observed in the blue contours. Both Al_2O_3 and LiF remove significantly this degeneracy and in the case of LiF we even obtain an inner contour around the correct value of σ^{SD}. In the case of $CaWO_4$ only the SI component can be determined but no further information on σ^{SD} is obtained.

So far we have observed that some targets perform better than others (in terms of complementarity) in certain regions of the parameter space. In particular, for each of the targets we can determine the regions in the parameter space for which complementarity is obtained. In Fig. 3.23 we indicate the area (dark blue) of the (σ^{SI}, σ^{SD}) plane for which we obtain closed contours in the reconstructed PL of the three DM parameters (m_χ, σ^{SI}, σ^{SD}) for each of the bolometric targets and a WIMP mass of $m_\chi = 50$ GeV. In order to obtain this region we have performed a grid scan in the SD-SI plane for which the separation among points is limited by computing time. The light blue region separates points leading to complementarity from the nearest which do not, hence indicating the resolution of our grid scan. The areas are different for the three bolometers studied. Consistently with the individual examples that were analysed previously, we observe that the areas for Al_2O_3 and LiF are larger as compared with the area for $CaWO_4$, and

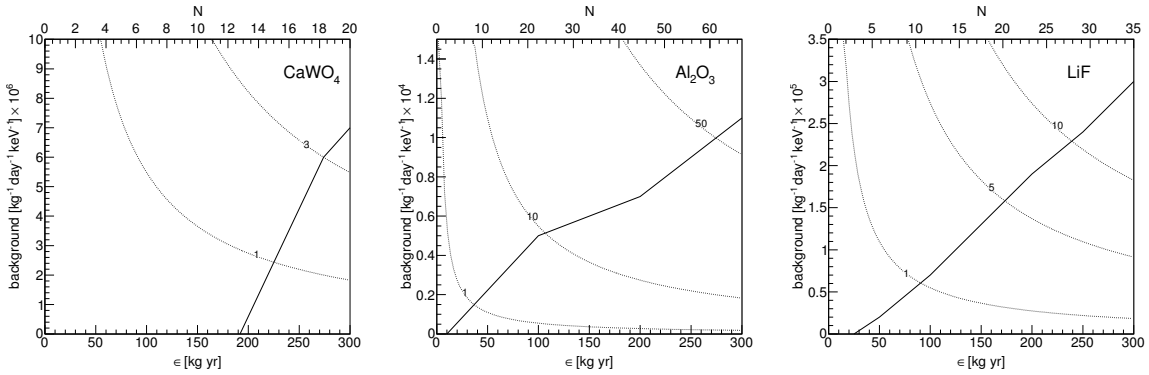

Figure 3.24: The solid line represents the maximum level of background for which complementarity is attained as a function of the exposure for each of the bolometric targets for representative benchmark points ($(\sigma^{SI}, \sigma^{SD}) = (6 \times 10^{-10}, 4 \times 10^{-4})$ pb for $CaWO_4$, $(10^{-9}, 5 \times 10^{-5})$ pb for Al_2O_3, and $(10^{-9}, 10^{-5})$ pb for LiF, from left to right) with $m_\chi = 50$ GeV. The expected total number of WIMP recoil events is indicated in the top horizontal axis. Dotted lines denote the number of background events per bin.

shifted towards smaller values of σ^{SD}. For $CaWO_4$ total complementarity only occurs for a small region, very close to the current upper constraint by XENON100. However, as we showed in various examples, it helps in the determination of the WIMP mass and σ^{SI}. Needless to say, a reduction in the exposure would result in a shift of the complementarity areas towards larger values of both σ^{SI} and σ^{SD}.

For completeness, we have determined the highest level of background for which complementarity is attained as a function of the exposure for each bolometer in a given benchmark point, and represented the results in Fig. 3.24. We see how, for zero background, the exposure for the three bolometers can be reduced. For Al_2O_3 and LiF this reduction can be very significant. For example, in the benchmarks that we have chosen in Fig. 3.24, it suffices to have a clear signal for DM in Al_2O_3 or LiF, even with a very reduced number of events (to determine the lower bound we considered that 1 event in a background free experiment is statistically significant). From these results we can also conclude that the complementary areas of Fig. 3.23 would not shrink significantly if a moderate background is included. We have to bear in mind that this computation was carried out assuming a flat background, for which a DM signal can be easily distinguished. This assumption can be considered equivalent to the estimate of the sensitivity of an experiment that does not surpass this background level in any bin of the energy window, independently of the background dependence on energy.

	m_χ (GeV)	σ^{SI} (pb)	σ^{SD} (pb)	$N_{\rm NaI}$ q=0.85	$N_{\rm NaI}$ q=1	$N_{\rm NaI}$ q=1.15	$N_{\rm Ge}$	$N_{\rm Xe}$
VL-SI	20	10^{-9}	10^{-5}	3.5 (2.9)	6.3 (5.3)	9.5 (8.2)	40.4 (39.3)	65.0 (61.6)
L-SD	50	10^{-10}	1.5×10^{-4}	51.2 (3.7)	60.9 (4.5)	69.2 (5.2)	29.3 (6.1)	94.7 (11.0)

Table 3.4: Number of WIMP recoils expected in the Ge, Xe and NaI targets for the benchmarks selected for this section. In all cases data correspond to an exposure of $\epsilon = 300$ kg×yr (see text for more details about the experimental setups considered). The number in parenthesis indicate the contribution from SI interaction. For NaI three different values of the quenching factor have been considered.

3.4.3 The effect of the thermal quenching factor

Before conclusions, we turn our attention to another source of uncertainty that can also arise from the detection technique itself. Now, we consider the effect of the thermal quenching factor, q[10], that measures the relative efficiency in the conversion into measurable thermal signal of the nuclear recoils energy deposition with respect to that corresponding to electron recoils, since the detectors are calibrated with gamma sources and the measured spectra are given in electron-equivalent energy. This factor is typically assumed equal to one for bolometers but small deviations (of about 10-15%) have been measured in different detectors (see for example Ref. [328] and references therein). To illustrate the influence of this uncertainty on q, we consider now three different values (q = 0.85, 1, and 1.15) for the a NaI target.

This target is one of the most widely used scintillators for γ spectroscopy due to its very high light yield. As mentioned above, this is the target used by DAMA/LIBRA and other proposed DM experiments looking for annual modulation such ANAIS. Although NaI is usually doped with Tl for room temperature applications, the pure material is known to scintillate better at temperatures of a few Kelvin (nevertheless, an increase in light yield of the Tl-doped material below 30 K has been recently reported[329]). Despite its high light yield at low temperature and intrinsic interest for DM searches, this material has not been tested yet as a bolometer due to its fragility and high hygroscopicity.

Following the same procedure as during this section, we analyze the complementarity prospects of a NaI target in combination with Ge and Xe targets. Since we want to focus on the effect of the thermal quenching factor, we only show our results by mean of 1D profile likelihood contours. In terms of complementarity, however, NaI behaves

[10] Not to be confused with the momentum transfer.

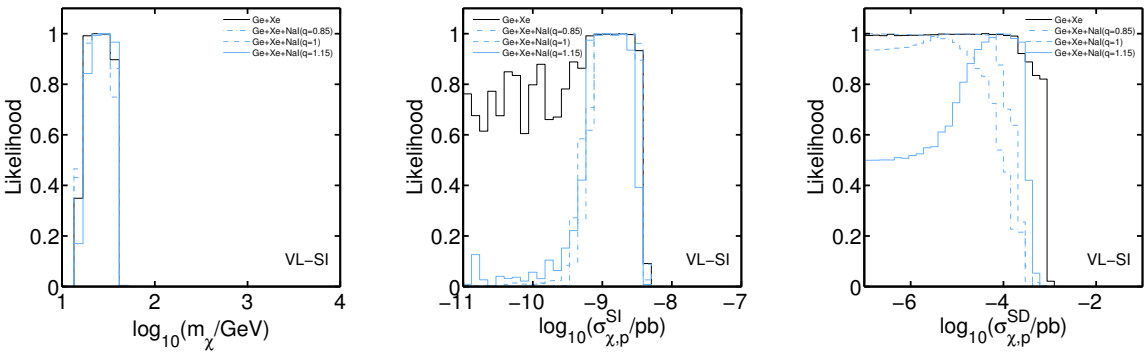

Figure 3.25: 1-D profile likelihood plots for Ge+Xe and Ge+Xe+NaI, considering three different thermal quenching values (q=0.85,1,1.15) for benchmark VL-SI.

very similar to $CaWO_4$ (analyzed in the previous section) since both are composed of a light and a heavy nucleus and are mainly SI sensitive. In table 3.4 we show the expected number of WIMP recoil events for the considered benchmarks over the whole energy range. Notice that, again, we have changed the cross sections and masses respect to the previous section. Regarding Ge and Xe, the same exposure (ϵ = 300 kg×yr) is assumed for both experiments, as well as zero background[11]. The experimental setup now is ES_2 (see Appendix 3), where the lower values account for the recent or potential improvements in nuclear recoil energy thresholds of some Xe and Ge experiments. Tab. 3.2 shows the expected number of WIMP recoil events for the considered benchmarks over the whole energy range. For NaI ϵ = 300 kg×yr and a reference window of [10-100] keV is used.

The change in the quenching factor (which can be understood as a shift in the energy window of nuclear recoils) leads to variations in the number of events due to SD and SI interactions. More importantly these do not change by the same amount, since the energy dependence of the SD and SI form factors is different. For NaI, in VL-SI benchmark point, we observe that the relative contribution due to the SD term increases as the quenching factor decreases, shifting from 14% at q=1.15 to 17% at q=0.85. This implies that, for this benchmark in which Ge and Xe signals are SI dominated, the complementarity with Ge and Xe is better for q = 0.85. The effect can be seen in the 1-D profile likelihood of the SD cross section shown in Fig. 3.25. Notice also that, although the upper limit on σ^{SD} is more stringent for q=0.85, the derived 1-D profile likelihood is practically flat

[11] In our previous section we have checked that the expected backgrounds for SuperCDMS and XENON1T are so low that have no impact in the results, so zero background can be safely assumed.

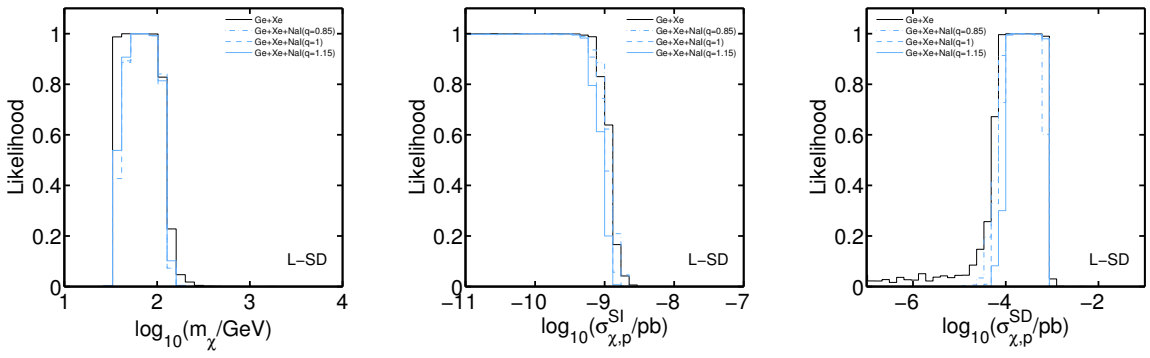

Figure 3.26: The same as Fig. 3.25 for the L-SD benchmark.

(see Fig. 3.25 right).

3.5 The importance of using different target materials (conclusions).

This chapter has showed us how important is to combine different direct detection target materials in order to understand the nature of DM. Although some of the benchmark examples given here would be already rule out by LUX, the conclusions and strategy remain valid, just increasing the exposure of the experiments and decreasing the DM cross sections. We have also learned that a proper understanding of the signal involves the knowledge of all the pieces that compose the physical processes of the DM elastic scattering off nuclei. In this sense, there are two important sources of uncertainty: the velocity distribution function of DM particles at Sun's position, and the form factors encoding the momentum dependence of the SD elastic scattering.

First off, an unbiased analysis of an hypothetical signal must include the SD contribution, mainly because otherwise it would lead to an overestimation of the SI contribution. Besides, due to the different spectral shape of a pure SI and a pure SD signals, the mass reconstruction might suffer some differences when reconstructing. Once the SD contribution is included, the next step is to include the uncertainties mentioned before. While the VDF and its impact on direct detection experiments has been widely studied in the literature, the SDSF lacked of a proper study. We have quantify the impact that choosing an inadequate SDSF has on the reconstruction of DM parameters. This impact can be separated into two different classes: firstly, differences at zero momentum transfer lead to a misreconstruction of the SD cross section, just like shifts in the local DM density.

Secondly, shifts in the slope and the height of the tail of SDSF's induces a misreconstruction of the DM mass. This can be very important when an experiment is sensitive to momentum transfers of the order of 100 keV, where the features of the SDSF's tail appears or if the number of WIMP events is very high and then the slope might play an important role. Then, we have proposed a parametrization in terms of three parameters: normalization (value at zero momentum), slope and height of the tail. This formula can account for these differences and allows to include in a consistent and systematic manner all these effects. This method has been tested for a Ge and Xe targets. Finally, we have shown that, in some circumstances, the uncertainties related to the SDSF's are at the same level as the astrophysical ones. All this, highlights how important is the knowledge of target material properties when analyzing an hypothetical signal.

Once a systematic and robust way to include the uncertainties has been found, we have investigated the determination of DM parameters from a combined use of different targets in direct detection experiments. More specifically, we study the determination of the WIMP mass and the SI and SD components of its scattering cross section off nucleons. We apply the method to a set of bolometric targets developed and characterized by the ROSEBUD collaboration (Al_2O_3 and LiF) or in use in CRESST ($CaWO_4$). We investigate the conditions under which the DM parameters can be obtained unambiguously when combining data from them and germanium and xenon experiments.

We first show how one ton scale germanium and xenon targets, which might excel in providing the first measurement of a WIMP, might not be able to measure all the DM properties. This is due to a degeneracy in the SI-SD plane that might be unresolved since both targets are mostly sensitive to the SI component of the WIMP cross section. Interestingly, SD-sensitive targets might provide extra information with which this degeneracy can be broken. We have studied the combination of germanium and xenon based targets with the one used by the COUPP collaboration (CF_3I). The presence of fluorine improves the reconstruction of DM parameters, however, COUPP does not provide information about the recoil spectrum, which limits its complementarity capability.

The situation is much more interesting for experiments which are sensitive to the SD WIMP-nucleon interaction and which can provide an accurate measurement of the energy spectrum, such as the scintillating bolometric targets developed and studied by the ROSEBUD and CRESST collaborations. We observe how the combined use of these detectors with germanium and xenon experiments can break the degeneracies in the determination of DM parameters and provide a good reconstruction of the WIMP mass and SI and SD scattering cross section. In particular, the inclusion of $CaWO_4$ can lead to a better determination of the WIMP mass and SI cross section. Nevertheless,

since its interaction with DM is dominated by the SI contribution, it only leads to a complementary results in a small window of the parameter space in which the rate in germanium and xenon is mainly due to SD interactions. This area is in fact very close to the region already excluded by XENON100. On the other hand, Al_2O_3 and LiF (being more sensitive to the SD contribution) can be complementary targets to germanium and xenon in regions of the parameter space where the rate in the latter is dominated by SI contributions. This can happen for values of the cross section as small as $\sigma^{SI} \gtrsim 2 \times 10^{-10}$ pb and $\sigma^{SD} \gtrsim 10^{-5}$ pb for a WIMP with a mass $m_\chi = 50$ GeV.

In some regions of the DM parameter space the exposure can be reduced to approximately 50 kg yr for Al_2O_3 and LiF without loosing complementarity under the assumption of zero background. Finally, we investigate the effect of the background and observe that complementarity can be achieved for large exposures with a background level as large as 10^{-4} kg^{-1} day^{-1} keV^{-1} for Al_2O_3 or 10^{-5} kg^{-1} day^{-1} keV^{-1} for LiF. In the case of $CaWO_4$ a larger exposure and smaller background level is required.

Finally, we have pointed out another source of uncertainty, the quenching factor. It was already know that the quenching factor can play an important role when interpreting DM signals. Namely, the DAMA favored region has been shown to shift when a different quenching was used. However, we have investigated the effect that the quenching factor could have for complementary purposes. Taking a NaI target as a case of study, we have seen that different thermal quenching factors alter the complementary power of this target in combination with Xe and Ge. The impact of the quenching shift is not trivial. In terms of complementarity, the most important quantity is the sensitivity between SI and SD contributions. Since the quenching shift induces a different change in the SI and SD expected signals, due to the different energy dependence of the form factors, the complementarity might be better for lower quenchings, even if this means less expected events respect to higher quenchings. This effect could be very relevant in the future if a DM signal is detected in different targets where the quenching factor has not a precise measurement.

Chapter 4

Dark Matter indirect detection. Gamma-ray astronomy in the inner Galaxy.

Until now, we have studied the appealing theoretical framework for WIMP DM provided by SUSY theories. We have also seen that direct detection experiments could disentangle the nature of DM by combining different target materials. As we introduced in Chapter 1, WIMP DM is not only a well motivated paradigm but also might be tested by direct detection experiments in the near future in a model independent approach.

In light of this situation, one also expects to have a hint of WIMP's coming from the sky. All the evidences for DM that we enumerated at the beginning of this thesis were related to the gravitational effects of DM at the different scales of the Universe. This pointed out that Galaxies, like ours, are surrounded by a DM halo and hence one might expect to see the byproducts created by DM annihilations or decays. Indirect detection experiments aim at detecting this byproducts. According to the electric charge carried by these final states, in Chapter 1, we classified these searches in: cosmic ray, gamma ray and neutrino astronomy. From now on, we will focus on the gamma-ray astronomy.

The strategy relies on the search for DM annihilation products in preferred regions of the sky, i.e., those with the highest expected DM concentrations and still close enough to yield high DM-induced fluxes at the Earth. For that reason, the GC, nearby dwarf dSphs satellites of the Milky Way, as well as local galaxy clusters are thought to be among the most promising objects for indirect DM searches. In particular, dSphs represent very attractive targets because they are highly DM-dominated systems and are expected to be free from any other astrophysical gamma-ray emitters that might contaminate any potential DM signal. Although the expected signal cannot be as large as that from the GC, dSphs may produce a larger signal-to-noise (S/N) ratio. This fact allows us to place

very competitive upper limits on the gamma-ray signal from DM annihilation [132, 259], using data collected by the Large Area Telescope (LAT) onboard the Fermi gamma-ray observatory [330]. These are often referred to as the most stringent limits on DM annihilation cross-section obtained so far.

Despite these interesting limits derived from dSphs, the GC is still expected to be the brightest source of DM annihilations in the gamma-ray sky by several orders of magnitude. Although several astrophysical processes at work in the crowded GC region make it extremely difficult to disentangle the DM signal from conventional emissions, the DM-induced gamma-ray emission is expected to be so large there that the search is still worthwhile. Furthermore, the DM density in the GC may be larger than what is typically obtained in N-body cosmological simulations. Ordinary matter (baryons) dominates the central region of our Galaxy [331]. Thus, baryons may significantly affect the DM distribution. As baryons collapse and move to the center they increase the gravitational potential, which in turn forces the DM to contract and increase its density. This is a known and qualitatively well understood physical process [332–334]. It is also observed in many cosmological simulations that include hydrodynamics and star formation [335–340]. If this is the only effect of baryons, then the expected annihilation signal will substantially increase [331, 341].

In this Chapter, we will take a look to the GC using *Fermi*-LAT inner Galaxy gamma-ray measurements by assuming some specific (and well motivated) DM distributions. Rather than try to search for a specific signal there, which would require to modellize other physical processes, the analysis will be more conservative. We will require that the expected DM signal does not exceed the gamma-ray emission observed by the *Fermi*-LAT in an optimized region around the GC. The region is selected to maximize the S/N ratio. Thus, we will be able to put upper bounds on the annihilation cross section of DM particles as a function of its mass, and then, compare with the predictions given in Chapter 2[1]. Finally, and also mentioned in Chapter 1, there could be hints of a light DM particle (the specific mass depends on the annihilation channel considered) annihilating at the GC [144–149]. We will take these analyses at face value and compare with predictions of Sneutrino DM in the NMSSM-RH model described before. We will see that if that signal is confirmed the Sneutrino scenario provides an appealing WIMP candidate which satisfies all the experimental bounds.

[1] The same can be done for decaying DM particles, however, we will focus on annihilating DM to compare with the models analyzed in this thesis.

4.1 Basics on indirect detection

As in the previous Chapter, we will start by summarizing the basic expressions related to indirect DM detection of gamma-rays. DM might produce high energy (in the GeV region) γ-rays both by direct (prompt) emission through hadronization, fragmentation and decays of the DM annihilation products, and by Inverse Compton Scattering (ICS) of $e^{\pm}$ produced by DM on the ambient light (secondary). Two other possible contributions to the expected gamma-ray flux from DM annihilation can be safely neglected in what follows: radiation from bremsstrahlung, which is expected to be sub-dominant with respect to ICS in the energy range considered (1 - 100 GeV) and a few degrees off the Galactic plane (see Fig. 14 in Ref. [342]), and synchrotron radiation, which is only relevant at radio frequencies below the *Fermi*-LAT threshold. The gamma-ray differential flux from DM annihilations from a given observational region $\Delta\Omega$ in the Milky Way halo can be written as follows:

$$\frac{d\Phi_\gamma}{dE_\gamma}(E_\gamma, \Delta\Omega) = \left(\frac{d\Phi_\gamma}{dE_\gamma}\right)_{\text{prompt}} + \left(\frac{d\Phi_\gamma}{dE_\gamma}\right)_{\text{ICS}} , \tag{4.1}$$

where E_γ represents the energy of the photon. Both contributions must be treated separately since their origins, as we have already mentioned, are quite different. However, in spite of this difference and under some assumptions[2], both can be factorized in the same way: a particle physics factor which takes into account the microscopic details of the DM particle, and an astrophysical factor which encodes the subtleties of the description of the Galaxy. It is worth mentioning that while the particle physics factor is very similar in both cases, the astrophysical one is very different. This difference leads us to describe both contributions separately.

4.1.1 DM density profiles for the Milky Way

As we have commented at the beginning of this Chapter, the high concentrations of DM around the GC, make it as a good place to search for DM annihilation products. It is clear then that in order to quantify the expected DM flux from there, a description of the DM density is needed. In Chapter 3 we already introduced, in the context of the DM phase space distribution, the most used density profiles. We turn back our attention to this subject with more detail.

Cosmological N-body simulations provide important results in this respect. These simulations suggest the existence of a universal DM density profile, valid for all masses

[2] If the product σv is velocity independent, as we will see.

and cosmological epochs. For conveniency, one can use the following parametrization for the DM halo density [343], which covers different approximations for DM density:

$$\rho(r) = \frac{\rho_s}{\left(\frac{r}{r_s}\right)^{\gamma}\left[1+\left(\frac{r}{r_s}\right)^{\alpha}\right]^{\frac{\beta-\gamma}{\alpha}}} \ , \tag{4.2}$$

where ρ_s and r_s represent a characteristic density and a scale radius, respectively. The NFW density profile [288], with $(\alpha,\beta,\gamma) = (1,3,1)$, is by far the most widely used in the literature. Notice that this type of profiles are divergent at the origin, thus unphysical, and an extrapolation must be made to renormalize the profile near the origin. Another approximation is the so-called Einasto profile [289]

$$\rho_{\rm Ein}(r) = \rho_s \exp\left\{-\frac{2}{\alpha}\left[\left(\frac{r}{r_s}\right)^{\alpha}-1\right]\right\} \ , \tag{4.3}$$

which provides a better fit than NFW to numerical results [289, 344]. Finally, we will also consider DM density profiles that possess a core at the center, such as the purely phenomenologically motivated Burkert profile [290]:

$$\rho_{\rm Burkert}(r) = \frac{\rho_s \ r_s^3}{(r+r_s)\ (r^2+r_s^2)} \ . \tag{4.4}$$

Early results on the central slopes of the DM profiles showed some significant disagreement between the estimates, with values ranging from $\gamma = 1.5$ [345] to $\gamma = 1$ [288]. As the accuracy of the simulations improved, this disagreement became smaller. For the Via Lactea II (VLII) simulation the slope in Ref. [346] was found to be $\gamma = 1.24$. A re-analysis of this data and new simulations performed by this group gave a slope range of $\gamma = 0.8 - 1.0$ [347], which is consistent with the Aquarius simulation [348]. Another improvement comes from the fact that the simulations now are able to resolve the cusp down to a radius of $\sim$ 100 pc, which means that less extrapolation is required in the inner region.

Yet, there is an additional ingredient which is expected to play a major role in the central regions of DM halos: baryons. Although only a very small fraction of the total matter content in the Universe is due to baryons, they represent the dominant component at the very centers of galaxies like the Milky Way. Actually, the fact that current N-body simulations are not able still to resolve the innermost regions of the halos with enough resolution, has less impact than the uncertainties due to the interplay between baryons and DM. There are two well known processes that affect the DM density close to the center: the adiabatic compression and the supernova feedback.

The baryons lose energy through radiative processes and fall into the central regions of a forming galaxy. As a consequence of this redistribution of mass, the resulting gravitational potential is deeper, and the DM must move closer to the center, increasing its density. This *compression* of DM halos due to baryonic infall was first studied in Ref. [332] for a spherically symmetric DM halo using simple simulations and adiabatic invariants. A convenient analytical approximation was provided in Ref. [333]. The model was later modified [334] to account for the eccentricity of orbits of DM particles. The effect seems to be confirmed by recent hydrodynamic simulations (see e.g. Refs. [335–340].). In Ref. [338], for instance, the authors ran a set of high-resolution hydrodynamic simulations that self-consistently included complex baryonic physics such as gas dissipation, star formation and supernova feedback. They all showed a clear steepening of the inner DM density profiles with respect to DM-only simulations. Indeed, it is argued by the authors that such effect should be always included in order to correctly model the mass distribution in galaxies and galaxy clusters.

As pointed out in Ref. [331], the effect of the baryonic adiabatic compression might be crucial for indirect DM searches, as it increases by several orders of magnitude the gamma-ray flux from DM annihilation in the inner regions, and therefore the DM detectability. In Ref. [341], this effect was used to study the detection of supersymmetric DM by the *Fermi*-LAT, with the conclusion that fluxes from the GC would be largely reachable in significant regions of the supersymmetric parameter space. The effect of compression on galaxy clusters was recently studied in Ref. [349].

Regarding the supernova feedback, this effect tends to decrease the DM density and flatten the DM cusp [350–352]. The mechanism relies on numerous episodes of baryon infall followed by a strong burst of star formation, which expels the baryons. At the beginning of each episode the baryons dominate the gravitational potential. The DM contracts to respond to the changed potential. A sudden onset of star formation drives the baryons out. The DM also moves out because of the shallower potential. Each episode produces a relatively small effect on the DM, but a large number of them results in a significant decline of the DM density. Indeed, cosmological simulations that implement this process show a strong decline of the DM density [353, 354]. Whether the process happens in reality is still unclear. Simulations with the cycles of infall-burst-expansion process require that the gas during the burst stage does not lose energy through radiation, which is not realistic. Still, the strong energy release needed by the mechanism may be provided by other processes and the flattening of the DM cusp may occur. If this happened to our Galaxy, then the DM density within the central ~ 500 pc may become constant [354]. This would reduce the annihilation signal by orders of magnitude. We note

Profile	α	β	γ	ρ_s [GeV cm^{-3}]	r_s [kpc]
Burkert	$--$	$--$	$--$	37.76	2
Einasto	0.22	$--$	$--$	0.08	19.7
NFW	1	3	1	0.14	23.8
NFW$_c$	0.76	3.3	1.37	0.23	18.5

Table 4.1: DM density profiles used to extract upper bounds on the DM annihilation cross section $\langle\sigma v\rangle_0$ as a function of its mass. The parameters follow the notation of Eq. (4.2) and (4.4).

that this mechanism would wipe out the DM cusp also in centers of dwarf galaxies [353]. Yet, a recent work that also includes stellar feedback offers a much more complicated picture in which galaxies may retain or not their DM cusps depending on the ratio between their stellar-to-halo masses [355].

Since the aim of this Chapter is to place constraints on DM annihilations taking place at the GC, special attention will be payed to those scenarios where the DM cusp is not flattened, and hence the gamma-ray will be higher. However, in order to quantify the uncertainty in the DM density profile, we will use the above mentioned profiles: Einasto, NFW and a compressed NFW (NFW$_c$), whose parameters have been constrained from observational data of the Milky Way, as well as a cored Burkert profile, also compatible with current constraints.

We have followed Ref. [331] to choose the parameters of both the NFW and the NFW$_c$. We have fitted the resulting data of that work with the power-law parametrization of Eq. (4.2). The results for both profiles are listed in Table 4.1. The effect of baryonic adiabatic compression is clearly noticed at small r as a steep power law $\rho \propto 1/r^{\gamma}$ with $\gamma = 1.37$ for NFW$_c$, which is in contrast to the standard NFW value, $\gamma = 1$. We note that a value of $\gamma = 1.37$ is indeed perfectly consistent with what has been found in recent hydrodynamic simulations [338] and it is also compatible with current observational constraints (mainly derived from microlensing and dynamics) on the slope of the DM density profile in the central regions of the Milky Way [318]. These studies actually allow for even steeper adiabatically contracted profiles. Concerning the Einasto profile we will use the parameters provided in Ref. [315]. Finally, for the Burkert profile, we decided to choose a core radius of 2 kpc. This core size is in line with previous works [261, 263] and with that suggested by recent hydrodynamic simulations of Milky Way size halos [356]. For the normalization of the profile we chose the value of the local density suggested in Ref. [315] for Milky Way Burkert-like profiles. The resulting profile

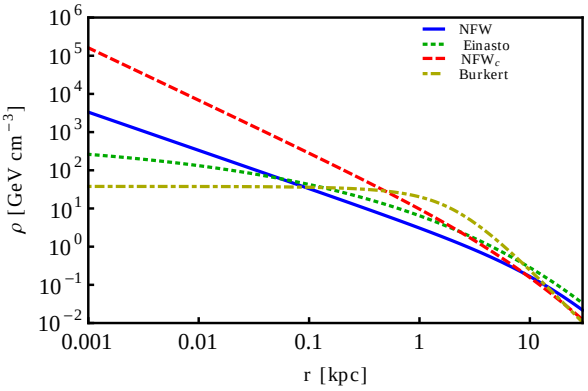

Figure 4.1: DM density profiles as a function of the radius in kpc, defined by the parameters given in Table 4.1. Blue (solid), red (long-dashed), green (short-dashed) and yellow (dot-dashed) lines correspond to NFW, NFW$_c$, Einasto and Burkert profiles, respectively. The four DM density profiles are compatible with current observational data (see text for more details).

is also compatible with current observational constraints [318]. Note, however, that a recent work favors a substantially larger core radius and a slightly higher normalization for Burkert-like profiles [357]. All the profile parameters are summarized in Table 4.1 and the four profiles are shown Figure 4.1.

As we have anticipated and as it can be seen in Figure 4.1 the NFW-like and the Einasto profiles are cuspy, and they grow rapidly towards the GC. The Burkert profile, however, remains more or less constant in the region $r \lesssim 1$ kpc. The difference between the NFW$_c$ and this profile in the inner region grows even more than three orders of magnitude, which gives us the idea of how big is this uncertainty. Notice as well that the Burkert profile predicts more DM than the others in the region ranging from 1-10 kpc approximately, which means that it predicts more DM at Sun's position and hence this is important for direct detection as we already knew from the previous chapter.

4.1.2 Prompt component

We are now ready to analyze in more detail the Eq. (4.1). For simplicity let us start with the prompt component. A continuous spectrum of gamma rays is expected to be produced mainly by the decays of π^0's generated in the cascading of annihilation products and also by internal bremsstrahlung. While the former process is completely determined for each given final state of annihilation (we will study $b\bar{b}$, $\tau^+\tau^-$, $\mu^+\mu^-$ and W^+W^- channels as representative cases of the results obtained in Chapter 2), the latter depends in general on the details of the DM model such as the DM spin and the properties of the

particle mediating the process. Nevertheless, it is known that internal bremsstrahlung always includes much model-independent final state radiation (FSR), which is emitted directly from charged particles in the external legs [358, 359]. In our analysis, just these FSR components of the internal bremsstrahlung are considered. This must be seen as a safe and a conservative choice, since the inclusion of model-dependent emission from virtual charged mediators would make constraints univocally stronger [135, 359].

Since the Neutralino and Sneutrino analyzed in Chapter 2 candidates are self-conjugated DM particles, the prompt contribution can be written as

$$\left(\frac{d\Phi_\gamma}{dE_\gamma}\right)_{prompt} = \sum_i \frac{dN_\gamma^i}{dE_\gamma} \frac{\langle\sigma_i v\rangle}{8\pi m_{DM}^2} \bar{J}(\Delta\Omega)\Delta\Omega \ . \tag{4.5}$$

Note that this equation has to be multiplied by an additional factor of 1/2 if the DM particle studied is not its own anti-particle. The sum must be performed over all DM annihilation channels, although to drop model dependencies we are going to consider the case of only one annihilation channel. dN_γ^i/dE_γ is the differential gamma-ray yield. For this quantity we have used pre-evaluated tables in [57], which are generated using `PYTHIA` [360] and thus containing FSR properly. $\langle\sigma_i v\rangle$ is the annihilation cross-section averaged over the velocity distribution of the DM particles, m_{DM} is used to denote the mass of the DM particle. The quantity $\bar{J}(\Delta\Omega)$ (commonly known as the *J-factor*) is defined as

$$\bar{J}(\Delta\Omega) \equiv \frac{1}{\Delta\Omega} \int d\Omega \int_{l.o.s.} \rho^2(r(l,\Psi))\, dl \ , \tag{4.6}$$

with

$$\Delta\Omega = 2\pi \int_{\Psi_{\min}}^{\Psi_{\max}} \sin\Psi d\Psi = 2\pi \left(\cos\Psi_{\min} - \cos\Psi_{\max}\right). \tag{4.7}$$

The J-factor accounts for both the DM distribution and the geometry of the system[3]. The integral of the DM density squared ρ^2 in the direction of observation Ψ is along the line of sight ($l.o.s$), and r and l represent the galactocentric distance and the distance to the Earth, respectively. For completeness, let us explicitly write the $r(l,\Psi)$ function,

$$r = \sqrt{l^2 + R_\odot^2 - 2lR_\odot \cos\Psi}, \tag{4.8}$$

[3] Although in principle the point-spread function (PSF) should be included in this formula (see e.g., Refs.[331, 361]), it turns out to be not relevant in our study mainly for two reasons: i) we deal with fluxes integrated in large regions of the sky, much larger than the PSF, and ii) we avoid the very center of the Galaxy, where the PSF would artificially smear out the cusps expected from some of the DM density profiles. See following sections for more details.

where $R_\odot$ is the Sun's distance to the GC.

Indeed, in Eq. (4.5), all the dependence on astrophysical parameters is encoded in the J-factor itself,whereas the rest of the terms encode the particle physics input. Strictly speaking, both terms are not completely independent of each other by three main reasons. First, the minimum predicted mass for DM halos is set by the properties of the DM particle and is expected to play an important role also in the J-factor when substructures are taken into account. The effect of substructures on the annihilation flux is not considered, since large substructure boosts are only expected for the outskirts of DM halos [362, 363], and thus they should have a very small impact on inner Galaxy studies. Finally, the velocity averaged cross section, $\langle\sigma v\rangle_0$, is not independent of the astrophysics unless we assume that the product σv is velocity independent[4]. As we have mentioned in chapter 3, the velocity distribution function is extracted by modeling the DM and baryons of the Milky Way and then by using the Eddington formalism. So, one should expect that this functions differ from one profile, say NFW, to other, say Einasto (see Ref. [291]). Another important thing to note is that these functions contains a spatial dependency, so they cannot be the same everywhere in our Galaxy[5]. Bearing it in mind, this quantity can be written in the following form [364],

$$\langle\sigma v\rangle_0(r) = \int \sigma v f(v^2, r) d(v^2), \tag{4.9}$$

where we have assumed spherical symmetry of the matter profiles. Due to the normalization of the distribution function $f(v^2, r)$, if the product σv is velocity independent then the previous integral can be neglected for each r. However, if the product depends on the velocity this integral must be properly evaluated at each position [365] and thus it must be included inside the J-factor calculation Eq. (4.6). We have adopted a velocity independent product for simplicity. All in all, let us remark that the most crucial aspect in the calculation of $\bar{J}(\Delta\Omega)\Delta\Omega$ is related to the modeling of the DM distribution itself in the GC.

In Figure 4.2, the $\bar{J}(\Delta\Omega)\Delta\Omega$ quantity corresponding to each of the four profiles discussed in the previous section is shown as a function of the angle Ψ from the GC. The associated observational regions $\Delta\Omega$ to each Ψ are taken around the GC. The angular integration is over a ring with inner radius of 0.5° and external radius of Ψ. Since as we have seen before those profiles following the functional form given in Eq. (4.2) are divergent at the origin, we have assumed a $r = 0.1$ pc constant density core for both

[4] The velocity referred is the relative velocity between the two DM particles colliding.

[5] This is in contrast to direct detection experiments where the velocity distribution must be evaluated at Sun's (Earth) position.

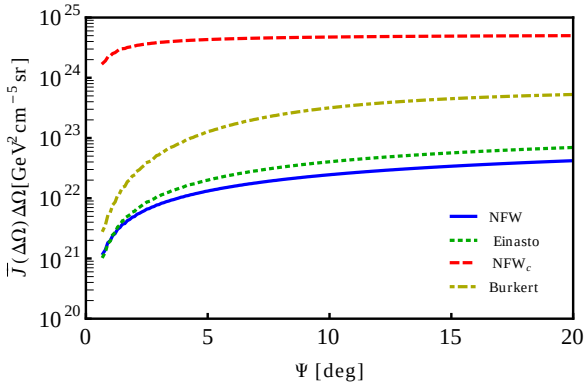

Figure 4.2: The $\bar{J}(\Delta\Omega)\Delta\Omega$ quantity integrated on a ring with inner radius of 0.5° ($\sim$ 0.07 kpc) and external radius of Ψ ($R_\odot \tan\Psi$) for the DM density profiles given in Table 4.1. The color code is the same as in Figure 4.1.

NFW and NFW$_c$ as a renormalization. Although it must be noted as discussed e.g. in Refs. [341, 366] that the results are almost insensitive to any core size below $\sim$1 pc (or even larger given the *Fermi*-LAT PSF). As expected, the adiabatic compression increases the DM annihilation flux by several orders of magnitude in the inner regions, i.e., the regions of interest in this study. Obviously, this effect will be determinant when deriving limits on the DM annihilation cross section. Remarkably, the Burkert profile value of $\bar{J}(\Delta\Omega)\Delta\Omega$ is larger than for the NFW and Einasto profiles. This is due to the relative high normalization used for this profile compared to the others and, especially, due to the annular region around the GC where we are focusing our studies, which excludes the GC itself (where such cored profiles would certainly give much less annihilation flux compared to cuspy profiles, see Figure 4.1). We note, however, that the use of another Burkert-like profile with a larger DM core than the one used here, as e.g., the one recently proposed in Ref. [357], may lead to substantially lower $\bar{J}(\Delta\Omega)\Delta\Omega$ values, and thus to weaker DM constraints. In particular, we have checked for the profile in Ref. [357] that the values of $\bar{J}(\Delta\Omega)\Delta\Omega$ in the region shown in Figure 4.2 are always smaller than about 10^{22} GeV^2 cm^{-5} sr. Notice finally that the NFW$_c$ profile reaches a constant value of $\bar{J}(\Delta\Omega)\Delta\Omega$ for a value of Ψ smaller than the other profiles. This is relevant for our discussion below for optimization of the region of interest for DM searches, since we see that for NFW$_c$ a larger region of analysis will not increase the DM flux significantly as for NFW, Einasto and Burkert profiles. It highlights that for the NFW$_c$ profile the main contribution comes from the very inner part of the Galaxy, and then to open the region towards larger radius does not increase $\bar{J}(\Delta\Omega)\Delta\Omega$ quantity.

4.1.3 Inverse compton scattering contribution

Electron and positron ($e^{\pm}$) fluxes are generated in DM annihilations mainly through the hadronization, fragmentation and decays of the annihilation products, since direct production of e^+e^- is supressed by small couplings in most DM models. These $e^{\pm}$ propagate in the Galaxy and produce high-energy gamma rays via ICS off the ambient photon background. The differential flux produced by ICS from a given observational region $\Delta\Omega$ in the Galactic halo is given by [57]

$$\frac{d\Phi_\gamma^{ICS}}{dE_\gamma} = \frac{2}{E_\gamma}\int d\Omega \int_{\text{l.o.s.}} dl \int_{m_e}^{m_\chi} dE_e \frac{P_{\text{IC}}(E_\gamma, E_e)}{4\pi} f_{e^\pm}(E_e; \mathbf{x}) \ , \tag{4.10}$$

where $f_{e^\pm}(E_e; \mathbf{x})$ is the differential number density of $e^\pm$ at $\mathbf{x}$, and $P_{\text{ICS}}(E_\gamma, E_e; \mathbf{x})$ is the differential emission power of photon at energy E_γ from $e^\pm$ with energy E_e scattering off the isotropic interstellar radiation. By taking the following convenient ansatz

$$f_{e^\pm}(E_e; \mathbf{x}) = \frac{1}{b_{\text{T}}(E_e; \mathbf{x})}\frac{1}{2}\left(\frac{\rho_\odot}{m_\chi}\right)^2 \int_{E_e}^{m_\chi} dE_I \sum \langle\sigma_i v\rangle \frac{dN^i_{e^\pm}}{dE_I}(E_I)\tilde{I}(E_e, E_I; \mathbf{x}) \ , \tag{4.11}$$

it can be written in a simpler form as

$$\frac{d\Phi_\gamma^{ICS}}{dE_\gamma} = \sum_i \frac{\langle\sigma_i v\rangle}{8\pi m_\chi^2}\int_{m_e}^{m_{DM}} \frac{dE_I}{E_\gamma}\frac{dN^i_{e^\pm}}{dE_e}(E_I)\int d\Omega \frac{I_{IC}(E_\gamma, E_I; \Psi)}{E_\gamma} \ , \tag{4.12}$$

where E_I is the $e^\pm$ injection energy, Ψ corresponds to the angular position where the ICS gamma rays are produced, and $I_{IC}(E_\gamma, E_s; \Psi)$ is given by

$$I_{IC}(E_\gamma, E_I; \Psi) = 2E_\gamma \int_{l.o.s.} dl \int_{m_e}^{E_I} dE_e \frac{P_{IC}(E_\gamma, E_e; \mathbf{x})}{b_{\text{T}}(E_e; \mathbf{x})}\tilde{I}(E_e, E_I; \mathbf{x}) \ , \tag{4.13}$$

with $\mathbf{x} = (l, \Psi)$ and $b_T \propto E^2$ is the energy-loss rate of the electron in the Thomson limit. At this point it is possible to establish a similarity between prompt and ICS components. As we have seen in the previous section, under some assumptions all the astrophysical information of the gamma-ray prompt component was encoded in the J-factor. For the ICS we can then relate the $I_{IC}(E_\gamma, E_I; \Psi)$ function to the J-factor. This function contains all the information about the astrophysics. However, it is obvious that in this case things are more complex than an integral along the line of sight of the density. The function P_{IC} is the photon emission power for ICS, and it depends on the interstellar radiation (ISR) densities for each of the species composing the photon background. It is known that the ISR in the inner Galactic region can be well modeled as a sum of separate black body radiation components corresponding to star-light (SL), infrared radiation (IR), and

cosmic microwave background (CMB) [367]. $P_{\rm IC}$ can be written in terms of differential photon number density of the ISR $n_{\rm ISR}(E;\mathbf{x})$

$$P_{\rm IC}(E_\gamma, E_e;\mathbf{x}) \equiv \frac{3\sigma_T}{4\gamma^2}E_\gamma \int_{1/4\gamma^2}^{1} {\rm d}q\; n_{\rm ISR}(E_\gamma^0(q),\mathbf{x})\left(1-\frac{1}{4q\gamma^2(1-\epsilon)}\right) \times\left(\frac{1}{q}+1+2\lambda_N q-2q+\frac{1}{2}\frac{\epsilon^2}{1-\epsilon}\frac{1-q}{q}\right), \tag{4.14}$$

where $\sigma_T = (8\pi/3)(\alpha_{\rm EM}/m_e)^2$ is the Thompson cross section, $\gamma = E_e/m_e$, $\epsilon = E_\gamma/E_e$, and $E_\gamma^0(q) = \frac{m_e}{4\gamma}\frac{\epsilon}{q(1-\epsilon)}$. It is known that the ISR in the inner Galactic region can be well modeled as a sum of separate black body radiation corresponding to SL, IR, and CMB. Under this assumption the differential photon number density of the ISR is given by

$$n_{\rm ISR}(E) = \sum_i N_i \frac{E^2}{\pi^2}\frac{1}{e^{E/T_i}-1}. \tag{4.15}$$

We have used `GALPROP` [368] to calculate the normalization and the temperature for each of these three components (N_i, T_i) obtaining $(9.02\times10^{-12}, 3.70\times10^{-10}{\rm GeV})$,$(6.61\times10^{-5}, 4.09\times10^{-12}{\rm GeV})$, and $(1, 2.35\times10^{-13}{\rm GeV})$ where i stands for the SL, IR and CMB components, respectively. Let us remark that the injection spectra of $e^\pm$ are extracted from the pre-evaluated tables of Ref. [57].

The last ingredient in Eq. (4.13) is the $\tilde{I}(E_e, E_I;\mathbf{x})$ function, which can be given in terms of the well- known halo function [57],

$$I(E, E_I;\mathbf{x}) = \tilde{I}(E, E_I;\mathbf{x})[(b_T(E)/b(E,\mathbf{x}))(\rho(\mathbf{x})/\rho_\odot)^2]^{-1}, \tag{4.16}$$

where $\rho_\odot$ is the DM density at Sun's position and $b(E,\mathbf{x})$ encodes the energy loss of the $e^\pm$. The $\tilde{I}(E_e, E_I;\mathbf{x})$ function obeys the diffusion loss equation [57],

$$\nabla^2\tilde{I}(E_e, E_I;\mathbf{x}) + \frac{E_e^2}{K(E_e;\mathbf{x})}\frac{\partial}{\partial E_e}\left[\frac{b(E_e;\mathbf{x})}{E_e^2}\tilde{I}(E_e, E_I;\mathbf{x})\right] = 0\ , \tag{4.17}$$

where we have used the ansatz given in Eq. (4.11) for the $e^\pm$ densities. The boundary conditions of this equation are

$$\tilde{I}(E_I, E_I;\mathbf{x}) = (b_T(E)/b(E,\mathbf{x}))(\rho(\mathbf{x})/\rho_\odot)^2, \tag{4.18}$$

$$\tilde{I}(E_e, E_I;\mathbf{boundaries}) = 0. \tag{4.19}$$

Notice that **boundaries** in the second condition stands for the geometric boundary of the region where the diffusion equation is solved (see Table 4.2). Commonly, it is solved by modeling the diffusion region as a cylinder with radius $R_{\rm max}$ =20 kpc, height

Benchmark model	K_0 [kpc^2/Myr]	δ	$L_{\rm max}$ [kpc]	$R_{\rm max}$ [kpc]
MIN	0.00595	0.55	1	20
MED	0.0112	0.70	4	20
MAX	0.0765	0.46	15	20

Table 4.2: Size of diffusion zone and diffusion parameters for MIN, MED and MAX models.

z equal to $2L$ and vanishing boundary conditions. The diffusion coefficient $K(E;\mathbf{x})$ is taken homogeneous inside the cylinder with an energy dependence following a power law $K(E) = K_0(E/1\text{GeV})^\delta$. For these three parameters L, K_0 and δ, the so called diffusion coefficients, we have adopted three sets referred to as MIN, MED and MAX models [369], which account for the degeneracy given by the local observations of the cosmic rays at the Earth including the boron to carbon ratio, B/C [370]. The value of these parameters can be seen in Table 4.2. We take these values as our benchmark points, although we note that MIN and MAX models do not imply minimal or maximal expected gamma-ray signal, respectively.

To solve this equation under the described conditions, we have used `BoxLib` [371] which is a general purpose partial differential equation solver with an adaptive mesh refinement method. We will show, however, that the use of the different diffusion models, MIN, MED, MAX, does not introduce a large variation in the DM constraints.

Let us finally remark about the importance of the energy loss function $b(E;\mathbf{x})$. The two main energy loss mechanisms of $e^\pm$ in the Galaxy are the ICS and synchrotron radiation produced by the interaction with the Galactic magnetic field. The former is the only contribution to the energy losses that is usually considered, since it is the most important one in studies of sources far from the GC. But when the $e^\pm$ energy reaches several hundreds of GeV, synchrotron radiation can dominate the energy loss rate due to the suppression factor in the ICS contribution in the Klein-Nishina regime. The energy loss function is expressed as follows,

$$b(E;\mathbf{x}) \;=\; \sum_i \frac{4\sigma_T}{3m_e^2} u_i(\mathbf{x}) E^2 R_i^{\rm KN}(E) + \frac{4\sigma_T}{3m_e^2} u_B(\mathbf{x}) E^2, \tag{4.20}$$

where $u_i(\mathbf{x}) = \int \mathrm{d}E\; n_i(E;\mathbf{x})$ and $u_B(\mathbf{x}) = B^2/2$ are the energy density of the i-th component of the interstellar radiation and the magnetic energy density, respectively. $R_i^{\rm KN}(E)$'s are the Klein-Nishina factors of each component. These factors can be deduced

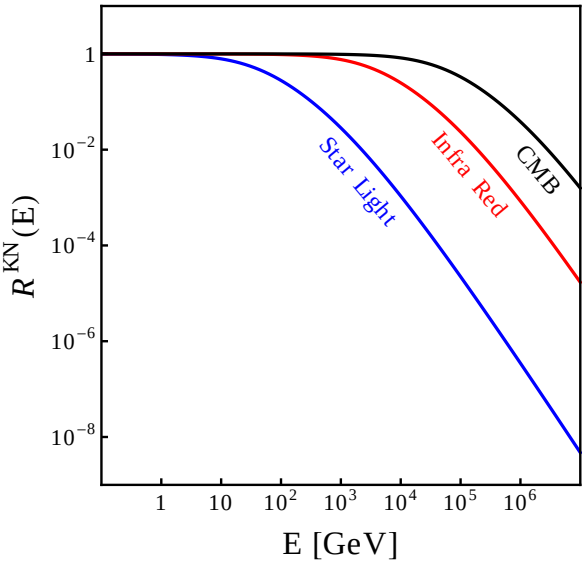

Figure 4.3: Klein-Nishina factors for each of the ISR component as a function of the energy. Below 1TeV the Klein-Nishina factor $R_i^{\rm KN}(E)$ factors are well approximated by one so the Thompson approximation is valid. For the SL component to be in the Thomson limit, the energy must be smaller than several tens of GeV.

from the numerical integral of the fully relativistic expression

$$b(E_e;\mathbf{x}) \equiv 3\sigma_T \int_0^\infty dE_\gamma^0\, E_\gamma^0 \int_{1/4\gamma^2}^1 dq\; n_{\rm ISR}(E_\gamma^0;\mathbf{x}) \frac{(4\gamma^2-\Gamma_\epsilon)q-1}{(1+\Gamma_\epsilon q)^3} \times \left[2q\lambda_N q + q + 1 - 2q^2 + \frac{1}{2}\frac{(\Gamma_\epsilon q)^2}{1+\Gamma_\epsilon q}(1-q)\right], \tag{4.21}$$

where $\gamma = E_e/m_e$ and $\Gamma_\epsilon = 4E_\gamma^0\gamma/m$. The numerical evaluation of the Klein-Nishina factor is shown in Fig. 4.3. As it can be seen, these factors reach the unity in the non-relativistic limit where the Thomson approximation is valid. However, for SL radiation this approximation holds only for energies below several tens of GeV. For this reason, we have taken the full expression of the Klein-Nishina factors regardless of the energy.

In contrast, synchrotron radiation losses do not have this suppression, and are driven by the magnetic field energy density $u_B(\mathbf{x}) = B^2/2$. Although the strength and exact shape of the Galactic magnetic field is not well known, in the literature it is broadly described by the following functional from [57],

$$B(r,z) = B_0\, \exp\left(-\frac{r-8.5\ \text{kpc}}{10\ \text{kpc}} - \frac{z}{2\ \text{kpc}}\right), \tag{4.22}$$

normalized with the strength of the magnetic field around the solar system, B_0, which is known to be in the range of 1 to 10 μG [368]. This field grows towards the GC

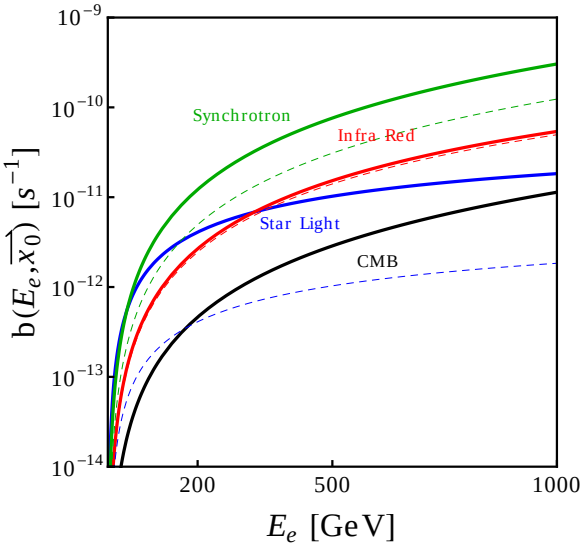

Figure 4.4: Energy losses for each component as function of the energy. These are evaluated at the Galactic plane ($z = 0$) and at two different radial distances $r = 500$ pc (solid) and $r = 5$ kpc (dashed). The reference value of the magnetic field has been fixed to $B_0 = 5$ μG. For the energy dependence we have used the full Klein-Nishina cross sections.

and therefore one should expect that the energy losses are dominated by synchrotron radiation in the inner part of the galaxy [57]. On the other hand, we can expect that when the magnetic field is stronger, the energy of the injected $e^{\pm}$ is more efficiently liberated in the form of synchrotron emission resulting in a softer spectrum, and producing therefore less stringent constraints on the DM annihilation cross-section.

In Figure 4.4 the energy losses for each component as function of the energy are depicted. These are evaluated at the Galactic plane ($z = 0$) and at two different radial distances $r = 500$ pc (solid) and $r = 5$ kpc (dashed). To evaluate the synchrotron losses, we have used a reference value of the magnetic field $B_0 = 5$ μG, which is the mean of the range we will consider. It is worth noting that for the energy dependence we have used the full Klein-Nishina factors deduced from Eq. (4.21). From this figure two main conclusions can be extracted. First, the energy losses are dominated by synchrotron even 5 kpc away from the GC in the whole energy range. It is interesting to see how the SL contribution is rapidly penalized since its Klein-Nishina factor starts to play a role at lower energies (see Figure 4.3), and then the IR starts to dominate the IC losses around 200 GeV. We have checked that for IR to be dominating at high energies, the reference value of the magnetic field at the Earth has to be below $\lesssim 2$ μG. Second, the variation of the losses with the position is rather small. This allows us to neglect the position

dependence of the energy losses, $b(E_e;\mathbf{x}) \approx b(E_e)$, which is welcomed since it greatly simplifies the diffusion equation (4.17).

4.2 The GC as a good place to search for DM

Now that theoretical grounds have been built, the next step is the experimental data. For this we have used the *Fermi*-LAT satellite data. It is the leading experiment for indirect searches in the GeV energy region, where light WIMP's signals are expected to show up. However, the GC is a relatively unknown place of our Galaxy, and thus although one would expect the J-factor (and WIMP signal) to be very high in this region, several other physical mechanisms might be occurring there producing GeV gamma-rays. For this reason, the data selection and processing must be very fine. This led us to calculate what regions around the GC are optimum for the dark matter searches.

4.2.1 Data selection and processing

The Fermi satellite was launched on June 11, 2008. Its main instrument, the Large Area Telescope (LAT) [330], collects high energy gamma rays ($\sim$ 20 MeV to $>$ 300 GeV) with a large effective area ($\sim$ 6200 cm^2 above 1 GeV for P7CLEAN_V6 at normal incidence [372]) and a large field of view (2.4 sr). For further details on the LAT we refer the reader to Ref. [330, 372].

In our analysis we have used the LAT photon data measured between August 4th, 2008, and June 15th, 2012, in the energy range between 1 GeV and 100 GeV. Events with zenith angles $< 100°$ are selected to reduce the contamination by gamma-ray emission from cosmic-ray interactions at the atmosphere. We have selected those events from the P7ULTRACLEAN_V6::FRONT class. This choice not only reduces the cosmic-ray background contamination but also takes advantage of a narrower PSF as compared to back-converting events. We make a reasonable assumption on systematic uncertainty extending it from Source and Clean classes. The systematic uncertainty of the effective area for both Source and Clean class events is quoted as 10% at 100 MeV, decreasing to 5% at 560 MeV, and increasing to 20% at 10 GeV and above [372]. Maps of flux for different energy ranges from a region of 30° around the GC have been made using the version V9r28 of the LAT Science Tools [373]. As we will show later, we can use a single flux map (built summing up the flux maps for the different energy ranges) to select the Region Of Interest (ROI) with the aim of maximizing the S/N ratio for each individual DM profile under study.

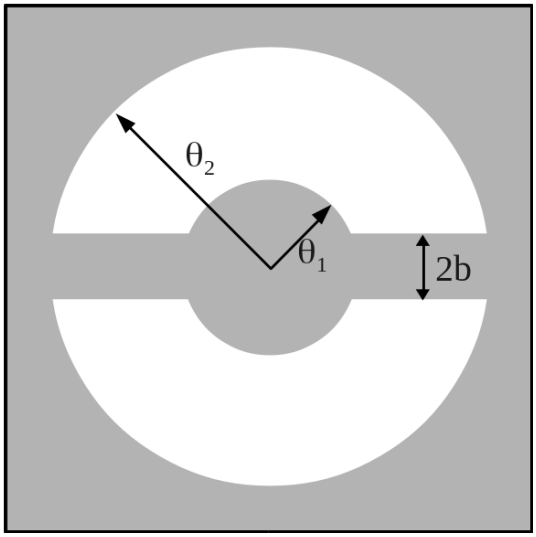

Figure 4.5: Schematic view of our choice of the ROI. The gray area represents the masked region.

4.2.2 Optimization of the region of interest for dark matter searches

An important step in our analysis is the optimization of the ROI using a data-driven procedure that maximizes the S/N ratio. In order to do so, we follow a procedure similar to the one presented in the appendix A of [135]:

1. We produce $40^\circ \times 40^\circ$ maps centered on the GC of the quantity $\bar{J}(\Delta\Omega)\Delta\Omega$ for the four DM density profiles considered (i.e., Einasto, NFW, NFWc and Burkert) and use them as signal. Each pixel i has an area of $0.2^\circ \times 0.2^\circ$ and contains a J-factor value J_i calculated with Eq. (4.6).

2. We use as noise the square root of the observed photon flux integrated in the energy range 1-100 GeV. We use a single map, instead of a different one for each energy bin since the morphology of the background does not exhibit strong variations in energy. The flux in pixel i is labelled as F_i.

3. A mask, defined by three angles θ_1, θ_2 and $|b|$ as shown in Figure 4.5, is introduced to cover the GC, the Galactic plane, and the high galactic latitude regions, where the statistical fluctuations of the Galactic foreground dominate over the expected DM signal.

4. The optimization procedure consists of finding the set of angles that mask a region such that the S/N ratio is the largest for each DM profile considered. What we technically do is to minimize the inverse of the following quantity

$$S/N = \frac{\sum_i J_i}{\sqrt{\sum_i F_i}} \tag{4.23}$$

with i running over unmasked pixels, varying masks. We use the numerical routine `Fmin` of the Python module `scipy.optimize` [6], which minimizes a function using the downhill simplex algorithm. We end up with four masks characterized by those angles given in Table 4.3. In the same Table, we also show the values of $\Delta\Omega$ and $\bar{J}(\Delta\Omega)\Delta\Omega$ for each profile. As expected, $\theta_1 = |b|$ for all the profiles, since the broadest emission in the Galactic plane is the one at the GC.

In Figure 4.6 we show the ROI that we have obtained for each DM density profile in Table 4.1. Clearly, the NFW$_c$ ROI is the smallest one. This can be easily understood by inspecting the right panel of Figure 4.2: the $\bar{J}(\Delta\Omega)\Delta\Omega$ quantity for NFW$_c$ becomes almost constant beyond only 5°, whereas for the other profiles this quantity becomes flat at much larger radii. Therefore, in the case of the NFW$_c$ profile, increasing the angular aperture by a few more degrees does not increase the S/N.

Note that the usual quantities to calculate S/N ratios are observed counts and expected DM-induced counts but in this work, instead, we use observed gamma-ray flux (rather than counts) and J-factors (formally proportional to the expected DM-induced gamma-ray flux). Nevertheless, we have checked that the use of observed fluxes and predicted J-factors turns out to be a very good approximation, which leads to similar optimized ROIs. We performed the following test. Using the gtobssim tool and assuming the NFW profile, we simulated the events that different DM models could produce in the LAT after 46 months of observation. We used the same IRFs, cuts and procedure to select events as those used for the real observations. Instead of using a fixed $1 - 100$ GeV energy range we further optimize this quantity choosing an energy range centered around the DM emission peak. We then compare the simulated DM counts maps and the actually observed counts map in the given energy range to re-derive the optimized S/N region. As anticipated above we find that the derived ROI's parameters using counts maps do not change significantly for different DM models from those calculated using observed fluxes and J-factors and a fixed energy range.

[6] http://docs.scipy.org/doc/scipy/reference/optimize.html#

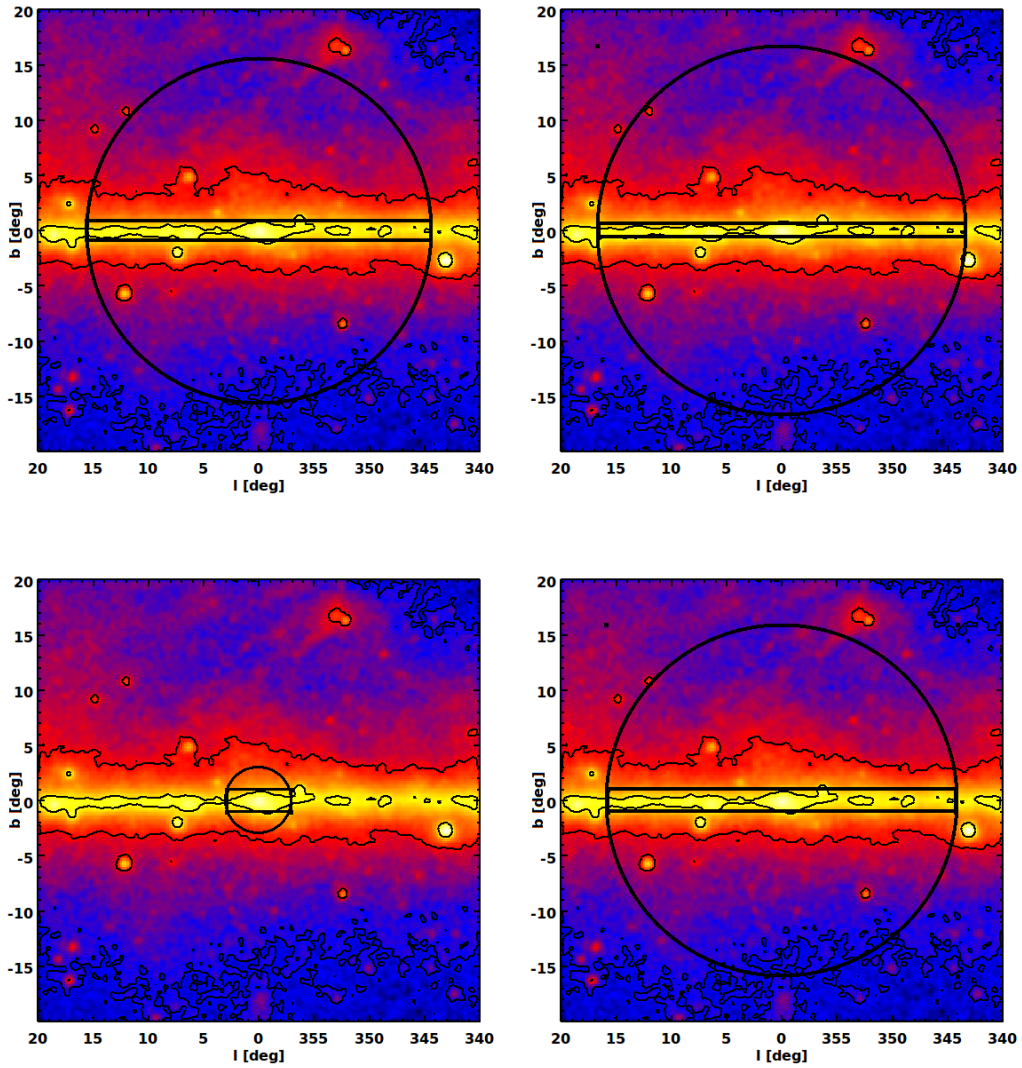

Figure 4.6: Maps of the observed flux by the *Fermi*-LAT in the energy range $1 - 100$ GeV, in units of photons cm^{-2} s^{-1}, for the four DM profiles studied. Upper left: Einasto, upper right: NFW, bottom left: NFW$_c$, and bottom right: Burkert. For each profile, the ROI is the region inside the circle excluding the band on the Galactic plane. Color scale is logarithmic, yellow, red and blue correspond to 3.6×10^{-9}, 6.4×10^{-10} and 1.2×10^{-10} photons cm^{-2} s^{-1}, respectively. These values also correspond to black contours. In order to reduce statistical noise and to bring up finer features in the inner galaxy the map is smoothed with a 0.2° FWHM Gaussian function.

Profile	θ_1 [°]	θ_2 [°]	$\lvert b\rvert$ [°]	$\Delta\Omega$ [sr]	$\bar{J}(\Delta\Omega)\,\Delta\Omega$ [$\times 10^{22}$ GeV^2 cm^{-5} sr]	Flux $(1-100$ GeV) [$\times 10^{-7}$ cm^{-2}s^{-1}]
Burkert	0.8	15.9	0.8	0.225	41.9	32.1 ± 0.3
Einasto	0.7	15.6	0.7	0.217	5.1	31.4 ± 0.3
NFW	0.6	16.7	0.6	0.253	3.3	38.0 ± 0.3
NFW$_c$	1.0	3.0	1.0	0.005	86.8	2.2 ± 0.1

Table 4.3: The optimized regions for the DM density profiles studied, defined by the angles shown in Figure 4.5. The corresponding values for $\Delta\Omega$, $\bar{J}(\Delta\Omega)\Delta\Omega$, and observed flux with statistical errors only (in the energy range between $1-100$ GeV) are also shown.

4.2.3 Flux measurement

Following the analysis described above, we show in Figure 4.6 the flux observed by the *Fermi*-LAT, and the ROIs corresponding to each of the DM profiles considered. The value of this flux integrated in the energy range $1-100$ GeV can be found in the last column of Table 4.3. The energy spectra from the ROI associated to each profile are shown in Figure 4.7. We limit the energy range of the analysis to be below 100 GeV in order to have a small statistical uncertainty in each bin, falling generally below the systematic uncertainty. In this way we remove the possibility for the upper limits to be accidentally dominated by a large downward fluctuation in the energy bins close to the peak of the gamma-ray emission from DM annhilation, which is the most constraining point when comparing to the measured flux.

To set constraints we require that the DM-induced gamma-ray flux does not exceed the flux upper limit (UL) evaluated as follows. We set 99.98% UL signal counts using the Bayesian approach presented in Ref. [374], for the case of absence of background with systematic uncertainties not included, which correctly takes into account the Poisson limit (i.e. the case of a small number of counts). Using exposure maps calculated with the gtexpcube2 tool of the Science Tools we are able to convert UL signal counts into the UL signal flux needed to set constraints.

4.2.4 Limits on the dark matter annihilation cross-section

As already discussed, we adopt a conservative approach in the analysis of the limits on the DM annihilation cross section, simply requiring that the integrated gamma-ray flux of the expected DM signal for each energy bin does not exceed the upper limit signal

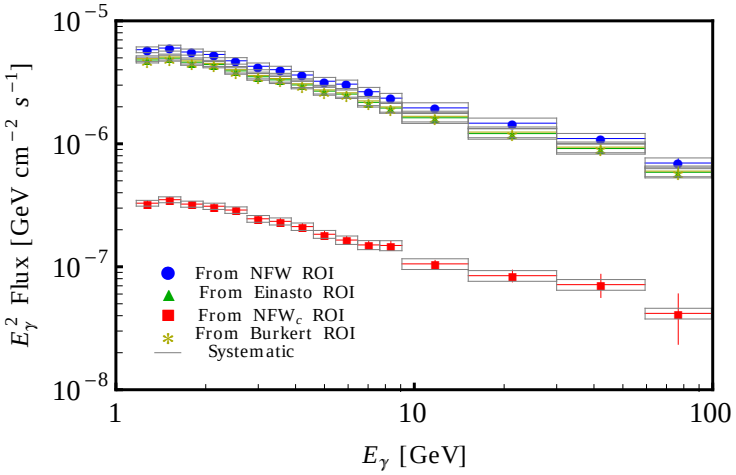

Figure 4.7: Energy spectra extracted from *Fermi*-LAT data for the optimized regions that are shown in Figure 4.6. Data are shown as points and the vertical error bars represent the statistical errors. The latter are in many cases smaller than the point size. The boxes represent the systematic error in the *Fermi*-LAT effective area.

flux evaluated following the Bayesian procedure in Ref. [374][7]. Let us remark that in this analysis we do not subtract any astrophysical background, which makes it very robust and reliable.

The results are presented in Figure 4.8, where the constraints obtained are shown for different final states. The case $\langle\sigma v\rangle_0 = 3\times10^{-26}$ cm^3 s^{-1} is also illustrated by means of an horizontal line, which corresponds to the value of the annihilation cross-section associated to the correct thermal relic abundance for a WIMP whose annihilation is dominated by the s-wave (velocity-independent $\langle\sigma v\rangle_0$ as we are considering) contribution and thus, $\Omega_{DM}\, h^2 \approx 3\times10^{-27}$ cm^3 s^{-1} $\langle\sigma v\rangle_0^{-1} \approx 0.1$ [47]. For comparison, the constraints are given considering only the contribution from prompt gamma rays and the total contribution from prompt plus ICS gamma rays.

Several things must be noted from these results. First, if the DM density follows an Einasto, NFW or Burkert profile, the upper limits on the annihilation cross section are always above the value of the thermal cross-section for any annihilation channel. This means that, without any background subtraction, the *Fermi*-LAT experiment does

[7]It is worth noting that even though we optimize the ROIs based on both, DM and observed distributions, to set limits on DM annihilation cross section we perform a spectral analysis. It would be interesting for a future work to check that at the upper limit cross sections derived here, the implied spatial distribution of the gamma-ray signal intensity does not significantly exceed the data anywhere within the ROI at any energy.

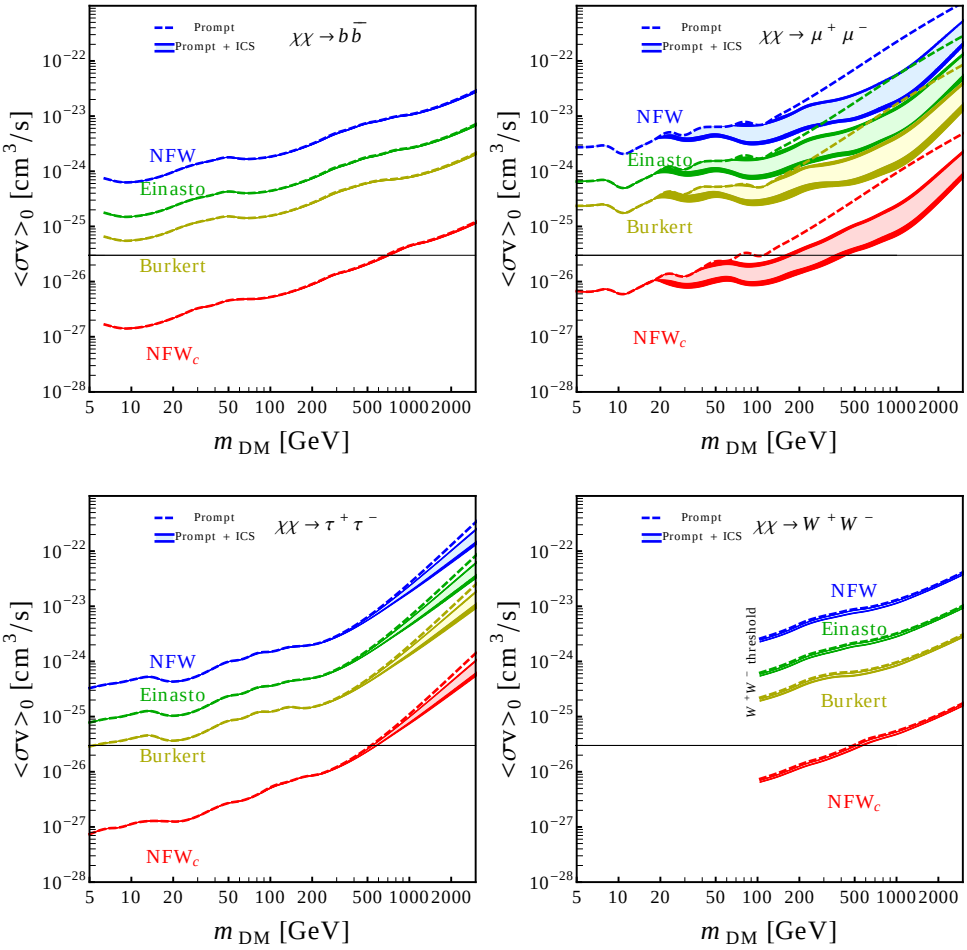

Figure 4.8: 3σ upper limits on the annihilation cross-section of models in which DM annihilates into $b\bar{b}$, $\mu^+\mu^-$ (upper panel), $\tau^+\tau^-$ or W^+W^- (lower panel), for the four DM density profiles discussed in the text. Upper limits set without including the ICS component in the computation are also given as dashed curves (prompt) for comparison. The uncertainty in the diffusion model is shown as the thickness of the solid curves (from top to bottom: MIN, MED, MAX) while the lighter shaded regions represent the impact of the different strengths of the Galactic magnetic field with lower(higher) values of the cross-section corresponding to $B_0 = 1$ μG($B_0 = 10$ μG). The horizontal line corresponds to the expected value of the thermal cross-section for a generic WIMP candidate.

not have enough sensitivity to explore thermal WIMPs annihilating at the GC for non contracted profiles. Nevertheless, the situation is drastically different when we consider the DM compression due to baryonic infall in the inner region of the Galaxy. Indeed, by adopting the NFW$_c$ profile and for a $b\bar{b}$, $\tau^+\tau^-$ and W^+W^- channel, the thermal annihilation cross-section is already reached for a DM mass of 680, 530 and 490 GeV, respectively. For the $\mu^+\mu^-$ channel the effect of the prompt gamma rays is less important

since generally fewer photons are produced in the FSR compared to the hadronic decays of the other channels. For example, in the W^+W^- final state, which is open when $m_{DM} \gtrsim 90$ GeV, the $W^\pm$ decays produce a large number of photons, especially at high energies. As indication of this, we can see that the lower bound associated with prompt gamma rays for $\mu^+\mu^-$ is 100 GeV compared to about 500-700 GeV in the other channels. Another important thing to note is the importance of the ICS component in this case. A final state of muons produces a relatively harder $e^\pm$ spectrum in comparison with the other final states[358]. This means that the energy injected to the $e^\pm$ is higher and more energetic gamma-rays are expected from ICS. Actually to see the importance of the ICS component in the other channels one has to reach DM masses above 3 TeV for the $e^\pm$ to be produced with enough energy to produce photons in the GeV energy range.

Another interesting fact of the ICS component (for the $\mu^+\mu^-$ channel) is that for $B_0 = 1$ μG the lower bound on the DM mass turns out to be 358 GeV and for $B_0 = 10$ μG the bound is 157 GeV, using the MIN diffusion model. For MED and MAX diffusion models the values turn out to be 404, 171 GeV and 439, 179 GeV, respectively. This is a consequence which follows the discussion in Subsection 4.1.3. When the magnetic field is stronger, the synchrotron easily dominates the energy losses at all energy ranges and in general at any position. Therefore, the energy of the injected $e^\pm$ is more efficiently liberated in the form of microwaves (synchrotron radiation) which falls well below the *Fermi*-LAT threshold. This results in a softer gamma-ray spectrum, and produces hence lower constraints . This clearly highlights that in those cases in which the ICS component is dominant (for heavy WIMP masses in general), the variation of the magnetic field can significantly alter the expected gamma-ray fluxes from the inner regions of the Galaxy.

Although these results could be interpreted in general as implying that vanilla WIMP models and contracted DM profiles are incompatible with the *Fermi*-LAT data, we already know from Chapter 2 that when one works in the framework of a specific particle physics model this conclusion might in principle be avoided in some regions of the parameter space. We have seen that the value of the annihilation cross section in the Galactic halo might be smaller than 3×10^{-26} cm^3 s^{-1} for a DM candidate that is thermally produced. For example, in the early Universe coannihilation channels can also contribute to $\langle \sigma v \rangle_0$, and resonances can enhance or decrease several orders of magnitude the cross section. Another obvious thing is that in general the final state is a combination of several annihilation channels. Using our results from Chapter 2, in the MSSM case we have seen that, although the final state was always almost 100 % $\tau^+\tau^-$, the annihilation cross section was temperature suppressed and then below the thermal cross section. In the NMSSM, we had annihilation modes of about 70% $\bar{b}b$ $-$ 30% $\tau^+\tau^-$ for a Bino-like

neutralino, and 100% W^+W^- for a Wino-like neutralino (which also happens in Higgs-portal models). On the other hand, the Sneutrino in the NMSSM was a clear case of how different the thermal cross section might be in an specific model. But, let us come back to these comparison in more detail in the next Section.

Another general remark is that the upper limits on the annihilation cross-section that we have obtained for the cases of NFW, Einasto and Burkert profiles are comparable to the ones previously reported by the *Fermi*-LAT collaboration [263], after a similar analysis of the Galactic halo without modeling of the astrophysical background (similar results were also obtained in Ref. [375, 376]). Modeling of the background was also considered in Ref. [263], and the results are competitive with those from dSphs [132, 259], where the upper limit of the annihilation cross section is below the thermal one for DM masses smaller than 27 and 37 GeV assuming a $b\bar{b}$ and a $\tau^+\tau^-$ channel, respectively.

Remarkably, when we take into account the baryonic infall in our conservative analysis, forcing the DM to contract in those inner regions of the Galaxy, we obtain much stronger limits. In particular, as discussed above, using our compressed DM density profile, NFW$_c$, the thermal cross section is excluded for a DM mass smaller than 680 and 530 GeV in the $b\bar{b}$ and $\tau^+\tau^-$ channel, respectively, thus improving those limits obtained from dSphs [132, 259], and also those obtained from galaxy clusters [377]. In the latter, DM masses smaller than about 100 GeV are constrained provided that DM subhalos significantly contribute to boost the DM signal.

4.3 Facing light SUSY DM with the upper limits from the GC.

Now it is the moment to test the SUSY models we analyzed in Chapter 2 against the limits we have extracted from the GC. Since using the uncompressed profiles (NFW, Einasto and Burkert) the sensitivity of Fermi is less than the necessary to constrain thermal DM candidates, only the NFW$_c$ profile is going to be used from now on.

To compare directly the limits on $\langle\sigma v\rangle_0$ with model predictions has some disadvantages as we have commented previously. However, to circumvent this issues we are going to compare only those model solutions in which we expect details not to change the main conclusions. To do so, the first thing to be done is to classify the model solution by final states of $\langle\sigma v\rangle_0$ at the halo, not using $\langle\sigma v\rangle$ at the freeze out as we did in Chapter 2 (see Table 2.2). The color code will be the same as before, however, now we will only compare solutions with more than 75% of $b\bar{b}$, $\tau^+\tau^-$ and W^+W^- final states.

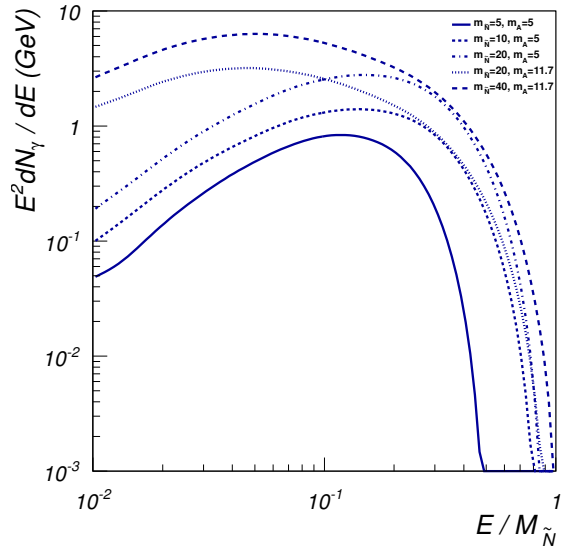

Figure 4.9: Photon spectra for the decay of A_1^0 into b-quarks and τ-leptons as a function of E_γ normalized to the Sneutrino mass. The labels denote the Sneutrino and CP-odd Higgs mass. Those cases with $m_{A_1^0} = 5$ GeV correspond to a 4τ final state, whereas those with $m_{A_1^0} = 11.7$ GeV correspond to a $4b$ final state.

For the Sneutrino, we saw that many solutions corresponded to $A_1^0 A_1^0$ or $H_1^0 H_1^0$ final states. On the one hand, when these particles are heavier than $2m_b$ they decay predominantly into b-quarks so $\mathrm{BR}(H_1^0(A_1^0) \to b\bar{b}) \approx 1$. This means that the annihilation of Sneutrinos in the Galactic halo in these cases would be the following $\tilde{N}_1\tilde{N}_1 \to H_1^0 H_1^0 (A_1^0 A_1^0) \to b\bar{b}b\bar{b}$, and then more quarks are expected in the final state in comparison with the pure $b\bar{b}$ final state. On the other hand, if these Higgses are lighter than $2m_b$, they typically decay into $\tau^+\tau^-$, and then the reaction $\tilde{N}_1\tilde{N}_1 \to H_1^0 H_1^0 (A_1^0 A_1^0) \to \tau^+\tau^-\tau^+\tau^-$ takes place.Taking all this into account, one can not compare these cases with typical bounds on $b\bar{b}$ or $\tau^+\tau^-$, these require a careful and dedicated individual analysis. On top of this, these final states might be very model dependent because, although the decay of CP-even and CP-odd Higgses into $b\bar{b}$ or $\tau^+\tau^-$ are dominant in general, the specific branching fractions vary across the parameter space of the model. As an example of this, in Figure 4.9 the gamma-ray yield for different $A_1^0 A_1^0$ final states is depicted. We show for three different Sneutrino masses the final state corresponding to 4τ, when $m_{A_1^0} = 5$ GeV. The remaining two cases represent the $4b$ final state, when $m_{A_1^0} = 11.7$ GeV. For the reasons exposed, we have left these cases for future work and here we will only analyze solutions with more than 80% of $b\bar{b}$, $\tau^+\tau^-$ and W^+W^- final states, as mentioned earlier.

4.3.1 The MSSM at the GC

Let us start by analyzing the neutralino in the MSSM as we did before. In this case we have learnt that the only possible final state is $\tau^+\tau^-$, reaching around 100% of the annihilation, through a t-channel mediated by the RH-stau. Eq. 2.33 highlighted that when both Staus have a small mixing the annihilation cross section in the Halo is dominated by the velocity dependent term b. For this reason, the cross sections in the points we analyzed were smaller than the thermal cross section and out of the reach of the GC searches presented here.

4.3.2 The NMSSM at the GC

Thanks to the new *singlino* component of the Neutralino in this SUSY construction, we have found that these particles might be as light as 3 GeV while allowed by all experimental constraints. However, the relic abundance imposes the presence of very light CP-odd or CP-even Higgses (singlet-like) for resonant annihilations to take place. The resonances have a strong impact on indirect detection prospects, as we have seen, and the $\langle\sigma v\rangle_0$ predictions were generally far below the thermal cross section.

In figure 4.10 the thermally averaged cross sections of Neutralinos in the NMSSM compared with the upper limits from the previous section using a NFW$_c$ are shown. As we have anticipated, the resonant annihilations in the Early Universe necessary to account for the correct abundance makes the constrain of very light Neutralinos ($\lesssim 50$ GeV) very weak even for the NFW$_c$ case. The only possibility for the region of the parameter space that we have analyzed is Neutralinos above m_W, where the W^+W^- channel opens and the relic density can be achieved without resonant annihilations. It is interesting to note that these kind of solutions can be constrained only with the compressed profile, since although the thermal cross section is close to the canonical value, the mass of the DM penalizes the upper limit.

Notice that in comparison with Fig. 2.9, now we have more solutions corresponding to a $\tau^+\tau^-$ final state. This is due to the classification criterium used in this case. Before we have used the $\langle\sigma v\rangle$ (Early Universe) and now we are using $\langle\sigma v\rangle_0$ (Halo). In Ref. **??** it is explicitly shown how the branching fractions for each channel can change when considering low velocities (cross section in the Halo). In fact, it can be seen how the annihilation into $\tau^+\tau^-$ becomes dominant in the Halo being subdominant in the Early Universe as it is occurring in some of the cases analyzed here. Furthermore, most of the solutions we had for neutralinos lighter than 30-35 GeV now are not shown. This is

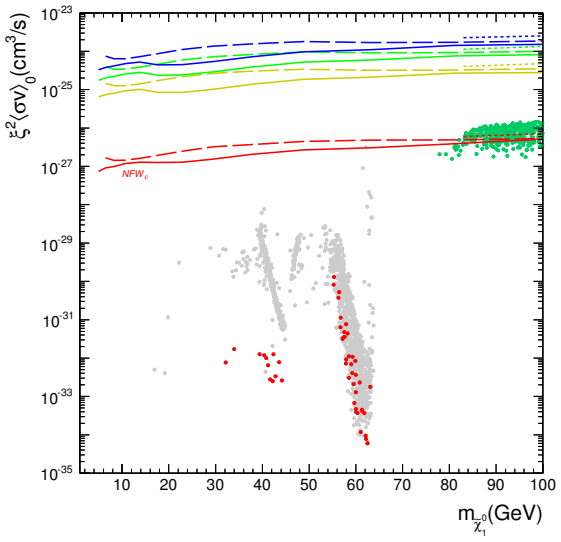

Figure 4.10: Thermally averaged cross sections of Neutralinos in the DM haloes weighted by their density squared (ξ^2) as a function of the Neutralino mass in the NMSSM. We have included the upper limits from figure 4.8 for $\tau^+\tau^-$ (solid), $b\bar{b}$ (dashed) and W^+W^- (dotted). The color code is as in Table 2.2 but using $\langle\sigma v\rangle_0$. We use solutions with more than 75% annihilation into the corresponding channel.

because in this case the mixing of different final states is very high, and then, imposing more than 75% of annihilation in the Halo makes them disappear.

4.3.3 The NMSSM-RH at the GC

The Sneutrino in the NMSSM is an excellent DM candidate. In Chapter 2 we showed the rich phenomenology associated to this construction, namely the variety of direct and indirect detection prospects. We also showed that there exists a deep connection between the Sneutrinos and the Higgs sector, since the Higgs boson is the responsible to communicate the DM and SM particles through a s-channel exchange. Therefore, the resonances between the Sneutrinos and the lightest Higgs appear in extensive regions of the parameter space conditioning both direct and indirect detection phenomenologies.

The Sneutrino thermal cross section is velocity independent since it is a scalar particle. Those channels which dominates in the early Universe will dominate the cross section in the Halo as well. This means that the variety of final states potentially produced by Sneutrino annihilations in the Galactic Halo is enormous. As in the previous cases, the bounds from the GC were extracted assuming the standard channels, hence here

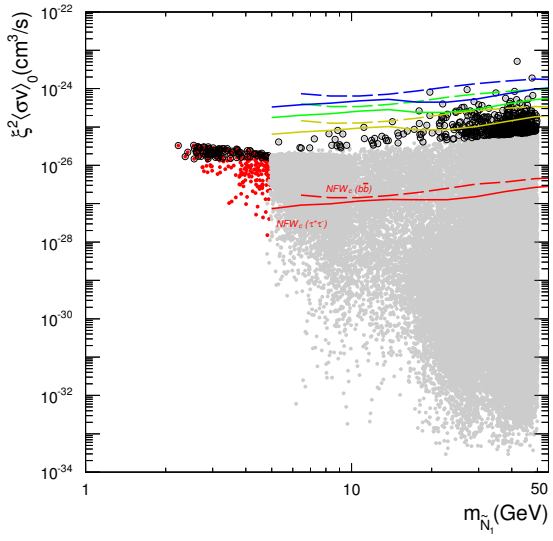

Figure 4.11: Same as right panel of Fig. 2.16 but including the upper limits from figure 4.8 for $\tau^+\tau^-$ (solid) and $b\bar{b}$ (dashed). The colors for the lines are the same. The color code for the points is as in Table 2.2 but using $\langle\sigma v\rangle_0$.

we will only concentrate on $\tau^+\tau^-$ and $b\bar{b}$ final states[8]. Also, when no resonances or coannihilations are present, the thermal cross section must lie around the canonical value. In all these cases and based on Fig. 4.8, we expect that if the DM profile of the MW follows a NFW$_c$ form, most of the solutions will be excluded.

In Figure 4.11 we represent the thermally averaged cross section of Sneutrinos as a function of its mass for points which are allowed by all the experimental constraints, just like right panel of Figure 2.16 but for $\tau^+\tau^-$ (red points) and $b\bar{b}$ (grey points) final states. The black circles denote those points excluded by dwarf analysis. The lines correspond to the upper limits from Fig. 4.8 with same color code and the solid and dashed lines denoting $\tau^+\tau^-$ and $b\bar{b}$ cases, respectively. The first thing one can notice is that both final state solutions are greatly constrained by the NFW$_c$ profile[9]. Another important is remark is that for the non-contracted profiles, the upper limits from the GC are in the same ballpark as the dwarf limits. It highlights that the very conservative limits we have

[8] We remind the reader that for the Sneutrino we concentrate in masses lighter than 50 GeV and thus the W^+W^- final state is no possible.

[9] The reader must note that the limits extend down in mass up to 5 GeV since it is the limit in the tables used to extract the limits. However, it is trivial to see how if one extrapolates the behavior of the upper limit to lower masses in the $\tau^+\tau^-$ case, almost all red points would be excluded by the contracted profile.

extracted from the GC are competitive with those extracted from dwarfs.

In summary, the NFW$_c$ profile would not be in conflict with light thermal Sneutrino DM in the NMSSM as long as a light Higgs (lighter than 100 GeV) exists providing a resonant annihilation of Sneutrinos in the early Universe. For the case of $\tau^+\tau^-$ final state, things are more difficult than in the $b\bar{b}$ case. A resonant annihilation would require the presence of a very light Higgs (lighter than 10 GeV), which would modify strongly the SM-Higgs properties. For this reason most of the $\tau^+\tau^-$ (red points) cases are around the canonical cross section and thus in conflict with the NFW$_c$ profile. Still, some of the red points are below the *Fermi*-LAT collaboration sensitivity for a contracted profile. Interestingly, some Sneutrino scenarios would be in conflict even with a Burkert profile, or an Einasto profile.

4.4 Sneutrinos in light of the GC excess

Finally, following the discussion in this chapter about DM in the GC of the MW, we would like to point out that if the low-energy excess in the gamma ray flux from the Galactic Centre was confirmed, as commented in chapter 1 the analyses of Refs. [129, 144–147, 258, 378] suggest that it could be explained by annihilation of light dark matter particles. The analysis of this excess in Ref. [148] favours DM with a mass in the range of around $8-65$ GeV, annihilating preferentially to a mixture of $\tau^+\tau^-$ and $b\bar{b}$ final states with $\langle\sigma v\rangle_0$ of order of the thermal relic value (see Fig. 10 and Table. IV in Ref. [148]). In Table 4.4, we show some examples of the RH sneutrino parameter space with dominant $b\bar{b}$ annihilation inside the 5σ confidence region derived in Ref. [148], as well as an example for the best-fit point. Findings in Ref. [148] are in agreement with the results of a recent work, which favours $31-40$ GeV DM annihilating to $b\bar{b}$ with $\langle\sigma v\rangle_0 = (1.4-2.0)\times 10^{-26}$ cm^{3}s^{-1} [378]. We also provide an example compatible with this range.

These analysis about a possible excess in the GC are completely different than the one we have performed. While in our case we did not assume a background, in these cases one has to assume a specific background. So the bounds we have extracted can not be directly applied to these results. Furthermore, the profile favored by the signal is not in correspondence with anyone we have used. Actually, it would correspond to a NFW$_c$ with much less adiabatic contraction, meaning that the profile would lie between our NFW and our NFW$_c$.

$m_{\tilde{N}_1}$(GeV)	$\xi^2\langle\sigma v\rangle_0$(cm^3/s)	$\%b\bar{b}$	$\%\tau^+\tau^-$	$\%c\bar{c}$	$\%gg$	$\xi\sigma^{SI}$(pb)
11.08	1.28×10^{-26}	88.25	6.81	4.29	0.59	3.03×10^{-9}
12.51	1.23×10^{-26}	89.28	6.75	3.21	0.72	4.14×10^{-10}
13.87	1.21×10^{-26}	86.86	6.68	5.42	0.97	1.72×10^{-11}
14.96	1.42×10^{-26}	89.74	6.81	2.56	0.83	4.09×10^{-10}
18.69	2.34×10^{-26}	86.84	6.80	4.63	1.65	1.04×10^{-9}
21.13	1.73×10^{-26}	87.56	6.94	3.67	1.74	7.17×10^{-12}
23.60*	2.10×10^{-26}	79.76	6.65	9.20	4.22	6.69×10^{-10}
27.35	1.72×10^{-26}	66.26	4.88	1.86	9.91	5.91×10^{-11}
35.62**	1.71×10^{-26}	90.54	7.70	0.47	1.22	1.05×10^{-10}
42.98	3.05×10^{-26}	73.47	6.77	7.86	11.29	4.91×10^{-12}
43.54	3.03×10^{-26}	91.19	7.92	0.38	0.45	7.35×10^{-13}
45.48	3.19×10^{-26}	52.50	5.11	16.11	24.45	4.31×10^{-11}
48.29	2.98×10^{-26}	91.13	8.16	0.08	0.56	2.33×10^{-10}

Table 4.4: Sample points within the 5σ region consistent with the observed low-energy excess in the gamma-ray emission at the GC identified in the Fermi LAT data (see Fig. 10 and Table. IV in Ref. [148]). For each point we indicate the RH sneutrino mass, thermally averaged annihilation cross-section, annihilation final states, and spin-independent elastic-scattering cross-section. The asterisk denotes an example compatible with the best fit point of Ref. [148] and two asterisks correspond to an example for Ref. [378].

4.5 Indirect searches at the GC (conclusions).

Indirect searches for DM are a very powerful tool. In this chapter we have extracted upper bounds on the annihilation cross section of DM particles using data from the GC of the *Fermi*-LAT satellite. Even following a conservative approach, a zero background has been assumed, the bounds obtained are relatively stringent in comparison with other studies. When an adiabatically compressed halo is considered, the bounds are extremely strong constraining DM masses as heavy as 500 GeV.

We started reviewing what are the main processes that are expected to create photons from DM annihilations in model independent way, namely the prompt and ICS components. Although the prompt component is tabulated and well known, we have carried out a detailed calculation of the ICS component. For this purpose, we have used information from sources like `Galprop` for the interstellar radiation field which must be properly

included in the energy losses of the inverse compton process. Besides, we have included in this calculation the effects of the galactic magnetic field, which has been found to be the dominant energy loss via synchrotron radiation. The impact of the magnetic field is rather strong in some cases. For instance, in the $\mu^+\mu^-$ final state, the bounds reach the thermal cross section with a difference of 150 GeV roughly corresponding to a difference in the reference value of the magnetic field of 10 μG. Actually, in all cases the effect of vary the diffusion parameters from MIN to MAX are almost negligible. Another important point is that we have shown that the ICS contribution at the inner galaxy for the gamma-ray case can be safely neglected for light DM candidates.

The inner galaxy has been demonstrated to be the perfect place to search for DM since the DM density in there is expected to be very high. However, it is a relatively unknown place. There might be physical processes there producing photons that are yet not described, or at least well described. For this reason our approach, assuming no background, is very reasonable. Although this assumption relaxes severely the constraints making not posible to constrain thermal DM candidates for the usual, non contracted, profiles NFW, Einasto and Burkert. For the NFW$_c$ we could constrain thermal candidates up to masses of 680, 530 and 490 GeV for $b\bar{b}$, $\tau^+\tau^-$ and W^+W^- channels, respectively.

A good way to test the goodness of these bounds we have used the results for the light Neutralino and light Sneutrino DM scenarios, previously analyzed in this thesis in the context of the MSSM, NMSSM and NMSSM-RH models. For the non-contracted profiles, since the bounds do not reach the canonical value, the only possibility was to constrain resonant annihilations. In effect, for the Sneutrino some resonant solutions for the $b\bar{b}$ final state could be ruled out. For the NFW$_c$ case, the bounds are able to rule out many of the solutions for the Sneutrino case, specially for the $\tau^+\tau^-$ final state. In contrast, the light Neutralino DM in the NMSSM could only be probed for some of the W^+W^- final states. All other cases were far from the sensitivity since they encode a resonant annihilation with a light singlet-like scalar (H_1^0 or A_1^0). Finally, in the MSSM the situation seems to be difficult. All solutions were $\tau^+\tau^-$ dominated and no resonant annihilation was present, however, the p-wave behavior of the cross section and the relatively heavy mass, around 40 GeV, made this case out of the sensitivity even for the contracted profile.

Finally, and for completeness, we have showed the Sneutrino could be a perfect candidate to account for the gamma-ray excess seen at the GC. Recent studies have claimed that *Fermi*-LAT data shows a clear bump at low energies that might be explained in terms of annihilating DM. If so, the mass and cross section which best fit the data are around 10-50 GeV and a canonical cross section approximately. As a s-wave annihilator,

the Sneutrino predicts cross sections close to the thermal value in most of the cases, and as we have seen the flexibility of the model allows very light masses rather easily.

Chapter 5

Conclusions

English

There is no doubt that the Universe is permeated by an exotic form of matter known as dark matter. Numerous astronomical observations, that began almost one hundred years ago, have shown that 85% of the matter content of the Universe is in form of dark matter whose only probed interaction with ordinary matter is purely gravitational. This states one of the greatest challenges in modern physics. On the one hand, in spite of the success of the Standard Model of particle physics, it does not include an appropriate dark matter candidate. Therefore, a theoretical effort must be done in order to extend this model providing a proper description of the dark matter in terms of elementary particles. On the other hand, it is crucial to test if dark matter interacts not only gravitationally with ordinary matter. In this sense, many experimental collaborations around the world are trying to detect dark matter via non gravitational interactions. The dark matter problem joins the efforts of both experimental and theoretical physicists.

This thesis addresses the issue of dark matter from these two perspectives. Focusing on light dark matter (with a mass below 100 GeV), the problem is faced from a theoretical point of view studying three supersymmetric WIMP candidates, and also analyzing theoretically the experimental side of both direct and indirect searches. The supersymmetric models analyzed, the Minimal Supersymmetric Standard Model and the Next-to-Minimal Supersymmetric Standard Model are shown to offer a theoretically well motivated framework in which light dark matter, represented by Neutralinos or right-handed Sneutrinos, is viable. Using the up to date experimental constraints derived from the LHC data, we have analyzed regions of the parameter space of these models in which light dark matter is feasible in light of the experimental constraints. We have

found that, in many cases, it might be detected by the next generation of direct detection experiments.

A direct detection in the future would certainly mean that dark matter has not only gravitational interactions, which would push the WIMP paradigm as a reality. However, a single detection would not provide much more information. There is a need to detect dark matter using different target materials, otherwise the amount of information we can extract from the signal is limited. Nowadays the biggest detectors are made of Germanium or Xenon, but as we have shown here, even assuming a detection in both of these targets the nature of dark matter would not be entirely reconstructed. Simulating a detection in several targets we have demonstrated that targets based on Fluorine, Aluminium or Tungsten, and with energy discrimination, may provide a complementary information to those based on Germanium and Xenon. Using this complementarity between different targets, and depending on the real nature of dark matter particles, the reconstruction could be unique. These targets are hence a good option for next generation experiments.

Nonetheless, the complementarity between different targets is not exempt of drawbacks. To maximize the amount of information one would extract from a single or multiple signals in direct detection experiments, the uncertainties must be under control. It is astonishing how direct detection signals are dependent on astrophysics, nuclear and particle physics, since it brings the opportunity to extract information about them from the experimental results. Nonetheless and for the same reason, this fact requires a good description of them in order to understand the results. In this sense, a good description of the uncertainties involved in direct detection experiments is crucial. We have performed the first systematic study of how the uncertainties on the spin-dependent structure functions can affect the reconstruction of a given signal. Our results show that these nuclear uncertainties can be as important as the astrophysical ones, which affect the velocity distribution of dark matter particles at Earth's position, and thus must be properly included when reconstructing a signal. In order to this, we have proposed a parametrization of the structure functions for all nuclei used in direct detection experiments in terms of three free parameters that capture the behavior of these functions, and it allows to include this effect in future studies.

Indirect searches for dark matter are present in this thesis as well. The amount of dark matter expected to be concentrated around the galactic centre is huge, specially if an adiabatic contraction took place dominantly when the galaxy formed. This makes this place of our galaxy an excellent target for gamma-ray indirect searches. Analyzing the *Fermi*-LAT data from the inner part of the Milky Way we have extracted upper bounds on the annihilation cross section of generic WIMP candidates. For the adiabatically

contracted halo considered the bounds are remarkably strong being able to constrain thermal candidates up to masses of several hundreds of GeV. Actually, we have shown that the adiabatic contraction of the Milky Way halo might be the only hope of indirectly detecting via gamma-rays some of the Neutralino and Sneutrino scenarios previously mentioned.

Fortunately we are living exciting days. The sensitivity of most of the experiments is expected to be high enough to probe almost all regions of light WIMP dark matter in the near future. Should dark matter be detected soon or not, we have to be flexible when trying to understand the results because it might happen that the dark Universe is more complex than what we are thinking. For this reason it is very important to face the dark matter problem making use of the knowledge we have, and we will have, about the different fields of study involved in this great challenge.

Castellano

No hay duda de que el Universo está lleno de una nueva y exótica forma de materia conocida como materia oscura. Numerosas observaciones astronómicas, de las cuales cumplirá un siglo dentro de poco, nos han demostrado que aproximadamente el 85% de toda la materia contenida en el Universo es materia oscura, y que además su única interacción con la materia ordinaria (bariónica) descubierta hasta la fecha es puramente gravitacional. Esto establece uno de los mayores retos conocidos para la física moderna. Por un lado, a pesar del éxito que ha mostrado tener el Modelo Estándar de física de partículas, este no incluye un candidato que pueda dar cuenta de la materia oscura en el Universo. Por lo tanto, la física teórica ha de hacer un esfuerzo para extender este modelo de forma que incluya una descripción apropiada de la materia oscura en términos de partículas elementales. Por otro lado, es crucial descubrir si la materia oscura interacciona con la bariónica de forma no gravitacional. Con este fin, diversas colaboraciones experimentales en todo el mundo tratan de dar caza a la materia oscura mediante interacciones no gravitacionales. El problema de la materia oscura, por lo tanto, ha de aunar los esfuerzos tanto de los físicos experimentales como de los teóricos.

En esta tesis se aborda el problema de la materia oscura desde ambas perspectivas. Centrándinos en la materia oscura ligera (con masas menores que 100 GeV), se afronta el problema de la materia oscura desde el punto de vista puramente teórico analizando tres candidatos supersimétricos a materia oscura de tipo WIMP, y además también analizamos la parte teórica de las búsquedas directas e indirectas de la misma. Se ha demostrado que los modelos supersimétricos analizados, el Modelo Estándar Super-

simétrico Mínimo (MSSM) y su extensión mínima (NMSSM), ofrecen un marco teórico debidamente motivado en el cual la materia oscura ligera, representada por Neutralinos o Sneutrinos, es viable. Usando los últimos datos del LHC, hemos analizado diferentes regiones del espacio de parámetros de cada modelo en los cuales la materia oscura ligera está permitida por todas las medidas experimentales hasta la fecha. Además hemos visto que en muchos casos estos candidatos podrían ser descubiertos por las siguientes generaciones de experimentos de detección directa.

Si un experimento de detección directa descubriese la materia oscura significaría que esta no solo interacciona gravitacionalmente, lo cual convertiría el paradigma WIMP en una realidad. Sin embargo, no podríamos obtener mucha más información que esta de una sola detección. Es por tanto que existe una necesidad real de que la materia oscura sea detectada usando detectores construidos a partir de materiales diferentes, de otra manera esta información que la detección nos daría estaría muy limitada. Hoy en día los mayores detectores construidos están hechos a partir de Germanio y Xenon, pero en esta tesis hemos demostrado que incluso si la materia oscura es descubierta en ambos experimentos, la cantidad de información que podríamos extraer acerca de la naturaleza de la materia oscura no sería completa. Mediante la simulación de una detección en varios detectores hemos demostrado que experimentos basados en detectores de Flúor, Aluminio y Tungsteno, y con la posibilidad de poder medir las energías de las colisiones, aportan información complementaria a aquellos basados en Germanio y Xenon. Usando esta complementariedad entre diferentes materiales, en muchos casos hemos mostrado que la naturaleza de la materia oscura podría ser extraída de forma unívoca. Por lo tanto este tipo de detectores son, sin duda, una buena opción para la siguiente generación de experimentos de detección directa.

Sin embargo, la complementariedad entre diferentes detectores no está exenta de inconvenientes. Para maximizar la información extraída a partir de un detector o de varios, las incertidumbres teóricas de los procesos físicos que tienen lugar en una colisión ha de estar bajo control. Es increíble como las señales en detección directa dependen de varios campos de la física, concretamente de la astrofísica, la física nuclear y la física de partículas, y como a partir de estos experimentos podemos conocer estos campos. Pero por la misma razón, esto requiere que estos procesos de estos campos de la física estén bien descritos. En este sentido, es crucial parametrizar correctamente nuestro desconocimiento de ellos. En esta tesis presentamos el primer estudio sistemático de como la incertidumbre que existe en el cálculo de las funciones de estructura dependientes del espín puede afectar en la reconstrucción de una señal de detección directa. Nuestros resultados muestran que este desconocimiento afecta con la misma importancia que aquel que envuelve a las

funciones de distribución de la velocidad de la materia oscura, y que por lo tanto debe ser incluido en estos estudios. Para ello hemos propuesto una parametrización de las funciones de estructura en términos de tres parámetros libres. Variando estos parámetros es posible incluir estos efectos, independientemente del material usado como detector, y por lo tanto permite su implementación en futuros estudios de este tipo.

Por último, también hemos estudiado las búsquedas indirectas de materia oscura. La cantidad de materia oscura que se espera este concentrada alrededor del centro de nuestra galaxia es enorme, especialmente si un proceso conocido como contracción adiabática tuvo lugar en la formación de esta. Esto hace del centro galáctico un lugar ideal para las búsquedas indirectas, concretamente aquellas a través de rayos gamma. Analizando los datos del centro de la galaxia recogidos por el satélite *Fermi*-LAT hemos puesto límites a la sección eficaz de aniquilación de la materia oscura. Para modelos de halo de la Via Láctea en cuya formación tuvo lugar una contracción adiabática apreciable, los límites son muy fuertes llegando a ser capaces de restringir masas de la materia oscura por debajo de cientos de GeV. De hecho, hemos mostrado que esta contracción puede ser nuestra única esperanza de detectar indirectamente y con rayos gamma algunas de las soluciones para los escenarios que hemos mencionado anteriormente, en los cuales el Neutralino o el Sneutrino es el candidato a materia oscura.

Afortunadamente estamos viviendo una época excitante. En el futuro próximo, se espera que la sensibilidad de los experimentos sea lo suficientemente alta como para probar la mayoría de las regiones del espacio de parámetros en los que la materia oscura ligera es viable. Tanto si se detecta pronto la materia oscura como si no, tenemos que ser flexibles a la hora de entender los resultados ya que podría ser que la parte *oscura* del Universo sea mas compleja de lo que pensamos. Es muy importante por lo tanto encarar el problema de la materia oscura haciendo de uso del conocimiento que tenemos, y el que tendremos, en los diferentes campos de la física que están envueltos en este gran reto y esta tesis supone un avance en este sentido.

Appendix A

Freeze-out of a light WIMP

Dark matter relic density evolution is governed by Boltzmann equation [45]:

$$\frac{dn}{dt} + 3nH = -\langle \sigma v_{rel} \rangle \left(n^2 - n_{eq}^2 \right), \tag{A.1}$$

where H is the Hubble parameter, n is the number density of the considered species and $\langle \sigma v_{rel} \rangle$ is the thermal average of the cross section times the relative velocity. This equation has two different parts. The right hand side of the equation accounts for particle physics features of the model considered whereas the left hand side contains information about cosmological properties of the Universe (FRW Universe). Let's say χ is the dark matter specie with a mass m_χ. The previous equation can be rewritten in terms of two variables: the Yield, $Y \equiv n/s$, and $x \equiv m_\chi/T$,

$$\frac{dY}{dx} = -\sqrt{\frac{\pi}{45G}} \frac{g_*^{1/2} m_\chi}{x^2} \langle \sigma v_{rel} \rangle \left(Y^2 - Y_{eq}^2 \right), \tag{A.2}$$

where G is the gravitational constant and

$$g_*^{1/2} \equiv \frac{h(T)}{\sqrt{g(T)}} \left(1 + \frac{T}{3h(T)} \frac{dh(T)}{dT} \right). \tag{A.3}$$

This quantity comes from the following definitions for the energy density and the entropy [257]:

$$\rho = g(T) \frac{\pi^2}{30} T^4 \qquad s = h(T) \frac{2\pi^2}{45} T^3 \tag{A.4}$$

Typically dark matter decouples at $x \approx 20$. For masses between $20 - 1000$GeV the frezee out temperature will be between $1 - 50$GeV. In this range of temperatures is a good approximation to take $g(T) = h(T) \approx 81$ obtaining the typical result for dark matter relic density (see for instance [379]).

Let us point out the assumptions under which the rate equation (A.2) is valid [257]: (i) Statistical mechanical factors are neglected, i.e., the Bose-Einstein or Fermi-Dirac distributions are approximated by the Maxwell-Boltzmann distribution, which is a very good approximation for temperatures $T \lesssim 3m_\chi$; (ii) the annihilation products are in thermal equilibrium; (iii) the species under consideration remain in kinetical equilibrium also after decoupling; (iv) the initial chemical potential of the species under consideration is negligible.

Notice that for dark matter with masses in the range $3-8$ GeV the freeze out temperature falls in the range of temperatures where the QCD quark-hadron phase transition occurs, that is, in the range $150-400$ MeV. This phase transition turns out to be a crossover instead of a first order phase transition, as the lattice-QCD results point out [380]. This crossover produces a smooth variation in the functions $g(T)$ and $h(T)$ in the range $150-400$ MeV separating them from the usual value, but it is important to note that even in this case $g(T) = h(T)$. The computation of $h(T)$ and $g(T)$ requires a model for the phase transition, and we have taken the results of the model described in Ref. [381] and we have read the values of $h(T)$ and $g(T)$ during the QCD phase transition from Ref. [382]. These functions can be seen in Figure A.1.

First we determine the temperature of freeze out T_F. Before decoupling, it is useful to work with the equation for $\Delta \equiv Y - Y_{eq}$

$$\frac{d\Delta}{dx} = -\sqrt{\frac{\pi}{45G}}\frac{g_*^{1/2} m_\chi}{x^2}\langle\sigma v_{rel}\rangle\Delta\left(\Delta + 2Y_{eq}\right) - \frac{dY_{eq}}{dx}. \tag{A.5}$$

Before decoupling we can neglect $d\Delta/dx$, because Y follows the equilibrium density. We define de freeze out moment at which $\Delta = \delta Y_{eq}$, thus the condition for freeze out is

$$\sqrt{\frac{\pi}{45G}}\frac{g_*^{1/2} m_\chi}{x^2}\langle\sigma v_{rel}\rangle Y_{eq}\delta(\delta+2) = -\frac{d\lambda_N Y_{eq}}{dx}, \tag{A.6}$$

and inserting the expression for the Yield in equilibrium we obtain

$$\sqrt{\frac{\pi}{45G}}\frac{45g}{4\pi^4}\frac{K_2(x)}{h(T)}g_*^{1/2} m_\chi\langle\sigma v_{rel}\rangle\delta(\delta+2) = \frac{K_1(x)}{K_2(x)} - \frac{1}{x}\frac{d\lambda_N h(T)}{d\lambda_N T}, \tag{A.7}$$

where K_i is the modified Bessel function of order i. The first term of the right hand side is relativistic in nature and goes to one in the non-relativistic regime. The second term is zero if one takes $g(T) = h(T)$. The value of δ is different in the literature, in [257] they take $\delta = 1.5$ while in [47] they take $\delta = 0.5$ with an accuracy of about 5-10%.

Thus the freeze out condition under the previous assumptions, reads

$$x_F = \lambda_N\left[\frac{m_\chi g}{4\pi^3}\sqrt{\frac{45}{2g(T)G}}\langle\sigma v_{rel}\rangle\delta(\delta+2)\frac{1}{\sqrt{x_F}}\right]. \tag{A.8}$$

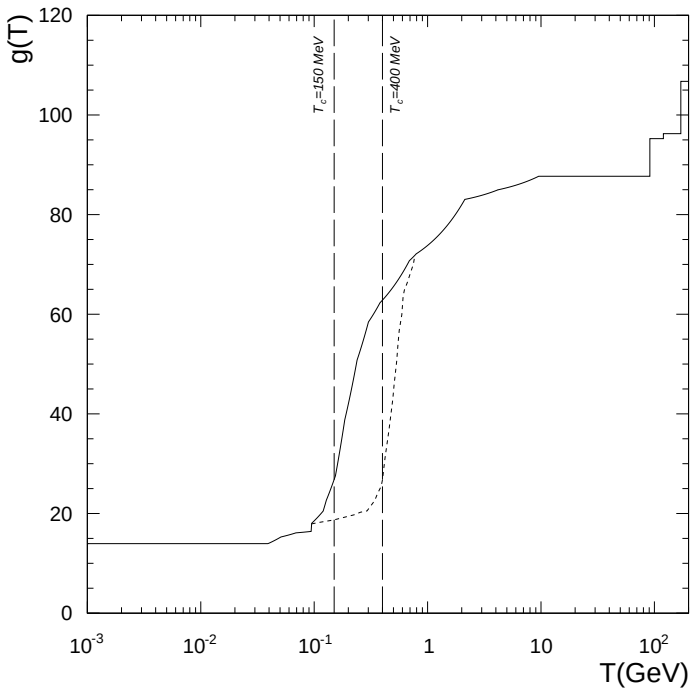

Figure A.1: SM degrees of freedom as a function of temperature. T_c is the QCD deconfinement temperature.

After decoupling, we can neglect Y_{eq} in (A.2) and integrate from T_F to T_0. We obtain

$$\frac{1}{Y_0} = \frac{1}{Y_F} + \sqrt{\frac{45G}{\pi}} \int_{T_0}^{T_F} \sqrt{g(T)} \langle \sigma v_{rel} \rangle dT. \tag{A.9}$$

Since T_0 is very small compared to the mass of the particles, we will replace it by zero. The result is

$$Y_0 = \sqrt{\frac{45G}{\pi}} \left[m_\chi \int_0^{z_F} \sqrt{g(z)} \langle \sigma v_{rel} \rangle dz \right]^{-1} \tag{A.10}$$

where $z \equiv x^{-1}$. Dark matter density is given by $\rho_\chi = m_\chi s_0 Y_0$:

$$\rho_\chi = \frac{1.66}{M_{pl}} \left(\frac{43}{11} \right) T_\gamma^3 \left[\int_0^{z_F} \sqrt{g(z)} \langle \sigma v_{rel} \rangle dz \right]^{-1} \tag{A.11}$$

where $s_0 = 2\pi^2 g(T_\gamma) T_\gamma^3/45$ is the entropy today, $g(T_\gamma) = 3.915$ are the degrees of freedom of photons and three families of neutrinos and T_γ is the CMB photons temperature. This formula is equivalent to formula (2.8) of [379] but in this case using a parametrization for degrees of freedom.

For heavier WIMPs, this is considering $\sqrt{g(T)} \approx 9$ for all the relevant part of the particle's thermal history, we can recover the usual expression for the relic density. This calculation requires an expansion in powers of the velocity for the cross section in order to be analytic. This expansion, in a non-relativistic scenario, can be expressed in terms of z, as it was defined previously, and it reads

$$\langle \sigma v_{rel} \rangle = a + bz \tag{A.12}$$

This expression is only valid far away from resonances and thresholds, regions which require a more careful computation of the cross section [379]. In this case the density is given by

$$\rho_\chi = \frac{1.66}{M_{pl}} \left(\frac{T_\chi}{T_\gamma} \right)^3 \frac{18 T_\gamma^3}{2az_f + bz_f^2} \tag{A.13}$$

where T_χ and T_γ are the present temperatures of the dark matter specie considered and the photon, respectively. The suppression factor $(T_\chi/T_\gamma)^3 \approx 1/20$ follows from entropy conservation in a comoving volume.

Appendix B

Sneutrino masses

The scalar potential responsible of the Sneutrino mass reads,

$$\begin{aligned} V(\tilde{L},\tilde{N}) \;\subset\; & |y_N H_2 \tilde{N}|^2 + |2\lambda_N S\tilde{N}|^2 + |-\lambda S H_1 + y_N \tilde{L}\tilde{N}|^2 \\ & + |-\lambda H_1 H_2 + \kappa S^2 + \lambda_N \tilde{N}^2|^2 + \mathrm{D-term} \\ & + m^2_{\tilde{L}}|\tilde{L}|^2 + m^2_{\tilde{N}}|\tilde{N}| + \left(\lambda_N A_{\lambda_N} S\tilde{N}^2 + y_N A_{y_N}\tilde{L}H_2\tilde{N} + \mathrm{H.c.}\right). \end{aligned} \tag{B.1}$$

Decomposing the left-handed sneutrino $\tilde{\nu}_L$ and right-handed sneutrino $\tilde{N}$ as

$$\tilde{\nu}_L \equiv \frac{1}{\sqrt{2}}(\tilde{\nu}_{L1} + i\tilde{\nu}_{L2}), \qquad \tilde{N} \equiv \frac{1}{\sqrt{2}}(\tilde{N}_1 + i\tilde{N}_2), \tag{B.2}$$

the sneutrino quadratic term can be written as

$$\frac{1}{2}(\tilde{\nu}_{L1}, \tilde{N}_1, \tilde{\nu}_{L2}, \tilde{N}_2)\mathcal{M}^2_{\mathrm{Sneutrino}} \begin{pmatrix} \tilde{\nu}_{L1} \\ \tilde{N}_1 \\ \tilde{\nu}_{L2} \\ \tilde{N}_2 \end{pmatrix}, \tag{B.3}$$

with

$$\mathcal{M}^2_{\mathrm{Sneutrino}} = \begin{pmatrix} m^2_{L\bar{L}} & \frac{m^2_{LR}+m^2_{L\bar{R}}+\mathrm{c.c}}{2} & 0 & i\frac{m^2_{LR}-m^2_{L\bar{R}}-\mathrm{c.c}}{2} \\ \frac{m^2_{LR}+m^2_{L\bar{R}}+\mathrm{c.c}}{2} & m^2_{R\bar{R}} + m^2_{RR} + m^{2*}_{RR} & i\frac{m^2_{LR}-m^2_{L\bar{R}}-\mathrm{c.c}}{2} & i(m^2_{RR} - m^{2*}_{RR}) \\ 0 & i\frac{m^2_{LR}-m^2_{L\bar{R}}-\mathrm{c.c}}{2} & m^2_{L\bar{L}} & \frac{-m^2_{LR}+m^2_{L\bar{R}}+\mathrm{c.c}}{2} \\ i\frac{m^2_{LR}-m^2_{L\bar{R}}-\mathrm{c.c}}{2} & i(m^2_{RR} - m^{2*}_{RR}) & \frac{-m^2_{LR}+m^2_{L\bar{R}}+\mathrm{c.c}}{2} & m^2_{R\bar{R}} - m^2_{RR} - m^{2*}_{RR} \end{pmatrix}. \tag{B.4}$$

Here, we defined

$$\begin{aligned} m^2_{L\bar{L}} &\equiv m^2_{\tilde{L}} + |y_N v_2|^2 + \mathrm{D-term}, \\ m^2_{LR} &\equiv y_N \left(-\lambda v_s v_1\right)^\dagger + y_N A_N v_2, \\ m^2_{L\bar{R}} &\equiv y_N v_2 \left(-\lambda v_s\right)^\dagger, \\ m^2_{R\bar{R}} &\equiv m^2_{\tilde{N}} + |2\lambda_N v_s|^2 + |y_N v_2|^2, \\ m^2_{RR} &\equiv \lambda_N \left(A_{\lambda_N} v_s + (\kappa v_s^2 - \lambda v_1 v_2)^\dagger\right). \end{aligned} \tag{B.5}$$

If these are real, in other words no CP violation, the real part and imaginary part of sneutrinos do not mix and its mass matrix (B.3) is simplified as

$$\begin{aligned} \text{Eq. (B.3)} \;=\; & \frac{1}{2}(\tilde{\nu}_{L1}, \tilde{N}_1) \begin{pmatrix} m^2_{L\bar{L}} & m^2_{LR} + m^2_{L\bar{R}} \\ m^2_{LR} + m^2_{L\bar{R}} & m^2_{R\bar{R}} + 2m^2_{RR} \end{pmatrix} \begin{pmatrix} \tilde{\nu}_{L1} \\ \tilde{N}_1 \end{pmatrix} \\ & + \frac{1}{2}(\tilde{\nu}_{L2}, \tilde{N}_2) \begin{pmatrix} m^2_{L\bar{L}} & -m^2_{LR} + m^2_{L\bar{R}} \\ -m^2_{LR} + m^2_{L\bar{R}} & m^2_{R\bar{R}} - 2m^2_{RR} \end{pmatrix} \begin{pmatrix} \tilde{\nu}_{L2} \\ \tilde{N}_2 \end{pmatrix}. \end{aligned} \tag{B.6}$$

Note that the mixing between left-handed and right-handed sneutrinos is induced by m^2_{LR} and $m^2_{L\bar{R}}$, both of which are proportional to the neutrino Yukawa coupling y_N. As mentioned in Section 2.5, y_N must be as small as $\mathcal{O}(10^{-(6-7)})$ to generate sub-eV left-handed neutrino mass via low scale seesaw mechanism according to Eq. (2.49). If we rewrite sneutrinos in the mass eigenstates,

$$\tilde{\nu}_i = N^{\tilde{\nu}}_{iL} \tilde{\nu}_L + N^{\tilde{\nu}}_{iR} \tilde{N}, \tag{B.7}$$

by rotating with an unitary matrix $N^{\tilde{\nu}}$, then, unless the diagonal elements of the mass matrix (B.6) are extremely degenerated, we find

$$(N^{\tilde{\nu}}_{iL}, N^{\tilde{\nu}}_{iR}) = \begin{cases} (1 + \mathcal{O}(y_N), \mathcal{O}(y_N)) \\ (\mathcal{O}(y_N), 1 + \mathcal{O}(y_N)) \end{cases}. \tag{B.8}$$

Thus, the mixing between left-handed and right-handed sneutrinos is also of $\mathcal{O}(10^{-6} - 10^{-7})$ and therefore negligible. For all practical purposes regarding DM phenomenology, we can ignore all off-diagonal elements in Eq. (B.6) and regard sneutrino mass eigenstates as pure left- or right-handed fields. One may see that m^2_{RR} splits the masses of $\tilde{N}_1$ and $\tilde{N}_2$. In particular, $\tilde{N}_2$ is heavier than $\tilde{N}_1$ for $m^2_{RR} < 0$ (and viceversa), and this is the situation we will consider throughout the rest of this work[1].

[1] We only do this for simplicity. The imaginary component of the right-handed sneutrino is as good a dark matter candidate as the real component. In fact they only differ in the expression for the annihilation into a pair of right-handed neutrinos.

Appendix C

Experimental features of the different targets

In this Appendix we detail the different experimental parameters that has been used for each detector. We have considered natural abundances of the different isotopes for a given target.

In both cases we have divided the energy window sensitive to recoils (from E_T to E_{max}) into N_{bin} evenly spaced bins with a size of ΔE keV, with $N_{bin} = (E_{max} - E_T)/\Delta E$. The estimated number of events in each bin is kept as a decimal number, without rounding it to an integer. This is, in principle, not physical and might overestimate the ability to discriminate different spectra. However it allows us to neglect the dependence of the

Target	$\{E_T,\ E_{max}\}$ (keV)	$\sigma(E)$ (keV)	ΔE (keV)	Background ($\mathrm{kg^{-1}day^{-1}keV^{-1}}$)
Ge	$\{10,\ 100\}$	$\sqrt{(0.3)^2 + (0.06)^2\, E/\mathrm{keV}}$	5	4×10^{-8}
Xe	$\{8.4,\ 44.6\}$	$0.6\sqrt{E/\mathrm{keV}}$	3.64	4×10^{-9}
C_3FI	$\{10,\ 200\}$	-	-	4.1×10^{-8}
$CaWO_4$	$\{10,\ 100\}$	5% FWHM	5	
Al_2O_3	$\{10,\ 100\}$	5% FWHM	5	
LiF	$\{10,\ 100\}$	5% FWHM	5	

Table C.1: Energy range, parameterization of the resolution and background for the different detectors for the experimental setup ES_1. The background level for the first three targets is inspired on estimates for SuperCDMS [383], XENON1T [384], and COUPP [385], that we consider energy-independent for simplicity.

Target	$\{E_T,\ E_{max}\}$ (keV)	$\sigma(E)$ (keV)	ΔE (keV)	Background ($kg^{-1}day^{-1}keV^{-1}$)
Ge	{3, 100}	$\sqrt{(0.3)^2 + (0.06)^2\, E/\text{keV}}$	5.1	0
Xe	{3, 43}	$0.6\sqrt{E/\text{keV}}$	4	0
NaI	{10, 100}	5% FWHM	5	

Table C.2: Same as Table C.1 but for the experimental setup ES_2.

reconstructed parameters on the particular realization chosen for the nominal number of events in the different bins (see Ref. [303]). This is an important source of uncertainty that has to be taken into account when dealing with real data, but we decide to neglect it here in order to study and estimate complementarity in a scenario uncompromised by statistical fluctuations, and also because, as found in Ref. [303] the relevance of those statistical fluctuations decreases as the number of experiments increases, thus we assume that coverage is good enough when dealing with signals from three detectors. Notice that, in the case of LiF, the thresholds obtained to this date are far from the 10 keV value used in this thesis. Additional R&D is needed on this target before using it for DM detectors.

In our analysis the energy resolution of the detector σ is included as a convolution of the differential rate with a Gaussian function with a variance σ^2 which depends on the recoil energy and on the particular experiment (see Table C.1 and C.2).

Bibliography

[1] P. Ade *et al.* Planck 2013 results. XVI. Cosmological parameters (2013). (cited on pages 1, 6, and 8)

[2] F. Zwicky. Die Rotverschiebung von extragalaktischen Nebeln. Helv.Phys.Acta **6**, 110 (1933). (cited on pages 1 and 3)

[3] J. Einasto. Dark Matter (2009). inSPIRE. (cited on pages 1 and 3)

[4] D. A. Dicus, E. W. Kolb, and V. L. Teplitz. Cosmological Upper Bound on Heavy Neutrino Lifetimes. Phys.Rev.Lett. **39**, 168 (1977). inSPIRE. (cited on p. 2)

[5] P. Hut. Limits on Masses and Number of Neutral Weakly Interacting Particles. Phys.Lett. **B69**, 85 (1977). inSPIRE. (cited on p. 2)

[6] G. R. Blumenthal, S. Faber, J. R. Primack, and M. J. Rees. Formation of Galaxies and Large Scale Structure with Cold Dark Matter. Nature **311**, 517 (1984). inSPIRE. (cited on p. 2)

[7] M. W. Goodman and E. Witten. Detectability of Certain Dark Matter Candidates. Phys.Rev. **D31**, 3059 (1985). (cited on p. 2)

[8] V. C. Rubin and J. Ford, W. Kent. Rotation of the Andromeda Nebula from a Spectroscopic Survey of Emission Regions. Astrophys.J. **159**, 379 (1970). (cited on pages 3 and 5)

[9] V. Rubin, N. Thonnard, and J. Ford, W.K. Rotational properties of 21 SC galaxies with a large range of luminosities and radii, from NGC 4605 /R = 4kpc/ to UGC 2885 /R = 122 kpc/. Astrophys.J. **238**, 471 (1980). (cited on pages 3 and 4)

[10] V. Rubin, D. Burstein, J. Ford, W.K., and N. Thonnard. Rotation velocities of 16 SA galaxies and a comparison of Sa, Sb, and SC rotation properties. Astrophys.J. **289**, 81 (1985). (cited on pages 3 and 4)

[11] T. van Albada, J. N. Bahcall, K. Begeman, and R. Sancisi. The Distribution of Dark Matter in the Spiral Galaxy NGC-3198. Astrophys.J. **295**, 305 (1985). (cited on p. 5)

[12] J. Tyson and P. Fischer. Measurement of the mass profile of abell 1689 (1995). (cited on p. 5)

[13] P. Fischer and J. A. Tyson. The Mass distribution of the most luminous X-ray cluster RXJ1347.5-1145 from gravitational lensing. Astron.J. **114**, 14 (1997). (cited on p. 5)

[14] S. D. White, J. F. Navarro, A. E. Evrard, and C. S. Frenk. The Baryon content of galaxy clusters: A Challenge to cosmological orthodoxy. Nature **366**, 429 (1993). (cited on p. 5)

[15] H. Bohringer, P. Schuecker, G. Pratt, M. Arnaud, T. Ponman, *et al.* The Representative XMM-Newton Cluster Structure Survey (REXCESS) of an X-ray Luminosity Selected Galaxy Cluster Sample. Astron.Astrophys. **469**, 363 (2007). (cited on p. 5)

[16] S. Snowden, R. Egger, M. Freyberg, D. McCammon, P. Plucinsky, *et al.* ROSAT Survey Diffuse X-Ray Background Maps. II. Astrophys.J. **485**, 125 (1997). (cited on p. 5)

[17] J. C. Mather, E. Cheng, R. Shafer, C. Bennett, N. Boggess, *et al.* A Preliminary measurement of the Cosmic Microwave Background spectrum by the Cosmic Background Explorer (COBE) satellite. Astrophys.J. **354**, L37 (1990). (cited on p. 6)

[18] A. Challinor and H. Peiris. Lecture notes on the physics of cosmic microwave background anisotropies. AIP Conf.Proc. **1132**, 86 (2009). (cited on p. 6)

[19] E. Wright, S. Meyer, C. Bennett, N. Boggess, E. Cheng, *et al.* Interpretation of the Cosmic Microwave Background radiation anisotropy detected by the COBE differential microwave radiometer. Astrophys.J. **396**, L13 (1992). (cited on p. 6)

[20] C. Bennett *et al.* The Microwave Anisotropy Probe (MAP) mission. Astrophys.J. **583**, 1 (2003). (cited on p. 6)

[21] D. Spergel *et al.* First year Wilkinson Microwave Anisotropy Probe (WMAP) observations: Determination of cosmological parameters. Astrophys.J.Suppl. **148**, 175 (2003). (cited on p. 6)

[22] D. Spergel *et al.* Wilkinson Microwave Anisotropy Probe (WMAP) three year results: implications for cosmology. Astrophys.J.Suppl. **170**, 377 (2007). (cited on p. 6)

[23] E. Komatsu *et al.* Five-Year Wilkinson Microwave Anisotropy Probe (WMAP)

Observations: Cosmological Interpretation. Astrophys.J.Suppl. **180**, 330 (2009). (cited on p. 6)

[24] E. Komatsu *et al.* Seven-Year Wilkinson Microwave Anisotropy Probe (WMAP) Observations: Cosmological Interpretation. Astrophys.J.Suppl. **192**, 18 (2011). (cited on p. 6)

[25] G. Hinshaw *et al.* Nine-Year Wilkinson Microwave Anisotropy Probe (WMAP) Observations: Cosmological Parameter Results. Astrophys.J.Suppl. **208**, 19 (2013). (cited on p. 6)

[26] E. S. A. official site. webpage. (cited on p. 6)

[27] J. Bekenstein and M. Milgrom. Does the missing mass problem signal the breakdown of Newtonian gravity? Astrophys.J. **286**, 7 (1984). inSPIRE. (cited on p. 7)

[28] D. Clowe, M. Bradac, A. H. Gonzalez, M. Markevitch, S. W. Randall, *et al.* A direct empirical proof of the existence of dark matter. Astrophys.J. **648**, L109 (2006). inSPIRE. (cited on p. 7)

[29] M. Markevitch, A. Gonzalez, D. Clowe, A. Vikhlinin, L. David, *et al.* Direct constraints on the dark matter self-interaction cross-section from the merging galaxy cluster 1E0657-56. Astrophys.J. **606**, 819 (2004). inSPIRE. (cited on p. 7)

[30] D. Clowe, A. Gonzalez, and M. Markevitch. Weak lensing mass reconstruction of the interacting cluster 1E0657-558: Direct evidence for the existence of dark matter. Astrophys.J. **604**, 596 (2004). inSPIRE. (cited on p. 7)

[31] G. W. Angus, H. Shan, H. Zhao, and B. Famaey. On the Law of Gravity, the Mass of Neutrinos and the Proof of Dark Matter. Astrophys.J. **654**, L13 (2007). inSPIRE. (cited on p. 8)

[32] S. A. Thomas, F. B. Abdalla, and O. Lahav. Upper Bound of 0.28eV on the Neutrino Masses from the Largest Photometric Redshift Survey. Phys.Rev.Lett. **105**, 031301 (2010). inSPIRE. (cited on p. 8)

[33] G. Bertone, J. Silk, B. Moore, J. Diemand, J. Bullock, *et al.* Particle Dark Matter: Observations, Models and Searches (2010). inSPIRE. (cited on p. 8)

[34] M. Taoso, G. Bertone, and A. Masiero. Dark Matter Candidates: A Ten-Point Test. JCAP **0803**, 022 (2008). inSPIRE. (cited on pages 8, 9, and 11)

[35] J. R. Primack and G. R. Blumenthal. What is the Dark Matter? Implications for Galaxy formation and particle physics (1983). inSPIRE. (cited on p. 9)

[36] J. R. Primack. Whatever happened to hot dark matter? SLAC Beam Line **31N3**, 50 (2001). inSPIRE. (cited on p. 9)

[37] A. A. Klypin, A. V. Kravtsov, O. Valenzuela, and F. Prada. Where are the missing Galactic satellites? Astrophys.J. **522**, 82 (1999). inSPIRE. (cited on p. 9)

[38] M. Boylan-Kolchin, J. S. Bullock, and M. Kaplinghat. Too big to fail? The puzzling darkness of massive Milky Way subhaloes. Mon.Not.Roy.Astron.Soc. **415**, L40 (2011). inSPIRE. (cited on p. 9)

[39] M. Viel, G. D. Becker, J. S. Bolton, and M. G. Haehnelt. Warm Dark Matter as a solution to the small scale crisis: new constraints from high redshift Lyman-alpha forest data. Physical Review **D88**, 043502 (2013). inSPIRE. (cited on p. 9)

[40] A. Schneider, D. Anderhalden, A. Maccio, and J. Diemand. Warm dark matter does not do better than cold dark matter in solving small-scale inconsistencies (2013). inSPIRE. (cited on p. 9)

[41] M. Maggiore. Gravitational wave experiments and early universe cosmology. Phys.Rept. **331**, 283 (2000). inSPIRE. (cited on p. 10)

[42] S. Davidson, S. Hannestad, and G. Raffelt. Updated bounds on millicharged particles. JHEP **0005**, 003 (2000). inSPIRE. (cited on p. 10)

[43] R. H. Cyburt, B. D. Fields, K. A. Olive, and E. Skillman. New BBN limits on physics beyond the standard model from He-4. Astropart.Phys. **23**, 313 (2005). inSPIRE. (cited on p. 10)

[44] K. Jedamzik. Did something decay, evaporate, or annihilate during Big Bang nucleosynthesis? Phys.Rev. **D70**, 063524 (2004). inSPIRE. (cited on p. 10)

[45] E. W. Kolb and M. S. Turner. The Early Universe. Front.Phys. **69**, 1 (1990). inSPIRE. (cited on pages 10 and 179)

[46] J. L. Feng, A. Rajaraman, and F. Takayama. SuperWIMP dark matter signals from the early universe. Phys.Rev. **D68**, 063504 (2003). inSPIRE. (cited on p. 11)

[47] G. Jungman, M. Kamionkowski, and K. Griest. Supersymmetric dark matter. Phys.Rept. **267**, 195 (1996). inSPIRE. (cited on pages 11, 13, 16, 46, 88, 161, and 180)

[48] L. Hui. Unitarity bounds and the cuspy halo problem. Phys.Rev.Lett. **86**, 3467 (2001). inSPIRE. (cited on p. 11)

[49] E. W. Kolb, D. J. Chung, and A. Riotto. WIMPzillas! 91–105 (1998). inSPIRE. (cited on p. 11)

[50] L. J. Hall, K. Jedamzik, J. March-Russell, and S. M. West. Freeze-In Production of FIMP Dark Matter. JHEP **1003**, 080 (2010). inSPIRE. (cited on pages 11 and 12)

[51] J. Lewin and P. Smith. Review of mathematics, numerical factors, and corrections for dark matter experiments based on elastic nuclear recoil. Astropart.Phys. **6**, 87 (1996). inSPIRE. (cited on pages 13, 88, 91, and 118)

[52] D. G. Cerdeno and A. M. Green. Direct detection of WIMPs (2010). inSPIRE. (cited on pages 13 and 86)

[53] K. Garrett and G. Duda. Dark Matter: A Primer. Adv.Astron. **2011**, 968283 (2011). inSPIRE. (cited on pages 13 and 14)

[54] G. Bertone. The moment of truth for WIMP Dark Matter. Nature **468**, 389 (2010). inSPIRE. (cited on pages 13, 14, 17, and 25)

[55] R. Schnee. Introduction to dark matter experiments (2011). inSPIRE. (cited on p. 13)

[56] J. Carr, G. Lamanna, and J. Lavalle. Indirect detection of dark matter. Rept.Prog.Phys. **69**, 2475 (2006). inSPIRE. (cited on p. 14)

[57] M. Cirelli, G. Corcella, A. Hektor, G. Hutsi, M. Kadastik, *et al.* PPPC 4 DM ID: A Poor Particle Physicist Cookbook for Dark Matter Indirect Detection. JCAP **1103**, 051 (2011). inSPIRE. (cited on pages 14, 78, 148, 151, 152, 154, and 155)

[58] M. Cirelli. Indirect Searches for Dark Matter: a status review. Pramana **79**, 1021 (2012). inSPIRE. (cited on pages 14 and 22)

[59] S. Funk. Indirect Detection of Dark Matter with gamma rays (2013). inSPIRE. (cited on p. 14)

[60] A. Birkedal, K. Matchev, and M. Perelstein. Dark matter at colliders: A Model independent approach. Phys.Rev. **D70**, 077701 (2004). inSPIRE. (cited on pages 14 and 66)

[61] M. Battaglia, I. Hinchliffe, and D. Tovey. Cold dark matter and the LHC. J.Phys. **G30**,

R217 (2004). inSPIRE. (cited on p. 14)

[62] V. A. Mitsou. Shedding Light on Dark Matter at Colliders. Int.J.Mod.Phys. **A28**, 1330052 (2013). inSPIRE. (cited on p. 14)

[63] E. Gildener. Gauge Symmetry Hierarchies. Phys.Rev. **D14**, 1667 (1976). inSPIRE. (cited on p. 15)

[64] E. Gildener and S. Weinberg. Symmetry Breaking and Scalar Bosons. Phys.Rev. **D13**, 3333 (1976). inSPIRE. (cited on p. 15)

[65] K. Griest. Cross-Sections, Relic Abundance and Detection Rates for Neutralino Dark Matter. Phys.Rev. **D38**, 2357 (1988). inSPIRE. (cited on p. 16)

[66] V. Berezinsky, A. Bottino, J. R. Ellis, N. Fornengo, G. Mignola, *et al.* Neutralino dark matter in supersymmetric models with nonuniversal scalar mass terms. Astropart.Phys. **5**, 1 (1996). inSPIRE. (cited on p. 16)

[67] H. Baer and M. Brhlik. Neutralino dark matter in minimal supergravity: Direct detection versus collider searches. Phys.Rev. **D57**, 567 (1998). inSPIRE. (cited on p. 16)

[68] L. Bergstrom, J. Edsjo, P. Gondolo, and P. Ullio. Clumpy neutralino dark matter. Phys.Rev. **D59**, 043506 (1999). inSPIRE. (cited on p. 16)

[69] J. L. Feng, K. T. Matchev, and F. Wilczek. Neutralino dark matter in focus point supersymmetry. Phys.Lett. **B482**, 388 (2000). inSPIRE. (cited on p. 16)

[70] D. Cerdeno and C. Munoz. Neutralino dark matter in supergravity theories with non-universal scalar and gaugino masses. JHEP **0410**, 015 (2004). inSPIRE. (cited on p. 16)

[71] T. Falk, K. A. Olive, and M. Srednicki. Heavy sneutrinos as dark matter. Phys.Lett. **B339**, 248 (1994). inSPIRE. (cited on pages 16 and 62)

[72] L. J. Hall, T. Moroi, and H. Murayama. Sneutrino cold dark matter with lepton number violation. Phys.Lett. **B424**, 305 (1998). inSPIRE. (cited on p. 16)

[73] T. Han and R. Hempfling. Messenger sneutrinos as cold dark matter. Phys.Lett. **B415**, 161 (1997). inSPIRE. (cited on p. 16)

[74] J. McDonald. Right-handed sneutrino condensate cold dark matter and the

baryon-to-dark matter ratio. JCAP **0701**, 001 (2007). inSPIRE. (cited on p. 16)

[75] C. Arina and N. Fornengo. Sneutrino cold dark matter, a new analysis: Relic abundance and detection rates. JHEP **0711**, 029 (2007). inSPIRE. (cited on pages 16 and 62)

[76] D. G. Cerdeno, C. Munoz, and O. Seto. Right-handed sneutrino as thermal dark matter. Phys.Rev. **D79**, 023510 (2009). inSPIRE. (cited on pages 16, 61, and 71)

[77] K. A. Olive, D. N. Schramm, and M. Srednicki. Gravitinos as the Cold Dark Matter in an omega = 1 Universe. Nucl.Phys. **B255**, 495 (1985). inSPIRE. (cited on p. 16)

[78] S. Borgani, A. Masiero, and M. Yamaguchi. Light gravitinos as mixed dark matter. Phys.Lett. **B386**, 189 (1996). inSPIRE. (cited on p. 16)

[79] F. Takayama and M. Yamaguchi. Gravitino dark matter without R-parity. Phys.Lett. **B485**, 388 (2000). inSPIRE. (cited on p. 16)

[80] J. R. Ellis, K. A. Olive, Y. Santoso, and V. C. Spanos. Gravitino dark matter in the CMSSM. Phys.Lett. **B588**, 7 (2004). inSPIRE. (cited on p. 16)

[81] D. G. Cerdeno, K.-Y. Choi, K. Jedamzik, L. Roszkowski, and R. Ruiz de Austri. Gravitino dark matter in the CMSSM with improved constraints from BBN. JCAP **0606**, 005 (2006). inSPIRE. (cited on p. 16)

[82] W. Buchmuller, L. Covi, K. Hamaguchi, A. Ibarra, and T. Yanagida. Gravitino Dark Matter in R-Parity Breaking Vacua. JHEP **0703**, 037 (2007). inSPIRE. (cited on p. 16)

[83] K.-Y. Choi, D. E. Lopez-Fogliani, C. Munoz, and R. R. de Austri. Gamma-ray detection from gravitino dark matter decay in the mu nu SSM. JCAP **1003**, 028 (2010). inSPIRE. (cited on pages 16 and 32)

[84] H.-C. Cheng, J. L. Feng, and K. T. Matchev. Kaluza-Klein dark matter. Phys.Rev.Lett. **89**, 211301 (2002). inSPIRE. (cited on p. 17)

[85] G. Servant and T. M. Tait. Is the lightest Kaluza-Klein particle a viable dark matter candidate? Nucl.Phys. **B650**, 391 (2003). inSPIRE. (cited on p. 17)

[86] D. Hooper and S. Profumo. Dark matter and collider phenomenology of universal extra dimensions. Phys.Rept. **453**, 29 (2007). inSPIRE. (cited on p. 17)

[87] H.-C. Cheng and I. Low. Little hierarchy, little Higgses, and a little symmetry. JHEP **0408**, 061 (2004). inSPIRE. (cited on p. 17)

[88] M. Schmaltz and D. Tucker-Smith. Little Higgs review. Ann.Rev.Nucl.Part.Sci. **55**, 229 (2005). inSPIRE. (cited on p. 17)

[89] A. Birkedal, A. Noble, M. Perelstein, and A. Spray. Little Higgs dark matter. Phys.Rev. **D74**, 035002 (2006). inSPIRE. (cited on p. 17)

[90] H. Hodges. Mirror baryons as the dark matter. Phys.Rev. **D47**, 456 (1993). inSPIRE. (cited on p. 17)

[91] C. Burgess, M. Pospelov, and T. ter Veldhuis. The Minimal model of nonbaryonic dark matter: A Singlet scalar. Nucl.Phys. **B619**, 709 (2001). inSPIRE. (cited on pages 17 and 67)

[92] A. Djouadi, O. Lebedev, Y. Mambrini, and J. Quevillon. Implications of LHC searches for Higgs–portal dark matter. Phys.Lett. **B709**, 65 (2012). inSPIRE. (cited on p. 17)

[93] A. Djouadi, A. Falkowski, Y. Mambrini, and J. Quevillon. Direct Detection of Higgs-Portal Dark Matter at the LHC. Eur.Phys.J. **C73**, 2455 (2013). inSPIRE. (cited on p. 17)

[94] N. G. Deshpande and E. Ma. Pattern of Symmetry Breaking with Two Higgs Doublets. Phys.Rev. **D18**, 2574 (1978). inSPIRE. (cited on p. 17)

[95] L. Lopez Honorez, E. Nezri, J. F. Oliver, and M. H. Tytgat. The Inert Doublet Model: An Archetype for Dark Matter. JCAP **0702**, 028 (2007). inSPIRE. (cited on p. 17)

[96] A. Drukier, K. Freese, and D. Spergel. Detecting Cold Dark Matter Candidates. Phys.Rev. **D33**, 3495 (1986). inSPIRE. (cited on p. 18)

[97] P. Smith and J. Lewin. Dark Matter Detection. Phys.Rept. **187**, 203 (1990). inSPIRE. (cited on pages 19 and 86)

[98] R. Agnese *et al.* Silicon Detector Dark Matter Results from the Final Exposure of CDMS II. Phys.Rev.Lett. **111**, 251301 (2013). inSPIRE. (cited on pages 19, 58, and 73)

[99] R. Bernabei, P. Belli, F. Cappella, R. Cerulli, F. Montecchia, *et al.* Dark matter search. Riv.Nuovo Cim. **26N1**, 1 (2003). inSPIRE. (cited on p. 19)

[100] R. Bernabei *et al.* First results from DAMA/LIBRA and the combined results with DAMA/NaI. Eur.Phys.J. **C56**, 333 (2008). inSPIRE. (cited on p. 19)

[101] C. Aalseth *et al.* Results from a Search for Light-Mass Dark Matter with a P-type Point

Contact Germanium Detector. Phys.Rev.Lett. **106**, 131301 (2011). inSPIRE. (cited on p. 19)

[102] G. Angloher, M. Bauer, I. Bavykina, A. Bento, C. Bucci, *et al.* Results from 730 kg days of the CRESST-II Dark Matter Search. Eur.Phys.J. **C72**, 1971 (2012). inSPIRE. (cited on pages 20 and 127)

[103] C. Aalseth, P. Barbeau, J. Colaresi, J. Collar, J. Diaz Leon, *et al.* Search for an Annual Modulation in a P-type Point Contact Germanium Dark Matter Detector. Phys.Rev.Lett. **107**, 141301 (2011). inSPIRE. (cited on p. 20)

[104] C. Aalseth *et al.* Search for An Annual Modulation in Three Years of CoGeNT Dark Matter Detector Data (2014). inSPIRE. (cited on p. 20)

[105] C. Aalseth, P. Barbeau, J. Colaresi, J. Collar, J. D. Leon, *et al.* Maximum Likelihood Signal Extraction Method Applied to 3.4 years of CoGeNT Data (2014). inSPIRE. (cited on p. 20)

[106] D. Akerib *et al.* First results from the LUX dark matter experiment at the Sanford Underground Research Facility (2013). inSPIRE. (cited on pages 20, 73, and 83)

[107] J. Angle *et al.* A search for light dark matter in XENON10 data. Phys.Rev.Lett. **107**, 051301 (2011). inSPIRE. (cited on p. 20)

[108] E. Aprile *et al.* Dark Matter Results from 225 Live Days of XENON100 Data. Phys.Rev.Lett. **109**, 181301 (2012). inSPIRE. (cited on pages 20 and 133)

[109] E. Aprile *et al.* Limits on spin-dependent WIMP-nucleon cross sections from 225 live days of XENON100 data. Phys.Rev.Lett. **111**, 021301 (2013). inSPIRE. (cited on pages 20, 47, and 48)

[110] Z. Ahmed *et al.* Dark Matter Search Results from the CDMS II Experiment. Science **327**, 1619 (2010). inSPIRE. (cited on p. 20)

[111] R. Agnese *et al.* CDMSlite: A Search for Low-Mass WIMPs using Voltage-Assisted Calorimetric Ionization Detection in the SuperCDMS Experiment. Phys.Rev.Lett. **112**, 041302 (2014). inSPIRE. (cited on pages 20 and 83)

[112] M. Felizardo, T. Girard, T. Morlat, A. Fernandes, A. Ramos, *et al.* Final Analysis and Results of the Phase II SIMPLE Dark Matter Search. Phys.Rev.Lett. **108**, 201302 (2012). inSPIRE. (cited on p. 20)

[113] S. Kim, H. Bhang, J. Choi, W. Kang, B. Kim, *et al.* New Limits on Interactions between Weakly Interacting Massive Particles and Nucleons Obtained with CsI(Tl) Crystal Detectors. Phys.Rev.Lett. **108**, 181301 (2012). inSPIRE. (cited on p. 20)

[114] Z. Ahmed *et al.* Combined Limits on WIMPs from the CDMS and EDELWEISS Experiments. Phys.Rev. **D84**, 011102 (2011). inSPIRE. (cited on p. 20)

[115] Z. Ahmed *et al.* Search for annual modulation in low-energy CDMS-II data (2012). inSPIRE. (cited on p. 20)

[116] R. Agnese *et al.* Search for Low-Mass WIMPs with SuperCDMS (2014). inSPIRE. (cited on pages 20, 73, and 83)

[117] J. Billard, L. Strigari, and E. Figueroa-Feliciano. Implication of neutrino backgrounds on the reach of next generation dark matter direct detection experiments. Phys.Rev. **D89**, 023524 (2014). inSPIRE. (cited on pages 20, 47, and 73)

[118] M. T. Frandsen, F. Kahlhoefer, C. McCabe, S. Sarkar, and K. Schmidt-Hoberg. The unbearable lightness of being: CDMS versus XENON. JCAP **1307**, 023 (2013). inSPIRE. (cited on p. 20)

[119] J. L. Feng, J. Kumar, and D. Sanford. Xenophobic Dark Matter. Phys.Rev. **D88**, 015021 (2013). inSPIRE. (cited on p. 20)

[120] G. Belanger, A. Goudelis, J.-C. Park, and A. Pukhov. Isospin-violating dark matter from a double portal (2013). inSPIRE. (cited on p. 20)

[121] M. I. Gresham and K. M. Zurek. Light Dark Matter Anomalies After LUX. Phys.Rev. **D89**, 016017 (2014). inSPIRE. (cited on p. 20)

[122] E. Del Nobile, G. B. Gelmini, P. Gondolo, and J.-H. Huh. Update on Light WIMP Limits: LUX, lite and Light (2013). inSPIRE. (cited on p. 20)

[123] E. Del Nobile, G. B. Gelmini, P. Gondolo, and J.-H. Huh. Halo-independent analysis of direct detection data for light WIMPs (2013). inSPIRE. (cited on p. 20)

[124] O. Adriani *et al.* An anomalous positron abundance in cosmic rays with energies 1.5-100 GeV. Nature **458**, 607 (2009). inSPIRE. (cited on p. 21)

[125] O. Adriani, G. Barbarino, G. Bazilevskaya, R. Bellotti, M. Boezio, *et al.* A new measurement of the antiproton-to-proton flux ratio up to 100 GeV in the cosmic radiation. Phys.Rev.Lett. **102**, 051101 (2009). inSPIRE. (cited on p. 21)

[126] M. Ackermann *et al.* Measurement of separate cosmic-ray electron and positron spectra with the Fermi Large Area Telescope. Phys.Rev.Lett. **108**, 011103 (2012). inSPIRE. (cited on p. 21)

[127] M. Aguilar *et al.* First Result from the Alpha Magnetic Spectrometer on the International Space Station: Precision Measurement of the Positron Fraction in Primary Cosmic Rays of 0.550 GeV. Phys.Rev.Lett. **110**, 141102 (2013). inSPIRE. (cited on pages 21 and 77)

[128] M. Di Mauro, F. Donato, N. Fornengo, R. Lineros, and A. Vittino. Interpretation of AMS-02 electrons and positrons data (2014). inSPIRE. (cited on p. 22)

[129] V. Vitale and A. Morselli. Indirect Search for Dark Matter from the center of the Milky Way with the Fermi-Large Area Telescope (2009). inSPIRE. (cited on pages 22, 75, and 169)

[130] A. Abdo *et al.* Constraints on Cosmological Dark Matter Annihilation from the Fermi-LAT Isotropic Diffuse Gamma-Ray Measurement. JCAP **1004**, 014 (2010). inSPIRE. (cited on pages 22 and 76)

[131] G. Zaharijas, A. Cuoco, Z. Yang, and J. Conrad. Constraints on the Galactic Halo Dark Matter from Fermi-LAT Diffuse Measurements. PoS **IDM2010**, 111 (2011). inSPIRE. (cited on p. 22)

[132] M. Ackermann *et al.* Constraining Dark Matter Models from a Combined Analysis of Milky Way Satellites with the Fermi Large Area Telescope. Phys.Rev.Lett. **107**, 241302 (2011). inSPIRE. (cited on pages 22, 49, 75, 76, 142, and 164)

[133] Search for Gamma-ray Spectral Lines with the Fermi Large Area Telescope and Dark Matter Implications. Physical Review D 88, **082002** (2013). inSPIRE. (cited on p. 22)

[134] G. A. Gomez-Vargas, M. A. Sanchez-Conde, J.-H. Huh, M. Peiro, F. Prada, *et al.* Constraints on WIMP Annihilation for Contracted Dark Matter in the Inner Galaxy with the Fermi-LAT **JCAP10**, 029 (2013). inSPIRE. (cited on pages 22, 76, and 78)

[135] T. Bringmann, X. Huang, A. Ibarra, S. Vogl, and C. Weniger. Fermi LAT Search for Internal Bremsstrahlung Signatures from Dark Matter Annihilation. JCAP **1207**, 054 (2012). inSPIRE. (cited on pages 22, 148, and 157)

[136] C. Weniger. A Tentative Gamma-Ray Line from Dark Matter Annihilation at the Fermi Large Area Telescope. JCAP **1208**, 007 (2012). inSPIRE. (cited on p. 22)

[137] E. Tempel, A. Hektor, and M. Raidal. Fermi 130 GeV gamma-ray excess and dark matter annihilation in sub-haloes and in the Galactic centre. JCAP **1209**, 032 (2012). inSPIRE. (cited on p. 22)

[138] A. Boyarsky, D. Malyshev, and O. Ruchayskiy. Spectral and spatial variations of the diffuse gamma-ray background in the vicinity of the Galactic plane and possible nature of the feature at 130 GeV. Phys.Dark Univ. **2**, 90 (2013). inSPIRE. (cited on p. 22)

[139] F. Aharonian, D. Khangulyan, and D. Malyshev. Cold ultrarelativistic pulsar winds as potential sources of galactic gamma-ray lines above 100 GeV (2012). inSPIRE. (cited on p. 22)

[140] D. P. Finkbeiner, M. Su, and C. Weniger. Is the 130 GeV Line Real? A Search for Systematics in the Fermi-LAT Data. JCAP **1301**, 029 (2013). inSPIRE. (cited on p. 22)

[141] A. Hektor, M. Raidal, and E. Tempel. Fermi-LAT gamma-ray signal from Earth Limb, systematic detector effects and their implications for the 130 GeV gamma-ray excess. Eur.Phys.J. **C73**, 2578 (2013). inSPIRE. (cited on p. 22)

[142] D. Whiteson. Disentangling Instrumental Features of the 130 GeV Fermi Line. JCAP **1211**, 008 (2012). inSPIRE. (cited on p. 22)

[143] D. Whiteson. Searching for Spurious Solar and Sky Lines in the Fermi-LAT Spectrum. Phys.Rev. **D88**, 023530 (2013). inSPIRE. (cited on p. 22)

[144] A. Morselli, B. Canadas, and V. Vitale. The Indirect Search for Dark Matter from the centre of the Galaxy with the Fermi LAT. Nuovo Cim. **C034N3**, 311 (2011). inSPIRE. (cited on pages 23, 75, 142, and 169)

[145] D. Hooper and L. Goodenough. Dark Matter Annihilation in The Galactic Center As Seen by the Fermi Gamma Ray Space Telescope. Phys.Lett. **B697**, 412 (2011). inSPIRE. (cited on pages 23, 75, 142, and 169)

[146] D. Hooper and T. Linden. On The Origin Of The Gamma Rays From The Galactic Center. Phys.Rev. **D84**, 123005 (2011). inSPIRE. (cited on pages 23, 75, 76, 142, and 169)

[147] K. N. Abazajian and M. Kaplinghat. Detection of a Gamma-Ray Source in the Galactic Center Consistent with Extended Emission from Dark Matter Annihilation and Concentrated Astrophysical Emission. Phys.Rev. **D86**, 083511 (2012). inSPIRE. (cited on pages 23, 142, and 169)

[148] C. Gordon and O. Macas. Dark Matter and Pulsar Model Constraints from Galactic Center Fermi-LAT Gamma Ray Observations. Phys.Rev. **D88**, 083521 (2013). inSPIRE. (cited on pages 23, 49, 142, 169, 170, and 228)

[149] K. N. Abazajian, N. Canac, S. Horiuchi, and M. Kaplinghat. Astrophysical and Dark Matter Interpretations of Extended Gamma Ray Emission from the Galactic Center (2014). inSPIRE. (cited on pages 23, 75, and 142)

[150] S. Chatrchyan *et al.* Observation of a new boson at a mass of 125 GeV with the CMS experiment at the LHC. Phys.Lett. **B716**, 30 (2012). inSPIRE. (cited on p. 23)

[151] G. Aad *et al.* Observation of a new particle in the search for the Standard Model Higgs boson with the ATLAS detector at the LHC. Phys.Lett. **B716**, 1 (2012). inSPIRE. (cited on p. 23)

[152] Combination of standard model Higgs boson searches and measurements of the properties of the new boson with a mass near 125 GeV (2013). inSPIRE. (cited on pages 23 and 53)

[153] Measurements of the properties of the Higgs-like boson in the two photon decay channel with the ATLAS detector using 25 fb^{-1} of proton-proton collision data (2013). inSPIRE. (cited on p. 23)

[154] Properties of the Higgs-like boson in the decay H to ZZ to 4l in pp collisions at sqrt s =7 and 8 TeV (2013). inSPIRE. (cited on p. 23)

[155] Measurements of the properties of the Higgs-like boson in the four lepton decay channel with the ATLAS detector using 25 fb?1 of proton-proton collision data (2013). inSPIRE. (cited on p. 23)

[156] S. Heinemeyer *et al.* Handbook of LHC Higgs Cross Sections: 3. Higgs Properties (2013). inSPIRE. (cited on p. 23)

[157] J. R. Espinosa, M. Muhlleitner, C. Grojean, and M. Trott. Probing for Invisible Higgs Decays with Global Fits. JHEP **1209**, 126 (2012). inSPIRE. (cited on pages 23 and 24)

[158] G. Belanger, B. Dumont, U. Ellwanger, J. Gunion, and S. Kraml. Status of invisible Higgs decays. Phys.Lett. **B723**, 340 (2013). inSPIRE. (cited on p. 23)

[159] A. Djouadi and G. Moreau. The couplings of the Higgs boson and its CP properties from fits of the signal strengths and their ratios at the 7+8 TeV LHC (2013). inSPIRE. (cited on pages 23 and 24)

[160] Search for invisible decays of a Higgs boson produced in association with a Z boson in ATLAS (2013). inSPIRE. (cited on p. 23)

[161] Search for the Higgs boson decaying to invisible particles produced in association with Z bosons decaying to bottom quarks (2013). inSPIRE. (cited on p. 23)

[162] G. Aad *et al.* Search for Invisible Decays of a Higgs Boson Produced in Association with a Z Boson in ATLAS (2014). inSPIRE. (cited on p. 23)

[163] G. Belanger, B. Dumont, U. Ellwanger, J. Gunion, and S. Kraml. Global fit to Higgs signal strengths and couplings and implications for extended Higgs sectors. Phys.Rev. **D88**, 075008 (2013). inSPIRE. (cited on p. 24)

[164] P. P. Giardino, K. Kannike, I. Masina, M. Raidal, and A. Strumia. The universal Higgs fit (2013). inSPIRE. (cited on p. 24)

[165] B. L. Roberts. Status of the Fermilab Muon $(g-2)$ Experiment. Chin.Phys. **C34**, 741 (2010). inSPIRE. (cited on p. 27)

[166] J. Bagger and J. Wess. Supersymmetry and supergravity (1990). inSPIRE. (cited on p. 30)

[167] S. Weinberg. The quantum theory of fields: Supersymmetry (2000). (cited on p. 30)

[168] I. Aitchison. Supersymmetry in Particle Physics. An Elementary Introduction (2007). inSPIRE. (cited on p. 30)

[169] I. J. Aitchison. Supersymmetry and the MSSM: An Elementary introduction (2005). inSPIRE. (cited on p. 30)

[170] M. Drees. An Introduction to supersymmetry (1996). inSPIRE. (cited on p. 30)

[171] L. J. Hall, J. D. Lykken, and S. Weinberg. Supergravity as the Messenger of Supersymmetry Breaking. Phys.Rev. **D27**, 2359 (1983). inSPIRE. (cited on p. 30)

[172] M. Dine and W. Fischler. A Phenomenological Model of Particle Physics Based on Supersymmetry. Phys.Lett. **B110**, 227 (1982). inSPIRE. (cited on p. 31)

[173] G. Giudice and R. Rattazzi. Theories with gauge mediated supersymmetry breaking. Phys.Rept. **322**, 419 (1999). inSPIRE. (cited on p. 31)

[174] L. Randall and R. Sundrum. Out of this world supersymmetry breaking. Nucl.Phys. **B557**, 79 (1999). inSPIRE. (cited on p. 31)

[175] E. Roulet and D. Tommasini. Cosmologically interesting neutrino decay in supersymmetry with broken R-parity. Phys.Lett. **B256**, 218 (1991). inSPIRE. (cited on p. 32)

[176] R. Barbier, C. Berat, M. Besancon, M. Chemtob, A. Deandrea, *et al.* R-parity violating supersymmetry. Phys.Rept. **420**, 1 (2005). inSPIRE. (cited on p. 32)

[177] D. Lopez-Fogliani and C. Munoz. Proposal for a new minimal supersymmetric standard model. Phys.Rev.Lett. **97**, 041801 (2006). inSPIRE. (cited on p. 32)

[178] Lep susy working group page. webpage. (cited on p. 33)

[179] Tevatron new phenomena and higgs working group page. webpage. (cited on p. 33)

[180] T. Adams. SUSY Searches at the Tevatron (2008). inSPIRE. (cited on p. 33)

[181] G. Aad *et al.* Multi-channel search for squarks and gluinos in $\sqrt{s} = 7$ TeV pp collisions with the ATLAS detector. Eur.Phys.J. **C73**, 2362 (2013). inSPIRE. (cited on p. 33)

[182] S. Chatrchyan *et al.* Search for new physics in the multijet and missing transverse momentum final state in proton-proton collisions at $\sqrt{s} = 7$ TeV. Phys.Rev.Lett. **109**, 171803 (2012). inSPIRE. (cited on p. 33)

[183] Atlas twiki link. pdf. (cited on p. 33)

[184] Cms twiki link. pdf. (cited on p. 33)

[185] R. Aaij *et al.* Measurement of the $B_s^0 \to \mu^+\mu^-$ branching fraction and search for $B^0 \to \mu^+\mu^-$ decays at the LHCb experiment. Phys.Rev.Lett. **111**, 101805 (2013). inSPIRE. (cited on p. 33)

[186] S. Chatrchyan *et al.* Measurement of the B(s) to mu+ mu- branching fraction and search for B0 to mu+ mu- with the CMS Experiment. Phys.Rev.Lett. **111**, 101804 (2013). inSPIRE. (cited on p. 33)

[187] See talk by m. galanti. Talk. (cited on p. 33)

[188] M. Ciuchini, G. Degrassi, P. Gambino, and G. Giudice. Next-to-leading QCD corrections to B X(s) gamma in supersymmetry. Nucl.Phys. **B534**, 3 (1998). inSPIRE. (cited on p. 34)

[189] G. D'Ambrosio, G. Giudice, G. Isidori, and A. Strumia. Minimal flavor violation: An Effective field theory approach. Nucl.Phys. **B645**, 155 (2002). inSPIRE. (cited on p. 34)

[190] M. Misiak, H. Asatrian, K. Bieri, M. Czakon, A. Czarnecki, *et al.* Estimate of B(anti-B X(s) gamma) at O(alpha(s)**2). Phys.Rev.Lett. **98**, 022002 (2007). inSPIRE. (cited on p. 34)

[191] M. Misiak and M. Steinhauser. NNLO QCD corrections to the anti-B X(s) gamma matrix elements using interpolation in m(c). Nucl.Phys. **B764**, 62 (2007). inSPIRE. (cited on p. 34)

[192] Y. Amhis *et al.* Averages of B-Hadron, C-Hadron, and tau-lepton properties as of early 2012 (2012). inSPIRE. (cited on p. 34)

[193] F. Feroz and M. Hobson. Multimodal nested sampling: an efficient and robust alternative to MCMC methods for astronomical data analysis. Mon.Not.Roy.Astron.Soc. **384**, 449 (2008). inSPIRE. (cited on pages 34 and 95)

[194] F. Feroz, M. Hobson, and M. Bridges. MultiNest: an efficient and robust Bayesian inference tool for cosmology and particle physics. Mon.Not.Roy.Astron.Soc. **398**, 1601 (2009). inSPIRE. (cited on pages 34 and 95)

[195] F. Feroz, M. Hobson, E. Cameron, and A. Pettitt. Importance Nested Sampling and the MultiNest Algorithm (2013). inSPIRE. (cited on p. 34)

[196] B. Allanach. SOFTSUSY: a program for calculating supersymmetric spectra. Comput.Phys.Commun. **143**, 305 (2002). inSPIRE. (cited on p. 35)

[197] U. Ellwanger, J. F. Gunion, and C. Hugonie. NMHDECAY: A Fortran code for the Higgs masses, couplings and decay widths in the NMSSM. JHEP **0502**, 066 (2005). inSPIRE. (cited on p. 35)

[198] U. Ellwanger and C. Hugonie. NMHDECAY 2.0: An Updated program for sparticle masses, Higgs masses, couplings and decay widths in the NMSSM. Comput.Phys.Commun. **175**, 290 (2006). inSPIRE. (cited on p. 35)

[199] G. Belanger, F. Boudjema, C. Hugonie, A. Pukhov, and A. Semenov. Relic density of dark matter in the NMSSM. JCAP **0509**, 001 (2005). inSPIRE. (cited on pages 35 and 52)

[200] G. Belanger, F. Boudjema, A. Pukhov, and A. Semenov. MicrOMEGAs 2.0: A Program to calculate the relic density of dark matter in a generic model. Comput.Phys.Commun. **176**, 367 (2007). inSPIRE. (cited on p. 35)

[201] G. Belanger, F. Boudjema, A. Pukhov, and A. Semenov. Dark matter direct detection

rate in a generic model with micrOMEGAs 2.2. Comput.Phys.Commun. **180**, 747 (2009). inSPIRE. (cited on pages 35, 46, and 94)

[202] G. Belanger, F. Boudjema, P. Brun, A. Pukhov, S. Rosier-Lees, *et al.* Indirect search for dark matter with micrOMEGAs2.4. Comput.Phys.Commun. **182**, 842 (2011). inSPIRE. (cited on p. 35)

[203] G. Belanger, F. Boudjema, A. Pukhov, and A. Semenov. micrOMEGAs 3: A program for calculating dark matter observables. Comput.Phys.Commun. **185**, 960 (2014). inSPIRE. (cited on pages 35 and 46)

[204] F. Feroz, K. Cranmer, M. Hobson, R. Ruiz de Austri, and R. Trotta. Challenges of Profile Likelihood Evaluation in Multi-Dimensional SUSY Scans. JHEP **1106**, 042 (2011). inSPIRE. (cited on pages 35 and 95)

[205] H. P. Nilles. Supersymmetry, Supergravity and Particle Physics. Phys.Rept. **110**, 1 (1984). inSPIRE. (cited on p. 36)

[206] H. E. Haber and G. L. Kane. The Search for Supersymmetry: Probing Physics Beyond the Standard Model. Phys.Rept. **117**, 75 (1985). inSPIRE. (cited on p. 36)

[207] H. E. Haber and R. Hempfling. Can the mass of the lightest Higgs boson of the minimal supersymmetric model be larger than m(Z)? Phys.Rev.Lett. **66**, 1815 (1991). inSPIRE. (cited on p. 39)

[208] J. R. Ellis, G. Ridolfi, and F. Zwirner. Radiative corrections to the masses of supersymmetric Higgs bosons. Phys.Lett. **B257**, 83 (1991). inSPIRE. (cited on p. 39)

[209] P. Draper, P. Meade, M. Reece, and D. Shih. Implications of a 125 GeV Higgs for the MSSM and Low-Scale SUSY Breaking. Phys.Rev. **D85**, 095007 (2012). inSPIRE. (cited on p. 39)

[210] M. Carena, S. Gori, N. R. Shah, and C. E. Wagner. A 125 GeV SM-like Higgs in the MSSM and the $\gamma\gamma$ rate. JHEP **1203**, 014 (2012). inSPIRE. (cited on pages 39 and 43)

[211] A. Bottino, N. Fornengo, and S. Scopel. Light relic neutralinos. Phys.Rev. **D67**, 063519 (2003). inSPIRE. (cited on p. 40)

[212] N. Fornengo, S. Scopel, and A. Bottino. Discussing direct search of dark matter particles in the Minimal Supersymmetric extension of the Standard Model with light neutralinos. Phys.Rev. **D83**, 015001 (2011). inSPIRE. (cited on p. 40)

[213] A. Bottino, N. Fornengo, and S. Scopel. Phenomenology of light neutralinos in view of recent results at the CERN Large Hadron Collider. Phys.Rev. **D85**, 095013 (2012). inSPIRE. (cited on p. 40)

[214] Search for MSSM Neutral Higgs Bosons Decaying to Tau Pairs in pp Collisions (2012). inSPIRE. (cited on p. 40)

[215] G. Aad *et al.* Search for charged Higgs bosons decaying via $H^+ \to \tau\nu$ in top quark pair events using pp collision data at $\sqrt{s} = 7$ TeV with the ATLAS detector. JHEP **1206**, 039 (2012). inSPIRE. (cited on p. 40)

[216] D. A. Vasquez, G. Belanger, C. Boehm, A. Pukhov, and J. Silk. Can neutralinos in the MSSM and NMSSM scenarios still be light? Phys.Rev. **D82**, 115027 (2010). inSPIRE. (cited on pages 40 and 52)

[217] D. Albornoz Vasquez, G. Belanger, and C. Boehm. Revisiting light neutralino scenarios in the MSSM. Phys.Rev. **D84**, 095015 (2011). inSPIRE. (cited on pages 40, 48, 52, 53, and 59)

[218] G. Belanger, S. Biswas, C. Boehm, and B. Mukhopadhyaya. Light Neutralino Dark Matter in the MSSM and Its Implication for LHC Searches for Staus. JHEP **1212**, 076 (2012). inSPIRE. (cited on p. 40)

[219] A. Pierce, N. R. Shah, and K. Freese. Neutralino Dark Matter with Light Staus (2013). inSPIRE. (cited on pages 40, 41, and 48)

[220] G. Blanger, G. Drieu La Rochelle, B. Dumont, R. M. Godbole, S. Kraml, *et al.* LHC constraints on light neutralino dark matter in the MSSM. Phys.Lett. **B726**, 773 (2013). inSPIRE. (cited on p. 40)

[221] A. Arbey, M. Battaglia, and F. Mahmoudi. Light Neutralino Dark Matter in the pMSSM: Implications of LEP, LHC and Dark Matter Searches on SUSY Particle Spectra. Eur.Phys.J. **C72**, 2169 (2012). inSPIRE. (cited on p. 41)

[222] J. Rosiek. Complete set of Feynman rules for the MSSM: Erratum (1995). inSPIRE. (cited on p. 41)

[223] P. Bechtle, O. Brein, S. Heinemeyer, G. Weiglein, and K. E. Williams. HiggsBounds: Confronting Arbitrary Higgs Sectors with Exclusion Bounds from LEP and the Tevatron. Comput.Phys.Commun. **181**, 138 (2010). inSPIRE. (cited on p. 43)

[224] P. Bechtle, O. Brein, S. Heinemeyer, O. Stl, T. Stefaniak, *et al.* HiggsBounds-4:

Improved Tests of Extended Higgs Sectors against Exclusion Bounds from LEP, the Tevatron and the LHC (2013). inSPIRE. (cited on p. 43)

[225] L. Aparicio, D. Cerdeno, and L. Ibanez. A 119-125 GeV Higgs from a string derived slice of the CMSSM. JHEP **1204**, 126 (2012). inSPIRE. (cited on p. 45)

[226] U. Ellwanger, C. Hugonie, and A. M. Teixeira. The Next-to-Minimal Supersymmetric Standard Model. Phys.Rept. **496**, 1 (2010). inSPIRE. (cited on p. 50)

[227] M. Maniatis. The Next-to-Minimal Supersymmetric extension of the Standard Model reviewed. Int.J.Mod.Phys. **A25**, 3505 (2010). inSPIRE. (cited on p. 50)

[228] U. Ellwanger, G. Espitalier-Noel, and C. Hugonie. Naturalness and Fine Tuning in the NMSSM: Implications of Early LHC Results. JHEP **1109**, 105 (2011). inSPIRE. (cited on p. 51)

[229] A. Arvanitaki and G. Villadoro. A Non Standard Model Higgs at the LHC as a Sign of Naturalness. JHEP **1202**, 144 (2012). inSPIRE. (cited on p. 51)

[230] Z. Kang, J. Li, and T. Li. On Naturalness of the MSSM and NMSSM. JHEP **1211**, 024 (2012). inSPIRE. (cited on p. 51)

[231] K. Agashe, Y. Cui, and R. Franceschini. Natural Islands for a 125 GeV Higgs in the scale-invariant NMSSM. JHEP **1302**, 031 (2013). inSPIRE. (cited on p. 51)

[232] S. King, M. Mhlleitner, R. Nevzorov, and K. Walz. Natural NMSSM Higgs Bosons. Nucl.Phys. **B870**, 323 (2013). inSPIRE. (cited on p. 51)

[233] D. A. Vasquez, G. Belanger, C. Boehm, J. Da Silva, P. Richardson, *et al.* The 125 GeV Higgs in the NMSSM in light of LHC results and astrophysics constraints. Phys.Rev. **D86**, 035023 (2012). inSPIRE. (cited on pages 51 and 68)

[234] F. Ferrer, L. M. Krauss, and S. Profumo. Indirect detection of light neutralino dark matter in the NMSSM. Phys.Rev. **D74**, 115007 (2006). inSPIRE. (cited on p. 52)

[235] J. F. Gunion, D. Hooper, and B. McElrath. Light neutralino dark matter in the NMSSM. Phys.Rev. **D73**, 015011 (2006). inSPIRE. (cited on p. 52)

[236] D. Das and U. Ellwanger. Light dark matter in the NMSSM: upper bounds on direct detection cross sections. JHEP **1009**, 085 (2010). inSPIRE. (cited on p. 52)

[237] J.-J. Cao, K.-i. Hikasa, W. Wang, J. M. Yang, K.-i. Hikasa, *et al.* Light dark matter in

NMSSM and implication on Higgs phenomenology. Phys.Lett. **B703**, 292 (2011). inSPIRE. (cited on p. 52)

[238] M. Carena, N. R. Shah, and C. E. Wagner. Light Dark Matter and the Electroweak Phase Transition in the NMSSM. Phys.Rev. **D85**, 036003 (2012). inSPIRE. (cited on p. 52)

[239] D. Albornoz Vasquez, G. Belanger, and C. Boehm. Astrophysical limits on light NMSSM neutralinos. Phys.Rev. **D84**, 095008 (2011). inSPIRE. (cited on pages 52 and 59)

[240] D. E. Lopez-Fogliani. Light Higgs and neutralino dark matter in the NMSSM. J.Phys.Conf.Ser. **384**, 012014 (2012). inSPIRE. (cited on p. 52)

[241] J. Kozaczuk and S. Profumo. Light NMSSM Neutralino Dark Matter in the Wake of CDMS II and a 126 GeV Higgs (2013). inSPIRE. (cited on pages 52 and 58)

[242] U. Ellwanger and C. Hugonie. Constraints from charge and color breaking minima in the (M+1)SSM. Phys.Lett. **B457**, 299 (1999). inSPIRE. (cited on p. 53)

[243] O. Stal and G. Weiglein. Light NMSSM Higgs bosons in SUSY cascade decays at the LHC. JHEP **1201**, 071 (2012). inSPIRE. (cited on p. 56)

[244] M. Ibe, H. Murayama, and T. Yanagida. Breit-Wigner Enhancement of Dark Matter Annihilation. Phys.Rev. **D79**, 095009 (2009). inSPIRE. (cited on p. 58)

[245] X.-J. Bi, X.-G. He, and Q. Yuan. Parameters in a class of leptophilic models from PAMELA, ATIC and FERMI. Phys.Lett. **B678**, 168 (2009). inSPIRE. (cited on p. 59)

[246] D. G. Cerdeno, J.-H. Huh, M. Peiro, and O. Seto. Very light right-handed sneutrino dark matter in the NMSSM. JCAP **1111**, 027 (2011). inSPIRE. (cited on pages 61, 71, and 74)

[247] D. G. Cerdeno and O. Seto. Right-handed sneutrino dark matter in the NMSSM. JCAP **0908**, 032 (2009). inSPIRE. (cited on pages 61, 64, and 71)

[248] S. Gopalakrishna, A. de Gouvea, and W. Porod. Right-handed sneutrinos as nonthermal dark matter. JCAP **0605**, 005 (2006). inSPIRE. (cited on p. 62)

[249] N. Arkani-Hamed, L. J. Hall, H. Murayama, D. Tucker-Smith, and N. Weiner. Small neutrino masses from supersymmetry breaking. Phys.Rev. **D64**, 115011 (2001). inSPIRE. (cited on p. 62)

[250] D. Hooper, J. March-Russell, and S. M. West. Asymmetric sneutrino dark matter and the Omega(b) / Omega(DM) puzzle. Phys.Lett. **B605**, 228 (2005). inSPIRE. (cited on p. 62)

[251] C. Arina. Sneutrino cold dark matter in extended MSSM models (2008). inSPIRE. (cited on p. 62)

[252] G. Belanger, M. Kakizaki, E. Park, S. Kraml, and A. Pukhov. Light mixed sneutrinos as thermal dark matter. JCAP **1011**, 017 (2010). inSPIRE. (cited on p. 62)

[253] B. Dumont, G. Belanger, S. Fichet, S. Kraml, and T. Schwetz. Mixed sneutrino dark matter in light of the 2011 XENON and LHC results. JCAP **1209**, 013 (2012). inSPIRE. (cited on p. 62)

[254] G. Belanger, J. Da Silva, and A. Pukhov. The Right-handed sneutrino as thermal dark matter in U(1) extensions of the MSSM. JCAP **1112**, 014 (2011). inSPIRE. (cited on p. 62)

[255] M. Srednicki, R. Watkins, and K. A. Olive. Calculations of Relic Densities in the Early Universe. Nucl.Phys. **B310**, 693 (1988). inSPIRE. (cited on p. 64)

[256] T. Nihei, L. Roszkowski, and R. Ruiz de Austri. Towards an accurate calculation of the neutralino relic density. JHEP **0105**, 063 (2001). inSPIRE. (cited on p. 64)

[257] P. Gondolo and G. Gelmini. Cosmic abundances of stable particles: Improved analysis. Nucl.Phys. **B360**, 145 (1991). inSPIRE. (cited on pages 65, 179, and 180)

[258] D. Hooper, I. Cholis, T. Linden, J. Siegal-Gaskins, and T. Slatyer. Millisecond pulsars Cannot Account for the Inner Galaxy's GeV Excess. Phys.Rev. **D88**, 083009 (2013). inSPIRE. (cited on pages 75 and 169)

[259] A. Geringer-Sameth and S. M. Koushiappas. Exclusion of canonical WIMPs by the joint analysis of Milky Way dwarfs with Fermi. Phys.Rev.Lett. **107**, 241303 (2011). inSPIRE. (cited on pages 75, 76, 142, and 164)

[260] M. Ackermann *et al.* Dark Matter Constraints from Observations of 25 Milky Way Satellite Galaxies with the Fermi Large Area Telescope. Phys.Rev. **D89**, 042001 (2014). inSPIRE. (cited on p. 75)

[261] D. Hooper, C. Kelso, and F. S. Queiroz. Stringent and Robust Constraints on the Dark Matter Annihilation Cross Section From the Region of the Galactic Center. Astropart.Phys. **46**, 55 (2013). inSPIRE. (cited on pages 76 and 146)

[262] Z. Li, Q. Yuan, and Y. Xu. Constraints on the dark matter annihilation from Fermi-LAT observation of M31 (2013). inSPIRE. (cited on p. 76)

[263] M. Ackermann *et al.* Constraints on the Galactic Halo Dark Matter from Fermi-LAT Diffuse Measurements. Astrophys.J. **761**, 91 (2012). inSPIRE. (cited on pages 76, 146, and 164)

[264] M. Ackermann *et al.* Fermi LAT Search for Dark Matter in Gamma-ray Lines and the Inclusive Photon Spectrum. Phys.Rev. **D86**, 022002 (2012). inSPIRE. (cited on p. 76)

[265] Constraints on the Galactic Dark Matter signal from the Fermi-LAT measurement of the diffuse gamma-ray emission (2013). inSPIRE. (cited on p. 76)

[266] M. Tavakoli, I. Cholis, C. Evoli, and P. Ullio. Constraints on dark matter annihilations from diffuse gamma-ray emission in the Galaxy. JCAP **1401**, 017 (2014). inSPIRE. (cited on p. 76)

[267] O. Adriani *et al.* PAMELA results on the cosmic-ray antiproton flux from 60 MeV to 180 GeV in kinetic energy. Phys.Rev.Lett. **105**, 121101 (2010). inSPIRE. (cited on p. 76)

[268] O. Adriani, G. Bazilevskaya, G. Barbarino, R. Bellotti, M. Boezio, *et al.* Measurement of the flux of primary cosmic ray antiprotons with energies of 60-MeV to 350-GeV in the PAMELA experiment. JETP Lett. **96**, 621 (2013). inSPIRE. (cited on p. 76)

[269] N. Fornengo, L. Maccione, and A. Vittino. Constraints on particle dark matter from cosmic-ray antiprotons (2013). inSPIRE. (cited on p. 76)

[270] L. Bergstrom, T. Bringmann, I. Cholis, D. Hooper, and C. Weniger. New limits on dark matter annihilation from AMS cosmic ray positron data. Phys.Rev.Lett. **111**, 171101 (2013). inSPIRE. (cited on p. 77)

[271] N. Bernal, A. Goudelis, Y. Mambrini, and C. Munoz. Determining the WIMP mass using the complementarity between direct and indirect searches and the ILC. JCAP **0901**, 046 (2009). inSPIRE. (cited on p. 83)

[272] L. Bergstrom, T. Bringmann, and J. Edsjo. Complementarity of direct dark matter detection and indirect detection through gamma-rays. Phys.Rev. **D83**, 045024 (2011). inSPIRE. (cited on p. 83)

[273] G. Bertone, D. Cerdeno, M. Fornasa, L. Pieri, R. Ruiz de Austri, *et al.* Complementarity of Indirect and Accelerator Dark Matter Searches. Phys.Rev. **D85**, 055014 (2012). inSPIRE. (cited on p. 83)

[274] Y. Mambrini, M. H. Tytgat, G. Zaharijas, and B. Zaldivar. Complementarity of Galactic radio and collider data in constraining WIMP dark matter models. JCAP **1211**, 038 (2012). inSPIRE. (cited on p. 83)

[275] D. Bauer, J. Buckley, M. Cahill-Rowley, R. Cotta, A. Drlica-Wagner, *et al.* Dark Matter in the Coming Decade: Complementary Paths to Discovery and Beyond (2013). inSPIRE. (cited on p. 83)

[276] S. Arrenberg, H. Baer, V. Barger, L. Baudis, D. Bauer, *et al.* Dark Matter in the Coming Decade: Complementary Paths to Discovery and Beyond (2013). inSPIRE. (cited on p. 83)

[277] C. Arina, G. Bertone, and H. Silverwood. Complementarity of direct and indirect Dark Matter detection experiments. Phys.Rev. **D88**, 013002 (2013). inSPIRE. (cited on p. 83)

[278] G. Bertone, D. G. Cerdeno, J. Collar, and B. C. Odom. WIMP identification through a combined measurement of axial and scalar couplings. Phys.Rev.Lett. **99**, 151301 (2007). inSPIRE. (cited on pages 83, 84, 118, and 119)

[279] M. Drees and C.-L. Shan. Model-Independent Determination of the WIMP Mass from Direct Dark Matter Detection Data. JCAP **0806**, 012 (2008). inSPIRE. (cited on pages 83, 84, 99, and 118)

[280] M. Cannoni, J. Vergados, and M. Gomez. A Scheme for the extraction of WIMP-nucleon scattering cross sections from total event rates. Phys.Rev. **D83**, 075010 (2011). inSPIRE. (cited on pages 83, 84, and 118)

[281] M. Pato, L. Baudis, G. Bertone, R. Ruiz de Austri, L. E. Strigari, *et al.* Complementarity of Dark Matter Direct Detection Targets. Phys.Rev. **D83**, 083505 (2011). inSPIRE. (cited on pages 83, 84, 97, and 118)

[282] A. Marchionni *et al.* ArDM: a ton-scale LAr detector for direct Dark Matter searches. J.Phys.Conf.Ser. **308**, 012006 (2011). inSPIRE. (cited on p. 84)

[283] H. Kraus, E. Armengaud, C. Augier, M. Bauer, N. Bechtold, *et al.* EURECA. PoS **IDM2010**, 109 (2011). inSPIRE. (cited on p. 84)

[284] S. Cebrian, N. Coron, G. Dambier, E. Garcia, I. Irastorza, *et al.* The ROSEBUD experiment at Canfranc: 2001 report. Nucl.Phys.Proc.Suppl. **110**, 97 (2002). inSPIRE. (cited on p. 84)

[285] C. Bobin, I. Berkes, J. Hadjout, N. Coron, J. Leblanc, *et al.* Alpha/gamma discrimination with a CaF-2(Eu) target bolometer optically coupled to a composite infrared bolometer. Nucl.Instrum.Meth. **A386**, 453 (1997). inSPIRE. (cited on p. 84)

[286] N. Coron, C. Cuesta, E. Garca, C. Ginestra, T. Girard, *et al.* Study of parylene-coated NaI(Tl) at low temperatures for bolometric applications. Astropart.Phys. **47**, 31 (2013). inSPIRE. (cited on p. 84)

[287] A. Kurylov and M. Kamionkowski. Generalized analysis of weakly interacting massive particle searches. Phys.Rev. **D69**, 063503 (2004). inSPIRE. (cited on p. 89)

[288] J. F. Navarro, C. S. Frenk, and S. D. White. A Universal density profile from hierarchical clustering. Astrophys.J. **490**, 493 (1997). inSPIRE. (cited on pages 90 and 144)

[289] J. F. Navarro, E. Hayashi, C. Power, A. Jenkins, C. S. Frenk, *et al.* The Inner structure of Lambda-CDM halos 3: Universality and asymptotic slopes. Mon.Not.Roy.Astron.Soc. **349**, 1039 (2004). inSPIRE. (cited on pages 90 and 144)

[290] A. Burkert. The Structure of dark matter halos in dwarf galaxies. IAU Symp. **171**, 175 (1996). inSPIRE. (cited on pages 90 and 144)

[291] M. Fornasa and A. M. Green. A self-consistent phase-space distribution function for the anisotropic Dark Matter halo of the Milky Way (2013). inSPIRE. (cited on pages 90 and 149)

[292] V. Bednyakov and F. Simkovic. Nuclear spin structure in dark matter search: The Zero momentum transfer limit. Phys.Part.Nucl. **36**, 131 (2005). inSPIRE. (cited on p. 91)

[293] P. Klos, J. Menndez, D. Gazit, and A. Schwenk. Large-scale nuclear structure calculations for spin-dependent WIMP scattering with chiral effective field theory currents. Physical Review D 88, **083516** (2013). inSPIRE. (cited on pages 91 and 92)

[294] V. Bednyakov and F. Simkovic. Nuclear spin structure in dark matter search: The Finite momentum transfer limit. Phys.Part.Nucl. **37**, S106 (2006). inSPIRE. (cited on p. 92)

[295] M. T. Ressell, M. B. Aufderheide, S. D. Bloom, K. Griest, G. J. Mathews, *et al.* Nuclear shell model calculations of neutralino - nucleus cross-sections for Si-29 and Ge-73. Phys.Rev. **D48**, 5519 (1993). inSPIRE. (cited on p. 93)

[296] V. Dimitrov, J. Engel, and S. Pittel. Scattering of weakly interacting massive particles from Ge-73. Phys.Rev. **D51**, 291 (1995). inSPIRE. (cited on p. 93)

[297] G. Bertone, D. G. Cerdeno, M. Fornasa, R. Ruiz de Austri, C. Strege, *et al.* Global fits of the cMSSM including the first LHC and XENON100 data. JCAP **1201**, 015 (2012). inSPIRE. (cited on p. 95)

[298] R. R. de Austri, R. Trotta, and L. Roszkowski. A Markov chain Monte Carlo analysis of the CMSSM. JHEP **0605**, 002 (2006). inSPIRE. (cited on p. 95)

[299] D. Cerdeno, M. Fornasa, J. Huh, and M. Peiro. Nuclear uncertainties in the spin-dependent structure functions for direct dark matter detection. Phys.Rev. **D87**, 023512 (2013). inSPIRE. (cited on pages 97 and 122)

[300] A. M. Green. Determining the WIMP mass using direct detection experiments. JCAP **0708**, 022 (2007). inSPIRE. (cited on p. 97)

[301] A. M. Green. Determining the WIMP mass from a single direct detection experiment, a more detailed study. JCAP **0807**, 005 (2008). inSPIRE. (cited on p. 97)

[302] A. H. Peter. WIMP astronomy and particle physics with liquid-noble and cryogenic direct-detection experiments. Phys.Rev. **D83**, 125029 (2011). inSPIRE. (cited on p. 97)

[303] C. Strege, R. Trotta, G. Bertone, A. H. Peter, and P. Scott. Fundamental statistical limitations of future dark matter direct detection experiments. Phys.Rev. **D86**, 023507 (2012). inSPIRE. (cited on pages 97 and 186)

[304] L. E. Strigari and R. Trotta. Reconstructing WIMP Properties in Direct Detection Experiments Including Galactic Dark Matter Distribution Uncertainties. JCAP **0911**, 019 (2009). inSPIRE. (cited on p. 99)

[305] A. M. Green. Extracting Information about WIMP Properties from Direct Detection Experiments: Astrophysical Uncertainties (2010). inSPIRE. (cited on p. 99)

[306] C. McCabe. The Astrophysical Uncertainties Of Dark Matter Direct Detection Experiments. Phys.Rev. **D82**, 023530 (2010). inSPIRE. (cited on p. 99)

[307] M. T. Frandsen, F. Kahlhoefer, C. McCabe, S. Sarkar, and K. Schmidt-Hoberg. Resolving astrophysical uncertainties in dark matter direct detection. JCAP **1201**, 024 (2012). inSPIRE. (cited on p. 99)

[308] A. M. Green. Astrophysical uncertainties on direct detection experiments. Mod.Phys.Lett. **A27**, 1230004 (2012). inSPIRE. (cited on p. 99)

[309] M. Fairbairn, T. Douce, and J. Swift. Quantifying Astrophysical Uncertainties on Dark

Matter Direct Detection Results. Astropart.Phys. **47**, 45 (2013). inSPIRE. (cited on p. 99)

[310] P. Gondolo and G. B. Gelmini. Halo independent comparison of direct dark matter detection data. JCAP **1212**, 015 (2012). inSPIRE. (cited on p. 99)

[311] E. Del Nobile, G. Gelmini, P. Gondolo, and J.-H. Huh. Generalized Halo Independent Comparison of Direct Dark Matter Detection Data. JCAP **1310**, 048 (2013). inSPIRE. (cited on p. 99)

[312] B. J. Kavanagh and A. M. Green. Model independent determination of the dark matter mass from direct detection experiments. Phys.Rev.Lett. **111**, 031302 (2013). inSPIRE. (cited on pages 100 and 119)

[313] B. Feldstein and F. Kahlhoefer. A new halo-independent approach to dark matter direct detection analysis (2014). inSPIRE. (cited on p. 100)

[314] M. Lisanti, L. E. Strigari, J. G. Wacker, and R. H. Wechsler. The Dark Matter at the End of the Galaxy. Phys.Rev. **D83**, 023519 (2011). inSPIRE. (cited on p. 100)

[315] R. Catena and P. Ullio. A novel determination of the local dark matter density. JCAP **1008**, 004 (2010). inSPIRE. (cited on pages 101 and 146)

[316] P. Salucci, F. Nesti, G. Gentile, and C. Martins. The dark matter density at the Sun's location. Astron.Astrophys. **523**, A83 (2010). inSPIRE. (cited on p. 101)

[317] M. Pato, O. Agertz, G. Bertone, B. Moore, and R. Teyssier. Systematic uncertainties in the determination of the local dark matter density. Phys.Rev. **D82**, 023531 (2010). inSPIRE. (cited on p. 101)

[318] F. Iocco, M. Pato, G. Bertone, and P. Jetzer. Dark Matter distribution in the Milky Way: microlensing and dynamical constraints. JCAP **1111**, 029 (2011). inSPIRE. (cited on pages 101, 146, and 147)

[319] Y.-Z. Chen, J.-M. Chen, Y.-A. Luo, H. Shen, and X.-Q. Li. Effects of nuclear deformation on the form factor for direct dark matter detection. Chin.Phys. **C36**, 505 (2012). inSPIRE. (cited on p. 101)

[320] M. Ressell and D. Dean. Spin dependent neutralino - nucleus scattering for A approximately 127 nuclei. Phys.Rev. **C56**, 535 (1997). inSPIRE. (cited on p. 114)

[321] J. Menendez, D. Gazit, and A. Schwenk. Spin-dependent WIMP scattering off nuclei.

Phys.Rev. **D86**, 103511 (2012). inSPIRE. (cited on p. 114)

[322] M. Hjorth-Jensen, T. Kuo, and E. Osnes. Realistic effective interactions for nuclear systems. Phys.Rept. **261**, 125 (1995). inSPIRE. (cited on pages 114 and 133)

[323] V. Stoks, R. Klomp, C. Terheggen, and J. de Swart. Construction of high quality N N potential models. Phys.Rev. **C49**, 2950 (1994). inSPIRE. (cited on p. 114)

[324] E. Caurier, J. Menendez, F. Nowacki, and A. Poves. The Influence of pairing on the nuclear matrix elements of the neutrinoless beta beta decays. Phys.Rev.Lett. **100**, 052503 (2008). inSPIRE. (cited on p. 114)

[325] J. Amare, B. Beltran, S. Cebrian, N. Coron, G. Dambier, *et al.* Scintillation of sapphire under particle excitation at low temperature. J.Phys.Conf.Ser. **39**, 200 (2006). inSPIRE. (cited on p. 127)

[326] M. Luca, N. Coron, C. Dujardin, H. Kraus, V. Mikhailik, *et al.* Scintillating and optical spectroscopy of Al(2)O(3): Ti for dark matter searches. Nucl.Instrum.Meth. **A606**, 545 (2009). inSPIRE. (cited on p. 127)

[327] M. Garny, A. Ibarra, M. Pato, and S. Vogl. On the spin-dependent sensitivity of XENON100. Phys.Rev. **D87**, 056002 (2013). inSPIRE. (cited on p. 133)

[328] N. Coron, E. Garcia, J. Gironnet, J. Leblanc, P. de Marcillac, *et al.* Thermal relative efficiency factor for recoiling Pb-206 nuclei in a sapphire bolometer. Phys.Lett. **B659**, 113 (2008). inSPIRE. (cited on p. 135)

[329] C. Sailer, B. Lubsandozhiev, C. Strandhagen, and J. Jochum. Low temperature light yield measurements in NaI and NaI(Tl). Eur.Phys.J. **C72**, 2061 (2012). inSPIRE. (cited on p. 135)

[330] W. Atwood *et al.* The Large Area Telescope on the Fermi Gamma-ray Space Telescope Mission. Astrophys.J. **697**, 1071 (2009). inSPIRE. (cited on pages 142 and 156)

[331] F. Prada, A. Klypin, J. Flix Molina, M. Martinez, and E. Simonneau. Dark Matter Annihilation in the Milky Way Galaxy: Effects of Baryonic Compression. Phys.Rev.Lett. **93**, 241301 (2004). inSPIRE. (cited on pages 142, 145, 146, and 148)

[332] Y. Zeldovich, A. Klypin, M. Y. Khlopov, and V. Chechetkin. Astrophysical constraints on the mass of heavy stable neutral leptons. Sov.J.Nucl.Phys. **31**, 664 (1980). inSPIRE. (cited on pages 142 and 145)

[333] G. R. Blumenthal, S. Faber, R. Flores, and J. R. Primack. Contraction of Dark Matter Galactic Halos Due to Baryonic Infall. Astrophys.J. **301**, 27 (1986). inSPIRE. (cited on pages 142 and 145)

[334] O. Y. Gnedin, A. V. Kravtsov, A. A. Klypin, and D. Nagai. Response of dark matter halos to condensation of baryons: Cosmological simulations and improved adiabatic contraction model. Astrophys.J. **616**, 16 (2004). inSPIRE. (cited on pages 142 and 145)

[335] M. Gustafsson, M. Fairbairn, and J. Sommer-Larsen. Baryonic Pinching of Galactic Dark Matter Haloes. Phys.Rev. **D74**, 123522 (2006). inSPIRE. (cited on pages 142 and 145)

[336] P. Colin, O. Valenzuela, and A. Klypin. Bars and cold dark matter halos. Astrophys.J. **644**, 687 (2006). inSPIRE. (cited on pages 142 and 145)

[337] P. B. Tissera, S. D. White, S. Pedrosa, and C. Scannapieco. Dark matter response to galaxy formation. Mon. Not. Roy. Astron. Soc. **406**, 922 (2010). inSPIRE. (cited on pages 142 and 145)

[338] O. Y. Gnedin, D. Ceverino, N. Y. Gnedin, A. A. Klypin, A. V. Kravtsov, *et al.* Halo Contraction Effect in Hydrodynamic Simulations of Galaxy Formation (2011). inSPIRE. (cited on pages 142, 145, and 146)

[339] M. Zemp, O. Y. Gnedin, N. Y. Gnedin, and A. V. Kravtsov. The impact of baryon physics on the structure of high-redshift galaxies. Astrophys.J. **748**, 54 (2012). inSPIRE. (cited on pages 142 and 145)

[340] J. Sommer-Larsen and M. Limousin. Moderate Steepening of Galaxy Cluster Dark Matter Profiles by Baryonic Pinching. Mon. Not. Roy. Astron. Soc. **408**, 1998 (2010). inSPIRE. (cited on pages 142 and 145)

[341] Y. Mambrini, C. Munoz, E. Nezri, and F. Prada. Adiabatic compression and indirect detection of supersymmetric dark matter. JCAP **0601**, 010 (2006). inSPIRE. (cited on pages 142, 145, and 150)

[342] Fermi-LAT Observations of the Diffuse Gamma-Ray Emission: Implications for Cosmic Rays and the Interstellar Medium. Astrophys.J. **750**, 3 (2012). inSPIRE. (cited on p. 143)

[343] A. V. Kravtsov, A. A. Klypin, J. S. Bullock, and J. R. Primack. The Cores of dark matter dominated galaxies: Theory versus observations. Astrophys.J. **502**, 48 (1998).

inSPIRE. (cited on p. 144)

[344] A. W. Graham, D. Merritt, B. Moore, J. Diemand, and B. Terzic. Empirical models for Dark Matter Halos. I. Nonparametric Construction of Density Profiles and Comparison with Parametric Models. Astron.J. **132**, 2685 (2006). inSPIRE. (cited on p. 144)

[345] B. Moore, T. R. Quinn, F. Governato, J. Stadel, and G. Lake. Cold collapse and the core catastrophe. Mon.Not.Roy.Astron.Soc. **310**, 1147 (1999). inSPIRE. (cited on p. 144)

[346] J. Diemand, M. Kuhlen, P. Madau, M. Zemp, B. Moore, *et al.* Clumps and streams in the local dark matter distribution. Nature **454**, 735 (2008). inSPIRE. (cited on p. 144)

[347] J. Stadel, D. Potter, B. Moore, J. Diemand, P. Madau, *et al.* Quantifying the heart of darkness with GHALO - a multi-billion particle simulation of our galactic halo. Mon. Not. Roy. Astron. Soc. **398**, L21 (2009). inSPIRE. (cited on p. 144)

[348] V. Springel, J. Wang, M. Vogelsberger, A. Ludlow, A. Jenkins, *et al.* The Aquarius Project: the subhalos of galactic halos. Mon.Not.Roy.Astron.Soc. **391**, 1685 (2008). inSPIRE. (cited on p. 144)

[349] S. Ando and D. Nagai. Fermi-LAT constraints on dark matter annihilation cross section from observations of the Fornax cluster. JCAP **1207**, 017 (2012). inSPIRE. (cited on p. 145)

[350] S. Mashchenko, H. Couchman, and J. Wadsley. Cosmological puzzle resolved by stellar feedback in high redshift galaxies. Nature **442**, 539 (2006). inSPIRE. (cited on p. 145)

[351] S. Mashchenko, J. Wadsley, and H. Couchman. Stellar Feedback in Dwarf Galaxy Formation. Science **319**, 174 (2008). inSPIRE. (cited on p. 145)

[352] A. Pontzen and F. Governato. How supernova feedback turns dark matter cusps into cores. Mon. Not. Roy. Astron. Soc. **421**, 3464 (2012). inSPIRE. (cited on p. 145)

[353] F. Governato, C. Brook, L. Mayer, A. Brooks, G. Rhee, *et al.* At the heart of the matter: the origin of bulgeless dwarf galaxies and Dark Matter cores. Nature **463**, 203 (2010). inSPIRE. (cited on pages 145 and 146)

[354] A. V. Maccio', G. Stinson, C. B. Brook, J. Wadsley, H. Couchman, *et al.* Halo expansion in cosmological hydro simulations: towards a baryonic solution of the cusp/core problem in massive spirals. Astrophys. J. Lett. **744**, L9 (2012). inSPIRE. (cited on p. 145)

[355] A. Di Cintio, C. B. Brook, A. V. Maccio, G. S. Stinson, A. Knebe, *et al.* The dependence of dark matter profiles on the stellar to halo mass ratio: a prediction for cusps vs cores (2013). inSPIRE. (cited on p. 146)

[356] J. Guedes, S. Callegari, P. Madau, and L. Mayer. Forming Realistic Late-Type Spirals in a LCDM Universe: The Eris Simulation. Astrophys.J. **742**, 76 (2011). inSPIRE. (cited on p. 146)

[357] F. Nesti and P. Salucci. The Dark Matter halo of the Milky Way, AD 2013. JCAP **1307**, 016 (2013). inSPIRE. (cited on pages 147 and 150)

[358] A. Birkedal, K. T. Matchev, M. Perelstein, and A. Spray. Robust gamma ray signature of WIMP dark matter (2005). inSPIRE. (cited on pages 148 and 163)

[359] T. Bringmann, L. Bergstrom, and J. Edsjo. New Gamma-Ray Contributions to Supersymmetric Dark Matter Annihilation. JHEP **0801**, 049 (2008). inSPIRE. (cited on p. 148)

[360] T. Sjostrand, S. Mrenna, and P. Z. Skands. PYTHIA 6.4 Physics and Manual. JHEP **0605**, 026 (2006). inSPIRE. (cited on p. 148)

[361] T. Bringmann, M. Doro, and M. Fornasa. Dark Matter signals from Draco and Willman 1: Prospects for MAGIC II and CTA. JCAP **0901**, 016 (2009). inSPIRE. (cited on p. 148)

[362] A. Pinzke, C. Pfrommer, and L. Bergstrom. Prospects of detecting gamma-ray emission from galaxy clusters: cosmic rays and dark matter annihilations. Phys.Rev. **D84**, 123509 (2011). inSPIRE. (cited on p. 149)

[363] L. Gao, C. Frenk, A. Jenkins, V. Springel, and S. White. Where will supersymmetric dark matter first be seen? Mon.Not.Roy.Astron.Soc. **419**, 1721 (2012). inSPIRE. (cited on p. 149)

[364] S. Campbell, B. Dutta, and E. Komatsu. Effects of Velocity-Dependent Dark Matter Annihilation on the Energy Spectrum of the Extragalactic Gamma-ray Background. Phys.Rev. **D82**, 095007 (2010). inSPIRE. (cited on p. 149)

[365] F. Ferrer and D. R. Hunter. The impact of the phase-space density on the indirect detection of dark matter. JCAP **1309**, 005 (2013). inSPIRE. (cited on p. 149)

[366] N. Fornengo, L. Pieri, and S. Scopel. Neutralino annihilation into gamma-rays in the Milky Way and in external galaxies. Phys.Rev. **D70**, 103529 (2004). inSPIRE.

(cited on p. 150)

[367] M. Cirelli and P. Panci. Inverse Compton constraints on the Dark Matter e+e- excesses. Nucl.Phys. **B821**, 399 (2009). inSPIRE. (cited on p. 152)

[368] A. W. Strong, I. V. Moskalenko, and O. Reimer. Diffuse continuum gamma-rays from the galaxy. Astrophys.J. **537**, 763 (2000). inSPIRE. (cited on pages 152 and 154)

[369] T. Delahaye, R. Lineros, F. Donato, N. Fornengo, and P. Salati. Positrons from dark matter annihilation in the galactic halo: Theoretical uncertainties. Phys.Rev. **D77**, 063527 (2008). inSPIRE. (cited on p. 153)

[370] D. Maurin, F. Donato, R. Taillet, and P. Salati. Cosmic rays below z=30 in a diffusion model: new constraints on propagation parameters. Astrophys.J. **555**, 585 (2001). inSPIRE. (cited on p. 153)

[371] Boxlib. webpage. (cited on p. 153)

[372] M. Ackermann *et al.* The Fermi Large Area Telescope On Orbit: Event Classification, Instrument Response Functions, and Calibration. Astrophys.J.Suppl. **203**, 4 (2012). inSPIRE. (cited on p. 156)

[373] F. science tools site. webpage. (cited on p. 156)

[374] F. Loparco and M. Mazziotta. A Bayesian approach to evaluate confidence intervals in counting experiments with background. Nucl.Instrum.Meth. **A646**, 167 (2011). inSPIRE. (cited on pages 160 and 161)

[375] M. Cirelli, P. Panci, and P. D. Serpico. Diffuse gamma ray constraints on annihilating or decaying Dark Matter after Fermi. Nucl.Phys. **B840**, 284 (2010). inSPIRE. (cited on p. 164)

[376] M. Papucci and A. Strumia. Robust implications on Dark Matter from the first FERMI sky gamma map. JCAP **1003**, 014 (2010). inSPIRE. (cited on p. 164)

[377] J. Han, C. S. Frenk, V. R. Eke, L. Gao, S. D. White, *et al.* Constraining Extended Gamma-ray Emission from Galaxy Clusters. Mon.Not.Roy.Astron.Soc. **427**, 1651 (2012). inSPIRE. (cited on p. 164)

[378] T. Daylan, D. P. Finkbeiner, D. Hooper, T. Linden, S. K. N. Portillo, *et al.* The Characterization of the Gamma-Ray Signal from the Central Milky Way: A Compelling Case for Annihilating Dark Matter (2014). inSPIRE. (cited on pages 169, 170, and 228)

[379] T. Nihei, L. Roszkowski, and R. Ruiz de Austri. Exact cross-sections for the neutralino WIMP pair annihilation. JHEP **0203**, 031 (2002). inSPIRE. (cited on pages 179, 181, and 182)

[380] E. Laermann and O. Philipsen. The Status of lattice QCD at finite temperature. Ann.Rev.Nucl.Part.Sci. **53**, 163 (2003). inSPIRE. (cited on p. 180)

[381] K. A. Olive. The Thermodynamics of the Quark - Hadron Phase Transition in the Early Universe. Nucl.Phys. **B190**, 483 (1981). inSPIRE. (cited on p. 180)

[382] K. A. Olive. The Violent Universe: The Big Bang 149–196 (2010). inSPIRE. (cited on p. 180)

[383] T. given by P. Cushman at IDM2012. pdf. (cited on pages 185 and 228)

[384] M. Selvi. Study of the performances of the shield and muon veto of the XENON1T experiment. PoS **IDM2010**, 053 (2011). inSPIRE. (cited on pages 185 and 228)

[385] T. given by Hugh Lippincott (Fermilab) at TAUPP 2011. . (cited on pages 185 and 228)

List of acronyms

This is a list of the acronyms used in the text (in alphabetical order).

1D	One Dimension
2D	Two Dimensions
3D	Three Dimensions
BBN	Big Bang Nucleosynthesis
BM	Benchmark points
BSM	Beyond the Standard Model
CDM	Cold Dark Matter
CMB	Cosmic Microwave Background
DE	Dark Energy
DM	Dark Matter
dSph	Dwarf Spheroidal Galaxies
EM	Electromagnetic
EWSB	ElectroWeak Symmetry Breaking
FIMP	Feebly Interacting Massive Particles
FSR	Final State Radiation
GC	Galactic Center
GH	Galactic Halo
GMSB	Gauge Mediated Supersymmetry Breaking
HDM	Hot Dark Matter
IACT	Imaging Atmospheric Cherenkov Telescopes
ICS	Inverse Compton Scattering
KK	Kaluza-Klein
LHC	Large Hadron Collider
LSP	Lightest Supersymmetric Particle
LSS	Large Scale Structure
MB	Maxwell-Boltzmann
MOND	Modified Newton Dynamics
MSSM	Minimal Supersymmetric Standard Model
NFW	Navarro-Frenk-White
NMSSM	Next to Minimal Supersymmetric Standard Model
RGE	Renormalization Group Equation
SD	Spin-Dependent
ShM	Shell-Model

SHM	Standard Halo Model
SI	Spin-Independent
SUGRA	Supergravity
SM	Standard Model
SUSY	Supersymmetry
UED	Universal Extra Dimensions
UV	Ultra Violet
VEV	Vacuum Expectation Value
WIMP	Weakly Interacting Massive Particle

List of Figures

List of Tables

List of publications

Publications related to the content of this Thesis:

1. *Low-mass right-handed sneutrino dark matter: SuperCDMS and LUX constraints and the Galactic Centre gamma-ray excess*. David G. Cerdeño, **Miguel Peiró** and S. Robles.
   arXiv:1404.2572.

2. *Scintillating bolometers: a key for determining WIMP parameters*. David G. Cerdeño, C. Cuesta, M. Fornasa, E. Garcia, C. Ginestra, C. Marcos, M. Martinez, Y. Ortigoza, **Miguel Peiró**, J. Puimedon and M.L. Sarsa. Accepted in **IJMPA**.
   arXiv:1403.3539.

3. *Constraints on WIMP Annihilation for Contracted Dark Matter in the Inner Galaxy with the Fermi-LAT*. German A. Gomez-Vargas, Miguel A. Sanchez-Conde, Ji-Haeng Huh, **Miguel Peiró**, Francisco Prada, Aldo Morselli, Anatoly Klypin, David G. Cerdeño, Yann Mambrini and Carlos Muñoz. **JCAP 1310 (2013) 029**.
   arXiv:1308.3515.

4. *Collider signatures of a light NMSSM pseudoscalar in neutralino decays in the light of LHC results*. David G. Cerdeño, Pradipta Ghosh, Chan Beom Park and **Miguel Peiró**. **JHEP 1402 (2014) 048**.
   arXiv:1307.7601.

5. *Complementarity of dark matter direct detection: the role of bolometric targets*. David G. Cerdeño, C. Cuesta, M. Fornasa, E. Garcia, C. Ginestra, Ji-Haeng Huh,

M. Martinez, Y. Ortigoza, **Miguel Peiró**, J. Puimedon, L.M. Robledo and M.L. Sarsa. **JCAP 1307 (2013) 028**.
arXiv:1304.1758.

6. *Nuclear uncertainties in the spin-dependent structure functions for direct dark matter detection* David G. Cerdeño, Mattia Fornasa, Ji-Haeng Huh and **Miguel Peiró**. **Phys.Rev. D87 (2013) 023512**.
arXiv:1208.6426.

7. *Very light right-handed sneutrino dark matter in the NMSSM*. David G. Cerdeño, Ji-Haeng Huh, **Miguel Peiró** and Osamu Seto. **JCAP 1111 (2011) 027**.
arXiv:1108.0978.

Agradecimientos

Es dificil expresar mis agradecimientos a tantas y tantas personas de forma tan breve. Es más dificil aún cuando uno se da cuenta que esta tesis no es solo fruto de un trabajo de cuatro años, sino de muchísimos más.

Primero agradecer a David G. Cerdeño por brindarme la oportunidad de empezar esta carrera, y por enseñarme a dar los primeros pasos en mi vida como investigador. Quería también agradecer a Carlos Muñoz hacerme partícipe del proyecto Multidark, a cuya gente debo estar igualmente agradecido.

A lo largo de estos cuatro años he tenido que gente que me ha enseñado mucho en el mundo de la investigación. Quería agradecer especialmente a tres personas, que aunque jóvenes aún, derrochan conocimientos. Gracias Ji-Haeng Huh, por tener la paciencia necesaria para enseñarme en mis inicios, gracias Mattia Fornasa por estar siempre dispuesto a ayudarme y escucharme, y gracias Pradipta Ghosh por contagiarme tu entusiasmo hacia la ciencia. No me puedo olvidar de otros que también han estado presentes como Chan Beom Park, Fabio Iocco, Krzysztof Rolbiecki...Quiero también mostrar mi agradecimiento al grupo de astropartículas de Universidad de Zaragoza, Maria Luisa Sarsa, Eduardo García, María Martinez, Ysrael Ortigoza, Clara Cuesta y otros muchos más, de los cuales he aprendido mucho de la parte experimental de detección directa.

A toda la gente del IFT que me ha acompañado este tiempo, empezando por mis compis de despacho Leyre y Germán. A Victor porque me ha ayudado mucho. A Susana por ser la más mítica Multidarkiana y ayudarnos a todos en todo momento. Al equipo de informática y especialmente a Andrés. A la madre de todos, Isabel. A unas estudiantes siempre dispuestas a ayudar como lo son Sandra y Cristina. Y en general a mucha buena gente que estuvo o está como Charo, Ginevra, Antonio, Amadeo, Diego, Pablo, Juan, Miguel, y seguro que me dejo a muchos, que hacen de el IFT un sitio muy agradable.

A todos mis amigos con los que he crecido de la mano, aunque estemos lejos nada ha cambiado entre nosotros y volveremos algún día con más fuerza. A Javi por haberme enseñado no solo como mirar a la física de forma diferente sino a la vida, y por haberme

hecho feliz en tantos y tantos momentos. A Diego, el mayor aventurero que conozco y uno de los pocos que me arrancan una sonrisa cuando le da la gana. A Juli, porque aunque no tenga colegas tiene un muy buenos amigos. A Pablo M. por ser tan buen amigo, por saber escuchar tan tan bien y por estar ahi incondicionalmente. A Pablo L. por ser como eres. Por supuesto no me olvido del trio calavera, Alvarito, Paez y Marcos. También a mis amigas: a mis Martas, Cris, Helena, Laura, Sara y Blanca, os quiero mucho. Finalmente, a los del Flori, con un recuerdo especial a los que nos dejaron.

A la gente de las mesas, porque han hecho del paso por la Universidad un suspiro, eso si, lleno de risas y anécdotas. Fito, gracias por haberme contagiado y haberme enseñado a querer tanto la física, y por haber hecho que me ría tanto contigo, eres como un hermano. Manuela, o Manu mejor, gracias por ser como eres y haberme aguantado tanto estando siempre dispuesta a ayudarme. Peibol, gracias por haberme acompañado en la aventura teórica y por haberme ayudado con tantas y tantas tedias, además haces que la Primavera se vea de otra manera. A Drino por ser un auténtico Zinedine. A Clara, por ser tan Clara. Y a Edu por ser tan Edu. Gracias Pepe por tu visiń tán cuántica del mundo. A Paloma, porque siempre me da que pensar. A Adri, porque su fruta en mal estado siempre consigue que me ría. Y en general a todos, Luis, Emilio, Ernesto, Alba y Vicky.

Muchas gracias Eduardo ya que sin ti ni estaría escribiendo esto ni miraría al mundo con los ojos con los que lo hago, con menos miedo. A la gente de las clases de los Domingos, a todos, porque creo que nos dais cuenta de que me enseñais más de lo que yo os enseño. A la gente del teatro, por hacer tan fácil que todos nos acerquemos al Arte. Gracias a todos por creer en mi de forma tan sincera, por darme vuestro empuje y vuestras fuerzas. Mención especial a los que habéis estado conmigo más cerca desde hace tanto: Antonio, Pablo(s), Guillermo, Andres, Juan, Laura, Badia, Helena, Nereida, Carmen, Clara, Julia, Edu, Katia, Manu, Hugo, Anne Sophie.

A mi familia debo estar muy muy agradecido. Lo primero de todo a mis padres. Siento que todo lo que escriba será poco. Siempre me habéis ayudado mucho, en lo buenos y en los malos momentos. Me habéis querido y cuidado mucho, siempre sin condiciones. Gracias Papa y Mama porque hemos conseguido esto juntos, esto es tan mío como vuestro, y conseguiremos muchas más cosas juntos. A mi hermana Ana, porque a pesar de todo, siempre he sabido que me has querido muchísimo. Además, también yo estoy muy orgulloso de ti, porque has traído a este mundo a un niño extraordinario, y estas haciendolo muy muy bien. Por supuesto, a mi sobrino Juan, que aunque él no sea consciente me dá muchísima fuerza. A mi abuela María que esté donde esté seguro que esta muy muy orgullosa. Gracias a mi abuela Uli. A mi abuelo Rafael, el primer científico de la familia.

A mis tías, tíos, primas y primos. A Raquel por compartir dos años geniales conmigo. A Miguel, que ya eres uno más.

Finalmente a Paula. Muchas gracias por hacer este camino conmigo. Esta tesis también te pertenece a ti. Me has dado ánimos, fuerzas, me has cuidado, ayudado, pero sobre todas las cosas me has querido mucho y eso lo hace todo mas fácil.